



**NTNU – Trondheim**  
Norwegian University of  
Science and Technology

# Use of Underwater Hyperspectral Imagery for geological characterization of the seabed

**Sigrun Melve Aarrestad**

Geology

Submission date: December 2014

Supervisor: Steinar Løve Ellefmo, IGB

Co-supervisor: Geir Johnsen, IBI  
Terje Thorsnes, NGU  
Margaret Dolan, NGU

Norwegian University of Science and Technology  
Department of Geology and Mineral Resources Engineering



# Abstract

This master's thesis presents an optical mapping method, Hyperspectral Imaging (HI) and its application to marine geological mapping - Underwater Hyperspectral Imaging (UHI). UHI uses similar technology as terrestrial HI to detect and identify objects on the seafloor by their optical signatures (reflectance spectra) in visible light (400-700 nm). The main aim of the thesis is to determine properties of marine sediments that can be detected and identified by UHI, and secondly to evaluate its applicability in context of established mapping methods in marine geology. The thesis focuses on carbonate content in marine sediments and the potential use of UHI for mapping and monitoring bioclastic carbonate sediments and other carbonate deposits on the seabed.

The work is based on literature studies of established marine geology mapping methods, previous work on geological HI and the development of UHI, in addition to new laboratory work. Spectral reflectance of different minerals, marine sediments with varying carbonate content and carbonate crusts were measured. A hyperspectral imager attached to a stereomicroscope was used to capture spectral reflectance from the samples and to create hyperspectral images. A Jaz spectrometer was used to validate the reflectance spectra obtained from the hyperspectral images.

Both the HI and the Jaz results showed reflectance spectra of dry samples and samples submerged in seawater. The two spectrometers showed relatively similar results, apart from the red (>600 nm) and blue (<500 nm) parts of the spectra, indicating that the Jaz spectrometer has better sensitivity than the HI spectrometer. Supervised classification of hyperspectral images showed that it is possible to classify the samples by their optical signature.

This study shows that UHI can supplement marine geological mapping with remotely sensed geochemical data of high resolution. UHI can detect geochemical properties such as changes in carbonate content based on the whiteness of the sediment, and iron and organic content based on spectral absorption features. Variations in grain size can be detected by varying reflectance intensity. Challenges include detection of marine minerals with absorption features only in the ultraviolet and infrared part of the electromagnetic spectrum. Such minerals include calcite and aragonite, thus UHI classification of carbonate deposits on the seabed has its limitations.



# Sammendrag

Masteroppgaven presenterer en optisk kartleggingsmetode, hyperspektral avbildning (HI) for anvendelse i maringeologisk kartlegging, kalt undervanns hyperspektral avbildning (UHI). Metoden bruker en tilsvarende teknologi som landbasert HI for å måle spektral reflektans av synlig lys (400-700 nm) fra havbunnen, som kan brukes til å identifisere objekter basert på unike optiske signaturer. Formålet med masteroppgaven er å bestemme hvilke marine sedimentegenskaper som kan gjenkjennes og identifiseres ved hjelp av UHI, med fokus på karbonatsedimenter. Det er videre gjort en vurdering av UHI for bruk i kartlegging og overvåkning av bioklastiske sedimenter og andre karbonatforekomster på havbunnen.

Oppgaven er basert på et litteraturstudie av etablerte maringeologiske kartleggingsmetoder, tidligere studier av geologisk HI og utviklingen av UHI, i tillegg til nytt laboratoriearbeid. Reflektans fra forskjellige prøver av marine mineraler, sedimenter med varierende karbonatinnhold samt karbonatskorper ble målt. Målingene ble utført med en hyperspektral avbilder koblet til et stereomikroskop som produserte hyperspektrale bilder. Et Jaz spektrometer brukt for å bekrefte reflektansspektrene fra de hyperspektrale bildene.

Både HI- og Jaz-resultatene viser reflektans-spekter av tørre prøver og prøver i sjøvann. Begge metodene viste relativt lik optisk signatur av prøvene, men i den blå (<500 nm) og røde (>600 nm) delen av spektrene var Jaz spektrometeret mer sensitivt enn HI spektrometeret. Kontrollert klassifisering av prøvene viste at prøvene kan klassifiseres basert på optiske signaturer i synlig lys.

Studiet viser at UHI kan bidra med høyoppløselige fjernmålinger av geokjemiske egenskaper til marine sedimenter som et supplement til etablerte maringeologiske kartleggingsmetoder. Endringer i karbonatinnhold kan måles ved å se på hvithetsgrad i sedimentene, mens jerninnhold og organisk innhold kan identifiseres fra formen til spekteret. Variasjoner i kornstørrelse kan bestemmes av endringer i reflektansintensitet. Utfordringer kan oppstå ved bestemmelse av mineraler som ikke absorberer synlig lys, men som absorberer ultrafiolett og infrarødt lys. Reflektans i disse delene av det elektromagnetiske spekteret er vanskelig å måle under vann. Kalsitt og aragonitt er eksempler på slike mineraler, UHI har således sine begrensninger ved bruk i kartlegging av karbonatforekomster på havbunnen.



# Preface

The master's thesis is written at the Department of Geology and Mineral Resources Engineering (IGB) at the Norwegian University of Science and Technology (NTNU). The laboratory work was carried out at Trondhjem Biological Station (TBS), which is NTNU's center for marine biological research, located at Trolla in Trondheim. The thesis is written in co-operation with the Geological Survey of Norway (NGU), which has been responsible for provision of some of the geological material for the laboratory work.

The main supervisor at NTNU has been Associate Professor Steinar Løve Ellefmo (IGB), and assistant supervisors at NTNU have been Professor Geir Johnsen (Department of Biology) and Associate Professor Murat Van Ardelan (Department of Chemistry). Supervisors at NGU have been Margaret Dolan and Terje Thorsnes.

I would like to express my gratitude to all the people helping me with this thesis. First of all, I would like to thank Steinar and Geir for brilliant guidance and their great engagement in this project, Murat for his help with the setup of the laboratory experiments, and Ragnhild Pettersen and Inga Aamot for teaching me how to perform HI- and Jaz-analyses.

At NGU, I would first like to thank Terje for introducing me to UHI for the first time at a Midsummer Eve gathering in my parents' neighborhood, selecting me as a master student on this project and providing me summer internships at NGU. It has been very interesting to learn about marine geology and the new mapping technologies that are being developed. Secondly, I would like to thank Margaret for guidance and help with the thesis, and everyone that provided me with geological material for my laboratory work.

I would also like to thank my friends and family for supporting me through this last hectic time of my studies. And at last, but not least, an extra thank to my dad for reading through my thesis and giving me helpful advices, to Matias for being patient, listening to my whining and encouraging me, and to all my classmates that did not finish their studies in five years and joined the "sixth graders". You rock!

Sigrun Melve Aarrestad, Trondheim 14.12.2014





# Table of Contents

Abstract .....	I
Sammendrag .....	III
Preface .....	V
Table of Contents .....	VII
List of Figures .....	XI
List of Tables .....	XVI
<b>Chapter 1 Introduction .....</b>	<b>1</b>
1.1 Background .....	1
1.2 Aims, outline and limitations .....	3
1.2.1 The aims of the study .....	3
1.2.2 Limitations .....	3
1.2.3 Outline .....	4
<b>Chapter 2 Marine carbonate sediments and geological mapping of the seabed .....</b>	<b>7</b>
2.1 Marine sedimentation of calcium carbonate .....	7
2.1.1 Properties of marine sediments .....	7
2.1.2 Abundant minerals in marine sediments .....	9
2.1.3 Calcite and aragonite .....	9
2.1.4 Carbonate deposits on the seabed .....	10
2.1.5 Environmental stressors on CaCO <sub>3</sub> in seawater .....	11
2.2 Traditional mapping of marine sediments .....	14
2.2.1 Acoustic methods .....	15
2.2.2 Video-analysis of the seabed .....	16
2.2.3 Sampling of sediments .....	17
2.2.4 Mapping of bioclastic sediments and cold-water coral reefs .....	17

## Table of Contents

---

2.3	Chapter summary.....	19
<b>Chapter 3 Marine optics and optical remote sensing.....</b>		<b>21</b>
3.1	Optical properties of the sea and of geological material .....	21
3.1.1	Light theory .....	21
3.1.2	Apparent and inherent optical properties of seawater .....	23
3.1.3	Case 1 and case 2 waters .....	25
3.1.4	Remote sensing reflectance .....	25
3.1.5	Optical properties of geological material .....	26
3.2	Optical remote sensing .....	29
3.2.1	Principles of multispectral and hyperspectral remote sensing .....	29
3.2.2	Classification based on optical signature .....	30
3.2.3	The start of marine optical remote sensing - mapping ocean color.....	32
3.2.4	Case studies related to geological hyperspectral imaging.....	33
3.2.5	Case studies related to hyperspectral imaging of the seabed .....	37
3.3	Underwater Hyperspectral Imaging.....	45
3.3.1	The underwater hyperspectral imager .....	45
3.3.2	Underwater platforms.....	45
3.3.3	Optical processing .....	46
3.3.4	Previous work on UHI at NTNU.....	47
3.4	Chapter summary.....	49
<b>Chapter 4 Materials and Methods .....</b>		<b>51</b>
4.1	Materials .....	51
4.1.1	Mineral samples .....	51
4.1.2	The artificial sediment samples.....	53
4.1.3	Natural sediment samples.....	54
4.1.4	Carbonate crust samples .....	57
4.2	Methods .....	59

---

4.2.1	Artificial sediment mix.....	59
4.2.2	Submerging samples .....	60
4.2.3	Hyperspectral imaging .....	60
4.2.4	Data processing using the software <i>yaPlaySpecX</i> .....	63
4.2.5	Supervised classification using <i>Image Calculator</i> .....	65
4.2.6	Jaz spectrometer .....	66
4.2.7	Sources of errors and variability .....	69
<b>Chapter 5</b>	<b>Results</b> .....	<b>71</b>
5.1	General description of laboratory results.....	71
5.2	Results from the mineral samples.....	73
5.2.1	Reflectance spectra.....	74
5.2.2	Supervised classification .....	80
5.3	Results from the artificial sediment samples.....	81
5.3.1	Reflectance spectra.....	83
5.3.2	Supervised classification.....	85
5.4	Results from the natural sediment samples .....	86
5.4.1	Reflectance spectra.....	87
5.4.2	Supervised classification .....	90
5.5	Results from the carbonate crusts.....	91
5.5.1	Reflectance spectra.....	94
5.5.2	Supervised classification .....	96
<b>Chapter 6</b>	<b>Discussion</b> .....	<b>97</b>
6.1	Discussion of laboratory results .....	97
6.1.1	Hyperspectral Images .....	97
6.1.2	Reflectance spectra.....	98
6.1.3	Supervised classification .....	104
6.1.4	Evaluation of the methodology of the laboratory work .....	106

## Table of Contents

---

6.2	Use of UHI in marine geological mapping.....	107
6.2.1	Mapping marine sediments .....	107
6.2.2	Application in industry .....	111
6.2.3	Challenges and limitation of UHI for geological purposes.....	112
<b>Chapter 7</b>	<b>Conclusions and recommendations .....</b>	<b>117</b>
7.1	Conclusions .....	117
7.2	Further work .....	118
<b>Chapter 8</b>	<b>References .....</b>	<b>119</b>

### Appendices

A - RGB images of all samples

B - Hyperspectral images

C - HI spectra of each sample

D - Visual description of natural sediment samples provided by NGU

# List of Figures

The list of figures includes shortened capture-texts.

<b>Figure 2.1</b> Udden-Wentworth grain-size scale for clastic sediment (Boggs, 2010; Wentworth, 1922).....	8
<b>Figure 2.2</b> Multibeam bathymetry and backscatter mapping of the seabed (to the left) provides data for interpretation. The figure is modified from Buhl-Mortensen et al. (2010).....	15
<b>Figure 2.3</b> Synthetic aperture sonar image showing a biogenic mound surrounded by a 30 m wide zone of bioclastic sediments (Bellec et al., 2014). ....	16
<b>Figure 3.1</b> Electromagnetic radiation from the sun (Sakshaug et al., 2009). ....	22
<b>Figure 3.2</b> In blue ocean water (to the left), the color is blue because the deepest penetrating wavelength is around 450 nm. Fjord water (to the right), has a green color where the deepest penetrating wavelength is around 550 nm (Sakshaug et al., 2009).....	23
<b>Figure 3.3</b> The absorption spectra of phytoplankton, CDOM, oceanic water and suspended non-living material (Johnsen et al., 2013). ....	25
<b>Figure 3.4</b> Diffuse reflectance spectra of natural (H-1) and synthetic hematite (H-2). Note the absorption features below 530 nm and at 850 nm (Sherman et al., 1982). ....	27
<b>Figure 3.5</b> Scattering efficiency ( $Q_{\text{scatt}}$ ) at 550 nm of single non-absorbing particles as a function of grain size. Dotted line show the scattering coefficient of a suspension with $1 \text{ g/m}^3$ of particles, $b$ = scattering coefficient (Kirk, 1994). ....	28
<b>Figure 3.6</b> Model illustrating the hyperspectral imager, the “push broom” technique and the spectral image cube (Volent et al., 2007).....	30
<b>Figure 3.7</b> The method of choosing monochromatic images from the spectral image cube to make specific identification images. (Volent, 2009).....	31
<b>Figure 3.8</b> Illustration of spectral mixing and unmixing (Malenovský et al., 2007).....	32
<b>Figure 3.9</b> A) Laboratory reflectance measurements of goethite, hematite and jarosite. B) Reflectance measurements of minerals from AVIRIS hyperspectral scanner (Sabins, 1999). 34	
<b>Figure 3.10</b> Reflectance spectra of soils with varying soil organic carbon (SOC) content (Bartholomeus et al., 2008). ....	36

**Figure 3.11** In situ optical reflectance spectra of bleached hermatypic coral, terrigenous mud and carbonate sand in a coral reef community. Modified from Hochberg et al. (2003). ..... 38

**Figure 3.12** Remote sensing reflectance,  $R_{RS}$ , of whittings, mud, sand and algal-covered grapestone sediment (Dierssen et al., 2009). ..... 39

**Figure 3.13** A) In situ reflectance spectrum of sand. B) Habitat map created using hyperspectral data. C) Substrate classes in figure B overlaid on model-derived bathymetry (Fearn et al., 2011). ..... 40-41

**Figure 3.14** Hyperspectral images from Collinderodden and Blixodden, Van Mijen-fjorden, Svalbard (2000). A) RGB image (490nm, 554nm and 633nm), B) Image in 730nm (IR), 578 and 490nm C) Unsupervised classification. (Johnsen et al., 2009). ..... 42

**Figure 3.15** Local hyperspectral imaging of a river plume taken from a mountain Platåfjellet (428 masl), Isfjorden, Svalbard (2007). (Johnsen et al., 2009). ..... 42

**Figure 3.16** A) RGB image of area 1. B) Classification results of kelp forest from BSC statistics. C) Correcting for the optical properties of the water. D) Results after DHE to increase contrast. (Volent et al., 2007). ..... 44

**Figure 3.17** Illustration of ROV and AUV as platforms for the underwater hyperspectral imager,  $n$  = amount of pixels in X-direction (Johnsen et al., 2013). ..... 46

**Figure 3.18** Unsupervised classification of minerals using different algorithms to identify OOI. (Johnsen et al., 2013). ..... 48

**Figure 3.19** Imagery from an underwater hyperspectral imager showing a 20 m transect of a coral reef (Ludvigsen et al., 2013). Image from Ecotone © (with permission). ..... 48

**Figure 4.1** Images of the minerals. M = muscovite, K = k-feldspar, Q = quartz,  $C_s$  = calcite marble (sand),  $C_c$  = calcite marble (clay),  $C_p$  = pure calcium carbonate, H = hematite. .... 52

**Figure 4.2** Artificial sediments. 0-100 % explain the weight percent of  $CaCO_3$  in the sediment. .... 54

**Figure 4.3** The selection of the samples provided by NGU around Magerøya in Finnmark, Norway. The figure is a modification of a map provided by NGU. .... 55

**Figure 4.4** Natural sediment samples. OM = organic mud, FS = fine sand, MS = medium sand, SS = shell sand, SG = shell gravel. .... 56

**Figure 4.5** Carbonate crusts. Original surface to the left (P1210035\_1B), fresh surface to the right (P1210006\_4A). The marked red squares are the areas captured by the HI. .... 58

---

<b>Figure 4.6</b> The splitter used to homogenously mixing the minerals. Yellow arrow show the sample input, black arrows show the separated samples.....	60
<b>Figure 4.7</b> A) HI setup. B) Setup of the samples measured by the HI in the moving directon. C) The setup of the submerged samples and the reference plate with a petri dish with seawater. ....	61
<b>Figure 4.8</b> Cuvette setup for dry and submerged samples. The samples on the same row were simultaneously measured by the hyperspectral imager.....	63
<b>Figure 4.9</b> Illustration of the method for making average spectra from HI images..	65
<b>Figure 4.10</b> Illustration of the improvement from one pixel spectrum to five and ten averaged pixels spectra, n = number of averaged pixels. ....	65
<b>Figure 4.11</b> Jaz spectrometer setup. ....	68
<b>Figure 4.12</b> Problems with submerging of samples. A) Floating of sediments on the top of the water surface (sample H1). B) Shirking of fine grained calcium carbonate (sample Cp1). ....	69
<b>Figure 4.13</b> Gray squares mark the area of the sample surface. Dark circles limit the areas used to make the average reflectance spectra. ....	70
<b>Figure 5.1</b> A) Upwelling radiance ( $L_u$ ) of the HI light source and B) The light source spectrum from the Jaz measurements..	72
<b>Figure 5.2</b> RGB-images and monochromatic images (570nm) of minerals (set 1) from the HI measurements. A) Dry samples. B) Submerged samples.....	73
<b>Figure 5.3</b> A) Average reflectance spectra from HI, M = muscovite, M(w) = submerged muscovite spectra. B) Reflectance spectra from Jaz spectrometer of muscovite samples.....	74
<b>Figure 5.4</b> A) Average reflectance spectra from HI, K = k-feldspar, K(w) = submerged k-feldspar. B) Reflectance spectra from Jaz spectrometer of k-feldspar samples. ....	75
<b>Figure 5.5</b> A) Average reflectance spectra from HI, Q = quartz, Q(w) = submerged quartz. B) Reflectance spectra from Jaz spectrometer of quartz samples. ....	75
<b>Figure 5.6</b> A) Average reflectance spectra from HI, Cs = calcite marble (sand), Cs(w) = submerged calcite marble (sand). B) Reflectance spectra from Jaz spectrometer of calcite marble (sand) samples. ....	76

**Figure 5.7** A) Average reflectance spectra from HI,  $C_c$  = calcite marble (clay),  $C_c(w)$  = submerged calcite marble (clay). B) Reflectance spectra from Jaz spectrometer of calcite marble (clay) samples..... 76

**Figure 5.8** A) Average reflectance spectra from HI,  $C_p$  = pure calcium carbonate,  $C_p(w)$  = submerged pure calcium carbonate. B) Reflectance spectra from Jaz spectrometer of calcium carbonate samples. .... 77

**Figure 5.9** Reflectance spectra from Jaz spectrometer of hematite samples..... 78

**Figure 5.10** Reflectance spectra from HI measurement used for making average spectra of hematite. .... 79

**Figure 5.11** Supervised classification of minerals with pixel defined classes ( $n=100$ ) on top of monochromatic images (570nm)..... 80

**Figure 5.12** RGB-images and monochromatic images (570nm) of artificial sediments..... 82

**Figure 5.13** A) Reflectance spectra of the dry artificial sediment samples from HI measurements. B) Reflectance spectra of the dry artificial sediment samples from Jaz measurements. .... 83

**Figure 5.14** A) Reflectance spectra of the submerged artificial sediments from HI measurements. B) Reflectance spectra of the submerged artificial sediment samples from Jaz measurements. .... 84

**Figure 5.15** Reflectance at 570 nm for dry sediments (A) and submerged sediments (B)..... 84

**Figure 5.16** Supervised classification of the artificial sediments ..... 85

**Figure 5.17** RGB-images and monochromatic images of natural sediments. A) Dry samples. B) Submerged samples. .... 86

**Figure 5.18** Average reflectance spectra from HI (A) and Jaz (B) of organic mud..... 87

**Figure 5.19** Average reflectance spectra from HI (A) and Jaz (B) of fine sand..... 87

**Figure 5.20** Average reflectance spectra from HI (A) and Jaz (B) of medium sand..... 88

**Figure 5.21** Average reflectance spectra from HI (A) and Jaz (B) of shell sand. .... 88

**Figure 5.22** Average reflectance spectra from HI (A) and Jaz (B) of shell gravel..... 89

**Figure 5.23** Supervised classification of the natural sediments. .... 90

**Figure 5.24** RGB-images and HI monochromatic images of the fresh surface of sample P1210006\_4A..... 92



---

<b>Figure 5.25</b> RGB-images and HI monochromatic images of a original surface of sample P1210035_1B.....	93
<b>Figure 5.26</b> Average reflectance spectra from HI and Jaz for dry and submerged carbonate crust (fresh surface). A) Cemented grains, B) Aragonite, C) Jaz .....	94
<b>Figure 5.27</b> Average reflectance spectra from HI and Jaz for dry and submerged carbonate crust (original surface). A) Surface a, B) Surface b, C) Surface c, D) Jaz.....	95
<b>Figure 5.28</b> Supervised classification of the fresh carbonate crust surface.....	96
<b>Figure 6.1</b> Illustration of the attenuation of light in seawater.. .....	113
<b>Figure 6.2</b> Illustration of the seabed and possible geological application of UHI.. .....	115

# List of Tables

**Table 6.1** Comparison of marine mapping methods. Numbers are based on subsea systems from Kongsberg Maritime (2014), except UHI numbers that are based on Johnsen et al. (2013)..... 111

# Chapter 1 Introduction

## 1.1 Background

Seabed mapping is often used to provide information on bathymetry, geology, biology and the environmental status of the ocean floor (Buhl-Mortensen et al., 2010). However, there are many challenges in seabed mapping. For instance, acoustic remote sensing is restricted by large water depths - and optical mapping methods are constrained by limited light penetration and turbidity in the oceans. To meet these challenges, new technologies are constantly being developed and tested, to widen our understanding and knowledge of the seabed. Co-operation between marine geology, biology and technology is important for further development of enabling technologies, and applications of these, both in marine science and for environmentally sustainable utilization of the seabed.

High quality maps of the seabed increase our understanding of relations between different marine processes. Marine geologists use acoustic remote sensing methods together with sediment sampling and underwater video and photography of the seabed to interpret and make maps (Buhl-Mortensen et al., 2010). Limitations of these approaches include the distance to the targets of interest and the influence of human interpretation.

This master's thesis presents an optical mapping method, Hyperspectral Imaging (HI), and its application to marine geological mapping - Underwater Hyperspectral Imaging (UHI). UHI is a mapping method where a hyperspectral imager is used underwater to capture optical properties of the seabed. Objective interpretations of optical properties have potential to create both quantitative and qualitative seabed maps (Johnsen et al., 2013).

The study also forms a part of the methodology development in Norway's national offshore seabed mapping program MAREANO ([www.mareano.no](http://www.mareano.no)). MAREANO is a co-operation program between The Geological Survey of Norway, Institute of Marine Research and The Norwegian Mapping Authority (Buhl-Mortensen et al., 2010). Optical remote sensing technologies, such as UHI, can potentially provide a complement to established marine mapping methods used in the MAREANO program.

Detecting minerals, soil properties and marine sediments by hyperspectral imaging from satellites and airplanes have been performed successfully on land and in coastal oceans

(Dierssen et al., 2009; Fearnls et al., 2011; Johnsen et al., 2009; Kruse, 2010; Mulder et al., 2011; Sabins, 1999; van der Meer et al., 2012; Volent et al., 2007). Moving the hyperspectral imager underwater can potentially provide many benefits because of the proximity to the targets. UHI as a technique has been developed and patented by the Norwegian University of Science and Technology's (NTNU's) spin-off company Ecotone AS and tested on different biological and geological objects (Johnsen et al., 2013; Ludvigsen et al., 2014). The tests were carried out both in laboratory and in field using underwater Remotely Operated Vehicles (ROVs) as platform for the imager. Results show great potential for seabed mapping by UHI, but further studies of the geological application of the method are needed.

## 1.2 Aims, outline and limitations

### 1.2.1 The aims of the study

The main aim of this master's thesis is to determine properties of marine sediments that can be detected and identified by UHI and secondly evaluate its applicability in the context of established mapping methods used in marine geology. The focus will be on calcium carbonate content in marine sediments, but other properties are also discussed. The reason for this focus is the potential application of UHI for mapping and monitoring bioclastic sediments and other carbonate features in cold waters, which are of relevance to MAREANO and other projects.

The following methods have been used to achieve the aims:

- ❖ Literature study of established marine geology mapping methods, previous work on geological HI and UHI.
- ❖ Laboratory work using a hyperspectral imager attached to a stereomicroscope to measure the spectral reflectance of different minerals, marine sediments with varying carbonate content and carbonate crusts. In addition to the imager, a Jaz spectrometer was used to get validations of the HI reflectance spectra.
- ❖ Semi-automated processing of the data. The software *yaPlaySpecX* was used to extract reflectance spectra from hyperspectral images of all samples and the software *Image Calculator* was used for creating supervised classification figures of the hyperspectral images.

### 1.2.2 Limitations

The theme of the thesis was developed in co-operation with NGU and focuses on certain topics of relevance to the MAREANO project. Evaluating mapping in cold-water regions is therefore set as a limitation, and the application of UHI on carbonate sediments in tropical waters is not discussed. The thesis focuses on marine geology, therefore biological mapping of coral reefs are not discussed.

The HI equipment and the software used are custom made, and are prototypes of the equipment used by Ecotone AS. The limitations of the equipment affect the results gained. The thesis does not include a thorough evaluation of the software, but the value of the results obtained from the

software are discussed. The HI and Jaz measurement were not done underwater due to limitations of the laboratory equipment. Only the samples were submerged by water in the laboratory, while all equipment are underwater when UHI is used in field measurements.

Fieldwork has not been carried out as a part of this thesis, but the author did participate in a NTNU cruise in the Trondheim Fjord in February 2014, where UHI was scheduled to be tested by NTNU and Ecotone AS. Due to technical problems with the ROV, no UHI data were acquired. The author did also participate in a MAREANO cruise in the Barents Sea during a summer internship at NGU, August 2013. This was in favor for understanding the mapping methods used by MAREANO in the field.

### 1.2.3 Outline

The master's thesis has the following structure:

#### *Chapter 1: Introduction*

Outlines the purpose of the thesis and its limitations.

#### *Chapter 2: Marine carbonate sediments and geological mapping of the seabed*

Introduces marine geological theory on calcium carbonate and environmental influences on marine carbonate deposits. Established mapping methods such as acoustic remote sensing, shallow seismic, underwater photography, video and sediment sampling are described to provide a background to the advantages of UHI in this setting.

#### *Chapter 3: Optical remote sensing*

Introduces theory of marine optics and optical remote sensing. In addition, several case studies related to hyperspectral remote sensing are included to show the development of the technology and mapping method the last decades. The principles of UHI and previous studies of this method are also found in this chapter.

#### *Chapter 4: Materials and methods*

Presents the materials and the methods used in the laboratory work, including sources of errors and variability.

### *Chapter 5: Results*

Presents results from the laboratory work. The results include light source spectra, RGB images and monochromatic images of samples, followed by reflectance spectra from HI and Jaz. Supervised classification figures are also included.

### *Chapter 6: Discussion*

The laboratory results are discussed in addition to an evaluation of UHI for geological mapping based on the results and the literature.

### *Chapter 7: Conclusions and recommendations*

Gives the conclusions of the study and suggestions to further work.





# Chapter 2 Marine carbonate sediments and geological mapping of the seabed

## 2.1 Marine sedimentation of calcium carbonate

The knowledge of marine sedimentation and sediment properties especially concerning calcium carbonate ( $\text{CaCO}_3$ ) in cold environments is important for understanding the variety of carbonate sediments along the Norwegian seabed and in other cold-water environments. The environmental stressors on  $\text{CaCO}_3$  in the ocean give the background for the importance of monitoring these type of sediments in the oceans.

### 2.1.1 Properties of marine sediments

Marine sediments are often defined by their visual properties and grain-size according to Boggs (2010). The main lithology, defined by dominant clastic or organic components, is normally used for definitions. Organic components include gyttja (organic mud from decayed organisms and plants) and peat (partially decayed vegetation). Clastic sediments are divided into categories after grain size. Gravel, sand, silt and clay are the main categories, which further are divided into coarse, medium and fine. The most used grain size-scale is the Udden-Wentworth scale (Figure 2.1). In addition, the fraction of bioclastic fragments (biogenic shell and skeletal fragments) and siliclastic fragments (transported terrestrial rock and minerals) can be used to characterize the sediments.

Millimeters	$\mu\text{m}$	Phi ( $\phi$ )	Wentworth size class	
4096		-20		
1024		-12	Boulder (-8 to -12 $\phi$ )	
256		-10		
64		-8	Pebble (-6 to -8 $\phi$ )	
16		-6		
4		-4	Pebble (-2 to -6 $\phi$ )	
		-2		
3.36		-1.75		Gravel
2.83		-1.50	Gravel	
2.38		-1.25		
2.00		-1.00		
1.68		-0.75		
1.41		-0.50	Very coarse sand	
1.19		-0.25		
1.00		-0.00		
0.84		0.25		
0.71		0.50	Coarse sand	
0.59		0.75		
1/2	500	1.00		
0.42	420	1.25		Sand
0.35	350	1.50	Medium sand	
0.30	300	1.75		
1/4	250	2.00		
0.210	210	2.25		
0.177	177	2.50	Fine sand	
0.149	149	2.75		
1/8	125	3.00		
0.105	105	3.25		
0.088	88	3.50	Very fine sand	
0.074	74	3.75		
1/16	63	4.00		
0.0530	53	4.25		
0.0440	44	4.50	Coarse silt	
0.0370	37	4.75		
1/32	31	5		
1/64	15.6	6	Medium silt	
1/128	7.8	7	Fine silt	
1/256	3.9	8	Very fine silt	
0.0020	2.0	9		Mud
0.00098	0.98	10		
0.00049	0.49	11		
0.00024	0.24	12	Clay	
0.00012	0.12	13		
0.00006	0.06	14		

**Figure 2.1** Udden-Wentworth grain-size scale for clastic sediments (Wentworth, 1922 in Boggs, 2010).

Grain size is fundamental for analyzing and interpreting a sediment. A proper analysis can reflect the depositional history of the sediment including weathering and erosion processes. After performing the grain size analysis in laboratory, a statistical treatment of the grain size data is carried out. This is useful when finding mean grain size and sorting. *Sorting* is a measure of the range of grain sizes present, and is mathematically expressed by standard deviation. Normally a less accurate visual description of sorting is made, varying from extremely poorly sorted to very well sorted.

A particle's shape is described by three factors - *form, roundness and surface texture*. Form is determined by the three major axis of a grain (long, intermediate and short). The degree of

sphericity is used to describe the form - equant or platy. Roundness describes the edges on the surface of the particle, if they are smooth or angular. Usually roundness analyses are performed visually by comparing to a grain roundness scale. The surface texture of a grain can be polished, frosted (matted) or contain marks like fractures and scratches. The grains have to be observed under a microscope to be described by surface texture.

*Grain orientation and packing* are properties describing the fabric of the sediment. Elongated or platy shaped grains are orientated in different ways depending on shape and outer influence like water currents and mass flows. Packing of a sediment is a function of grain size, shape and degree of compaction. It reflects the spacing between the grains and the density patterns of the sediments (Boggs, 2010).

### 2.1.2 Abundant minerals in marine sediments

Terrigenous sediments in the ocean origin from weathered and eroded rocks on land and consist of rock and mineral fragments of the source rock. Quartz and feldspar in fine and coarse fraction are abundant minerals in terrigenous sediments. Micas like biotite and muscovite are clay minerals often found in these sediments as well. Biogenous sediments consist of hard parts of shell-building organisms. These can be both carbonates and silicates found in large amount on the seabed and are often mixed with a red pelagic clay. The terrigenous red clay has its color because of an iron or manganese oxide coating on the minerals (Pinet, 2009).

### 2.1.3 Calcite and aragonite

Calcite and aragonite are polymorph minerals of the chemical structure  $\text{CaCO}_3$ . The minerals have different crystal structures – the calcite structure is rhombohedral, while the aragonite structure is orthorhombic. Aragonite reacts easily to calcite in water. Modern marine carbonate minerals are often aragonite, but in deep waters, calcite dominates (Boggs, 2010).

Magnesium (Mg) and calcium (Ca) ions have the same size and charge, which makes it easy for magnesium to substitute calcium in the calcium carbonate minerals. The amount of magnesium varies in calcite. Low-magnesium calcite consists of less than 4% magnesium, while high-magnesium calcite have more than 4%. In another carbonate mineral, dolomite ( $\text{CaMg}(\text{CO}_3)_2$ ), magnesium have occupied half of the sites of the calcium ions. The crystal lattice consists of planes of  $\text{Mg}^{2+}$ -ions alternating with planes of  $\text{CO}_3^{2-}$  and  $\text{Ca}^{2+}$  ions.

Shells and skeleton from dead organisms are found in bioclastic sediments, which is a mix of minerogenic and biogenic material. The amount of biogenic material in sediments vary with the different living conditions for the organisms. Shell-building organisms like molluscs, gastropods, pteropods, chitons, cephalopods, coccolithophores (plankton algae), stromatolites, corals and annelids, normally use aragonite in their shell. Echinoids, crinoids, benthonic foraminifera and coralline red and green algae are often high-magnesian calcite, while the planktonic foraminifera, coccolithophores and brachiopods use low-magnesian calcite to build shell (Boggs, 2010).

#### 2.1.4 Carbonate deposits on the seabed

The largest carbonate provinces are located in sub-tropical environments with clear warm water and lack of siliclastic input giving feasible conditions for coral-growth. In addition, cold-water corals are found in cooler environments, both on the continental shelf and slope and in fjords. There are several cold-water coral habitats along the Norwegian coast, like the Sula Reef in Nord-Trøndelag and the Røst reef in Nordland. These are some of the world's largest known cold-water coral reefs, built by the stone coral *Lophelia pertusa*. The framework of the stone coral consists of aragonite, and the coral can build carbonate mounds in shallow and deep waters. Cold-water coral mounds are large carbonate structures from several periods of coral reef development. Coral rubble and dead coral blocks from the reef extend its periphery, and bioclastic sediments are found in marginal zones around the mounds (Fosså et al., 2005; Hovland & Mortensen, 1999; Roberts et al., 2006).

Carbonate sand and gravel (shell sand and gravel) deposits are important resources in the carbonate industry and consist of partly decayed carbonate shells and skeleton from marine organisms. These deposits are described by Bøe & Olsen (2011). The most important organisms are molluscs, balanidae, sea urchins and red calcareous algae. The growth of these organisms depends on ecological parameters such as food availability, light climate (intensity, spectral compositions and day length), current speed and direction, bottom topography, water chemistry, wave activity and siliclastic sediment input. Deposits are normally found in areas with high wave and current activity, e.g. in narrow straits, on the landward side of islets and in bays with harsh climate. However, deposits can also be found in deeper marine basins (Bøe & Olsen, 2011).

According to Boggs (2010) grain size is mostly controlled by shell-building organisms, but can also be altered by recrystallization from abiotic precipitation of  $\text{CaCO}_3$ . Silt and sand sized clasts can also origin from terrestrial denudation of carbonate rocks. Ooids, peloids and grapestones are different kind of carbonate clasts. Ooids are circular grains consisting of concentric rings of calcite or aragonite coated around a core of shell fragment, pellet or a mineral grain. Ooids normally occur in areas with bottom currents and agitated-water conditions, but also in waters with high saturating levels of calcium bicarbonate. Grains of microcrystallin or cryptocrystallin calcite or aragonite without internal structure are called peloids. They are smaller than ooids and are produced by undigested mud from organisms feeding on the seabed. Carbonate grains can be aggregated by carbonate matrix (micrite) or carbonate cement (sparry calcite) and are then called grapestones or lumps. Micrite are small calcite or aragonite crystals deposited together with the rest of the sediment, while sparry calcite are recrystallized calcite or aragonite growing after deposition (Boggs, 2010).

Carbonate crusts can be found around hydrothermal vents or where methane gas leaks from the seabed. Microorganisms that use methane gas and reduced sulfides in their metabolism can start the process of calcite and aragonite precipitations. The carbonate precipitates as cement in the marine sediments surrounding the gas leaks resulting in carbonate crusts (Hovland et al., 1987). Early generation carbonate occur as cement filling the pore space in the sediments. These cemented sediments are occasionally broken in mm- to cm-scale clasts, which also are lithified by carbonate. A late stage carbonate formation occur at cavity rims within the crust forming concentric layers of pure aragonite (Aivo Lepland, pers. comm., November 2014).

In the deeper oceans, the seafloor is covered with pelagic sediments. Clay and silt are the dominating grain sizes accumulating from particles suspended in the ocean and from planktonic organisms with siliceous and calcareous shells. The deposits from organisms are called biogenous ooze, consisting of more than 30% biogenous material (Pinet, 2009).

### 2.1.5 Environmental stressors on $\text{CaCO}_3$ in seawater

The surface ocean takes up about a third of the anthropogenic  $\text{CO}_2$  from human fossil use and deforestation (Doney et al., 2009). The atmospheric  $\text{CO}_2$  levels have increased the last centuries, and this could affect the environment in the ocean. Inorganic dissolution and precipitation of  $\text{CaCO}_3$ , both calcite and aragonite, are influenced by the amount of dissolved  $\text{CO}_2$  in the water, because  $\text{CO}_2$  affect the acidity of the water by releasing hydrogen ions (Boggs, 2010).

The CO<sub>2</sub> uptake in the ocean causes pH reductions and affects chemical balances, which results in ocean acidification. This possible feedback from an increased atmospheric CO<sub>2</sub> level is called “the other CO<sub>2</sub> problem” (Doney et al., 2009). Raven et al. (2005) indicate that the average pH in the ocean surface water has decreased by approx. 0.1 units since preindustrial times. Theoretically, the amount of CO<sub>2</sub> will affect the amount of CaCO<sub>3</sub> precipitation. In natural conditions, this is not always the case. The ocean has a high alkalinity implicating that small amounts of CO<sub>2</sub> will not change the pH of the water, because the ocean will work as a buffering media (Boggs, 2010). However, regarding large amounts of CO<sub>2</sub>, studies have shown that it will affect the CaCO<sub>3</sub> content in the sediment (Hall-Spencer et al., 2008; Raven et al., 2005).

The oceans ability to absorb atmospheric CO<sub>2</sub> depends on photosynthetic CO<sub>2</sub> assimilation of inorganic carbon to organic carbon (food source and vertical flux of particles embedded at the seafloor) and CaCO<sub>3</sub> dissolution, both in the water column and in sediments (Boggs, 2010). The saturation state for CaCO<sub>3</sub> affect the formation and dissolution rates which varies over centuries and longer timescales. A change in saturation state can affect the living organisms in the ocean, because of ocean acidification. Laboratory studies show that acidification can cause reduced calcification rates, even in aragonite and calcite saturated waters (Raven et al., 2005). A change in the saturation levels of calcite and aragonite to a shallower water depth can change and restrict current areas of coral growth. A study by Hall-Spencer et al. (2008) was done on a benthic community around volcanic CO<sub>2</sub> vents. They found an absence and reduction of calcareous organisms around the vents, due to lower pH caused by high level of CO<sub>2</sub>.

Although an acidification of seawater in theory will affect calcification rates, this is not proved for long-term increase of CO<sub>2</sub> partial pressure. The complexity of the ocean and the ability for the calcium carbonate producing species to adapt to these conditions, make this question difficult to answer. Direct geological or historical evidence of changes in the ocean acidity causing decrease in calcification rate is lacking. There are many processes affecting the carbon cycle and the carbonate system in the seawater through history, e.g. continental weathering, volcanism, ocean chemistry, sea floor spreading and biological evolution, which all makes the geological evidence hard to interpret (Doney et al., 2009).

Norway has a potential for Carbon dioxide Capture and Storage (CCS) in empty oil and gas reservoirs in the North Sea. Scientists at the FME SUCCESS-center (Center for environment-friendly energy research, Subsurface CO<sub>2</sub> storage – Critical Elements and Superior Strategy) study technology and consequences related to CCS. The CCS technology has shown a great progress the last years, due to the interest of lowering CO<sub>2</sub> emissions from the industry. The

consequences of storing CO<sub>2</sub> can be damaging for the marine environment, with concerns including CO<sub>2</sub> leakages and resulting acidification of the water. Leakages from the seafloor can be difficult to monitor because of natural variations of the acidity in the ocean. The leakages can be too small for sensors to detect, and the area of the reservoirs is too large to be observed simultaneously. There is therefore a need for a better monitoring technique (FME SUCCESS, 2014). Based on the theoretical background, a decrease in calcium carbonate content in the sediments over time could be an indication of CO<sub>2</sub> leakage, and thus the carbonate content may be used as a monitoring parameter (Johnsen et al., 2013).

There are several other stressors on CaCO<sub>3</sub> in the ocean described in Boggs (2010), including mechanisms leading to less CO<sub>2</sub>. This is mainly caused by an increase in temperature or a decrease of water pressure. Warm water holds less CO<sub>2</sub>. Water pressure is lowered when waves agitate during storm activities or because of breaking waves towards land, circulation of deep pressurized water to shallower waters or an atmospheric pressure decrease, and will affect the partial pressure of CO<sub>2</sub> in the ocean. Low salinity and low ionic strength indicate a low amount of other ions than Ca<sup>2+</sup> and CO<sub>3</sub><sup>-</sup>, favoring precipitation of CaCO<sub>3</sub>. Ions like Mg<sup>2+</sup> will interfere with the chemical composition of the CaCO<sub>3</sub>, making it unstable and increase the solubility. The crystal structure of aragonite is more resistant against magnesium incorporation, so in magnesium rich oceans, aragonite will be favored (Boggs, 2010).

Due to the special conditions in which CaCO<sub>3</sub> precipitates, calcite and aragonite will not be found everywhere in the ocean (Pinet, 2009). The calcium carbonate compensation depth (CCD) is the depth where dissolution and precipitation of CaCO<sub>3</sub> is in equilibrium. Deeper than this limit, which has an average depth of 4500m, the CO<sub>2</sub> level is high and CaCO<sub>3</sub> will be dissolved in the water. The conditions on deep water are cold and the water pressure is high. The aragonite have a shallower limit than calcite, because aragonite is more soluble than calcite. The lysocline is the limit where the dissolution of CaCO<sub>3</sub> strongly increases. Both this limit and the CCD is deeper in the Atlantic than in the Pacific Ocean, and deeper around equator than in polar areas, because of different oceanic conditions (Pinet, 2009).

Other important biological processes affecting and regulating the CO<sub>2</sub> concentration in the ocean, includes skeletal and shell building organisms, photosynthesis, biological induced precipitation and decay of dead organisms (Boggs, 2010). For instance photosynthetic plankton algae (phytoplankton), producing ~45% of primary production globally heavily influences CO<sub>2</sub> uptake from light reactions in photosynthesis and releasing CO<sub>2</sub> through respiration (Falkowski & Raven, 2013).

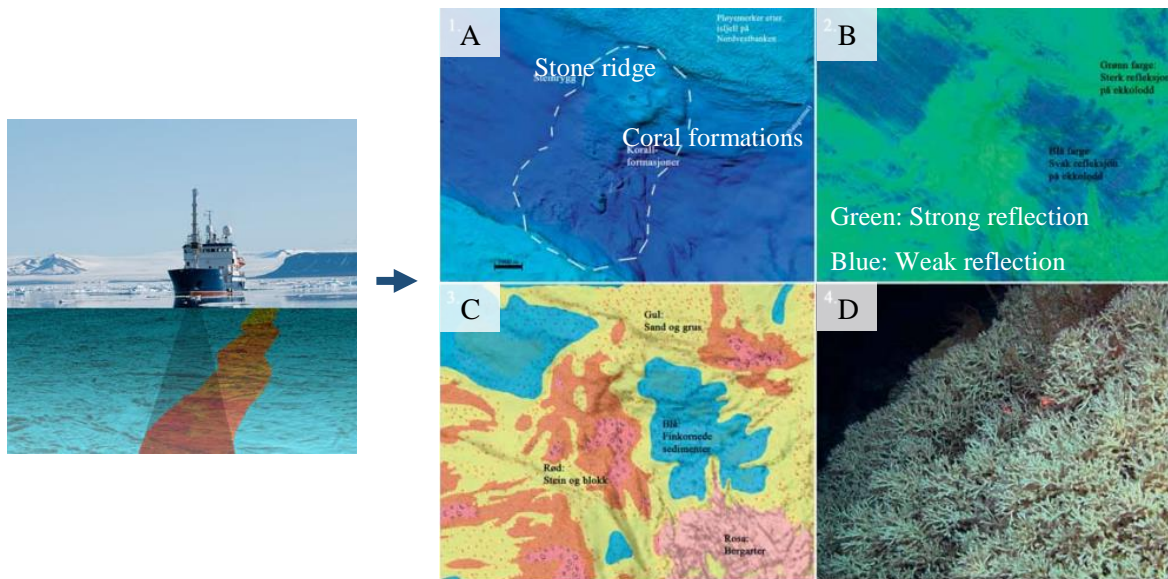
## 2.2 Traditional mapping of marine sediments

The most common modern day approach for mapping marine sediments starts with acoustic remote sensing from a marine vessel followed by different methods of visual observation and/or physical sampling of seafloor sediments for ground truthing. Sampling sites are chosen from the information gained by remote observation. Information like sediment types, sedimentary processes, marine environments and seabed topography can be mapped by this approach, which is useful in disciplines like geotechnical mapping, environmental monitoring, fishing industry and marine habitat mapping (Van Lancker et al., 2012).

The MAREANO program uses this marine mapping approach to obtain information regarding the marine geology and habitats of the Norwegian seabed (Buhl-Mortensen et al., 2010). The majority of ground truth data is visual obtained from underwater towed video observations. However, physical samples are obtained at around 20% of the sampling stations.

Figure 2.2 shows an example from Buhl-Mortensen et al. (2010) of how MAREANO data are used for interpretation of coral formations. A hill is found in the terrain model (A), the backscatter data show a strong reflection on the hill (B), the sediment classification map, sampling and seismic data show moraine sediments with rocks and boulders (C) and video observations verify that corals are present on this hill (D).





**Figure 2.2** Multibeam bathymetry and backscatter mapping of the seabed (to the left) provides data for interpretation. A) A stone ridge is located on the terrain model from bathymetry data. Small hills are interpreted as coral formations. B) The backscatter map show a strong reflection on the ridge. C) A sediment classification map shows rocks and blocks on the ridge (red color). Blue = fine grained sediments, pink = bedrock, yellow = sand and gravel. Sampling and seismic data of the ridge were interpreted as moraine material on top of a sedimentary bedrock. D) Video lines verify the occurrence of corals. The figure is modified from Buhl-Mortensen et al. (2010).

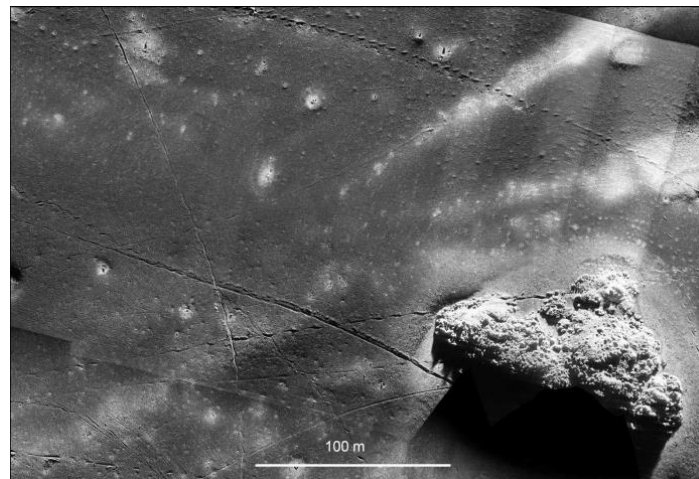
### 2.2.1 Acoustic methods

Side-scan sonar, single-beam and multi-beam echosounders (MBES) are the technology used to gain backscatter information. Acoustic backscatter data are used to discriminate between seafloor characteristics based on different intensities of backscattering of the returning echo. Information on geotechnical properties such as compaction, porosity, sorting and grain size are possible to estimate from the backscatter signal using appropriate software, but often interpretation is performed on the basis of the decibel amplitude value of a backscatter image, which indicates the strength of the returned signal from the seabed. Soft, fine-grained sediments are relatively easy to interpret, because of a strong linear correlation between the signal strength and grain-size. Hard and variable substrate will have more incoherent backscatter signals, varying with hardness and textural seabed parameters (Van Lancker et al., 2012).

Bathymetry data are used for making a digital terrain model of the seabed, which often is visualized as a shaded relief image in two dimensions, or can be rendered in three dimensions using appropriate software. Bathymetry data give information on landforms, depth and orientation of the terrain. It is an advantage to use MBES for seabed mapping, because this can simultaneously collect both backscatter and bathymetry data (Brown et al., 2011).

High resolution seismic data can be used in addition to backscatter and bathymetry data to interpret the top sediments of the seabed. TOPAS, which is a parametric sub-bottom profiler, is normally used on MAREANO cruises for collecting shallow seismic data. Top sediment layers can be interpreted from the seismic profiles, revealing sediment thickness and sediment characteristics (Bellec et al., 2014). Penetration depth capability of this sub-bottom profiler can reach ~200 m (Kongsberg Maritime, 2014).

Synthetic Aperture Sonar (SAS) mounted on Autonomous Underwater Vehicles (AUVs) is an emerging acoustic technology giving ultrahigh-resolution sonar images (Figure 2.3) and bathymetry data of the seabed (Bellec et al., 2014). It is possible to get very close to the seabed using an AUV as a platform and the resolution of SAS data can reach a few centimeters. With the HiSAS synthetic aperture sonar developed by the Norwegian Defense Research Establishment (FFI) and Kongsberg Maritime, the theoretical coverage of the seabed is 2.6 km<sup>2</sup>/h with 20\*20 mm resolution (Ludvigsen et al., 2014). SAS is not currently one of the standard methods used in the MAREANO program, but it offers great potential for future application and is due to be tested by MAREANO in 2015 (Margaret Dolan, pers. comm., December 2014).



**Figure 2.3** Synthetic aperture sonar image showing a biogenic mound surrounded by a 30 m wide zone of bioclastic sediments (Bellec et al., 2014).

### 2.2.2 Video-analysis of the seabed

Video transects of approx. 700 m are used for visual interpretation of the seabed on the MAREANO cruises. The method is described in Buhl-Mortensen et al. (2010). On average, there is taken one video-transect per 100 square kilometers. Two cameras are connected to a

video rig, which can capture sea bottom as deep as 3000 m. The rig is towed close to the seabed while capturing the main video transect and lands on the seabed at the start and end of each transect to allow for technical setup and zooming in for detailed observations of geology and biology. Ancillary sensors on the rig measure position, depth, height, temperature, current and particle content.

In the field, preliminary interpretation of different sediment types and bottom fauna are logged and geo-referenced in a database. The video transects are analyzed in detail on land and are used to compare different areas. Advantages of analyzing the seabed by video are the application on all bottom types in all kind of terrain and the minimal risk of disturbing the habitats (Buhl-Mortensen et al., 2010).

### 2.2.3 Sampling of sediments

Sampling has to be carried out to directly measure the properties of the sediments. Different sampling methods useful for different kinds of sediments are described in Buhl-Mortensen et al. (2010) and in Bellec et al. (2014). A grab is suitable for gravel and samples the uppermost 10 cm of the sediments. A box-corer is better for cohesive fine-grained material and obtains a sample of the 50 cm top sediments. The grab is not suitable for hard bottoms with large rocks and boulders, because these can prevent the grab from closing. Undisturbed samples are hard to get, because of loss of the finest fraction. A multi-corer is a good alternative to the box corer when needing several samples and more material. Six plastic tubes are used to get undisturbed samples of the uppermost 50 cm sediments. Multicore samples also provide the necessary material for organic and inorganic geochemical analysis.

Sampling will only provide point data, which have to be supported by additional information of the seabed from acoustic methods or video data. Field-geologists visually describe the samples, and sub-samples are often sent to laboratories for further analysis. Visual description are done on board the MAREANO cruises according to the SOSI (“Samordnet Opplegg for Stedfestet Informasjon”) - classification (Bellec et al., 2014; Buhl-Mortensen et al., 2010; Statens Kartverk, 2006).

### 2.2.4 Mapping of bioclastic sediments and cold-water coral reefs

A method for shell bed mapping is described by Bøe & Olsen (2011). They used shallow seismic, TOPAS, to map possible shell beds and the thickness of the deposit. The data were

used to select areas for sediment sampling by grab. Carbonate content and thickness of the deposits were used to classify the areas as “proved shell beds” or “possible shell beds”. Detailed water depth data were used to define the limits of the shell beds found in basins and flat areas.

In the 1990s, shell sand mapping at NGU was carried out to map carbonate resources. Today, shell sand samples are often used for mapping biological diversity, e.g. as part of the National program for mapping and monitoring of marine biodiversity in Norway (Bekkby et al., 2011). Sample data can be used in oceanographic and biological modelling. Only the top 20-30 cm of the bottom sediments are mapped and the limit for classifying the sediment as pure shell sand is a carbonate content of 85%. Sediments with a carbonate content of 50-85% are classified as impure shell sand (Bøe & Olsen, 2011).

Acoustic methods can be used to detect coral reefs, because these have characteristic bathymetric and backscatter signatures (Brown et al., 2011). However, there are some problems due to spatial scale and interpretation difficulties described below. In an article by Somoza et al. (2014) cold water coral reefs and mounds mapping methods by indirect acoustic and direct sampling were described. Bathymetry, backscatter and seismic data were collected at the Galicia Bank west of Portugal at depths of 1125 m to 620 m. The exposed mounds were possible to detect in seismic profiles by their dome structure and the lacking internal changes of seismic impedance. The buried mounds were observed as cone structures in the seismic profiles and mapped by combining backscatter and bathymetry data. The mounds showed very high intensity backscatter values compared to the surrounding sediments. It was not possible to map the living reefs by backscatter or bathymetry because the grid cell size of the terrain model were 50 m, which was too large for recognizing reefs. Seismic and coral sampling were used for mapping living reefs, where they were characterized as acoustically transparent domes.

In a report from NGU (Bellec et al., 2014), the grid resolution of the multibeam bathymetry used was 5 m, but still the minimum dimensions for interpreting structures as mounds were 20 m in diameter. The report also highlights the difficulties of distinguishing bioclastic sediments from bedrock and identifying biogenic mounds in slide areas because of the morphological similarity to mounds created by sliding.

## 2.3 Chapter summary

- ❖ Marine sediments are defined by their clastic or organic content, visual characteristics and grain size.
- ❖ Calcite and aragonite are polymorph minerals of  $\text{CaCO}_3$  found in marine sediments.
- ❖ Carbonate deposits in cold waters include bioclastic sand, carbonate crusts, cold-water coral reefs and biogenous ooze.
- ❖ Inorganic dissolution and precipitation of  $\text{CaCO}_3$ , both calcite and aragonite, are influenced by the amount of dissolved  $\text{CO}_2$  in the water.
- ❖ Traditional seabed mapping methods used by marine geologists include acoustic mapping (backscatter, bathymetry and shallow seismic data), video recordings and sediment sampling.



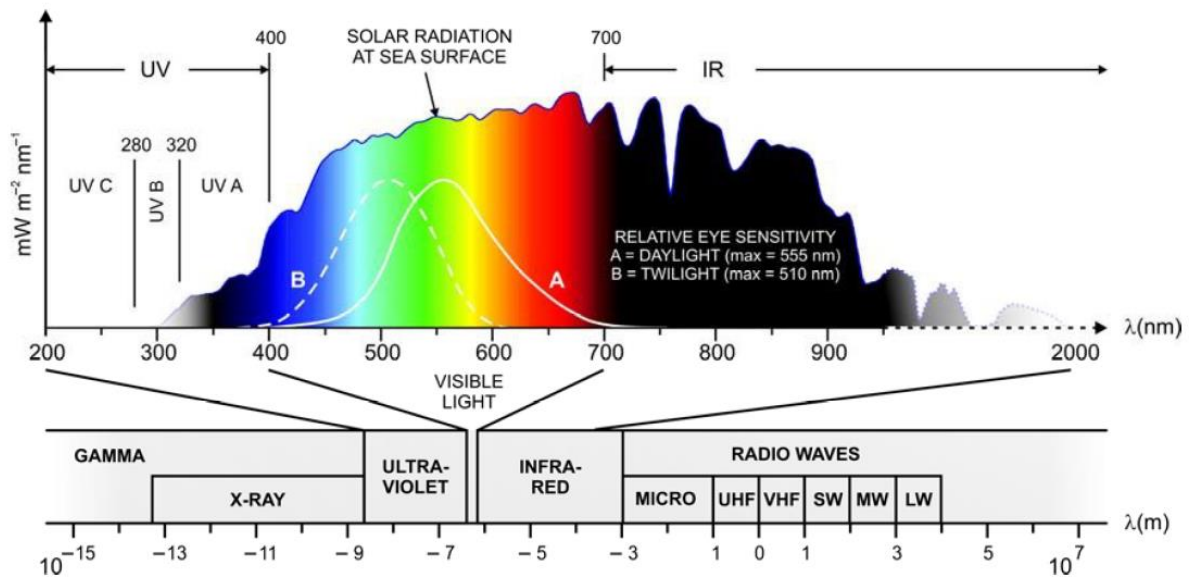
## Chapter 3 Marine optics and optical remote sensing

### 3.1 Optical properties of the sea and of geological material

Optics describe the physics of light when it interferes with a matter. Light theory, how light behaves in water and optical properties of different material are basic knowledge for understanding UHI and its applications to marine geological mapping.

#### 3.1.1 Light theory

Light is electromagnetic radiation behaving both as a stream of particles and as waves (Kirk, 1994). Light particles are called photons or quanta, and every particle has a wavelength and a wave frequency. Wavelength is expressed in nanometer (nm) and the spectral range of the electromagnetic radiation from the sun can be separated into gamma rays, ultraviolet light (UV), visible light, infrared light (IR) and radio waves (Figure 3.1). The visible light ranges from 400-700 nm. The human eye interprets the different wavelengths as colors based on the energy of the photons. A photon in the red band of the spectrum has more energy than a photon in the blue band. The amplitude of the wave or the flux of the photons determine the brightness of the light (Kirk, 1994).



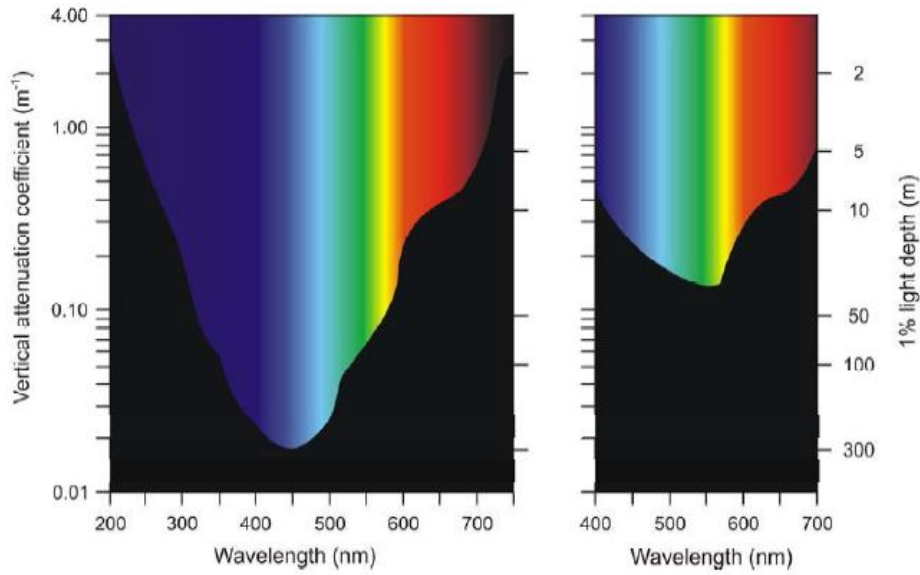
**Figure 3.1** Electromagnetic radiation from the sun (Sakshaug et al., 2009).

The radiant flux is the time rate of flow of radiant energy, expressed in watts (W). Radiance,  $L$ , is the radiant flux per solid angle per unit area at a plane perpendicular to the direction of flow, and has the unit  $\text{Wm}^{-2}\text{sr}^{-1}$ . Irradiance,  $E$ , is the radiant flux per unit area of a surface where the area is an infinitesimal element. The unit of  $E$  is  $\text{Wm}^{-2}$ . Downwelling,  $E_d$ , and upwelling irradiance,  $E_u$ , are the irradiance from the downwelling light and the upwelling light respectively. The ratio between  $E_u$  and  $E_d$  is the reflectance parameter,  $R$  (Kirk, 1994).

When the light interferes with a matter, the photons can be reflected, transmitted, absorbed and scattered. Absorption removes photons, scattering changes the direction of the photons. Transmittance occur when the photons penetrate through the matter. If the light beam hits a smooth surface a specular reflection occurs where the angle of the reflected light equals the incident angle. Diffuse reflection happens when the light hits a rough surface and the light beam is scattered in several directions (Jerlov, 1976).

As light propagates through water, light is absorbed and scattered in the water column. UV- and IR-light are heavily attenuated in water. In clear ocean water, the deepest penetrating light is in the blue part of the spectrum with a maximum 1% light depth of  $\sim 300$  m, which is the depth where the light energy is 1% of the energy at the surface. Compared with fjord waters, where the color is in the green part (Figure 3.2), maximum 1% light depth is  $\sim 50$  m (Volent, 2009).





**Figure 3.2** In blue ocean water (to the left), the color is blue because the deepest penetrating wavelength is approx. 450 nm. Fjord water (to the right), has a green color where the deepest penetrating wavelength is approx. 550 nm (Sakshaug et al., 2009).

### 3.1.2 Apparent and inherent optical properties of seawater

The optical properties of seawater can be described in two ways, the apparent (AOPs) and the inherent optical properties (IOPs) (IOCCG, 2000). When experimenting with optical measurements in the laboratory or *in situ*, it is very important to have control on the AOPs and IOPs of the water.

AOPs are used to describe the properties of the water dependent on the geometrical distribution of the ambient light field and the substances in the water (Johnsen et al., 2013). This property changes when the light field changes. The apparent color of the sea in Figure 3.2 is an example of an AOP. Measurements from passive sensors include parameters like the diffuse attenuation coefficients for upwelling ( $K_u(\lambda)$ ,  $m^{-1}$ ) and downwelling irradiance ( $K_d(\lambda)$ ,  $m^{-1}$ ). These parameters describe the rate of decrease of irradiance as a function of optical path length (Johnsen et al., 2009). The ratio between these is ocean reflectance ( $R(\lambda)$ ):

$$R(\lambda) = \frac{K_u(\lambda)}{K_d(\lambda)} \quad [Eq. 1]$$

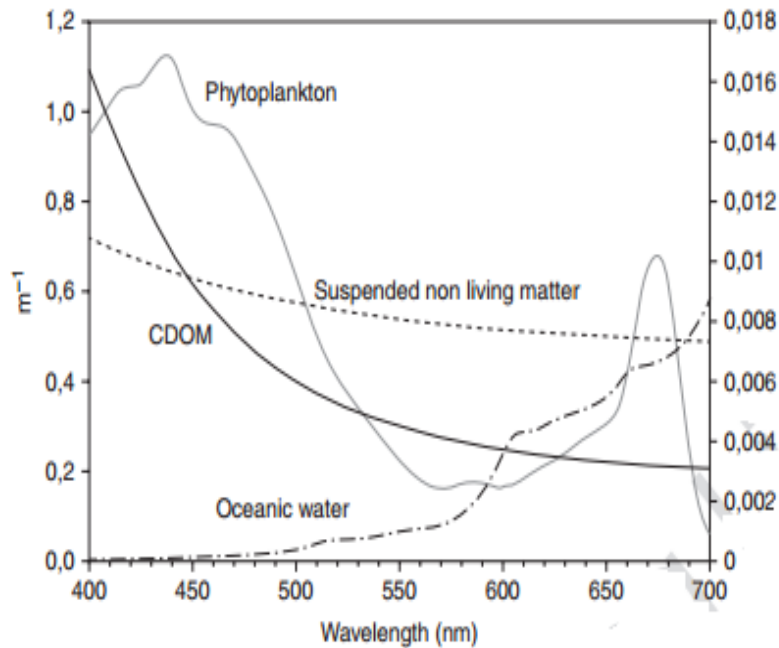
IOPs are independent of the ambient light field and describes the properties of water only affected by its contents. The properties are measured using an active light source, resulting in independence of variations in the angular distribution of the incident light field. The absorption coefficient ( $a(\lambda)$ ,  $m^{-1}$ ) and the scattering coefficient ( $b(\lambda)$ ,  $m^{-1}$ ) are IOPs used to find the total

volume attenuation coefficient ( $c(\lambda)$ ,  $\text{m}^{-1}$ ), which describes the light beam attenuation (Johnsen et al., 2009):

$$c(\lambda) = a(\lambda) + b(\lambda) \quad [Eq. 2]$$

AOPs are easy to measure, but hard to interpret, while IOPs are hard to measure, but much easier to interpret (Johnsen et al., 2013).

Substances in water affecting its optical properties are water molecules, phytoplankton, colored dissolved organic matter (CDOM) and total suspended matter (TSM). Water molecules absorb in the blue part of the spectrum and scatter in the red part of the spectrum. Phytoplankton are living organisms using light for photosynthesis. The main pigment in phytoplankton absorbing photons is chlorophyll a (Chl $a$ ). It absorbs photons highest in the green (440 nm) and the red (675 nm) part of the spectrum. CDOM originate from the decomposition of organic material (plant and planktonic tissue) and is only absorbing, not scattering. It has a maximum absorbance in the UV and blue part of the spectrum. TSM can be separated into particulate organic material (POM) and particulate inorganic material (PIM) (Johnsen et al., 2009). Due to the intense scattering from TSM, absorbance is difficult to measure. However, absorbance of PIM has been measured to be high in the red end of the spectrum, gently decreasing with increasing wavelength (Johnsen et al., 2013). The absorption spectra of suspended substances are shown in Figure 3.3.



**Figure 3.3** The absorption spectra of phytoplankton, CDOM, oceanic water and suspended non-living material (Johnsen et al., 2013).

#### 3.1.3 Case 1 and case 2 waters

Analyses of optical signals of marine objects need algorithms to correct for the optical properties of the substituents in the water. Different algorithms are needed for different types of water, which can be divided into case 1 and case 2 waters (Jerlov, 1976):

- ❖ *Case 1* waters include blue oceanic waters. The optical properties of these waters are mainly affected by the phytoplankton concentration as the other components play a small role. The concentration of Chl<sub>a</sub> can be estimated.
- ❖ *Case 2* waters are optically complex waters, with larger amounts of other constituents as well as phytoplankton. Information of CDOM and TSM concentrations, in addition to the Chl<sub>a</sub> concentration can be found. This is typical coastal waters affected by freshwater runoff from rivers.

#### 3.1.4 Remote sensing reflectance

Remote sensing reflectance ( $R_{RS}(\lambda)$ ) for water is defined as “the normalized radiant signal just above the water surface” (Johnsen et al., 2009). This coefficient describes the upwelling light

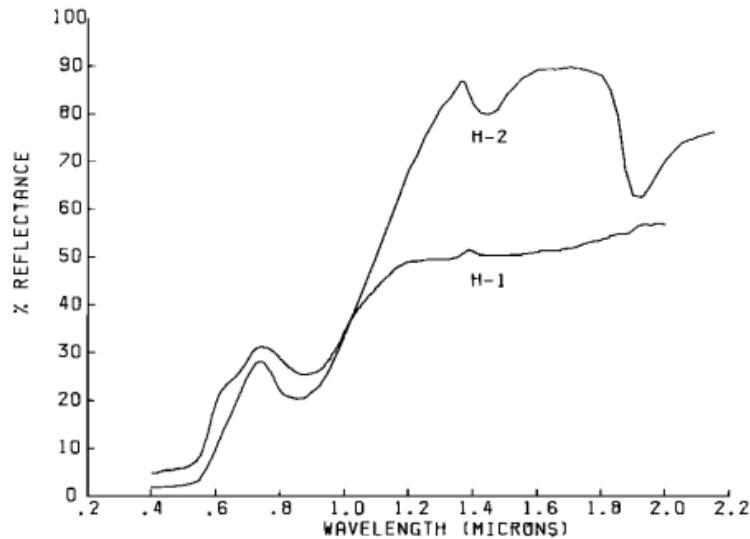
and is used to derive the in-water optical constituents. Remote sensing reflectance is different from reflectance ( $R(\lambda)$ ) in the way that upwelling radiance ( $L_u(\lambda)$ ) is substituted instead of irradiance ( $E_u(\lambda)$ ):

$$R_{RS}(\lambda) = \frac{L_u(\lambda)}{E_d(\lambda)} \quad [Eq. 3]$$

### 3.1.5 Optical properties of geological material

Several minerals absorb radiation, making them easy to identify by position and character of absorption features (van der Meer et al., 2012; Viscarra Rossel et al., 2006). Ultraviolet, visible-near infrared to thermal infrared (UV-VNIR-TIR) light are used for identification of minerals. Absorption features in reflectance spectra of minerals in the UV - VNIR region (approx. 0.1 - 1  $\mu\text{m}$ ) are dependent on transition metal ions (e.g., Fe, Cr, Co, Ni). These ions obtain absorption features due to electronic processes (e.g. transitions like  $\text{Fe}^{2+}$  -  $\text{Fe}^{3+}$ ). There are four major electronic processes resulting in absorption features according to Hunt (1977) - the crystal-field effect, charge transfer, color centers and conduction band transitions.

Crystal-field transitions occur when absorption of electromagnetic radiation changes the energy state of transition elements in a mineral. The outermost electrons of the ion determine the energy levels. Crystal-fields are electrostatic fields due to surrounding anions or dipolar groups, which can influence the arrangement of the energy levels. This results in different spectra for the same ion. The position of an absorption feature will thus depend on the site the ion occupies in the mineral (Hunt, 1977). Hematite is a mineral with absorption features below 530 nm and at 850 nm due to crystal-field transitions, with reflectance spectra as shown in Figure 3.4 (Sherman et al., 1982).



**Figure 3.4** Diffuse reflectance spectra of natural (H-1) and synthetic hematite (H-2). Note the absorption features below 530 nm and at 850 nm (Sherman et al., 1982).

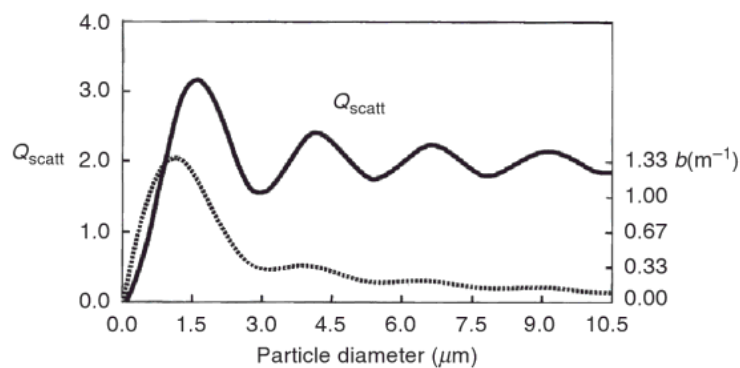
Charge transfer is the process when an electron migrate between neighboring ions, or between ions and ligands, due to absorbed energy (Hunt, 1977). Features occurring from charge transfer are more intense than features from crystal-field transitions. Some minerals show absorption features from lattice defects called color centers, this is particularly minerals like halides where the features cannot be explained by chemistry or impurities.

Free electrons can transfer from a low-energy valence band to a high-energy conduction band. In some mineral spectra, it is possible to observe the transition from intense absorption in the conduction band to complete transmission in the forbidden gap, which is the zone of energy between the two bands. This is shown as well defined absorption edges in the spectrum (Hunt, 1977).

In the shortwave infrared (SWIR) region (approx. 1-3  $\mu\text{m}$ ) absorption features are dependent on vibrational processes in water molecules, hydroxyl (OH), carbonate ( $\text{CO}_3$ ), sulfate ( $\text{SO}_4$ ) and ammonium ( $\text{NH}_4$ ) (Kruse, 2010; van der Meer et al., 2012). There are a restricted number of motions in a molecule, and each of these vibrations has a quantum number and a frequency. If the normal vibration is excited by more quanta of energy an overtone occurs. Vibrations and overtones are seen as absorption features in the SWIR region of the spectrum (Hunt, 1977). The most regular minerals in rocks have spectral features due to vibrational processes in the TIR region (approx. 3-15 $\mu\text{m}$ ), this include carbonates, silicates and mafic minerals (Mulder et al., 2011).

The grain size of the particles also affect the absorption and scattering of light. The internal pathway determine the absorption ability. According to Beers law, a larger grain with a longer internal pathway may absorb more photons than a small grain. Based on this theory, the reflection drops when the grain size increases (van der Meer et al., 2012). Hunt (1977) shows in his article that the smallest particle sizes have the highest reflectance, but also the least contrast of the features in the spectral band.

White minerals like calcite and quartz do not absorb visible light, but scattering of light from these minerals intensifies the reflectance (Kirk, 1994). For non-absorbing spherical particles the scattering efficiency,  $Q_{scatt}$  is highest for particles with diameter  $\sim 1.6 \mu\text{m}$  at 550 nm and decreases and increases in oscillations for larger grain sizes. This is shown in Figure 3.5 from Kirk (1994). The black curve is a scattering result of a single particle, while the dotted line is the result of suspended particles to show how the scattering varies with particle size for a fixed concentration by weight. When the diameter decreases, the amount of particles increases. The result of this is a maximum scattering at  $1.1 \mu\text{m}$  and smaller oscillations of the scattering coefficient for larger grains.



**Figure 3.5** Scattering efficiency ( $Q_{scatt}$ ) at 550 nm of single non-absorbing particles as a function of grain size. Dotted line show the scattering coefficient of a suspension with  $1 \text{ g/m}^3$  of particles,  $b =$  scattering coefficient (Kirk, 1994).

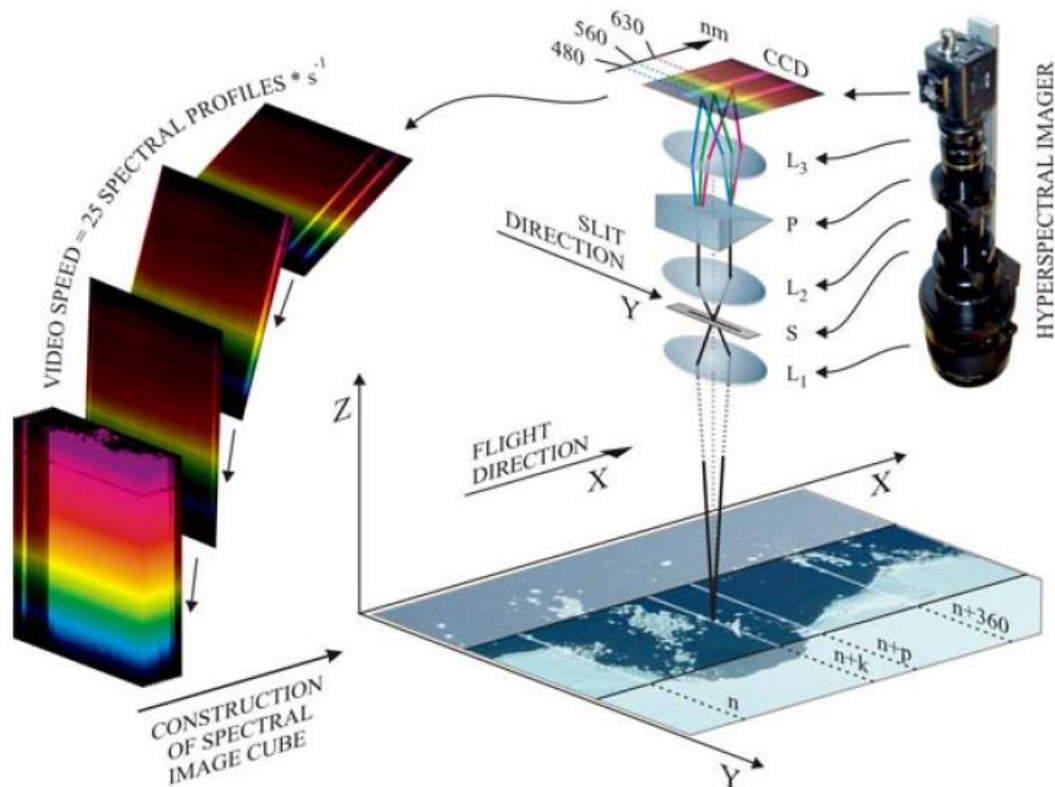
## 3.2 Optical remote sensing

Optical remote sensing is a mapping and monitoring technique using optical signatures to discriminate between different substances. Multispectral and hyperspectral spectrometers attached to platforms like satellites and airplanes are used to detect optical signals from the surface of the earth.

### 3.2.1 Principles of multispectral and hyperspectral remote sensing

The spectral resolution of the human eye is limited to three wavelengths, red (~600 nm), green (~550 nm) and blue (~450 nm), giving us a trichromatic perception of colors (RGB-vision). Television, cameras and other artificial digital image displays and sensing systems normally use “pseudo-true” colors in RGB images, with bands centered at 450 nm, 550 nm and 650 nm. A multispectral imager, used for remote sensing from satellites, captures more than three wave bands. Typically, it uses 10-20 bands in the ultraviolet, visible and near-infrared part of the electromagnetic spectrum. Multispectral (>5 nm wavebands) and hyperspectral imaging are based on the same principles, but the HI has a better spectral resolution than the multispectral, providing wavelengths with 1 nm spectral resolution (Johnsen et al., 2013).

A hyperspectral imager is a spectrometer equipped with a camera. The spectrometer separates reflected solar energy from the surface into spectral bands, which are narrow wavelength intervals (Sabins, 1999). In this study, the sensor used for the camera is a charge coupled device sensor producing images of the target consisting of pixels with different optical properties. Images are captured through an entrance slit and are reconstructed into an image of the entire area of interest with high spectral and spatial resolution, by merging the spectral profiles into an image cube (Figure 3.6). This is called the “push-broom technique” (Volent et al., 2007).



**Figure 3.6** Model illustrating the hyperspectral imager, the “push broom” technique and the spectral image cube. L1 = front lens, S = entrance slit, L2 = collector lens, P = grism, L3 = camera lens and CCD = imaging detector (Charged Coupled Device),  $n$  = amount of pixels in X-direction (Volent et al., 2007).

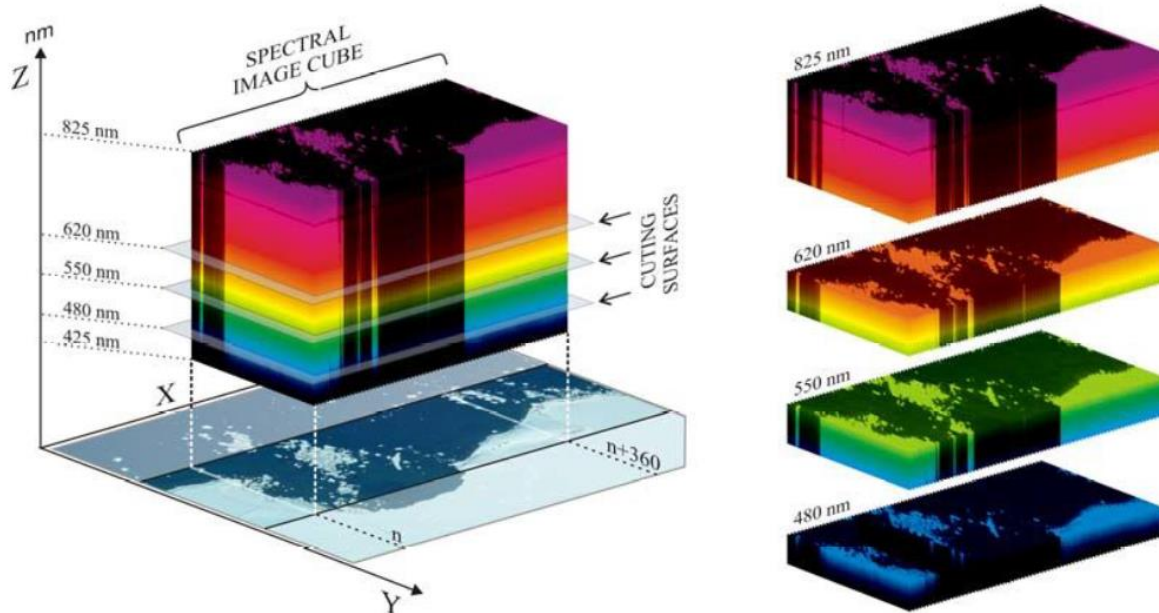
### 3.2.2 Classification based on optical signature

A hyperspectral image provides a full reflectance spectrum per image pixel. The reflectance spectrum shows the reflectance per wavelength (1 nm resolution). Spectral features are observed as peaks and drops in the spectrum and determine the optical signature (shape of the spectrum), which can be obtained from a pixel and used to classify the objects in the pixel (Johnsen et al., 2009). In addition, the intensity of the optical signature can be used to separate objects. By using the optical signatures of objects on the seabed it is possible to identify and map the biogeochemical patterns of interest. Monochromatic images can be extracted from the image cube (Figure 3.7). These images show the upwelling radiance intensity of the selected wavelength and intensities are given in  $\text{mWm}^{-2}\text{nm}^{-1}$  (Johnsen et al., 2013).

Pettersen (2013) describes two methods of classifying objects based on optical signature. A supervised classification of a hyperspectral image can be accomplished by choosing classes based on optical signature and use these to classify pixels in the image. Statistical software is used for the classification. An unsupervised classification is done without predefined classes.

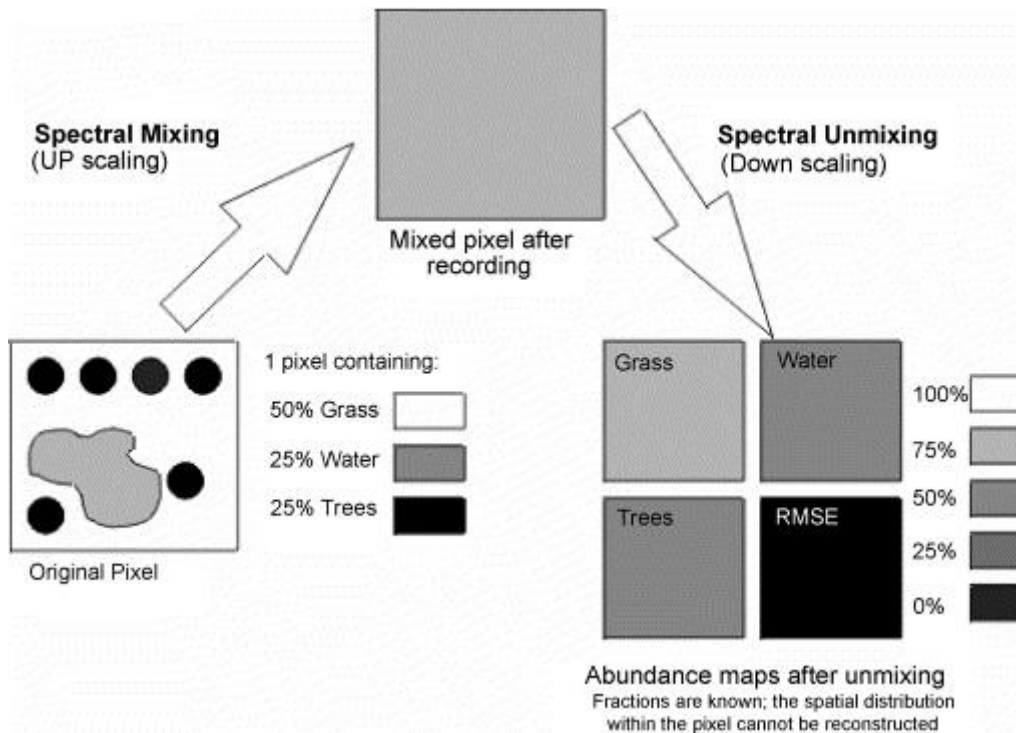


This classification is also accomplished by statistical software where pixels are classified based on differences in radiation and reflectance.



**Figure 3.7** The method of choosing monochromatic images from the spectral image cube to make specific identification images. At the cutting surfaces, the pixels of horizontal planes show reflection intensities at one specific wavelength (Volent, 2009).

A problem in classification of pixels occurs when the pixel consists of several objects with different optical signatures called endmembers (Malenovsky et al., 2007). This can be solved by algorithms of spectral unmixing, illustrated in Figure 3.8. Optical signatures of objects are mixed in one pixel after recording and can be unmixed by reversing this process, resulting in abundance maps. Reflectance spectra of objects that can be used to reconstruct the recorded mixed spectra are chosen as endmembers. These spectra can be found in spectral libraries, by field reflectance measurements, or they can be extracted from the remote sensed image. Only the fraction of the endmember is known and spatial distribution cannot be reconstructed.



**Figure 3.8** Illustration of spectral mixing and unmixing. Spectral mixing occurs during recording of the pixel and spectral unmixing of this pixel can find the abundance of endmembers. RMSE = root mean square error, indicating lacking endmembers in the pixel (Malenovský et al., 2007).

### 3.2.3 The start of marine optical remote sensing - mapping ocean color

Remote sensing of ocean color is used to find dissolved and suspended particles in the world oceans and to get qualitatively and quantitatively measurements of these (Johnsen et al., 2009). Satellites are equipped with spectrometers, also called spectral radiometer imagers or spectroradiometers, which detect spectral characteristics of the upwelling light from the surface, in the visible and infrared spectral range. The satellites provide a global coverage of the reflected sunlight, giving useful information of ocean conditions such as sea-surface temperatures, algal blooms, snow and ice cover. This is a passive observation, because the measurements are based on sunlight as light source. Sunlight restricts the recordings due to cloud cover, lack of light during nighttime and polar night at high latitudes.

In 1978, NASA launched the first dedicated ocean color sensor, the Coastal Zone Color Scanner (CZCS), the Nimbus-7 satellite. This was a multispectral sensor, storing six spectral wave bands. Data collected were used to identify and map areas of biological productivity, suspended inorganic material, fresh water run-off, pollution and shallow coastal areas. The first sensors had a need for improvement, concerning insufficient spectral, spatial and temporal resolution, sensitivity of the sensors and algorithms for atmospheric corrections. Today, the technology of

the instruments are much better and several sensors are attached to satellites orbiting the earth giving high-resolution images (Johnsen et al., 2009).

Local remote sensing from aircraft-platforms can be used to map coastal areas. Several studies have shown that recently developed airborne hyperspectral imaging is an excellent tool to map coastal features as kelp forests (Volent et al., 2007), sea-ice age/geomorphology, ocean color, particles from freshwater and glacial runoff in addition to vegetation and minerals on land. Compared to satellite remote sensing, airborne remote sensing does not have problems regarding cloud cover and needs less atmospheric correction for the upwelling light. Aircrafts can monitor closer to the target, which gives a higher spatial resolution (about 1 m per image pixel spatial resolution) than satellites (typically 300-1000 m spatial resolution) (Johnsen et al., 2009).

### 3.2.4 Case studies related to geological hyperspectral imaging

Hyperspectral imaging from satellites and airplanes are used in geological mapping on land. Optical remote sensing of geology started in the 1980s with the Landsat multispectral scanner using VNIR bands. The Landsat Thematic Mapper (TM) caused an uptake in the geological remote sensing by allowing mapping of lithology, minerals, structural geology, volcanic deposits and volcano monitoring, coral reef mapping, natural oil seep detection and landslide mapping. In the Goldfield mining district in Nevada, United States, TM images were used for recognizing iron rich minerals (goethite ( $\text{FeO}(\text{OH})$ ), hematite ( $\text{Fe}_2\text{O}_3$ ), jarosite ( $\text{KFe}^{3+}_3(\text{OH})_6(\text{SO}_4)_2$ )). Figure 3.9A shows the laboratory reflectance spectra for these minerals, which have low reflectance in the blue region and high in the red and IR regions (Sabins, 1999).

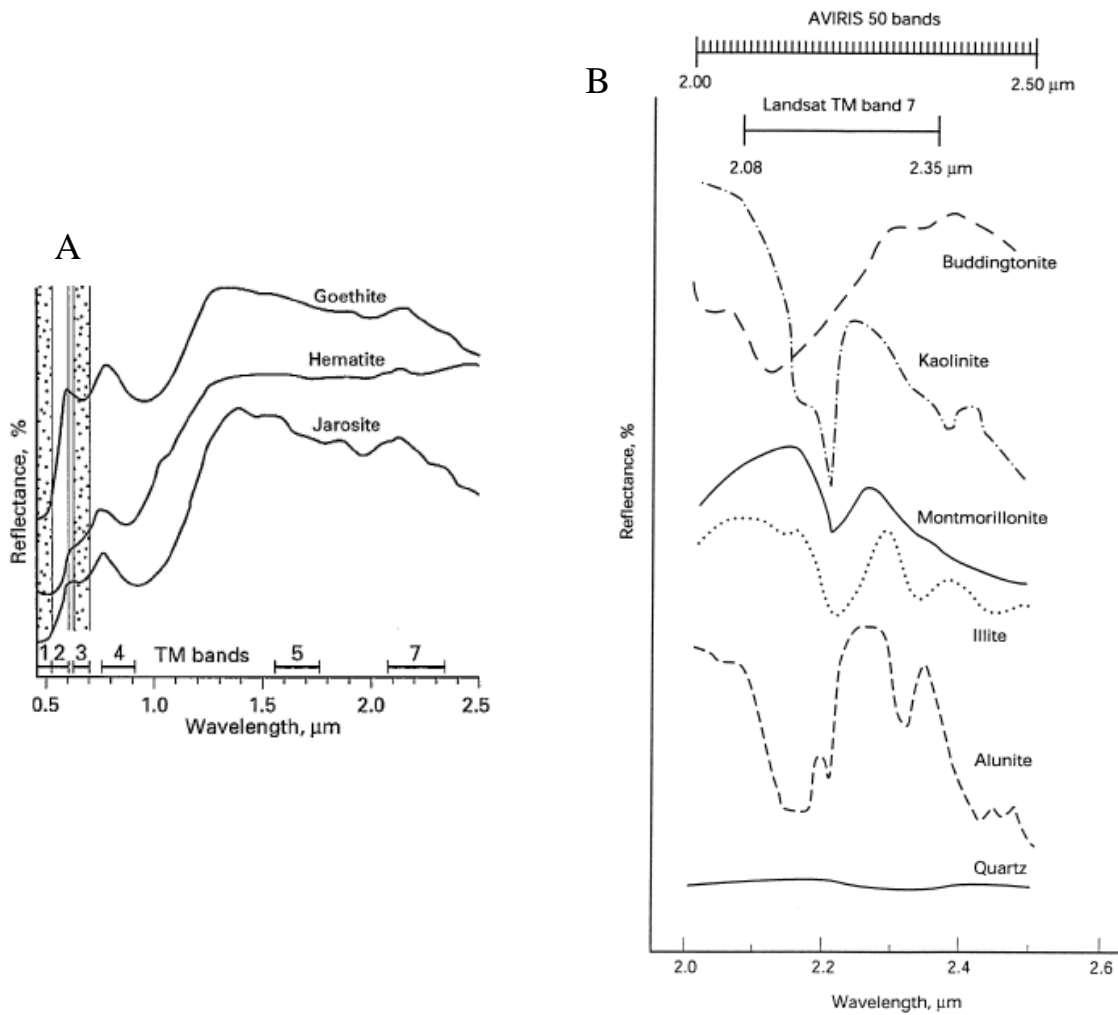
A review of optical remote sensing used for geological mapping on land is given by van der Meer et al. (2012). The Advanced Spaceborne Thermal Emission and Reflectance Radiometer (ASTER), was launched in 1999. This was an imaging multispectral radiometer with three channels in the VNIR region, six channels in the SWIR region and five channels in the TIR. Data collected were used to produce geological maps of clay minerals (kaolinite, illite), sulfate minerals (alunite), carbonate minerals (calcite, dolomite), iron oxides (hematite, goethite) and silica (quartz). The information was used to map alteration facies of the bedrock.

Hyperspectral images have been available for the last 20 years. Since 1998, NASA has operated a hyperspectral spectrometer - the Airborne Visible/Infrared Imaging Spectrometer (AVIRIS) with 224 bands in the 0.4-2.5  $\mu\text{m}$  region. HyMAP, the Australian Hyperspectral MAPper, in

addition to AVIRIS, are the most used hyperspectral imagers for geological mapping. HyMAP has 126 bands in the 0.4-2.5  $\mu\text{m}$  region. Many companies develop hyperspectral imagers and there are several ongoing hyperspectral missions, for instance there are two hyperspectral imagers circling the planet Mars (van der Meer et al., 2012).

Several studies on applications of HI for geologic exploration have been successful (Chabrilant et al., 2002; Kruse et al., 2003; Mulder et al., 2011; Sabins, 1999; van der Meer et al., 2012). Spectral libraries for different materials' specific reflectance spectrum are provided at several institutes, including both minerals and rocks (e.g. USGS Spectral Library). The mining industry is the main driver and most studies relates to hydrothermal systems. Such systems consist of spectrally active minerals, like hydroxyl-bearing minerals, ammonium-bearing minerals, phyllosilicates, iron oxides and carbonates (van der Meer et al., 2012).

In the study of Goldfield mining district by Sabins (1999), TM images could not identify specific alteration minerals because of the limited spectral resolution. In Figure 3.9B, some of these minerals are listed with their reflectance spectrum recorded by AVIRIS hyperspectral scanner with a spectral resolution of 50 bands in the region 2-2.5  $\mu\text{m}$ . As seen in the figure, quartz is missing defined spectral features in this range of wavelengths and cannot be recognized by VNIR or SWIR light reflection. To detect quartz, the HI has to be equipped with a thermal IR region.



**Figure 3.9** A) Laboratory reflectance measurements of goethite, hematite and jarosite. The TM bands and ranges are shown in the figure. B) Reflectance measurements of minerals from AVIRIS hyperspectral scanner. AVIRIS have 50 bands ranging from 2.00-2.50  $\mu\text{m}$ , giving a better resolution compared with the multispectral TM band 7 (Sabins, 1999).

Mine tailings are also possible to analyze with HI according to van der Meer et al. (2012). The distribution of acid-generating minerals as pyrite and the oxidation product can be used as an indicator on pollution (Riaza & Müller, 2010; Shang et al., 2009).

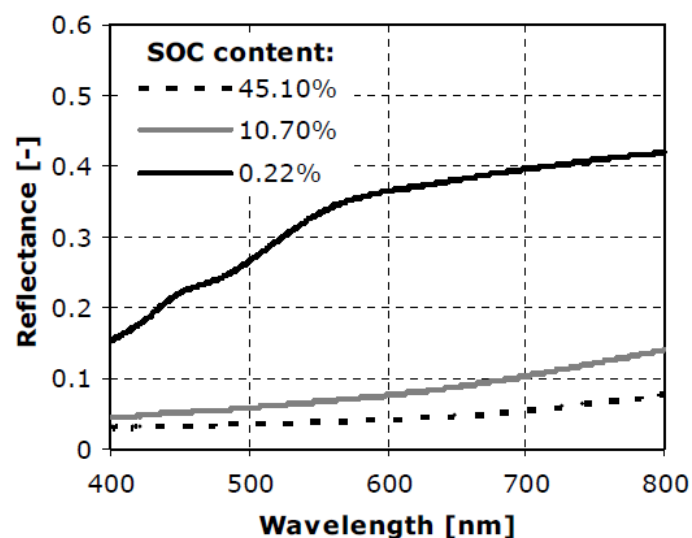
A study from Cuprite (Nevada, US) and Northern Death valley (California and Nevada, US), shows reflectance spectra of different minerals and gives a comparison of spectra from different sites and different sensors. NASA's AVIRIS (airborne) and Hyperion (spaceborne) hyperspectral sensors were used for the optical imaging of these areas. This study shows that there are some differences in the reflectance spectra due to remote sensing at different heights and when the same mineral is measured at separate locations. Because of a smaller signal-to-noise ratio in the Hyperion measurements than the AVIRIS, the reflectance spectra cannot be

used to separate mineral variability or crystal structure differences. The study also shows that minerals with similar spectral signatures can result in mapping errors when making regional maps based on the reflectance, such as muscovite and kaolinite, and buddingtonite and alunite (Kruse et al., 2003).

In a review of the use of remote sensing in soil mapping, Mulder et al. (2011) present studies showing possibilities of mapping soil mineralogy, soil texture (sand, silt and clay), soil organic carbon, soil moisture, iron content, soil salinity, carbonates and soil weathering state. The spectral features determining these soil properties are found in the VNIR, SWIR and TIR regions.

Bartholomeus et al. (2007) showed that HI could be used to find the iron content in soils where hematite was the main iron bearing mineral. The results show an overall decrease in reflectance when the iron content increases. Redness indexes of the soil reflectance were calculated and this index gave a medium correlation with the iron content.

A correlation between the soil organic carbon (SOC) content and the slope of the reflectance spectra in visible light is shown in an article by Bartholomeus et al. (2008). The slope of the reflectance spectra between 400-800 nm increases with increasing SOC content (Figure 3.10).



**Figure 3.10** Reflectance spectra of soils with varying soil organic carbon (SOC) content (Bartholomeus et al., 2008).

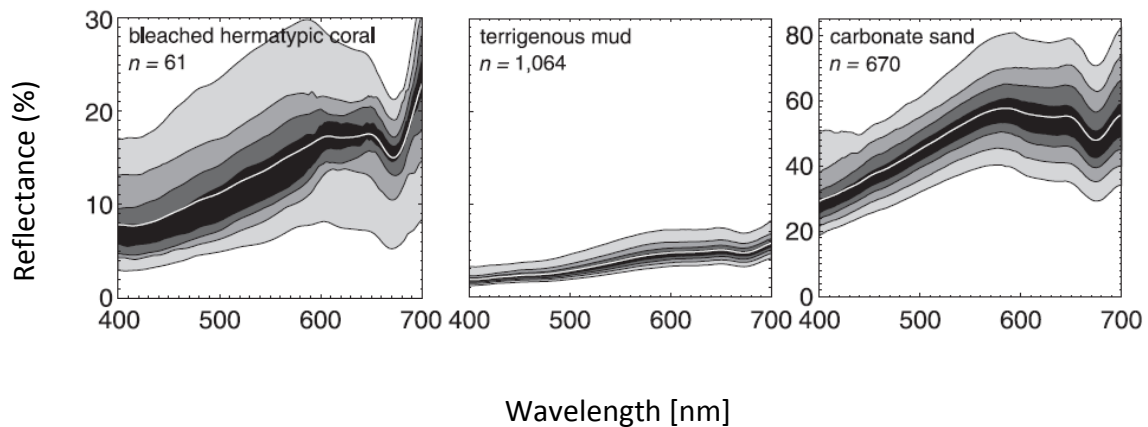
A study by Chabrilant et al. (2002) examined HI for use in identification and mapping of expansive soils. Regional mapping of clay minerals by HI was successful. The study shows that

it is possible to discriminate between pure smectite and mixed layers of illite/smectite in an outcrop in the region 1.9-2.4  $\mu\text{m}$ , based on absorption bands. This is interesting in the application of HI for drill core analysis and outcrop analysis.

### 3.2.5 Case studies related to hyperspectral imaging of the seabed

Bottom types give different reflectance spectra depending on several factors like the mineralogical and organic content of the sediment and the biology of the seabed. For instance, microalgae typically absorb in the blue and red part of the visible spectrum (due to pigments like chlorophylls, carotenoids and phycobiliproteins) and bacteria in the blue part of the spectrum due to carotenoids. Organic content in sediments are often degradation products. The absorption features of the degradation products of chlorophylls have slightly different spectral signatures than the living, but they also absorb in blue and red. Color of shell sand varies due to pigments that can keep the coloration long after death. For instance, pink shell reflects red light in the samples and this color comes from phycobiliproteins, which are light harvesting pigments for photosynthesis (Roy et al., 2011).

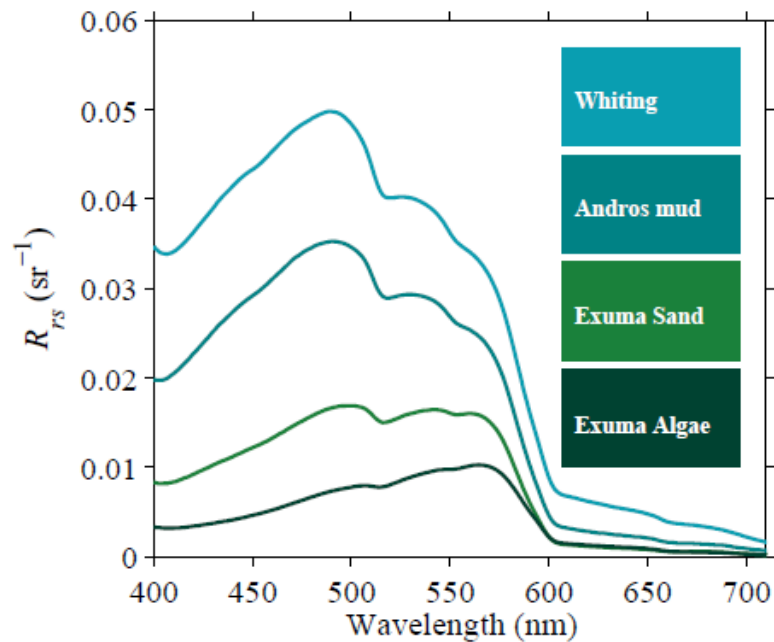
It is important to consider that satellites and airborne remote sensing, due to the absorption and scattering of UV and IR light in the water, only can detect the visible light reflectance from the seabed. Studies on reflection and remote sensing of shallow sea bottoms show a range of different reflectance spectra. Hochberg et al. (2003) measured visible light reflectance of different algae, corals, sea grass, terrigenous mud and carbonate sand. The study shows that bottom-types can be discriminated based on their characteristic spectral shape of the reflectance spectrum, and that the reflectance spectra are consistent across biogeographic regions. Figure 3.11 shows some of the reflectance spectra. Carbonate sand has a different scale because of its high reflection. The spectra is a result of the calcium carbonate sand grains and chlorophyll in benthic microalgae. In contrast, the terrigenous mud shows a very low reflection. The sand has a similar reflectance spectrum shape as a bleached coral, so these can be misinterpreted.



**Figure 3.11** *In situ* optical reflectance spectra of bleached hermatypic coral, terrigenous mud and carbonate sand in a coral reef community. Spectra were measured by a diver-carried portable spectrometer. Shaded areas give the ranges in percent at which all spectra lie within. Light gray=2.5-97.5%, medium-gray=12.5-87.5%, dark grey=25-75% and black=37.5-62.5%. White lines show mean reflectance. Modified from Hochberg et al. (2003).

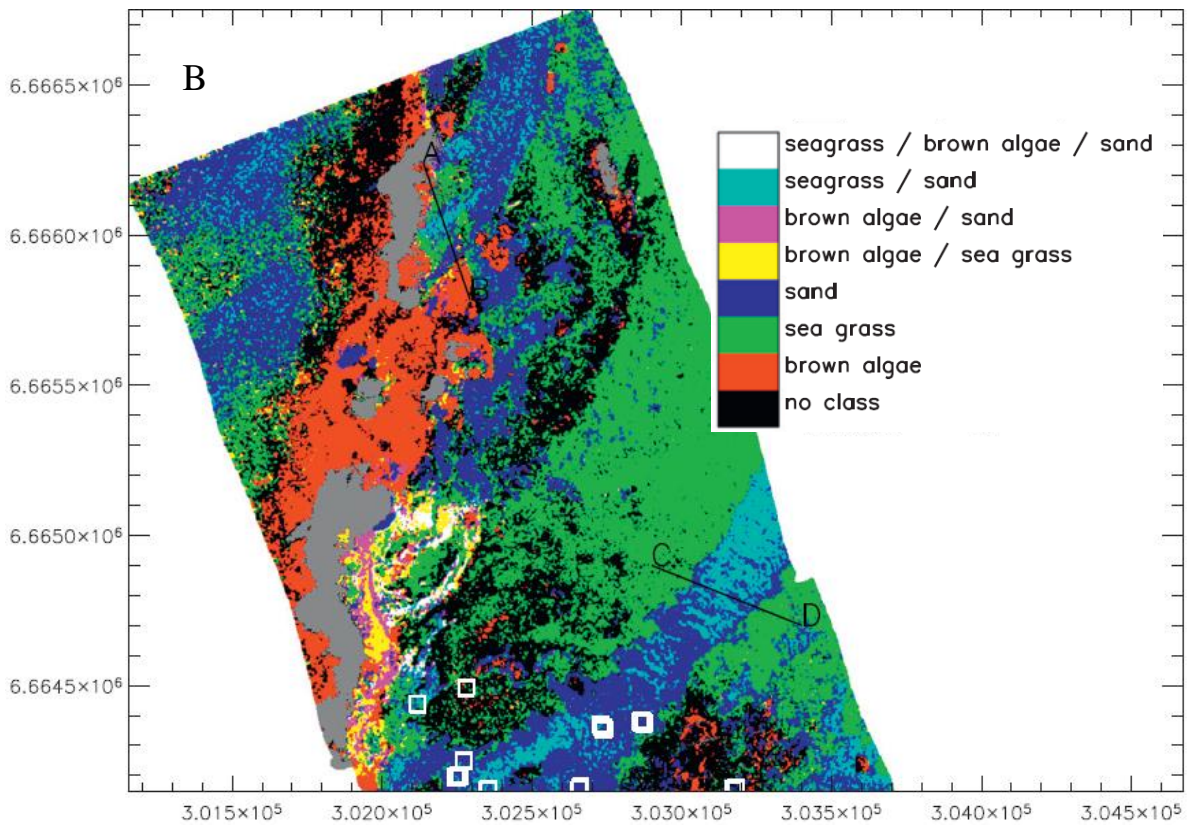
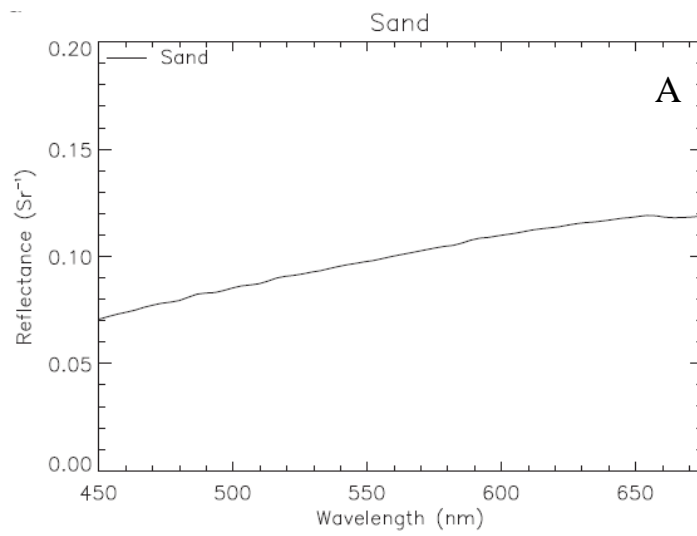
In a study by Dierssen et al. (2009) remote sensing reflectance was derived from MODIS images at 1 km resolution across the Bahama Banks. The aim was to see if remote sensing could be used to observe whittings consisting of suspended fine-grained aragonite mud. Sediments in the region consist of carbonate muds and fine sands. Figure 3.12 shows remote sensing reflectance from whittings and carbonate sands. The fine-grained spectrum shows a turquoise color, while the sand spectrum shows a green color. In addition to less reflection from larger grain sizes, the sand consisting of grapestones was covered by algal-biofilm. For the whittings, the reflection is stronger than for the seabed mud, due to a more proximal occurrence to the sea surface and the small particles.

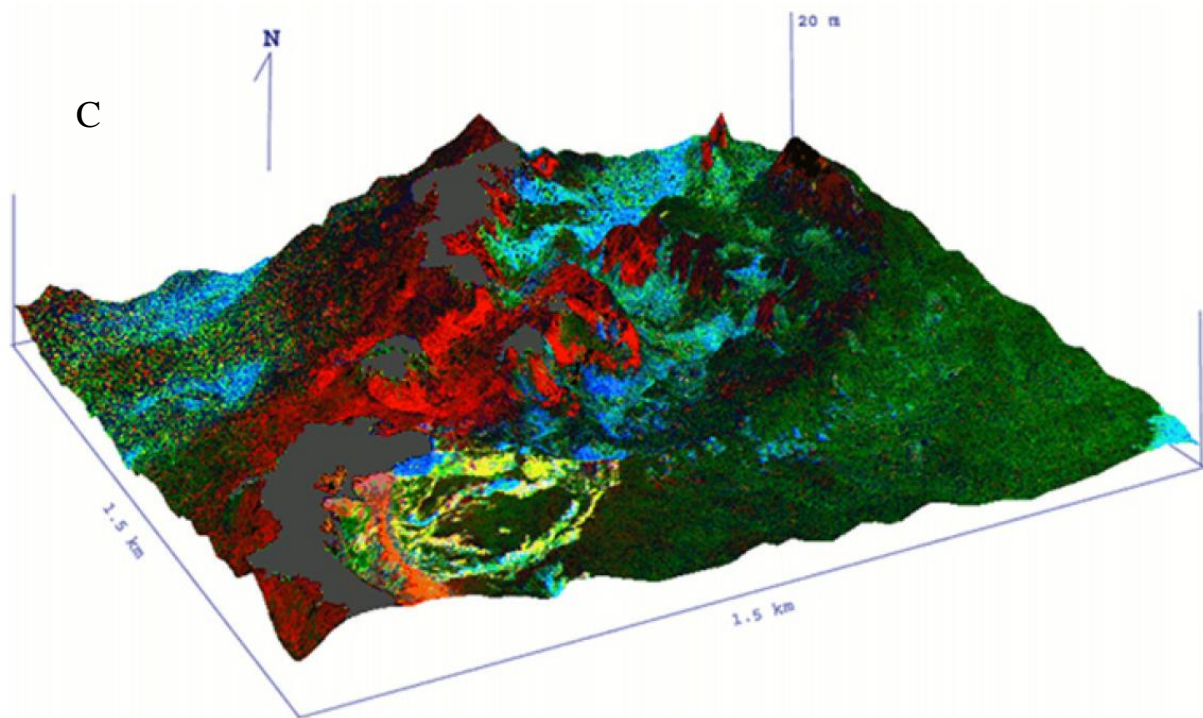




**Figure 3.12** Remote sensing reflectance,  $R_{RS}$ , of whittings, mud, sand and algal-covered grapestone sediment. All measurements are taken at places with 5m water depth, Andros and Exuma are names of the sampling spots. Colors in the figure reflect a quantified apparent color of the sediments (Dierssen et al., 2009).

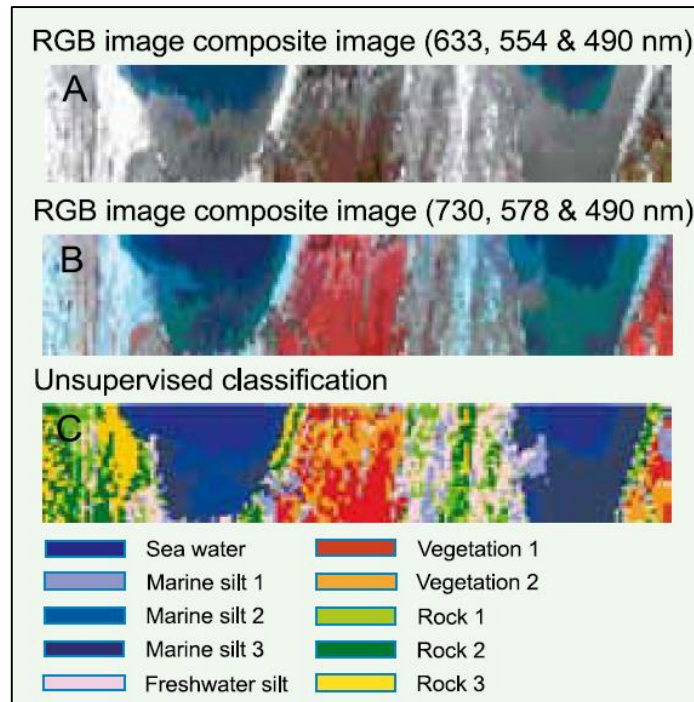
Fearns et al. (2011) used HI from an airborne HyMap sensor to produce a habitat map of a shallow water region in Western Australia. Three classes of bottom types were classified based on *in situ* measurements of reflectance using a hyperspectral radiometer – sand (Figure 3.13A), sea grass and brown algae. The reflection within each pixel corresponding to the different classes were displayed with different colors in the map (Figure 3.13B). In addition, pixels containing mixed substrates were included in the model. The map was overlaid on a bathymetry map giving a 3D picture of the seabed (Figure 3.13C).



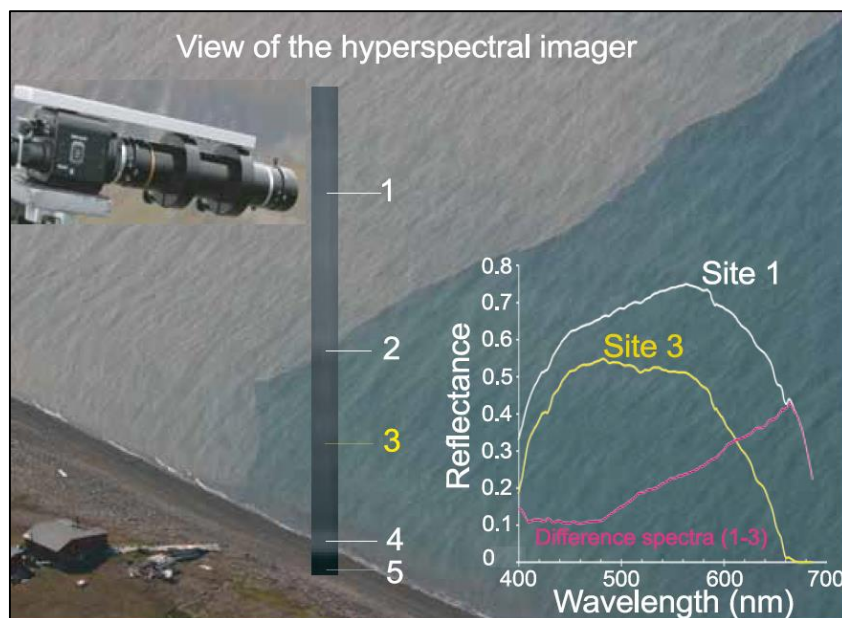


**Figure 3.13** A) *In situ* reflectance spectrum of sand. B) Habitat map created using hyperspectral data. Grey regions are islands, exposed reef, land and breaking waves. White squares indicate sampling sites. C) Substrate classes in figure B overlain on model-derived bathymetry (Fearn et al., 2011).

Two examples of local HI from Svalbard are shown in Figure 3.14 and Figure 3.15. The first is a result of airborne remote sensing showing unsupervised classification of water, land vegetation and rocks. Three different marine silt sediments (unknown content) and three types of rock (unknown rock types) were detected in the classification. In the second example, a hyperspectral imager is stationary placed on a mountain top in combination with an autonomous underwater vehicle (AUV) collecting *in situ* data in the water. The figure show the reflectance spectrum from a river plume containing suspended red clay and how the reflectance differ from water around the river plume (Johnsen et al., 2009).

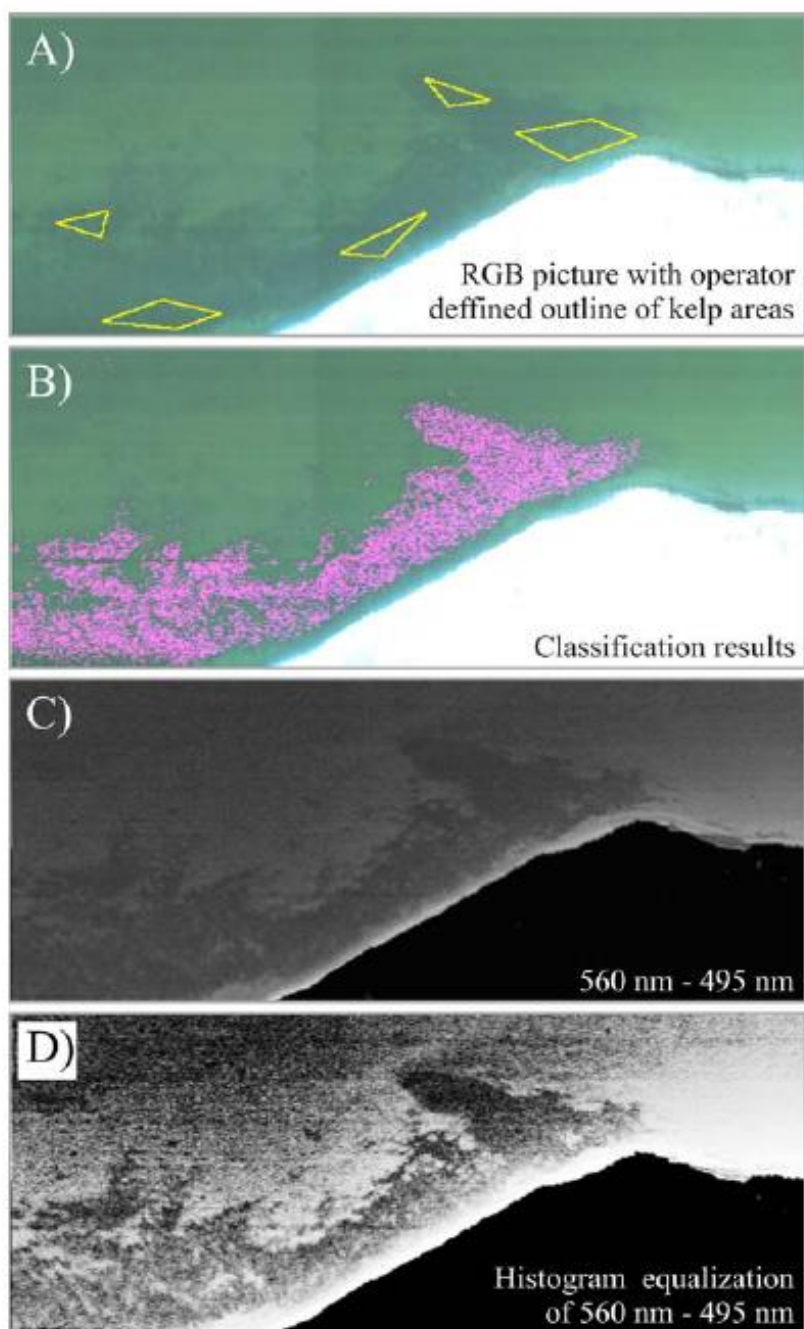


**Figure 3.14** Hyperspectral images from Collinderodden and Blixodden, Van Mijen-fjorden, Svalbard (2000). A) RGB image (490 nm, 554 nm and 633 nm) to get optical signature from shallow water, B) Image in 730 nm (IR), 578 nm and 490 nm to get optical signature from vegetation on land. C) Unsupervised classification of different optical signatures (Johnsen et al., 2009).



**Figure 3.15** Local HI of a river plume taken from a mountain Platåfjellet (428 masl), Isfjorden, Svalbard (2007). The plume water from the river Bjørndalselva contains reddish silt, giving the reflectance spectrum at Site 1. Site 3 give the reflectance spectrum of the ocean water and the bottom. A difference spectrum indicates the different optical properties of the river plume and ocean water. A slit from the HI show a monochromatic image (490 nm) and the optical properties of the sites given this wavelength (Johnsen et al., 2009).

Volent et al. (2007) performed an airborne HI project in Kongsfjord (Ny Ålesund, Spitsbergen) from a height of 2950 m. The study shows that HI of coastal waters is a cost efficient method for kelp forest and bottom substrate mapping. The bottom substrate contained sediments with grain size from stones (up to 10 cm) to clay, but there are no information on the mineralogical content. *In situ* measurements were done simultaneously to verify the results from the HI. Figure 3.16 shows spectral imager results from area 1 out of three areas examined. The identification process was carried out in five steps. First, kelp areas were identified by scuba-divers and in RGB images (A). This was used for target recognition by using a Bayesian Supervised Classification (BSC) technique (B). The monochromatic image at 560 nm gave the deepest penetration of light in the water column. Upwelling radiance at  $L_u(495 \text{ nm})$  was subtracted from  $L_u(560 \text{ nm})$ , because this wavelength represented the optical properties of the seawater, and had to be corrected for (C). Finally, a Differential Histogram Equalization (DHE) technique gave the image better contrast (D).



**Figure 3.16** A) RGB image of area 1. B) Classification results of kelp forest from BSC statistics. C) Correcting for the optical properties of the water. D) Results after DHE to increase contrast. (Volent et al., 2007).

### 3.3 Underwater Hyperspectral Imaging

An article by Johnsen et al. (2013) gives a good review of Underwater Hyperspectral Imaging (UHI) in the context of creating biogeochemical maps of the seabed, including a description of the hyperspectral imager, potential underwater platforms and processing of optical data.

#### 3.3.1 The underwater hyperspectral imager

When a hyperspectral imager is attached to airborne platforms, the light source used is electromagnetic radiation from the sun. This is a passive method of remote sensing, without control of the light source. Moving the imager below the water surface and using an artificial light source give better control of the measurements and make this an active remote sensing method. With an artificial light source, it is possible to measure the seabed at depths below the 1% sunlight depth (Figure 3.2). The underwater hyperspectral imager gives the opportunity to get closer to the target and get a better spatial and spectral resolution of the optical measurements of the objects of interest (Johnsen et al., 2013).

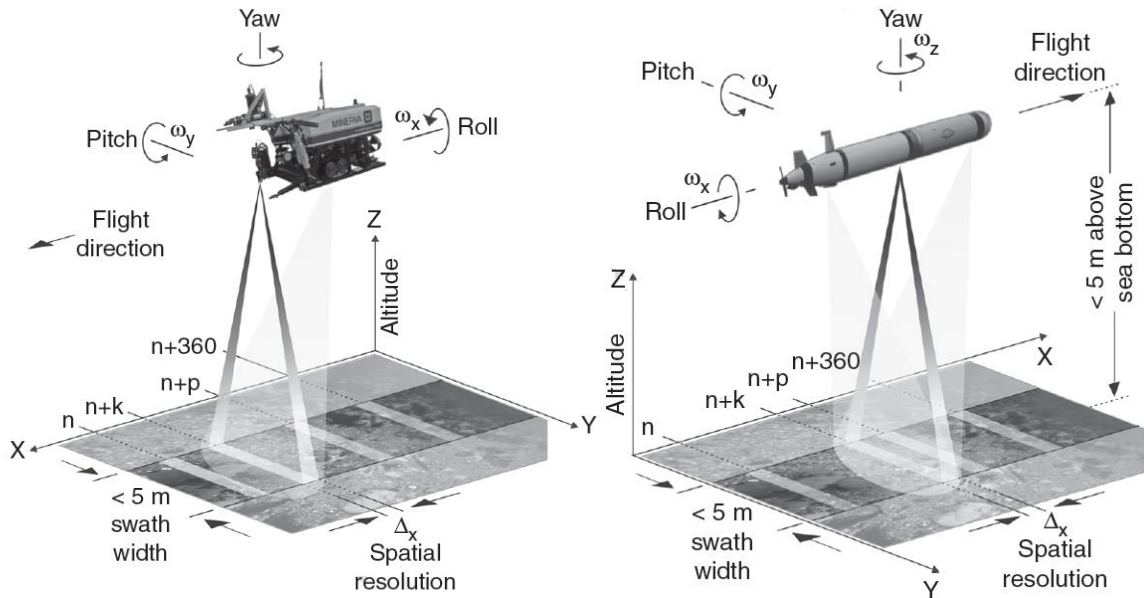
#### 3.3.2 Underwater platforms

To use the hyperspectral imager underwater it needs a water pressure housing and to be deployed on mobile underwater robots, which make it possible to map areas of 1 m<sup>2</sup> - 1000 km<sup>2</sup> (Johnsen et al., 2013). Remotely operated vehicles (ROVs) and autonomous underwater vehicles (AUVs) are possible platforms for the imager (Figure 3.17). Pitching, yawing and rolling of the platforms can disturb the recorded images and have to be measured and allowed for.

The ROV is deployed to and tethered from a ship, giving an on-line control of the instrument and collection of the data stream. In addition, sensors for measuring water column optical properties (Chl*a*, CDOM and TSM) and acoustic sensors to map bathymetry and bottom substrate can be attached to the ROV.

The AUV has a propeller-driven system with high power capacity and good sampling capabilities over large distances. Using a AUV as a platform, instead of a ROV, makes it unnecessary to use tether and ship-based crew. The small AUVs can dive down to 100-500 m depth, while the large AUVs can reach depths of 6000 m and travel distances of several hundred kilometers. A large AUV is therefore the best alternative as platform for the imager. Other

benefits are the altitude control on the AUV and the possibility to predefine sampling patterns (Johnsen et al., 2013).



**Figure 3.17** Illustration of ROV and AUV as platforms for the underwater hyperspectral imager,  $n$  = amount of pixels in X-direction (Johnsen et al., 2013).

### 3.3.3 Optical processing

The optical properties of the water column affect underwater hyperspectral measurements. The distance between the imager and the target make optical processing of the imagery necessary. Substances in the water absorb and scatter the light from the light source and affect the true reflectance of the target. UHI uses an active light source where the intensity and spectral characteristics vary with the lamp. These two factors in addition to the ambient light at the water depth, have to be corrected for to find the true reflectance of the target. The raw upwelling radiance ( $L_{u\text{ raw}}(\lambda)$ ) is divided by the spectral characteristics of the light source, the ambient light and the water constituents ( $L_{u\text{ light}}(\lambda)$ ) to record the true reflectance (Pettersen, 2013; Volent et al., 2007, 2009):

$$R(\lambda) = \frac{L_{u\text{ raw}}(\lambda)}{L_{u\text{ light}}(\lambda)} \quad [\text{Eq. 4}]$$

An optically white or grey plate, reflecting all colors, can be used to find the  $L_{u\text{ light}}(\lambda)$ . The plate must be placed on a known distance from the imager, preferably close to the target. It is

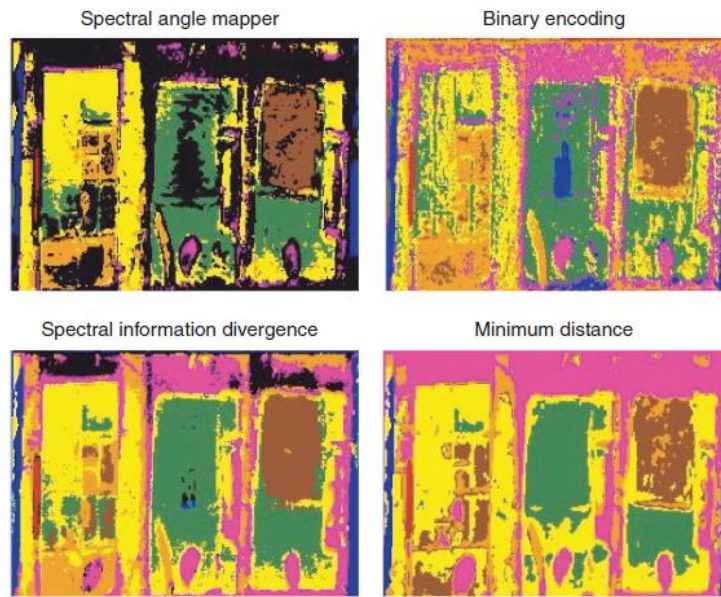


also possible to estimate the inherent and apparent optical properties of the water by modelling. Properties of the water column are then measured by sensors on the platform (Johnsen et al., 2013).

### 3.3.4 Previous work on UHI at NTNU

UHI was tested in Hopavågen, central Norway, as a marine biology experiment looking at different benthic organisms such as the cold-water coral *Lophelia pertusa*. Hyperspectral images of white, orange and dead corals were captured and other material like sand and rocks on the sea bottom were included in the images. A custom made cart running on tracks on the seabed was used as a platform for the imager. A halogen and a LED lamp were used as light sources and a spectroradiometer measured the spectral output of these (Johnsen et al., 2013; Pettersen, 2013).

In addition to corals, images of natural seafloor fauna, bottom substrate (shell, sand and rocks), minerals, metals, and kelp species were captured by UHI. The images of the minerals were used in a study of changes in geochemistry. Manganese nodules and artificial mixed sediments of different content like manganese oxide ( $\text{MnO}_2$ ), manganese sulfate ( $\text{MnSO}_4$ ), ferric oxide ( $\text{Fe}_2\text{O}_3$ ) and ferric sulfate ( $\text{FeSO}_4$ ) were used. The images showed a distinct discrimination of the different geochemical objects seen in Figure 3.18. Different algorithms such as spectral angle mapper, binary encoding, spectral information divergence and minimum distance were used in an unsupervised classification. The spectral information divergence method proved to be the best algorithm for discrimination between the objects (Johnsen et al., 2013).



**Figure 3.18** Unsupervised classification of minerals using different algorithms to identify objects of interest. Blue = blue metal frame, orange = rusted piece of iron, magenta = manganese nodules, yellow = substrate 1 dominated by ferric sulfate, brown = substrate 2 dominated by oxidized iron, green = substrate 3 consisting of ferric sulfate, red = red pencil. The biofilm content and the amount of oxidized elements varies between the substrates (Johnsen et al., 2013).

The Applied Underwater Robotics Laboratory (AUR-Lab) at NTNU and the Norwegian Defence Research Establishment (FFI) arranged a collaborative cruise in the Trondheim Fjord in 2012 where UHI was tested on coral reef on the Tautra Ridge (Ludvigsen et al., 2014). The UHI sensor, measuring optical signatures in the range 350-850 nm, was connected to a ROV together with two 250 W halogen lamps. The altitude of the ROV was 1.5-3 m above the sea floor, mapping 20-30 m long and 2-3 m wide transects with a speed of 0.2-0.3 m/s. Figure 3.19 display a 20 m long UHI transect from this survey (Ludvigsen et al., 2013). The image show reflection in red, green and blue and it is possible to see the condition of the reef. Red color indicate the coral *Paragorgia arborea*, white is *Lophelia pertusa* and brown color is dead *Lopheila*. The results of this image show successful reflectance spectra in the pixels covering the entire visible light range.



**Figure 3.19** Imagery from an underwater hyperspectral imager showing a 20 m transect of a coral reef (Ludvigsen et al., 2013). Image from Ecotone © (with permission).

### 3.4 Chapter summary

- ❖ The ratio between  $E_u$  and  $E_d$  is the reflectance parameter,  $R$ .
- ❖ UV- and IR-light are heavily attenuated in water, thus visible light reflectance is used in optical reflectance measurements under water.
- ❖ AOPs and IOPs describe the optical properties of seawater affecting optical reflectance measurements.
- ❖ Absorption features in reflectance spectra of minerals are found in the UV-VNIR region, and are determined by electronic and vibrational processes.
- ❖ Grain size affects the reflectance from sediments.
- ❖ Optical remote sensing (including hyperspectral imaging) is a mapping and monitoring technique using optical signatures obtained from imaging spectrometers to discriminate between different objects.
- ❖ A hyperspectral imager is a spectrometer equipped with a camera. The spectrometer separates reflected solar energy from the surface into spectral bands, which are narrow wavelength intervals.
- ❖ Several studies on applications of satellite-borne and airborne HI for geologic exploration have been successful, both on terrestrial geology and on shallow sea bottom substrate.
- ❖ The underwater hyperspectral imager offers the opportunity to get closer to the target and get high spatial and spectral resolution of the optical measurements of the objects on the seabed.



## Chapter 4 Materials and Methods

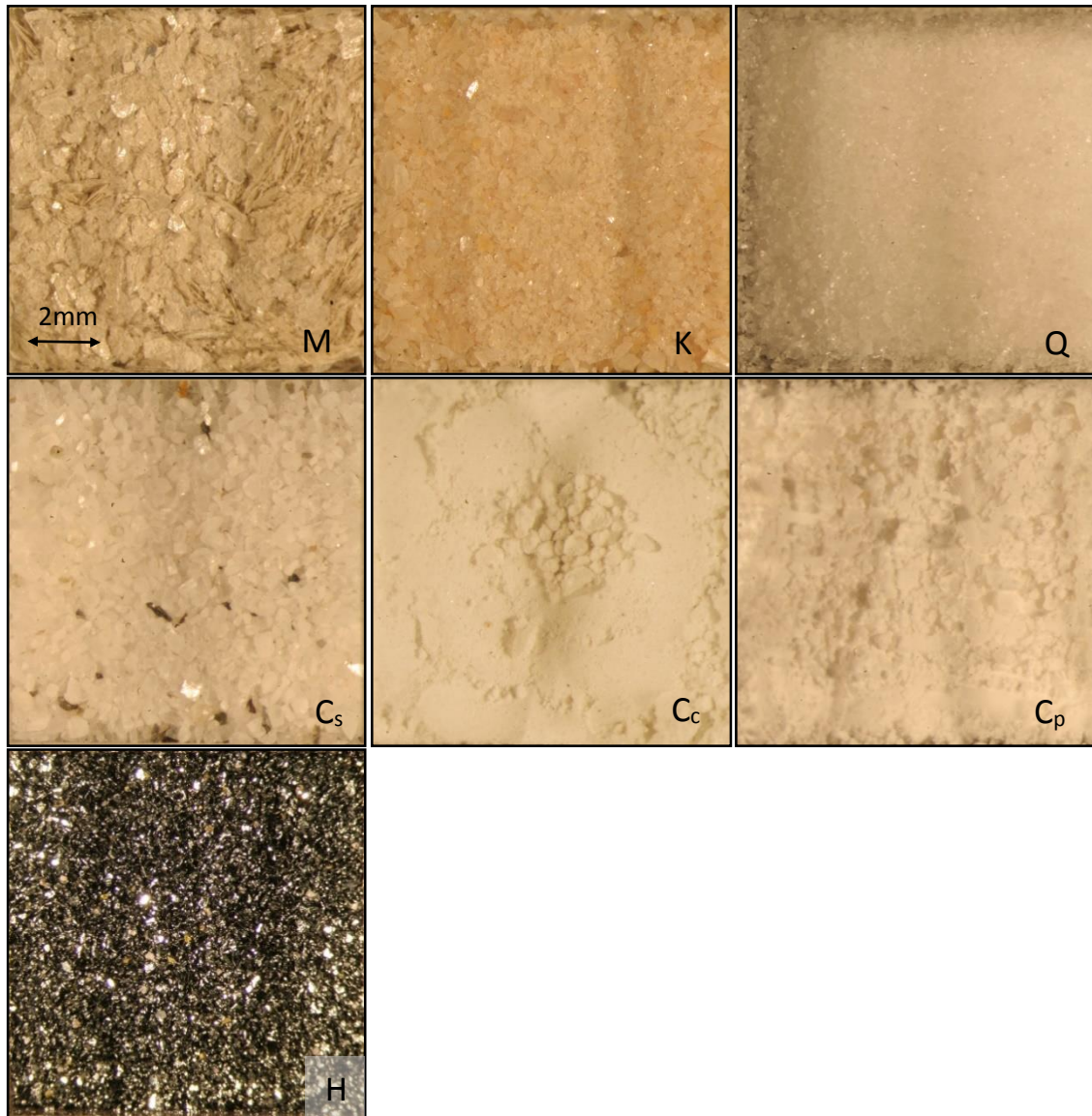
### 4.1 Materials

In the laboratory work, reflectance spectra were made of seven mineral samples, nine artificial sediment samples composed by the minerals, five natural sediment samples and two carbonate crust samples.

#### 4.1.1 Mineral samples

Six mineral samples were provided by the mineral processing laboratory at NTNU – calcite from calcite marble (both sand and clay samples), quartz, k-feldspar, muscovite and hematite. Pure calcium carbonate was provided by NGU. The descriptions of the minerals and the quantitatively estimates of mineral percentage are based on interpretation from stereomicroscopy. A visual grain size classification was performed according to the classification scheme in Figure 2.1. Figure 4.1 shows images of the mineral samples.

The reason for selecting these minerals was to compound a realistic artificial marine sediment. Quartz and feldspars are abundant minerals in marine sediments. Muscovite was used because this was available as a pure mineral in the laboratory. Hematite sand was added to give the sediment a darker color and this could also represent the iron (red clay) often found with carbonates in marine sediments. The calcite marble was available in two grain sizes, and was thus used to look at reflectance related to grain size.



**Figure 4.1** Images of the minerals. *M* = muscovite, *K* = k-feldspar, *Q* = quartz, *C<sub>s</sub>* = calcite marble (sand), *C<sub>c</sub>* = calcite marble (clay), *C<sub>p</sub>* = pure calcium carbonate, *H* = hematite.

**Muscovite (M)** has the chemical formula  $\text{KAl}_2(\text{AlSi}_3\text{O}_{10})(\text{F},\text{OH})_2$ . The sample had a light gray color and grain size ranged from clay size to medium sand. Since muscovite is a sheet-silicate mineral, the grains had a platy shape with large ratio between the long and short axes of the grain. The surface area of the sample dominated of grains oriented with the largest face upwards. Muscovite and the other mineral samples are crushed from larger samples in laboratory and the grains therefore had angular edges.

**K-feldspar (K)** has the chemical formula  $\text{KAlSi}_3\text{O}_8$  and is a tecto-silicate mineral. The sample had an orange color. Other minerals could have been present in the sample, but the amount was

less than 1%. Main grain size was medium sand. The grain shape was equant with smooth surfaces due to the mineral's cleavage.

The pure **quartz (Q)** sample had a dominating grain size of fine sand fraction. Quartz is a tecto-silicate mineral with formula  $\text{SiO}_2$ . The grain shape was equant with a rough surface typical for quartz.

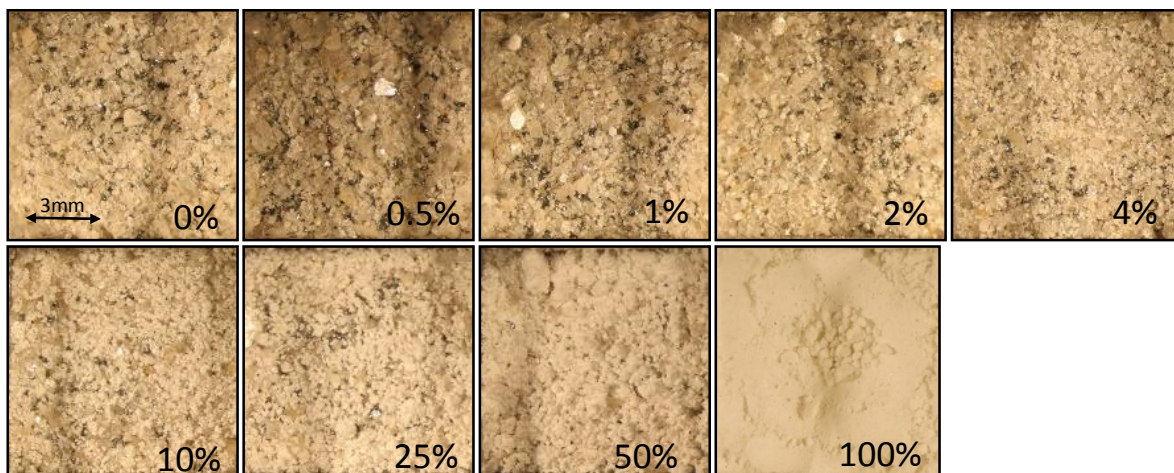
**Calcite marble**,  $\text{CaCO}_3$ , in clay fraction (**C<sub>c</sub>**) and in medium sand fraction (**C<sub>s</sub>**) were crushed Akselberg graphite-spotted calcite marble from the company Brønnøy Kalk AS. The samples contained ~98% calcite and the remaining ~2% consists of graphite, pyrite, quartz, feldspar and smaller amounts of apatite and diopside (Ingjerd Olden Bunkholt, pers. comm., October 2014). The grain shape of the sand fraction sample was equant and the surfaces were determined by the calcite's rhombohedra cleavage.

The pure **calcium carbonate (C<sub>p</sub>)**,  $\text{CaCO}_3$ , used as the carbonate part in the artificial sediment mix was precipitated in a laboratory (*Thermo Fisher Scientific*). Grain size was clay fraction. Crystal lattice was unknown, but the crystal lattice of calcite is often dominating in precipitated  $\text{CaCO}_3$ .

**Hematite (H)** is an iron oxide with chemical formula  $\text{Fe}_2\text{O}_3$ . This sample consisted of ~98% hematite and ~2% other minerals (iron silicates and quartz). The grains had a black color with red metallic shine and the grain size was medium sand with equant shapes. The hematite grains the grains had smooth surfaces, which can lead to specular reflection.

#### 4.1.2 The artificial sediment samples

An artificial sediment was composed by quartz, k-feldspar, muscovite and hematite, called the basis sediment. Pure calcium carbonate were added to the basis sediment in different amounts resulting in eight samples containing 0 wt%, 0.5 wt%, 1 wt%, 2 wt%, 4 wt%, 10 wt%, 25 wt% and 50 wt%  $\text{CaCO}_3$  (Figure 4.2). The sample **C<sub>p</sub>** was used as the 100 wt%  $\text{CaCO}_3$  sample in the HI and Jaz measurements. The method of mixing these samples is described in chapter 4.2.

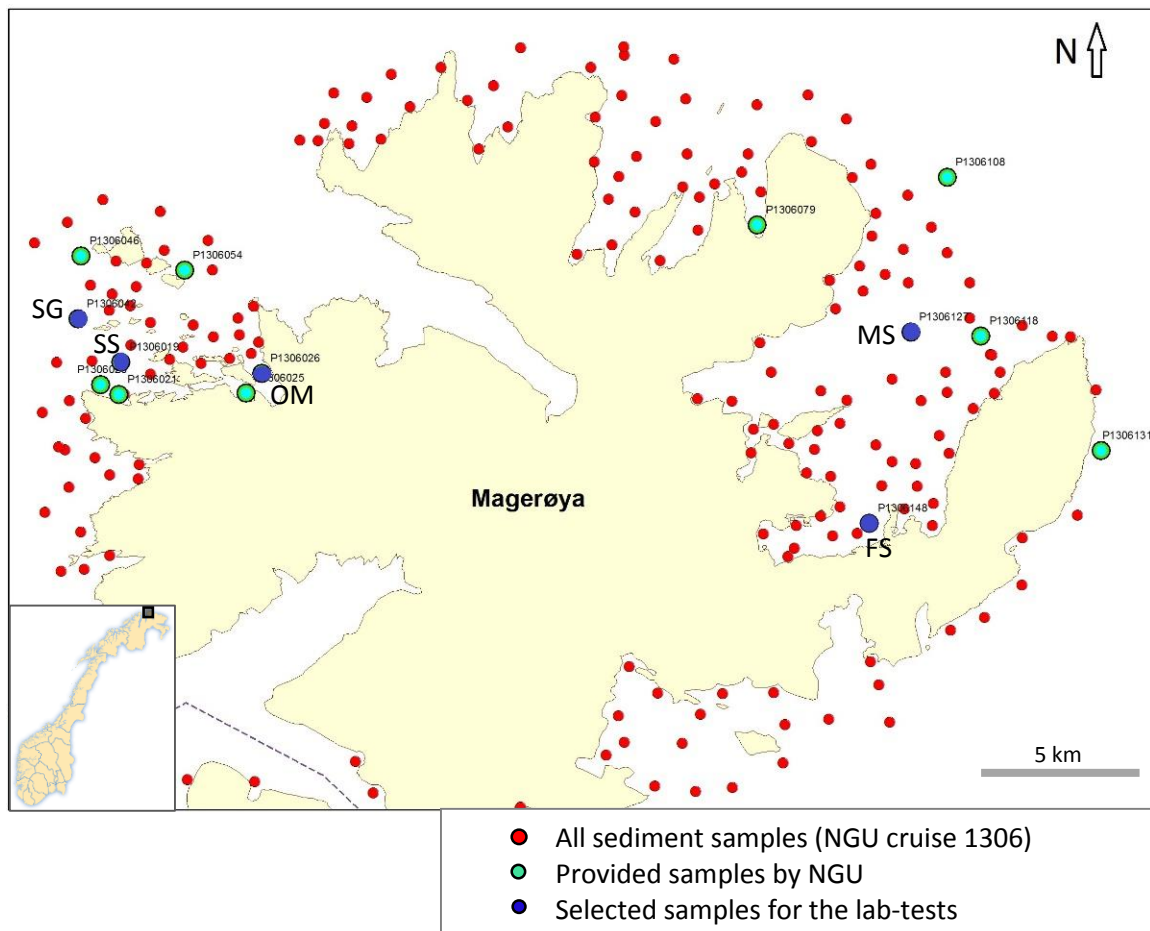


**Figure 4.2** Artificial sediments. 0-100 % explain the weight percent (wt%) of  $\text{CaCO}_3$  in the sediment.

#### 4.1.3 Natural sediment samples

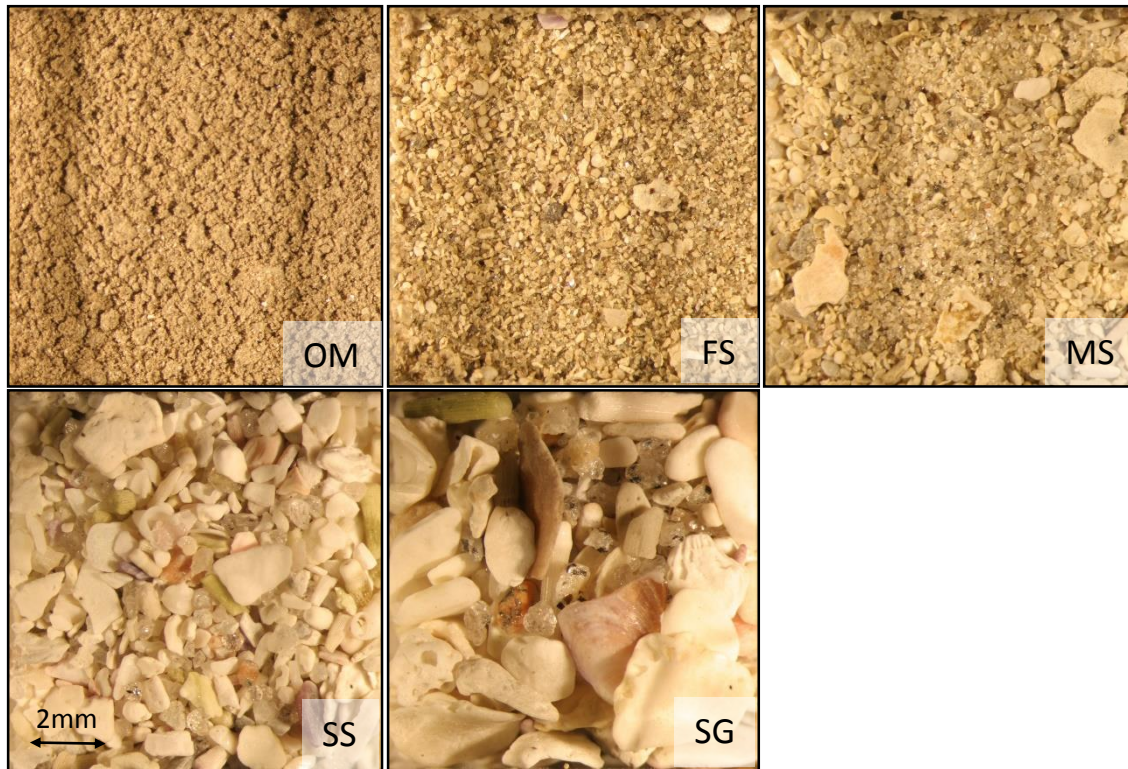
NGU provided the natural sediment samples for the laboratory tests. They were collected in 2013 close to the shore on the western and eastern part of Magerøya in Finnmark, Norway (Figure 4.3). The purpose of the cruise (cruise 1306) was of mapping shell sand deposits for use in shell sand modelling, but no field report exists. Field scientists at NGU have made a visual description of these sediments, shown in appendix D. Water depths ranges from 30-66 m. Out of 14 samples provided - five samples were used for tests in this study, due to their variety in grain size and carbonate content. Images of the sediments are shown in Figure 4.4.





**Figure 4.3** The selection of the samples provided by NGU around Magerøya in Finnmark, Norway. Red dots show the positions of all the samples NGU has sampled around Magerøya, the green dots show the position of the samples provided to this study. The blue dots show the five samples selected for reflectance measurements – OM = organic mud, FS = fine sand, MS = medium sand, SS = shell sand, SG = shell gravel. The figure is a modification of a map provided by NGU.

The following description of the sediments are based on information given by NGU and interpretation of the sediments from stereomicroscopy. The sediments were dried in a drying cabinet for 24 hours on 60°C. Sample P1306026 (organic mud) needed 48 hours to dry. This sample hardened in large lumps of dry mud and was crushed in a mortar.



**Figure 4.4** Natural sediment samples. OM = organic mud, FS = fine sand, MS = medium sand, SS = shell sand, SG = shell gravel.

Sample P1306026, was an **organic mud (OM)**, consisted of ~95% organic material and clay minerals (unidentified) and ~5% shell fragments. The sample was light brown in color and moderately sorted.

Sample P1306148, **fine sand (FS)**, consisted of ~40% carbonates (shell fragments, foraminifera), ~30% quartz, ~10% clay minerals, ~5% organic material, ~15% unidentified minerals. The foraminifera were double the size of the other minerals, and the sample was poorly sorted with a main grain size of fine sand. Shell fragments of coarse sand fraction occurred. Carbonates had rounded shapes while the other minerals had angular shapes. The sample had a dark, greyish brown color.

Sample P1306127, **medium sand (MS)**, consisted of ~50% carbonates (shell fragments, foraminifera), ~40% quartz and ~10% unidentified minerals. The amount of organic material and clay minerals were low. The foraminifera and shell fragments were larger than the other minerals, and the sample was poorly sorted. Carbonates had rounded shapes while the other minerals had angular shapes. Color was olive grey and light brown.

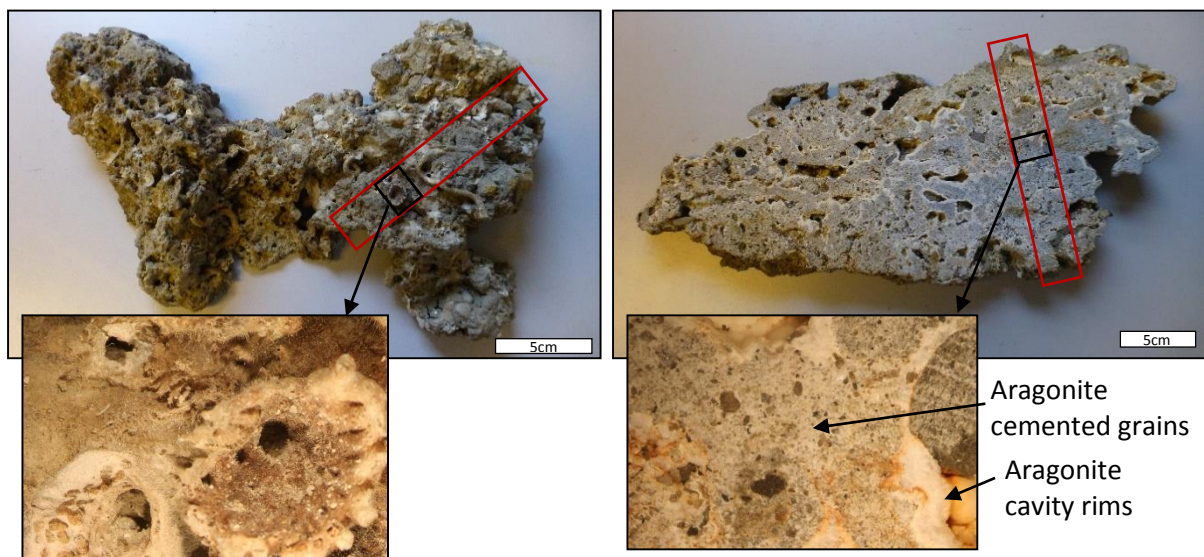
Sample P1306019, was classified as **shell sand (SS)**. It consisted of ~90% shell, corals and shell fragments of coarse grain size. It was moderately sorted with medium sand fraction quartz, and some shells fragments of very coarse sand fraction. Colors were white, pink, green and purple.

Sample P1306042, was classified as **shell gravel (SG)**. This sample consisted of ~90% shell, corals and shell fragments. Quartz was the dominating mineral apart from the carbonates. The quartz fragments were of coarse sand fraction and had angular shapes. It was moderately sorted with a main grain size of gravel. Colors were white, pink, green and purple.

#### 4.1.4 Carbonate crust samples

In addition to the sediment and mineral samples, two carbonate crusts were analyzed. These were also provided by NGU, and were collected on a research cruise in the southwestern Barents Sea in 2012. They were sampled approx. 60 km in distance from each other. One of the crusts, sample P1210035\_1B, still have the original surface. The other sample, P1210006\_4A, is cut in a cross section, showing a fresh surface of the crust. These were found at depths of 390 m and 320 m, respectively. Figure 4.5 show the crusts and the marked red squares are the areas captured by the HI.

The carbonate crusts consisted of grains and shell from marine sediments cemented together by aragonite (Aivo Lepland, pers. comm., November 2014). This gave the crust a grey color. The grain size of the cemented sediments ranged from fine sand to gravel. Concentric layers of pure aragonite were seen in cavities within the crust, forming white cavity rims. The original surface had a darker gray color. The surface consisted of organic mud and skeleton and shells of different organisms like bristle worms (*Polychaete*) and moss animals (*Bryozoa*), which covered the aragonite cement and sediment grains.



**Figure 4.5** Carbonate crusts. Original surface to the left (P1210035\_1B), fresh surface to the right (P1210006\_4A). The marked red squares are the areas captured by the HI.

## 4.2 Methods

A hyperspectral imager connected to a stereomicroscope was used for capturing hyperspectral images of the samples. To verify the reflectance spectra from the HI, a Jaz spectrometer was used to get the true reflectance spectra from the surface of the samples. However, no guidelines exist on how these devices should be used for sediment samples, and the experiments are based on trial and error.

The mineral and sediment samples were added to cuvettes (10mm\*10mm\*45mm). To get more significant results, three replicates of each sample were measured by HI and Jaz. This resulted in a division of samples into three sets. Sample sets of minerals and natural sediments were numbered 1, 2 and 3, while the artificial sample sets were named A, B and C.

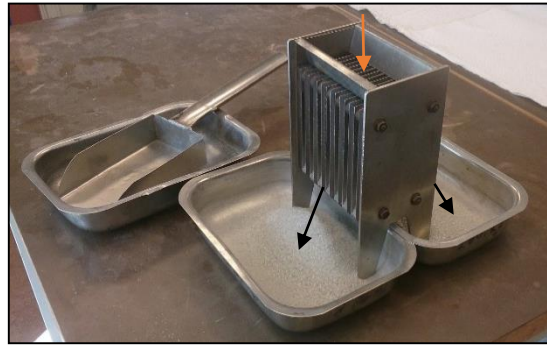
### 4.2.1 Artificial sediment mix

The artificial sediments were made mixing 100g quartz, 100g k-feldspar, 50g muscovite and 100g hematite. The minerals were mixed with a “splitter” by adding the minerals with a spade. The “splitter” splits the mineral into two parts of similar size, as seen in Figure 4.6. It is important to fill the spade completely in its width to avoid segregation in the spade. Mineral samples are homogenously mixed when this procedure is repeated seven times. The sample was separated into seven parts of ~50g. Calcium carbonate mass were measured to find the correct weight to be mixed with the artificial sediment. The CaCO<sub>3</sub> mass was calculated by using the equation:

$$\frac{x}{m+x} * 100 = p \quad [Eq. 5]$$

where  $x$  = calcium carbonate mass [g],  $m$  = artificial sediment mass [g],  $p$  = percent calcium carbonate in the mixed sediment (wt%).

The sediment and the calcium carbonate were homogenously mixed with the splitter, and each sample was added to three cuvettes (resulting in set A, set B and set C). Seven different mineral mixtures were made containing 0.5 wt%, 1 wt%, 2 wt%, 4 wt%, 10 wt%, 25 wt% and 50 wt% CaCO<sub>3</sub>. It is important to note that the CaCO<sub>3</sub> content in this experiment is expressed as weight percent, while visual classifications, often used for descriptions of marine sediments, provide area percent of the CaCO<sub>3</sub> content.



**Figure 4.6** The splitter used to homogenously mixing the minerals. Yellow arrow show the sample input, black arrows show the separated samples.

#### 4.2.2 Submerging samples

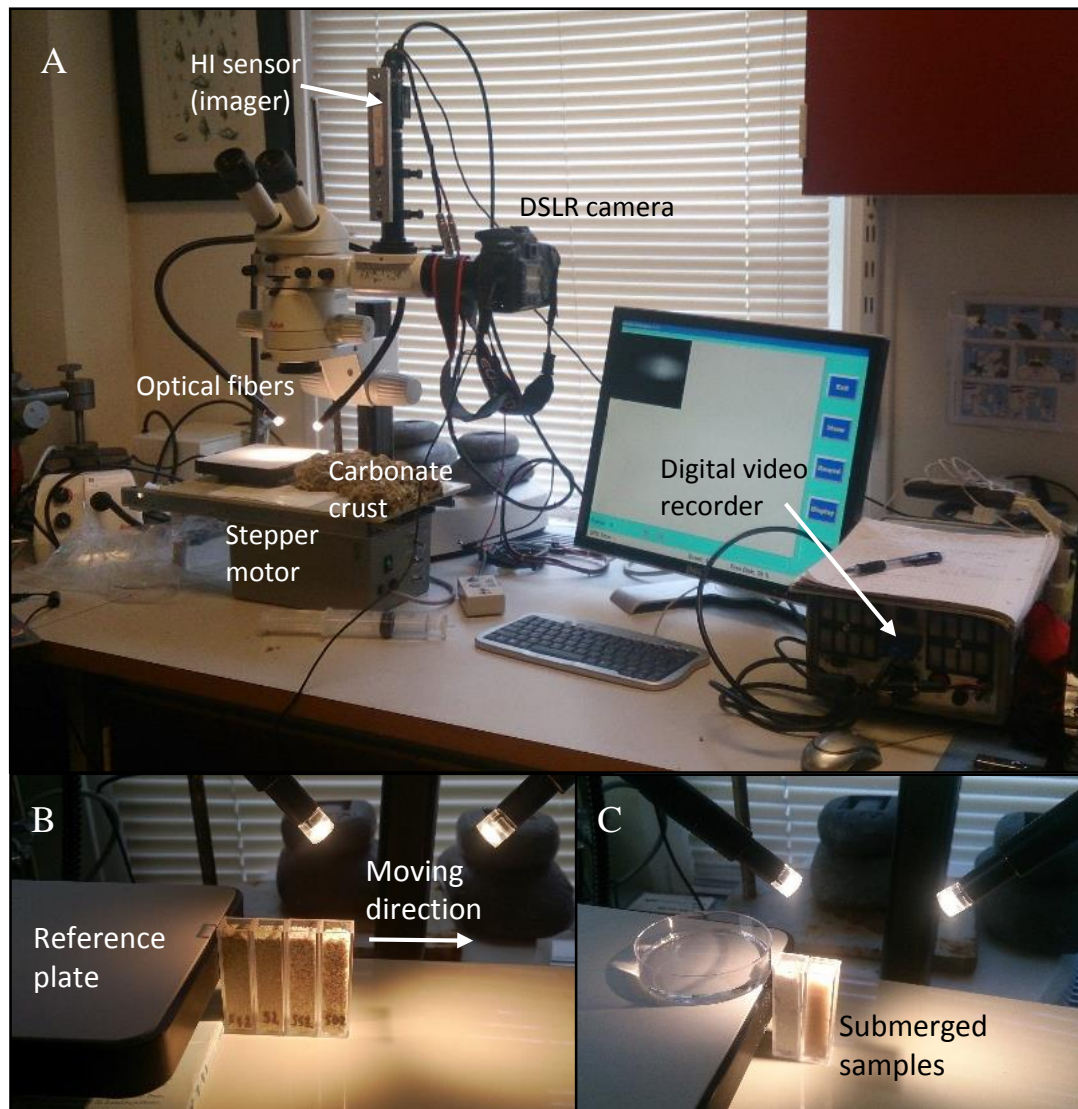
Water used for submerging the samples was filtered seawater from 200 m depth in the Trondheim fjord collected from a pump at TBS. The water was filtered through 0.2  $\mu\text{m}$  sterile syringe filters (cellulose acetate) attached to a 500 ml syringe (BD Perfusion) when it was added to the samples. The sample surfaces were covered by 2-4 mm water. Some samples contracted due to the water, and had to be refilled to reach the same height in the cuvette as the other samples.

#### 4.2.3 Hyperspectral imaging

##### **Instrumentation**

The hyperspectral imaging instruments were set up according to Pettersen et al. (2013) and Volent et al. (2009). The hyperspectral imager used in the measurements is custom made and is a solid-state push-broom imager, 2 cm long, 4 cm wide, 600 g, with power requirement of 12 V, 139 mA. Frame rate was set to 25 images per second and the camera was equipped with a 12-mm Schneider (f:1.2) front lens with aperture set to 2.8 to enhance depth of field. The spectral resolution was one nanometer in the region 420-680 nm. The spatial resolution perpendicular to the moving direction was approx. 2 mm/pixel. Data from the imager were stored as video files (avi-format) from a digital video recorder (Route Scene Navigator 2.4.4 - Video Navigation). The hyperspectral imager was connected to a Leitz Leica MZ6 stereomicroscope. A Leitz CLS 150X halogen lamp was used as light source, emitting light through two optical fiber bundles. The light bundles had an angle of about 45° to the sample surface. The samples were placed on a moving table with a stepper motor moving the samples

$2.6 \text{ mms}^{-1}$ . A Canon 20D DSLR-camera fitted to the stereomicroscope through a phototube was used for capturing RGB pictures of the samples. See Figure 4.7 for setup.



**Figure 4.7** A) HI setup showing the hyperspectral imager and DSLR camera connected to a stereomicroscope. The digital videorecorder is seen to the right in the picture, and the HI slit image is shown on the screen. B) Setup of the samples measured by the imager in the moving direction. Reference plate is shown to the left. C) The setup of the submerged samples and the reference plate with a petri dish with seawater.

*The methodology of the HI-measurements*

The HI measurements were carried out for three replicates of each of the dry and submerged samples. See Figure 4.8 for cuvette setup of the samples measured simultaneously by the imager. High-resolution RGB images of each replicate samples, both dry and submerged, were captured by the DSLR camera.

By using this method, several samples were analyzed at identical light conditions. The darkest samples, like hematite and organic mud, were measured separately because they needed other light conditions than the white minerals. The previous setup of the cuvettes was changed because the dark samples became darker when they were submerged in water and needed other light conditions. For the carbonate crusts, only one section of each surface was measured, due to restrictions in the spatial resolution of the slit in the imager.

A white Spectralon optical reference plate with 50% reflection of 400-700 nm was used as a white reference to correct for the spectral lamp output and other light sources in the room. In wet conditions, the reflection properties of the Spectralon changes, thus the plate was not submerged in water. As an alternative, a Petri dish with ~2 mm filtered seawater was put on top of the reference plate when the submerged samples were measured. Pettersen et al. (2013) have shown that the distance and inherent optical properties in the water do not have a significant impact on the reflectance signature when a reference plate is used for correction.



## DRY SAMPLES:

Ref	M1	K1	Q1	C <sub>s</sub> 1	C <sub>c</sub> 1	C <sub>p</sub> 1			
Ref	M2	K2	Q2	C <sub>s</sub> 2	C <sub>c</sub> 2	C <sub>p</sub> 2			
Ref	M3	K3	Q3	C <sub>s</sub> 3	C <sub>c</sub> 3	C <sub>p</sub> 3			
Ref	H1	H2	H3						
Ref	FS1	MS1	SS1	SG1					
Ref	FS2	MS2	SS2	SG2					
Ref	FS3	MS3	SS3	SG3					
Ref	OM1	OM2	OM3						
Ref	0%A	0.5%A	1%A	2%A	4%A	10%A	25%A	50%A	100%A
Ref	0%B	0.5%B	1%B	2%B	4%B	10%B	25%B	50%B	100%B
Ref	0%C	0.5%C	1%C	2%C	4%C	10%C	25%C	50%C	100%C

M = muscovite

K = k-feldspar

Q = quartz

C<sub>s</sub> = calcite marble (sand)C<sub>c</sub> = calcite marble (clay)C<sub>p</sub> = pure CaCO<sub>3</sub>

H = hematite

OM = organic mud

FS = fine sand

MS = medium sand

SS = shell sand

SG = shell gravel

% = wt% CaCO<sub>3</sub>

## SUBMERGED SAMPLES:

Ref <sub>w</sub>	K1	Q1	C <sub>s</sub> 1	C <sub>c</sub> 1	C <sub>p</sub> 1				
Ref <sub>w</sub>	K2	Q2	C <sub>s</sub> 2	C <sub>c</sub> 2	C <sub>p</sub> 2				
Ref <sub>w</sub>	K3	Q3	C <sub>s</sub> 3	C <sub>c</sub> 3	C <sub>p</sub> 3				
Ref <sub>w</sub>	M1	M2	M3						
Ref <sub>w</sub>	H1	H2	H3						
Ref <sub>w</sub>	MS1	SS1	SG1						
Ref <sub>w</sub>	MS2	SS2	SG2						
Ref <sub>w</sub>	MS3	SS3	SG3						
Ref <sub>w</sub>	FS1	FS2	FS3						
Ref <sub>w</sub>	OM1	OM2	OM3						
Ref <sub>w</sub>	0%A	0.5%A	1%A	2%A	4%A				
Ref <sub>w</sub>	0%B	0.5%B	1%B	2%B	4%B				
Ref <sub>w</sub>	0%C	0.5%C	1%C	2%C	4%C				
Ref <sub>w</sub>	10%A	25%A	50%A	100%A					
Ref <sub>w</sub>	10%B	25%B	50%B	100%B					
Ref <sub>w</sub>	10%C	25%C	50%C	100%C					

**Figure 4.8** Cuvette setup for dry and submerged samples. The samples on the same row were simultaneously measured by the hyperspectral imager. Numbers refer to the sample set (1, 2 and 3) of the minerals and natural sediment samples. Letters (A, B and C) refer to the sample set of the artificial sediments. Ref = reference plate and Ref<sub>w</sub> = submerged reference plate.

4.2.4 Data processing using the software *yaPlaySpecX*

*yaPlaySpecX* is a custom-made software used to extract monochromatic images and raw reflectance spectra from pixels in the images. It is possible to make monochromatic images for every 1 nm wavelength. The images were made at a wavelength of 570 nm, which proved to give the best signal-to-noise ratio.

Raw spectra ( $L_{u \text{ raw}}(\lambda)$ ) and the light source spectrum ( $L_{u \text{ light}}(\lambda)$ ), were extracted as mean spectra of chosen pixels. This function is called “running mean spectra” in *yaPlaySpecX*. The spectral data were saved as text-files. The mean spectra obtained in this program do not show standard errors of the averaging of data.

The following approach was used for making the resulting reflectance spectra of the samples:

- ❖ To make raw spectra, five chosen pixels were averaged within three areas of the sample resulting in three raw spectra of each sample (illustrated in Figure 4.9). A number of five pixels was chosen because it gave a smoother plot as demonstrated in Figure 4.10.

This figure shows an improvement of the spectrum from a single spectrum to a mean spectrum of five pixels and a mean spectrum of ten pixels. The improvement from one to five pixels is good, while five to ten is small. By averaging five spectra in three different areas, it is easier to control the reflectance differences of the spectra used for the resulting reflectance spectra. Therefore, five pixels were chosen. This was important when measuring the surface of these samples, because the mineral content of the surface areas varies. If more pixels were used for averaging, the variation due to different content would vanish.

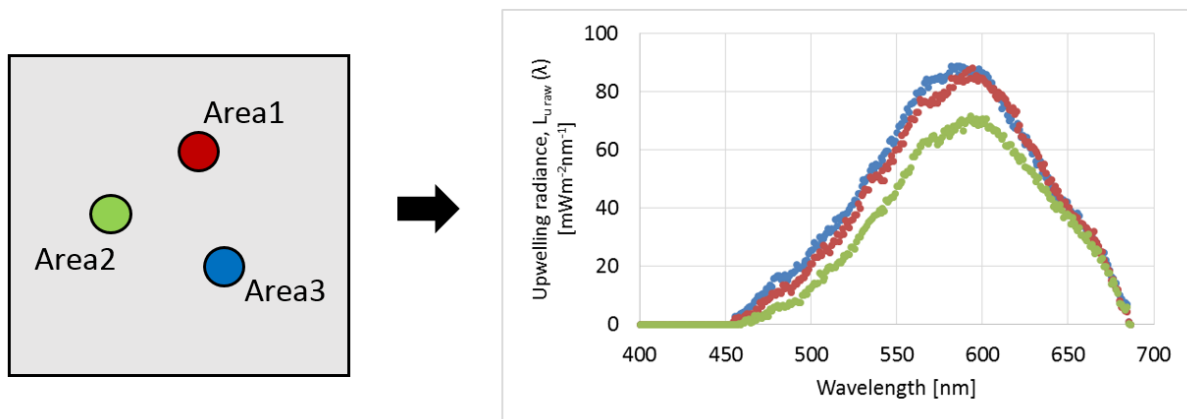
- ❖ The pixels were chosen randomly within the areas, but they could not be overexposed or underexposed by the light source. Overexposed pixels showed flat spectra at maximum radiance intensity and underexposed pixels had a low signal-to-noise ratio.
- ❖ Fifty pixels from the white reference were averaged to find the mean spectrum of the light source. Fifty pixels were used because the reference plate did not have variations across the surface. The spectral reflectance values of the reference plate were doubled, because the plate only reflected 50% of the light.
- ❖ The resulting reflectance spectrum  $R(\lambda)$  of each sample was obtained using eq. 4 in chapter 3.3.3. The resulting reflectance spectrum of one material is an average of the nine spectra obtained from the three replicate samples. Each resulting spectrum has a standard error (SE) to show the variation of the estimated spectra from these nine averaged spectra. The resulting spectra have a spectral range from 460-680 nm. Values beyond these were excluded because of a low signal-to-noise factor in these parts of the spectrum.

Standard errors (SE) of the reflectance (R) were calculated by the following equations, using the standard deviation (SD) of an assortment:

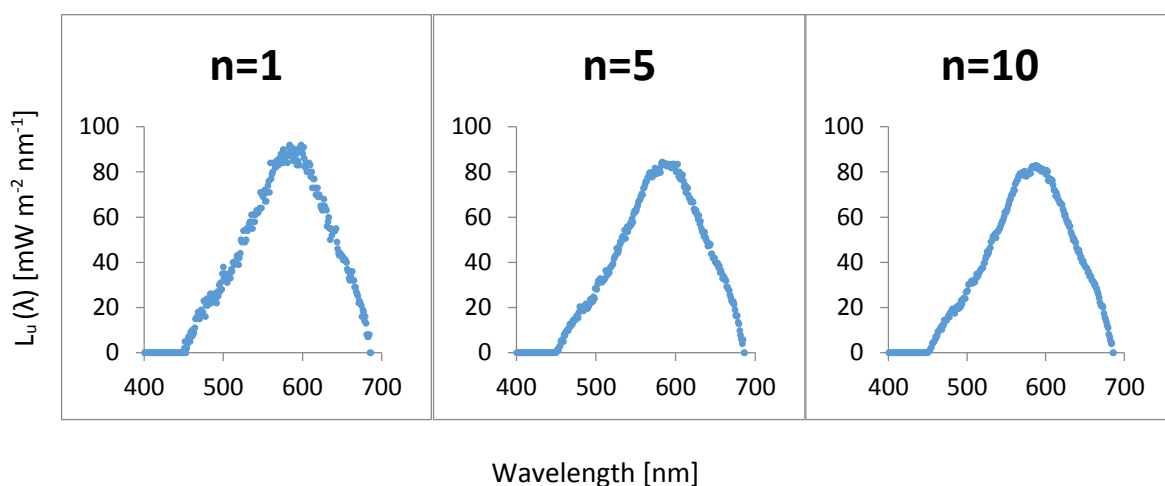
$$SD = \sqrt{\frac{\sum(x-\bar{x})^2}{n-1}} \quad [Eq. 6]$$

$$SE = \frac{SD}{\sqrt{n}} \quad [Eq. 7]$$

where  $x$  = the reflectance values and  $n$  = number of values.



**Figure 4.9** Illustration of the method for making mean spectra from hyperspectral images. Five randomly chosen pixels were averaged in selected areas of the sample surface (to the left). Nine mean spectra like these (to the right) were averaged to get the resulting spectrum of the material.



**Figure 4.10** Illustration of the improvement from one pixel spectrum to five and ten averaged pixels spectra,  $n$  = number of averaged pixels.

#### 4.2.5 Supervised classification using *Image Calculator*

Supervised classifications of samples were accomplished using *Image Calculator*, which is a custom-made software for classifying objects in hyperspectral images. The software was developed on the purpose of performing image analysis on img-files, generated by imaging spectrometers. It is possible to use a minimum distance classification or a Bayes classification with Gaussian probability densities, and the latter was used for the classifications according to Volent et al. (2007). A minimum distance analysis uses the mean vectors for each class and

calculates the distance from each unknown pixel to the mean vector for each class. The pixels are classified as the closest class. The Bayes classification assumes that the statistics for each class in each band are normally (Gaussian) distributed and calculates the probability that a given pixel belongs to a specific class. Each pixel is classified as the class with the highest probability (Richards, 1999). These calculations were done with default settings in the software.

Fifteen monochromatic images with 15 nm steps ranging from 465-675 nm made in *yaPlaySpecX* were used in the classification. It is possible to use two different class-defining approaches in the program - sector defined classes and pixel defined classes. According to Pettersen et al. (2013), pixel defined classification gives a better control of the defined classes. 100 pixels of each sample were used to define the classes. The pixels chosen were not overexposed or in shadow areas. Only objects in the same hyperspectral image can be classified simultaneously. This software limitation resulted in a limited assortment of the hyperspectral images chosen for classification.

#### 4.2.6 Jaz spectrometer

##### *Instrumentation and setup*

A spectrometer, *SpectroClip-JAZ-TR* (Ocean Optics Inc.), was used to measure reflection from the same samples as measured by the HI. This spectrometer is not an imager like the HI. It measures reflectance of wavelengths from 400-700 nm and has a better sensitivity in the red and blue part of the light spectrum than the HI spectrometer and all RGB cameras and video recorders. The Ocean Optics software *SpectraSuite* was used for controlling the measurements. The setup of the Jaz is described underneath and is based on guidelines from the *SpectraSuite* software manual (Ocean Optics, 2009) and recommendations from Inga Aamot at TBS (pers. comm., March 2014).

The spectrometer (Jaz) was connected to a Leica M80 stereomicroscope placing the detecting optical fiber inside the microscope's left phototube, 90° to the sample surface to measure both specular and diffuse reflection. Setup is shown in Figure 4.11. A 100 W halogen cold light source "Intralux® 4100" was used, and two optical fiber bundles were placed in a 45° angle to the surface of the sediment. This setup made it possible to check that the detecting fiber's field of view was completely and evenly illuminated, and only capturing the sediment and not the surroundings. To make sure that light transmitted through the sample was not reflected from the surface below, it was important to have a "light trap" - a black surface underneath the sample. Light conditions were the same for all measurements.

After connecting the Jaz Spectrometer to a computer, the measuring was controlled by the *SpectraSuite* software to extract reflectance spectra from each surface. A dark box were constructed around the microscope with a black curtain, so that light from other light sources, e.g. day light or stray light from fluorescence tubes, did not disturb the signal.

To measure reflectance in *SpectraSuite*, a white and a dark reference were needed. An optically white and spectrally neutral Spectralon reference plate was used as the “white” reference - this is supposed to reflect 75% of the light and all wavelengths equally. For the submerged samples, a Petri dish with filtered seawater was placed on top of the reference plate. The dark reference was used to correct for background noise in the signal, and this was measured by turning off the light source. “*Boccar width*” and “*scans of average*” were both set to 3, in order to get a smoother curve. The corrections for the white and dark reference were done automatically in the software by the following equation (OceanOptics, 2009):

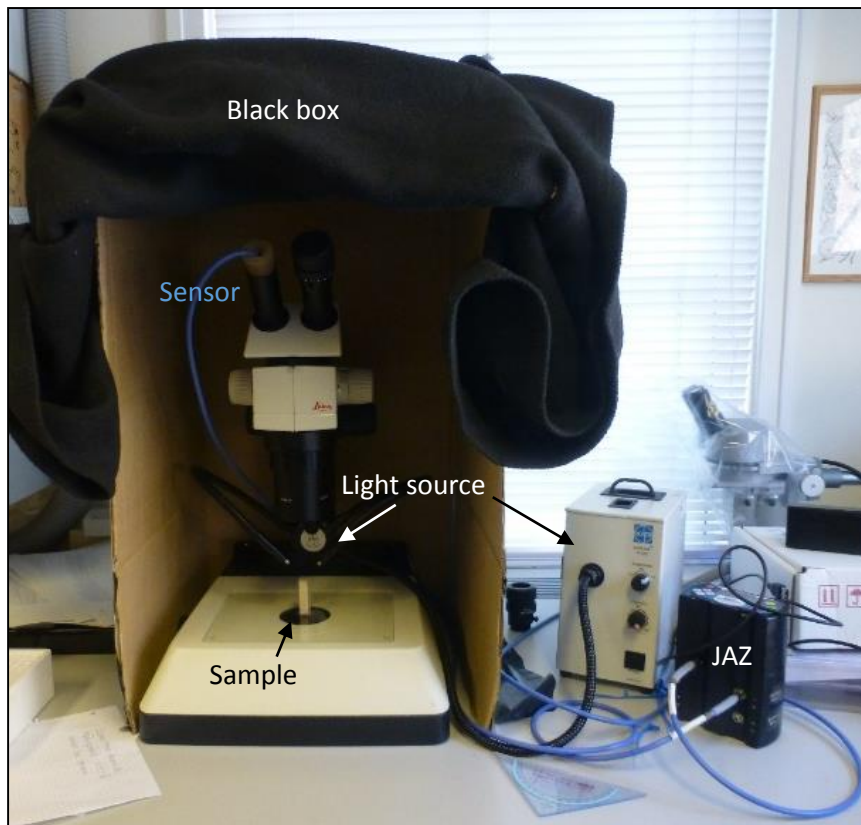
$$\%R(\lambda) = \frac{S(\lambda) - D(\lambda)}{R(\lambda) - D(\lambda)} * 100\% \quad [Eq. 8]$$

$\%R(\lambda)$  = reflectance expressed as percentage

$S(\lambda)$  = the intensity from the sample at wavelength  $\lambda$

$R(\lambda)$  = the intensity from the white reference at wavelength  $\lambda$

$D(\lambda)$  = the intensity from the dark reference at wavelength  $\lambda$



**Figure 4.11** Jaz spectrometer setup.

### ***Methodology of the Jaz measurements***

All surfaces of the samples were measured by the Jaz spectrometer, both dry and submerged in water. Three areas of the carbonate crust surfaces were selected from the section measured by the HI.

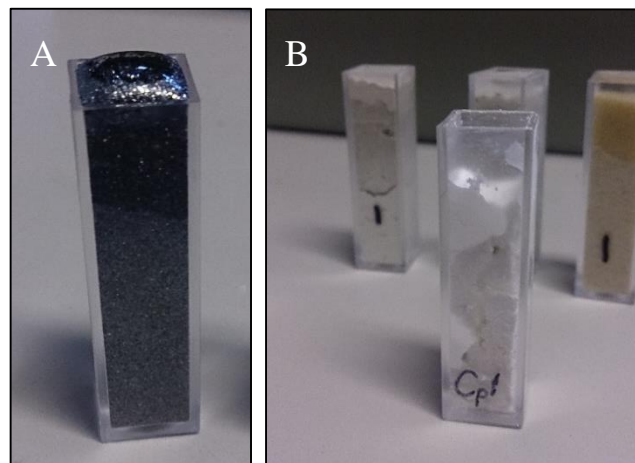
The reflectance data were copied from the software into Excel-files to make reflectance spectra plots. The *SpectraSuite* software gave the reflectance values in R% (0-100) and then transformed to R with values of 0-1. Since the correction for the light spectrum was made in the software, it automatically corrected for a light reflectance of 75% resulting in overestimated reflectance. A correction factor of 0.75 was multiplied to R to get the correct reflectance. This is shown in the equations underneath, using eq. 4 from chapter 3.3.3:

$$R(\lambda) = \frac{L_{u\ raw}(\lambda)}{0.75L_{u\ light}(\lambda)} \Rightarrow 0.75R(\lambda) = \frac{L_{u\ raw}(\lambda)}{L_{u\ light}(\lambda)} \quad [Eq. 9]$$

#### 4.2.7 Sources of errors and variability

Different readings could come from differences in composition of the samples. Impurities in the mineral samples could have influenced the reflectance measurements from both the HI and the Jaz. The three replicates of each sample did not have exactly the same composition. Interpretation errors of the content in the samples are also possible, since these were based on visual interpretations through a stereomicroscope.

There were some problems concerning the submerging of the samples. Some of the material floated to the surface of the water (Figure 4.12A) and had to be removed because it covered the sample surface. Some samples shrank when adding water (Figure 4.12B), and more material had to be added to the cuvette. The dry samples and the submerged samples did therefore not have identical surfaces. Clay sized minerals were easily suspended in the water and settled on the surface of some samples. This happened especially for the artificial sediments with high content of calcium carbonate.

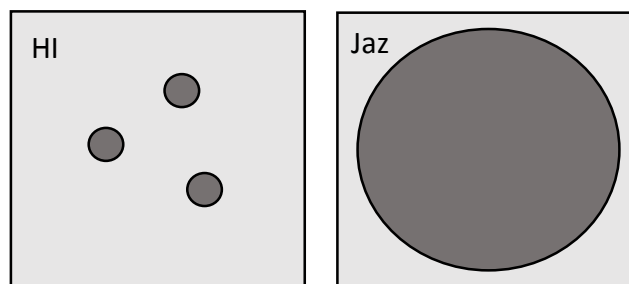


**Figure 4.12** Problems with submerging of samples. A) Floating of sediments on the top of the water surface (sample H1). B) Shirking of fine grained calcium carbonate (sample Cp1).

The light conditions in the room could have influenced the HI measurements despite the correction by using the reference plate. There were some daylight coming through the window blinds, but there were no direct daylight on the samples.

The Jaz spectra were used as a verification of how the HI spectra should look like, but the reflectance measurements of these two methods were not identical. In the HI measurements it was possible to choose which and how many pixels that should be used for the mean spectra.

Pixels were picked in three limited areas of each sample. The Jaz spectrometer automatically made a mean spectrum from a larger area, and it was not possible to choose pixels. The difference of the areas used for reflectance measurements is illustrated in Figure 4.13. In addition, HI measures radiance with a fixed angle through a slit, while Jaz measures reflectance from several angles.



**Figure 4.13** Light gray squares mark the area of the sample surface. Dark circles limit the areas used to make the mean reflectance spectra.



## Chapter 5 Results

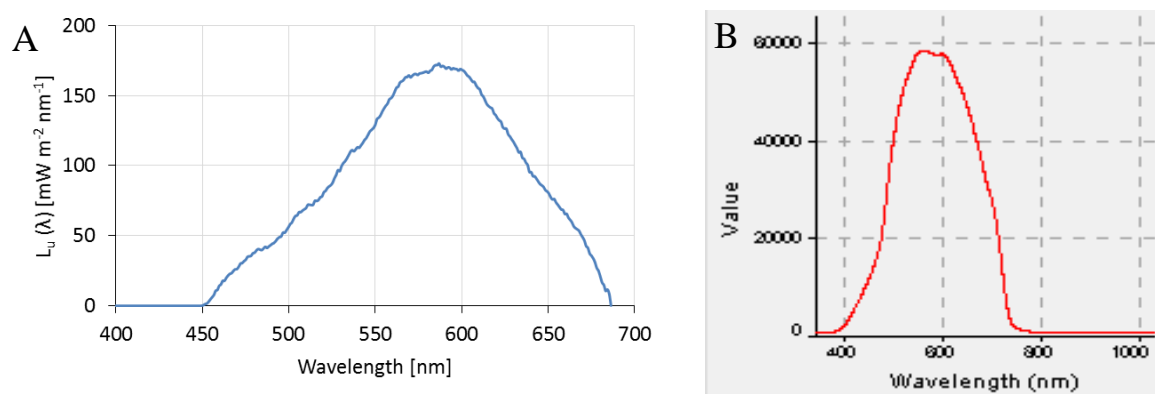
### 5.1 General description of laboratory results

RGB images were captured by the DSLR-camera through the stereomicroscope. The monochromatic images are results from the HI measurements described in the previous chapter. Only images from set 1 of the mineral and sediment samples are included in the results, images of set 2 and set 3 are found in appendix A and B. For larger RGB images of set 1, see appendix A. The monochromatic images show reflection of light at 570 nm, which is the spectral band with the best reflectance signals in the measurements.

Reflectance spectra from HI measurements are mean spectra plotted with standard errors. Normal distribution is assumed and it is 68% probability that the estimated spectra is found within estimated spectra +/- one standard error. Reflectance values have a scale from 0-1, where 1 refers to 100% reflection of incoming light.

The results from the Jaz show reflectance spectra from all three series, for both dry and submerged samples. Three measurements were considered as too few to make mean spectra values. An exception was made for the artificial sediments, where the spectra of the three replicates were averaged to make the figure easier to understand.

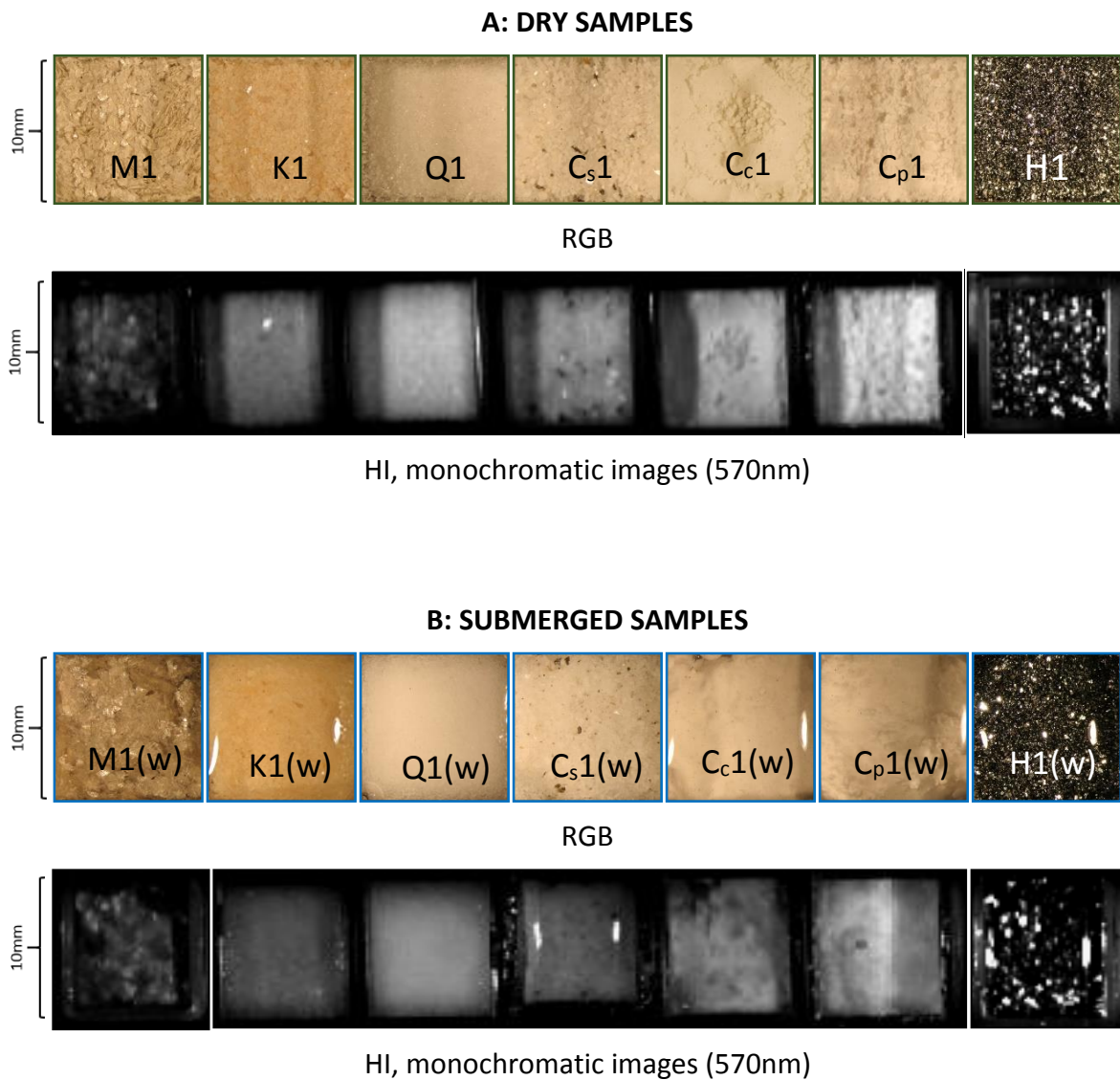
The light source spectra from the reference plate measured by the HI and Jaz are shown in Figure 5.1. Respectively, the reference plate reflected 50 % and 75 % of all visible light, equally for all wavelengths.



**Figure 5.1** A) Upwelling radiance ( $L_u$ ) of the HI light source and B) The light source spectrum from the Jaz measurements (copied from SpectraSuite settings of the white reference). Value refer to upwelling radiance measured in counts per time (integration time = 10 358  $\mu\text{s}$ ).

## 5.2 Results from the mineral samples

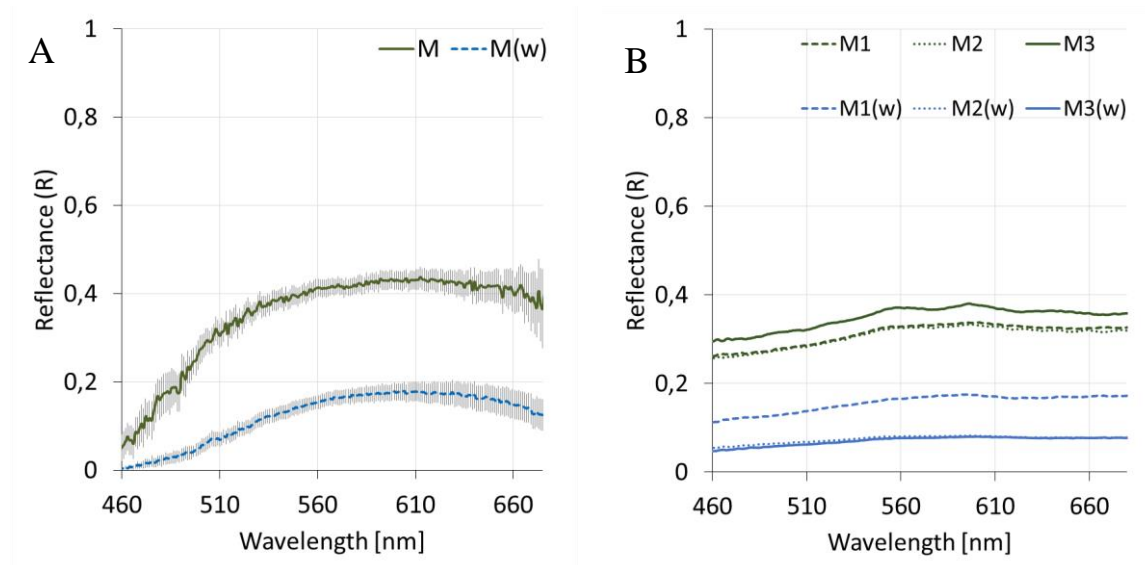
RGB images and monochromatic images (570 nm) from HI measurements of the minerals in set 1 are presented in Figure 5.2. Color of the image frames correspond to the color of the reflectance spectra of the samples.



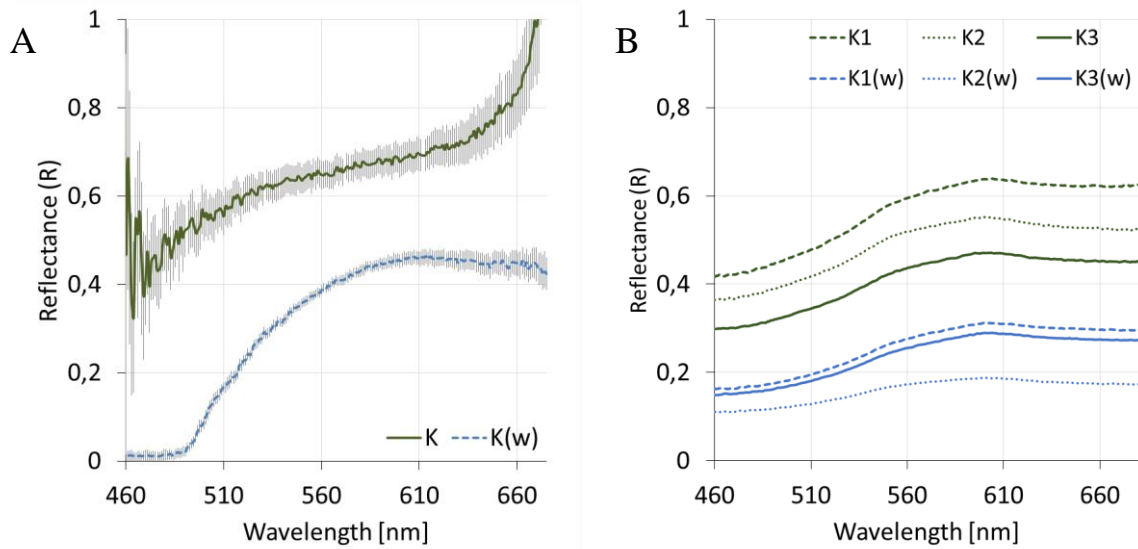
**Figure 5.2** RGB-images and monochromatic images (570nm) of minerals (set 1) from the HI measurements. A) Dry samples. B) Submerged samples. *M* = muscovite, *K* = k-feldspar, *Q* = quartz, *C<sub>s</sub>* = calcite marble (sand), *C<sub>c</sub>* = calcite marble (clay), *C<sub>p</sub>* = pure calcium carbonate, *H* = hematite, (*w*) = submerged samples.

### 5.2.1 Reflectance spectra

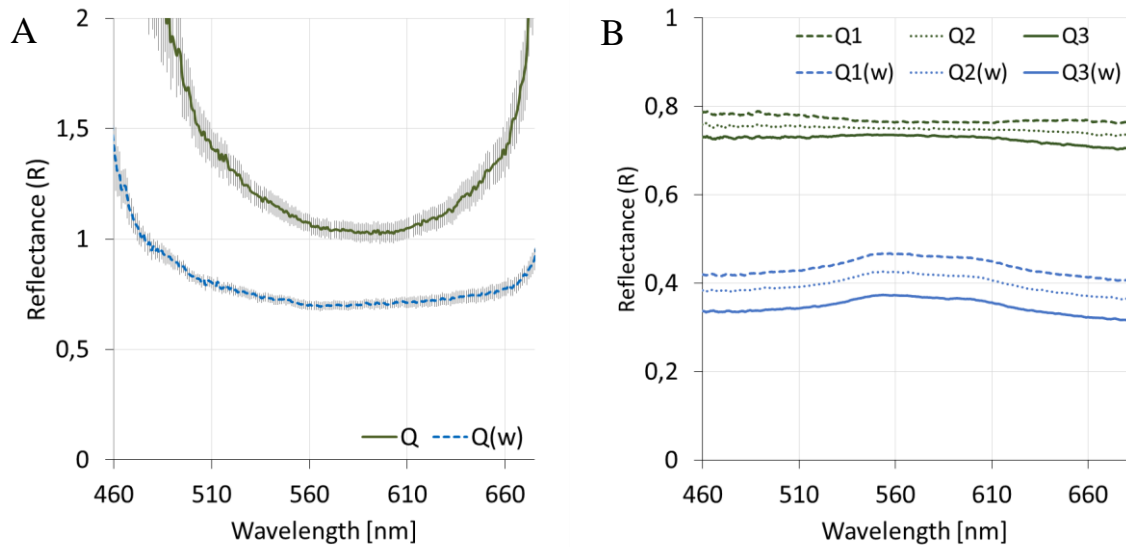
Reflectance spectra of each mineral sample are presented below - muscovite (Figure 5.3), k-feldspar (Figure 5.4), quartz (Figure 5.5), calcite marble sand (Figure 5.6), calcite marble clay (Figure 5.7), pure calcium carbonate (Figure 5.8) and hematite (Figure 5.9 and Figure 5.10).



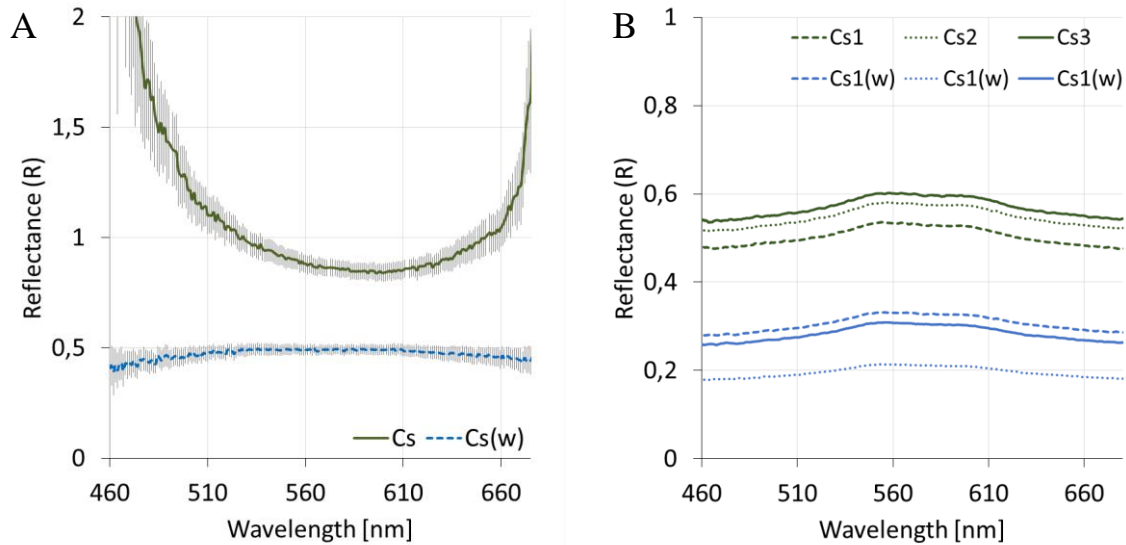
**Figure 5.3** A) Average reflectance spectra from HI,  $M$  = muscovite,  $M(w)$  = submerged muscovite. Error bars show standard error (SE) of the estimated spectra from  $n=9$  reflectance spectra. B) Reflectance spectra from Jaz spectrometer of muscovite samples from set 1 ( $M1$ ), set 2 ( $M2$ ) and set 3 ( $M3$ ), and of submerged muscovite from set 1 ( $M1(w)$ ), set 2 ( $M2(w)$ ), and set 3 ( $M3(w)$ ).



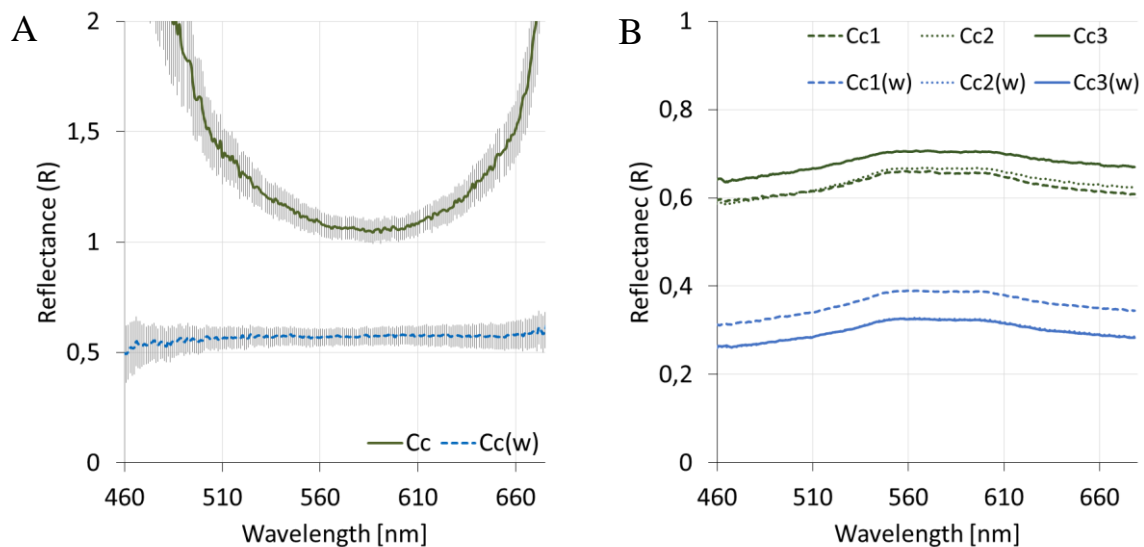
**Figure 5.4** A) Average reflectance spectra from HI,  $K$  = k-feldspar,  $K(w)$  = submerged k-feldspar. Error bars show standard error (SE) of the estimated spectra from  $n=9$  reflectance spectra. B) Reflectance spectra from Jaz spectrometer of k-feldspar samples from set 1 ( $K1$ ), set 2 ( $K2$ ) and set 3 ( $K3$ ), and of submerged k-feldspar from set 1 ( $K1(w)$ ), set 2 ( $K2(w)$ ), and set 3 ( $K3(w)$ ).



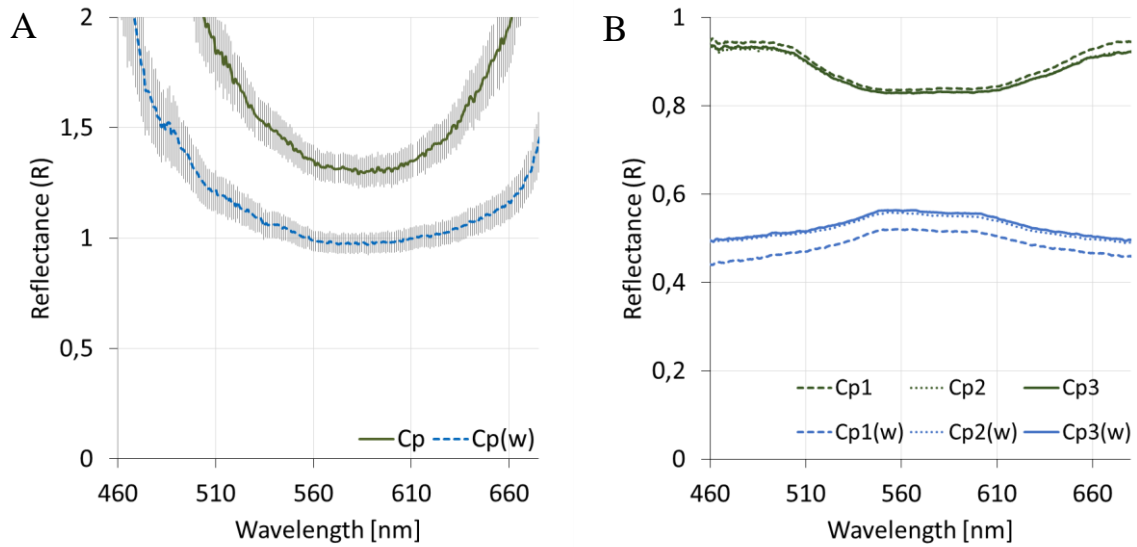
**Figure 5.5** A) Average reflectance spectra from HI,  $Q$  = quartz,  $Q(w)$  = submerged quartz. Error bars show standard error (SE) of the estimated spectra from  $n=9$  reflectance spectra. Note that reflectance scale is set to 2, because of an apparent reflection larger than 100%. B) Reflectance spectra from Jaz spectrometer of quartz samples from set 1 ( $Q1$ ), set 2 ( $Q2$ ) and set 3 ( $Q3$ ), and of submerged quartz from set 1 ( $Q1(w)$ ), set 2 ( $Q2(w)$ ), and set 3 ( $Q3(w)$ ).



**Figure 5.6** A) Average reflectance spectra from HI, Cs = calcite marble (sand), Cs(w) = submerged calcite marble (sand). Error bars show standard error (SE) of the estimated spectra from  $n=9$  reflectance spectra. Note that reflectance scale is set to 2, because of an apparent reflection larger than 100%. B) Reflectance spectra from Jaz spectrometer of calcite marble (sand) samples from set 1 (Cs1), set 2 (Cs2) and set 3 (Cs3), and of submerged calcite marble (sand) from set 1 (Cs1(w)), set 2 (Cs2(w)), and set 3 (Cs3(w)).

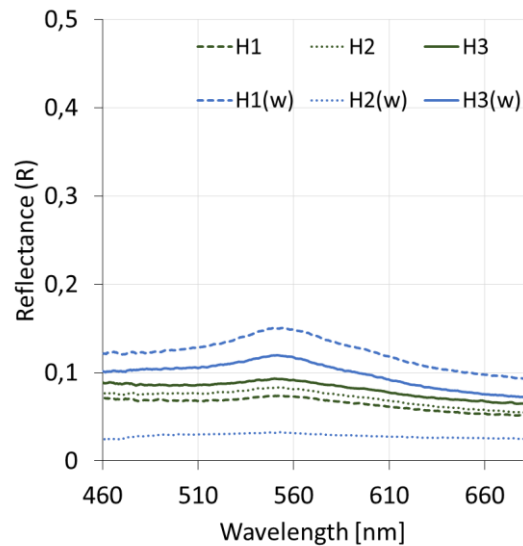


**Figure 5.7** A) Average reflectance spectra from HI, Cc = calcite marble (clay), Cc(w) = submerged calcite marble (clay). Error bars show standard error (SE) of the estimated spectra from  $n=9$  reflectance spectra. Note that reflectance scale is set to 2, because of an apparent reflection larger than 100%. B) Reflectance spectra from Jaz spectrometer of calcite marble (clay) samples from set 1 (Cc1), set 2 (Cc2) and set 3 (Cc3), and of submerged calcite marble (clay) from set 1 (Cc1(w)), set 2 (Cc2(w)), and set 3 (Cc3(w)).



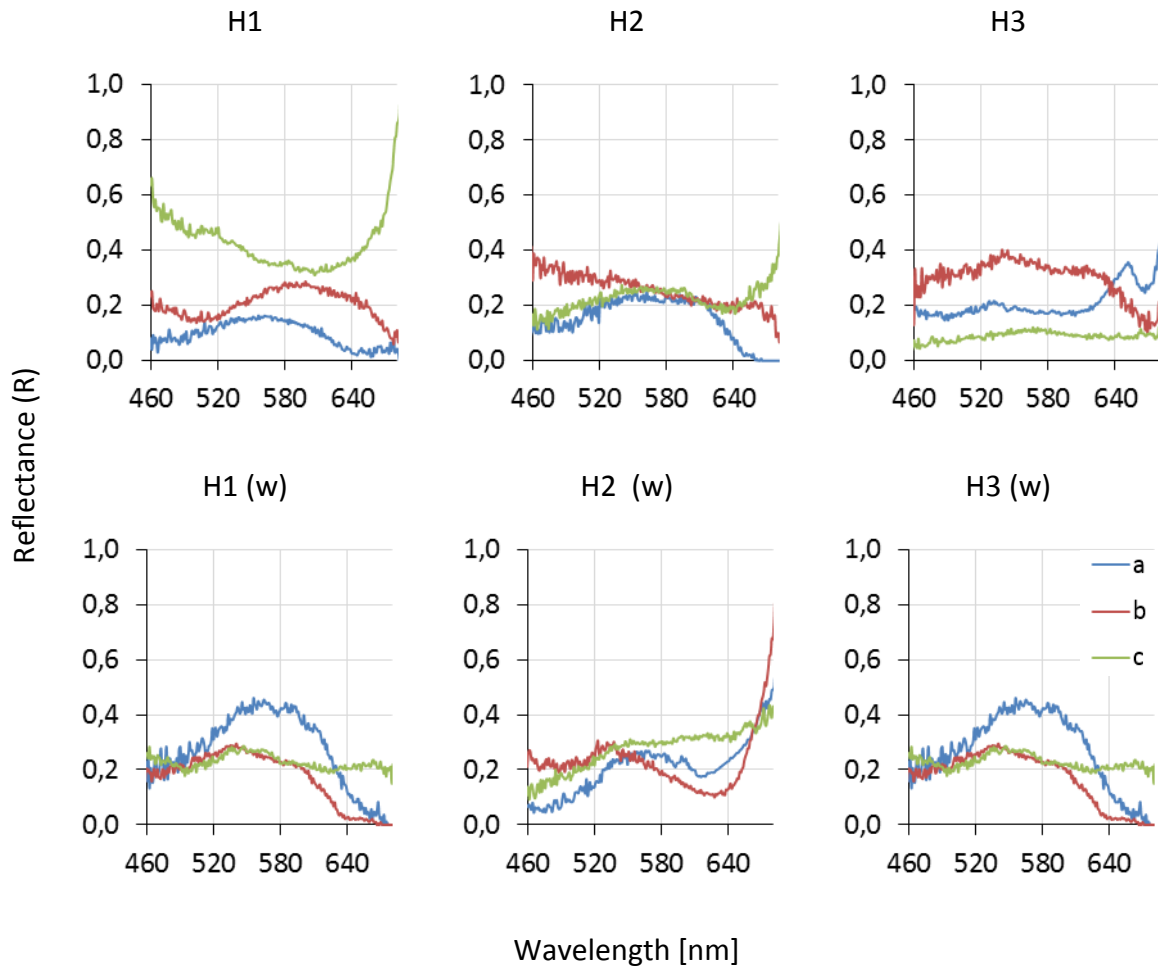
**Figure 5.8** A) Average reflectance spectra from HI, Cp = pure calcium carbonate, Cp(w) = submerged pure calcium carbonate. Error bars show standard error (SE) of the estimated spectra from  $n=9$  reflectance spectra. Note that reflectance scale is set to 2, because of an apparent reflection larger than 100%. B) Reflectance spectra from Jaz spectrometer of calcium carbonate samples from set 1 (Cp1), set 2 (Cp2) and set 3 (Cp3), and of submerged calcium carbonate from set 1 (Cp1(w)), set 2 (Cp2(w)), and set 3 (Cp3(w)).

The Jaz spectra of hematite are shown in Figure 5.9. Hematite is the mineral with the largest variations in shape of the HI spectra extracted from three areas in each sample (Figure 5.10). A resulting mean spectrum of these nine HI spectra is therefore not representative for the mineral and not included in the results.



**Figure 5.9** Reflectance spectra from Jaz spectrometer of hematite samples from set 1 (H1), set 2 (H2) and set 3 (H3), and of submerged hematite from set 1 (H1(w)), set 2 (H2(w)), and set 3 (H3(w)).

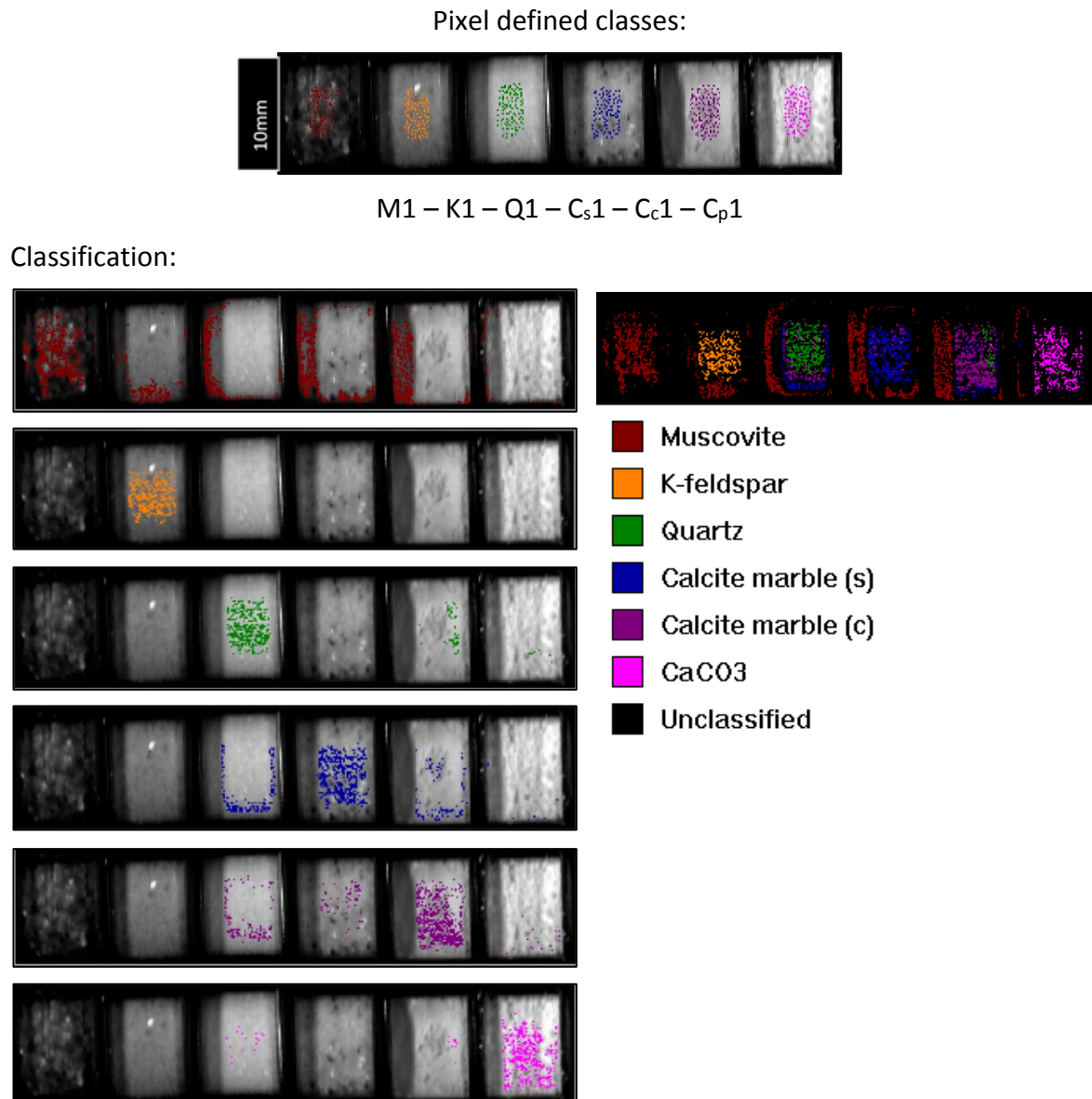




**Figure 5.10** Reflectance spectra from HI measurement used for making man spectra of hematite. *a*, *b* and *c* define the areas where 5 pixels were extracted from a sample in a hyperspectral image to make an average spectra plot, *a* = area 1, *b* = area 2 and *c* = area 3.

### 5.2.2 Supervised classification

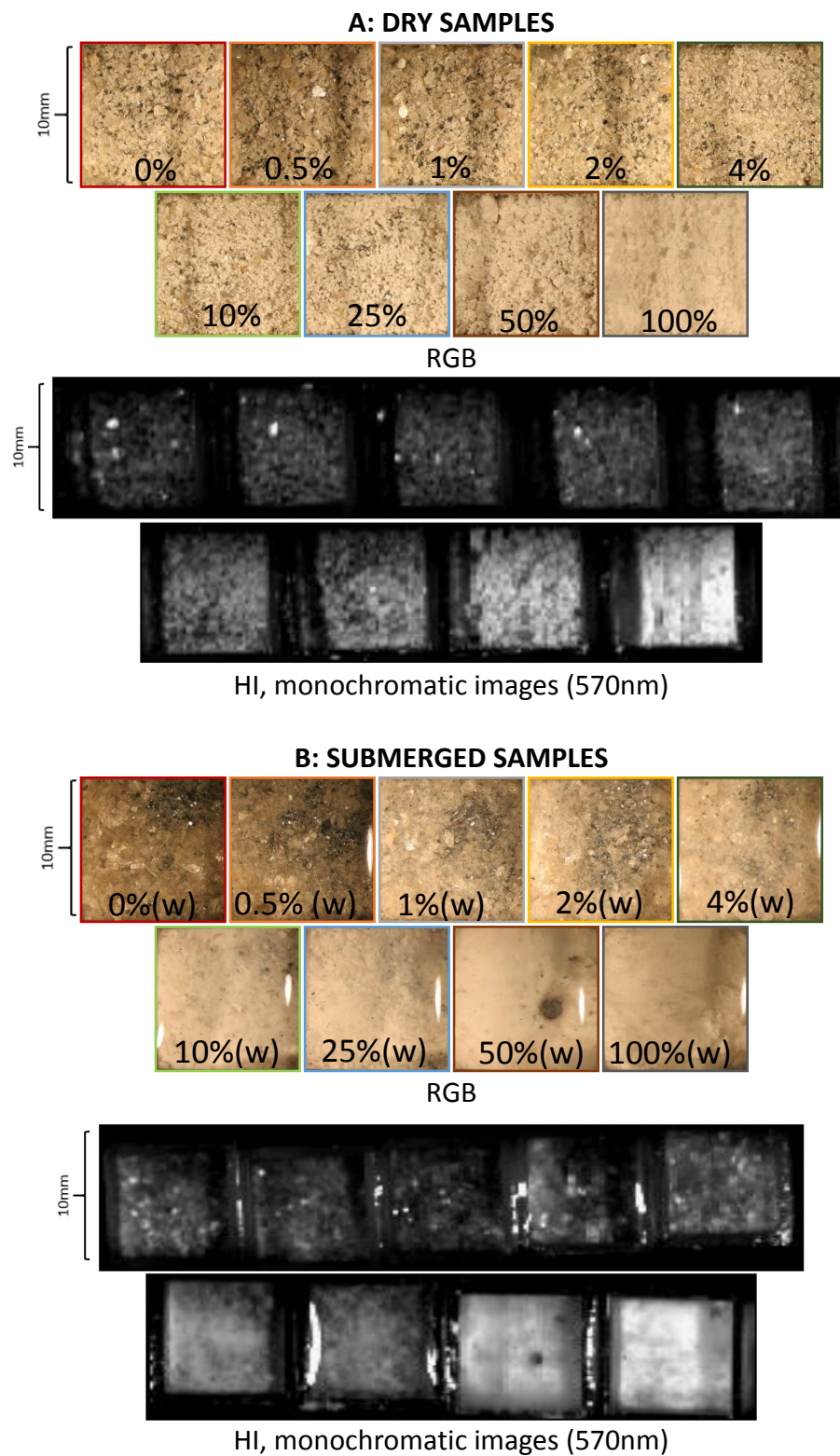
A Bayesian supervised classification of six mineral samples, consisting of muscovite, k-feldspar, quartz, calcite marble (both sand and clay samples) and pure calcium carbonate, is shown in Figure 5.11. The classes are pixel defined in *Image Calculator* using 100 pixels for each class. The classification results were overlaid on monochromatic images at 570 nm.



**Figure 5.11** Bayesian supervised classification of minerals with pixel defined classes ( $n=100$ ) on top of monochromatic images (570nm). Samples used are M1, K1, Q1, C<sub>s</sub>1, C<sub>c</sub>1 and C<sub>p</sub>1.

### **5.3 Results from the artificial sediment samples**

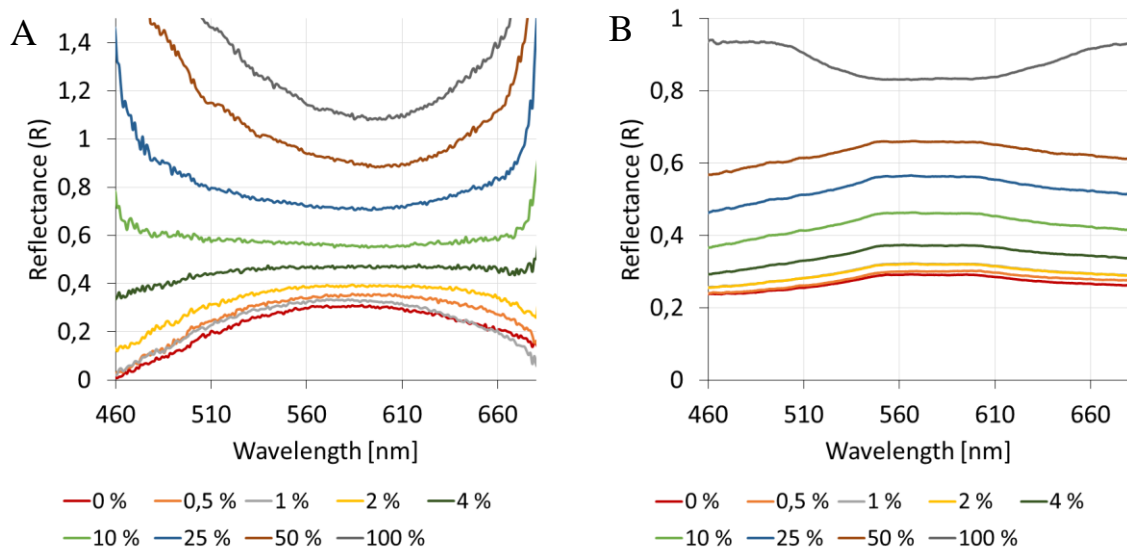
RGB and monochromatic images of the artificial sediments with a carbonate content varying from 0-100 wt% are shown in Figure 5.12. The colors of the sample frames correlate to the colors of the reflectance spectra of the corresponding sample.



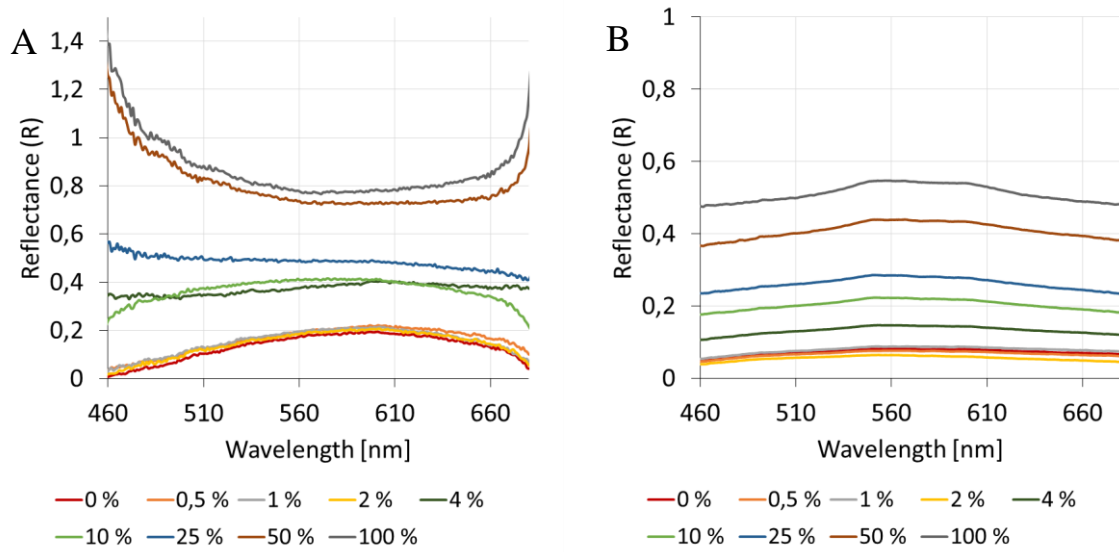
**Figure 5.12** RGB-images and monochromatic images (570nm) of artificial sediments (set A) from the HI measurements. 0-100% explain the wt% of  $\text{CaCO}_3$  in the sediment, (w) = submerged samples. Frame colors reflect the colors in the reflectance spectra in the reflectance spectra.

## 5.3.1 Reflectance spectra

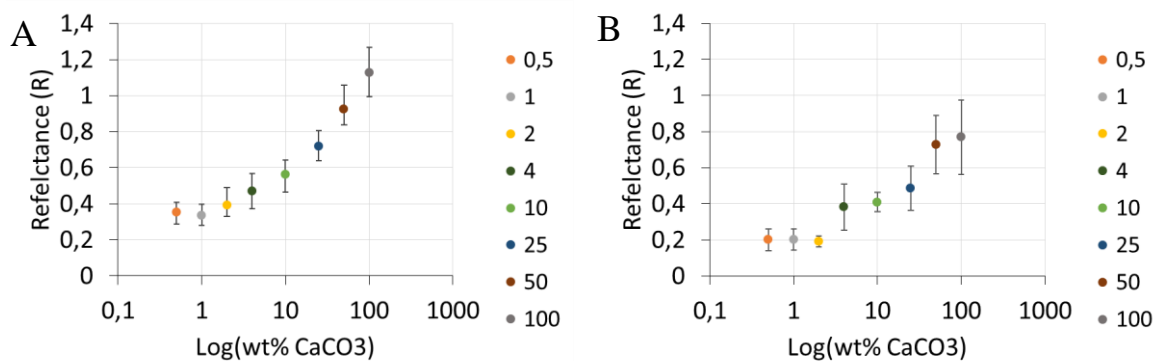
Figure 5.13 and Figure 5.14 the reflectance spectra of the artificial sediments with increasing carbonate content. Error bars are not included in the reflectance spectra, but the variation of the HI measurements are possible to see in appendix C. The Jaz measurements show average spectra of three samples. Figure 5.15 shows HI reflectance at 570 nm for all samples, this plot is included to give a better presentation of the samples with a low carbonate content. The artificial sediment samples without  $\text{CaCO}_3$  is not included due to logarithmic values on the x-axis.



**Figure 5.13** A) Reflectance spectra of the dry artificial sediment samples from HI measurements. Each spectra is an average of  $n=9$  HI spectra. B) Reflectance spectra of the dry artificial sediment samples from Jaz measurements. Each spectra is an average of  $n=3$  Jaz spectra.



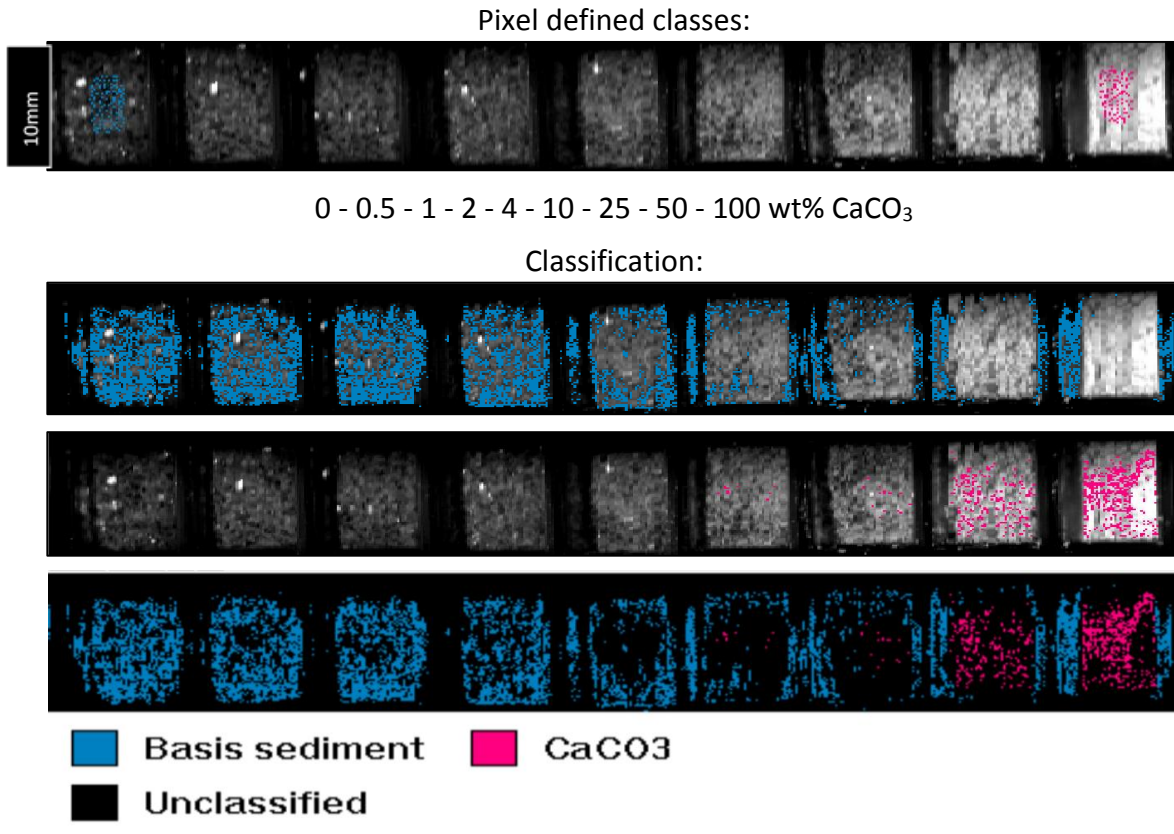
**Figure 5.14** A) Reflectance spectra of the submerged artificial sediments from HI measurements. Each spectra is an average of  $n=9$  HI spectra. B) Reflectance spectra of the submerged artificial sediments from Jaz measurements. Each spectra is an average of  $n=3$  Jaz spectra.



**Figure 5.15** Reflectance at 570 nm for dry sediments (A) and submerged sediments (B). Data points are average reflectance intensity from nine HI spectra, error bars show one standard deviation.

## 5.3.2 Supervised classification

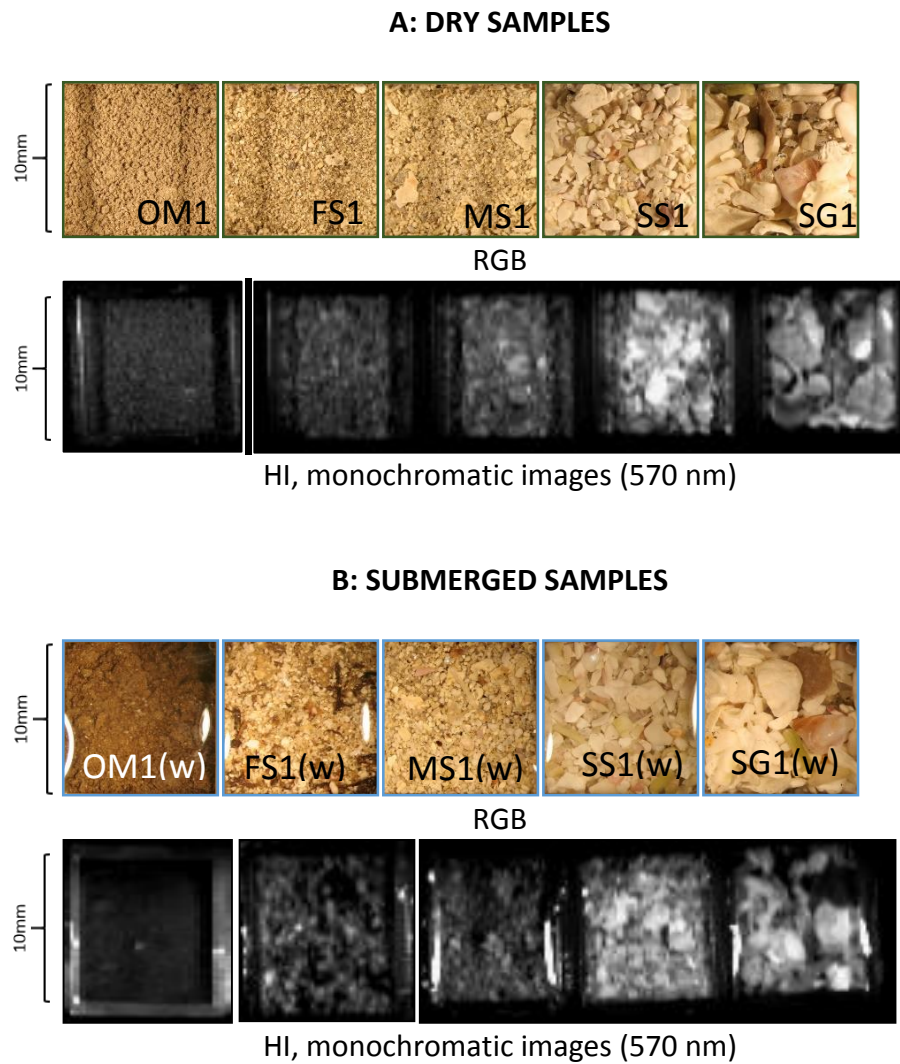
Figure 5.16 shows a Bayesian supervised classification of the classes “basis sediment” and “CaCO<sub>3</sub>”. One hundred pixels were used to define the classes. These two classes were chosen to find out if CaCO<sub>3</sub> could be recognized in the samples. The classification results were overlaid on monochromatic images at 570 nm.



**Figure 5.16** Bayesian supervised classification of the artificial sediments with pixel defined classes ( $n=100$ ) on top of monochromatic images (570nm).

## 5.4 Results from the natural sediment samples

RGB images and monochromatic images of the natural sediments (set 1) are shown in Figure 5.17.

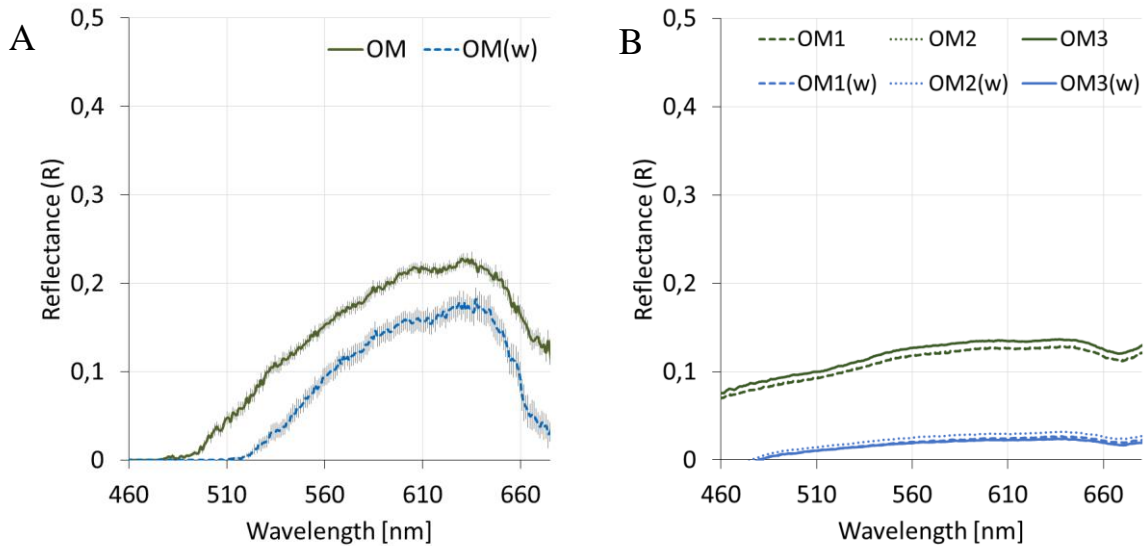


**Figure 5.17** RGB-images and monochromatic images (570nm) of natural sediments (set 1) from the HI measurements. OM = organic mud, FS = fine sand, MS = medium sand, SS = shell sand, SG = shell gravel. (w) = submerged samples.

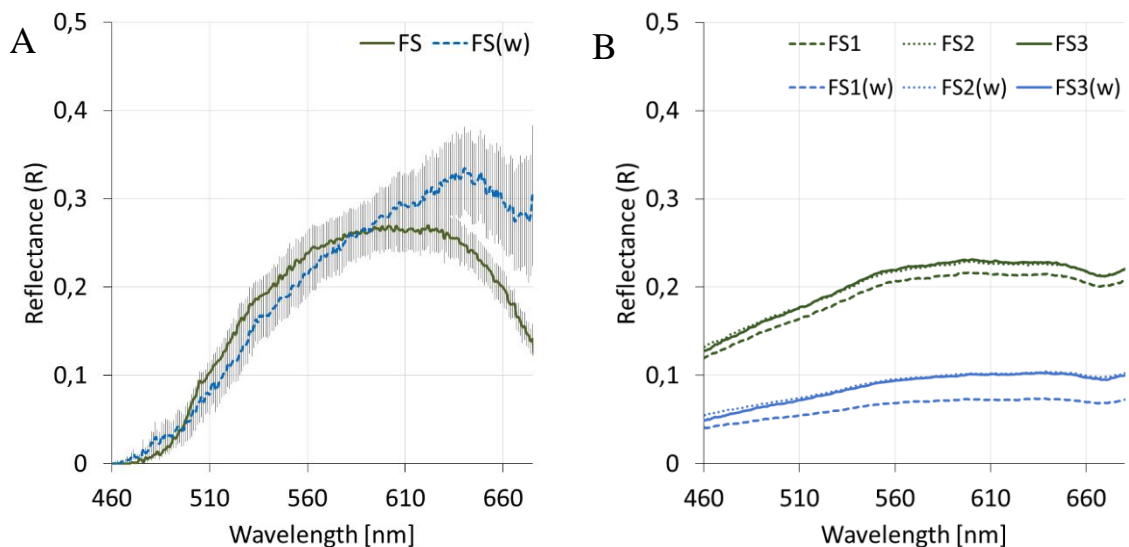


## 5.4.1 Reflectance spectra

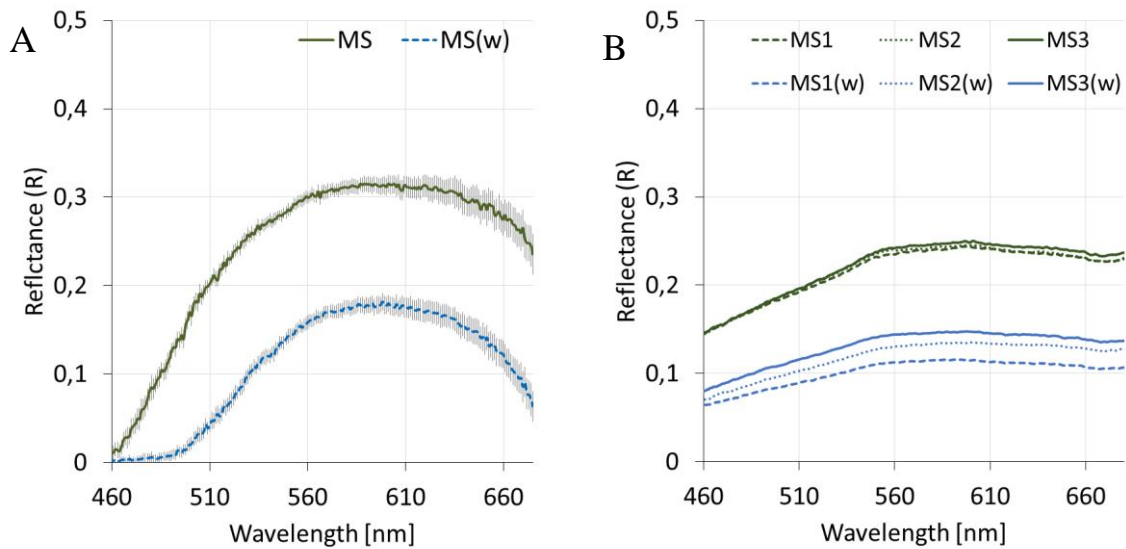
The reflectance spectra of the natural sediments are seen in Figure 5.18 (organic mud), Figure 5.19 (fine sand), Figure 5.20 (medium sand), Figure 5.21 (shell sand) and Figure 5.22 (shell gravel).



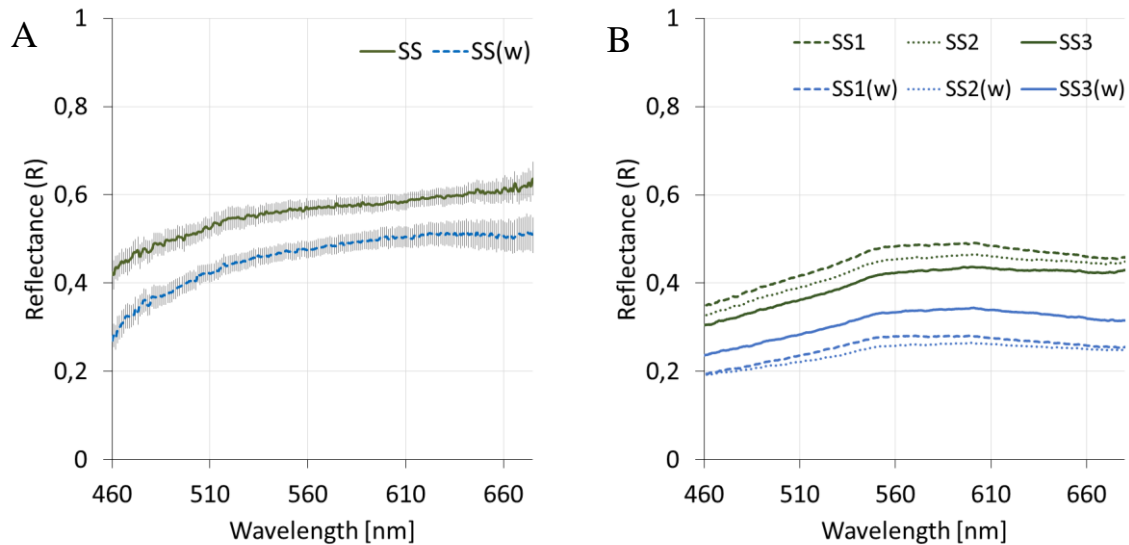
**Figure 5.18** A) Average reflectance spectra from HI, OM = organic mud, OM (w) = submerged organic mud. Error bars show standard error (SE) of the estimated spectra from  $n=9$  reflectance spectra. B) Reflectance spectra from Jaz spectrometer of organic mud samples from set 1 (OM1), set 2 (OM2) and set 3 (OM3), and of submerged organic mud from set 1 (OM1(w)), set 2 (OM2(w)), and set 3 (OM3(w)).



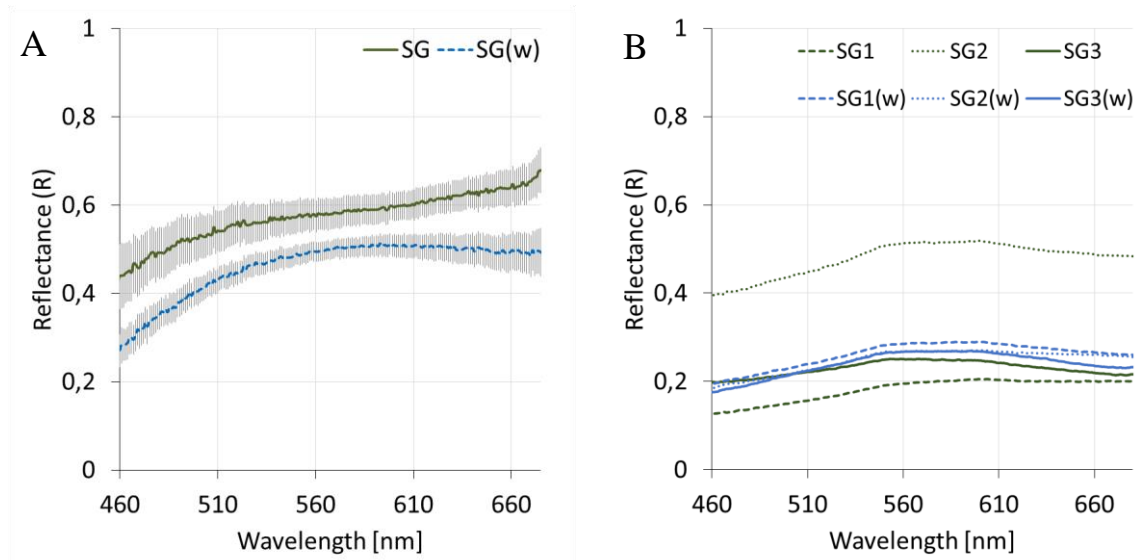
**Figure 5.19** A) Average reflectance spectra from HI, FS = fine sand, FS(w) = submerged fine sand. Error bars show standard error (SE) of the estimated spectra from  $n=9$  reflectance spectra. B) Reflectance spectra from Jaz spectrometer of fine sand samples from set 1 (FS1), set 2 (FS2) and set 3 (FS3), and of submerged fine sand from set 1 (FS1(w)), set 2 (FS2(w)), and set 3 (FS3(w)).



**Figure 5.20** A) Average reflectance spectra from HI, MS = medium sand, MS(w) = submerged medium sand. Error bars show standard error (SE) of the estimated spectra from  $n=9$  reflectance spectra. B) Reflectance spectra from Jaz spectrometer of medium sand samples from set 1 (MS1), set 2 (MS2) and set 3 (MS3), and of submerged medium sand from set 1 (MS1(w)), set 2 (MS2(w)), and set 3 (MS3(w)).



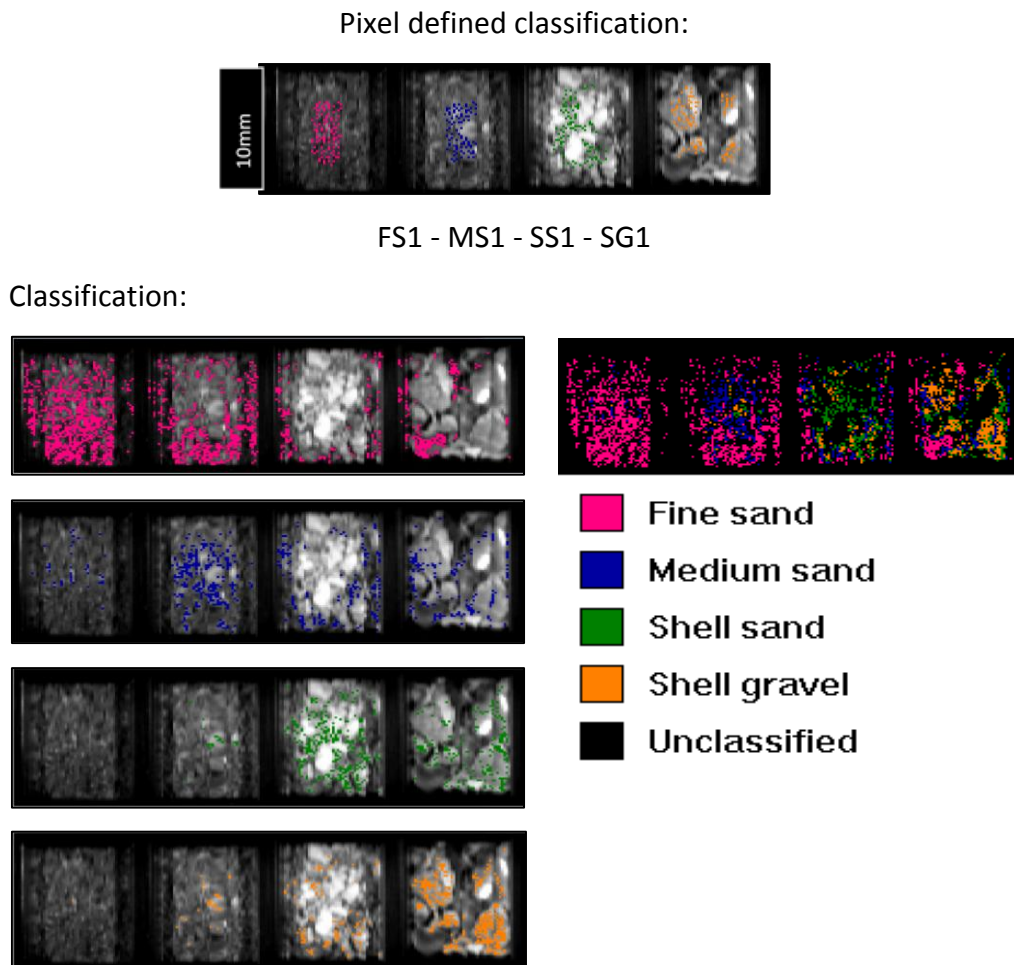
**Figure 5.21** A) Average reflectance spectra from HI, SS = shell sand, SS(w) = submerged shell sand. Error bars show standard error (SE) of the estimated spectra from  $n=9$  reflectance spectra. B) Reflectance spectra from Jaz spectrometer of shell sand samples from set 1 (SS1), set 2 (SS2) and set 3 (SS3), and of submerged shell sand from set 1 (SS1(w)), set 2 (SS2(w)), and set 3 (SS3(w)).



**Figure 5.22** A) Average reflectance spectra from HI, SG = shell gravel, SG(w) = submerged shell gravel. Error bars show standard error (SE) of the estimated spectra from  $n=9$  reflectance spectra. B) Reflectance spectra from Jaz spectrometer of shell gravel samples from set 1 (SG1), set 2 (SG2) and set 3 (SG3), and of submerged shell gravel from set 1 (SG1(w)), set 2 (SG2(w)), and set 3 (SG3(w)).

### 5.4.2 Supervised classification

A Bayesian supervised classification of natural sediments (set 1) with classes “fine sand”, “medium sand”, “shell sand” and “shell gravel” is shown in Figure 5.23. Pixel defined classes were made using 100 pixels per class. The classification results were overlaid on monochromatic images at 570 nm.



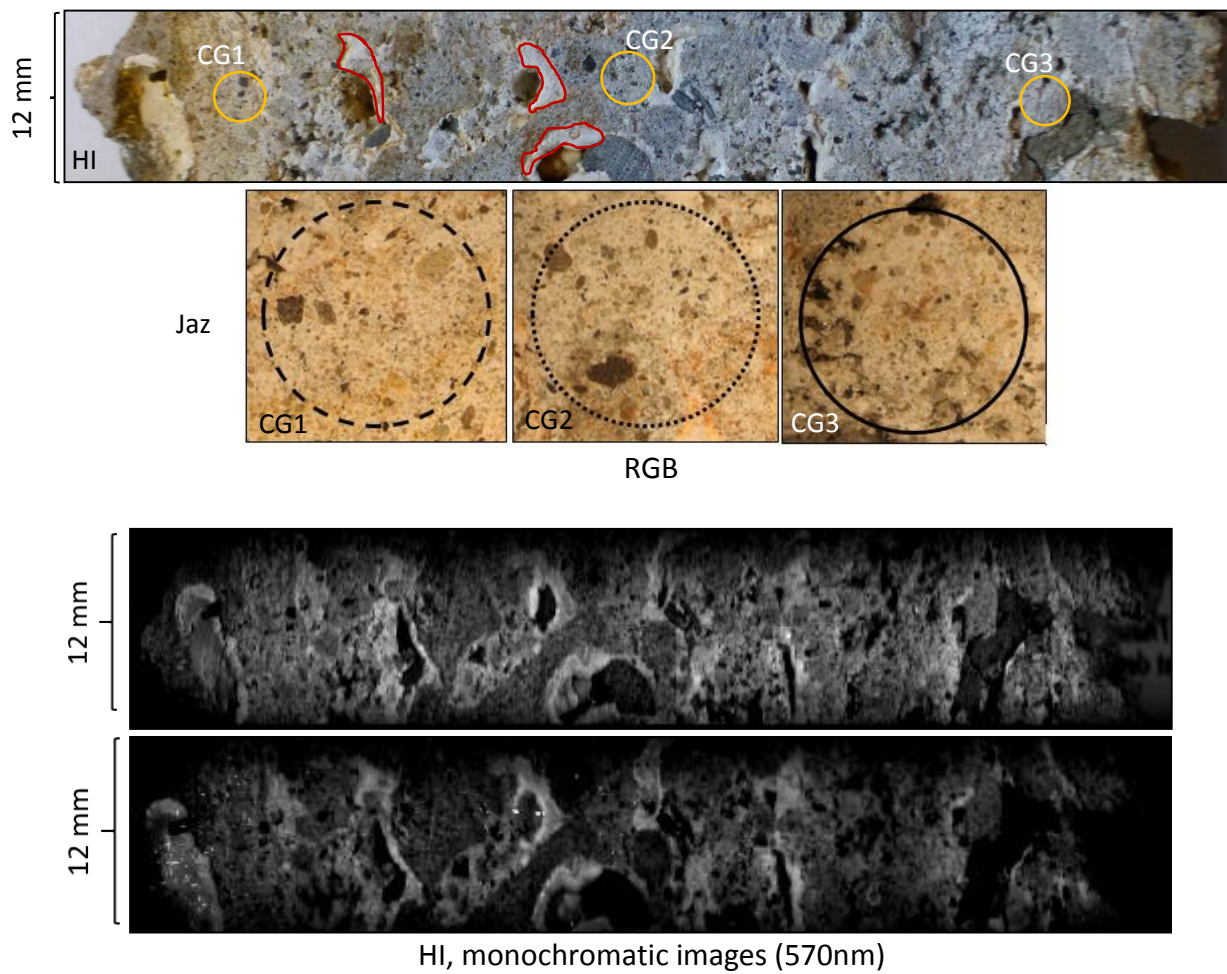
**Figure 5.23** Bayesian supervised classification of the natural sediments with pixel defined classes ( $n=100$ ) on top of monochromatic images (570nm). Samples used are FS1, MS1, SS1 and SG1.

## 5.5 Results from the carbonate crusts

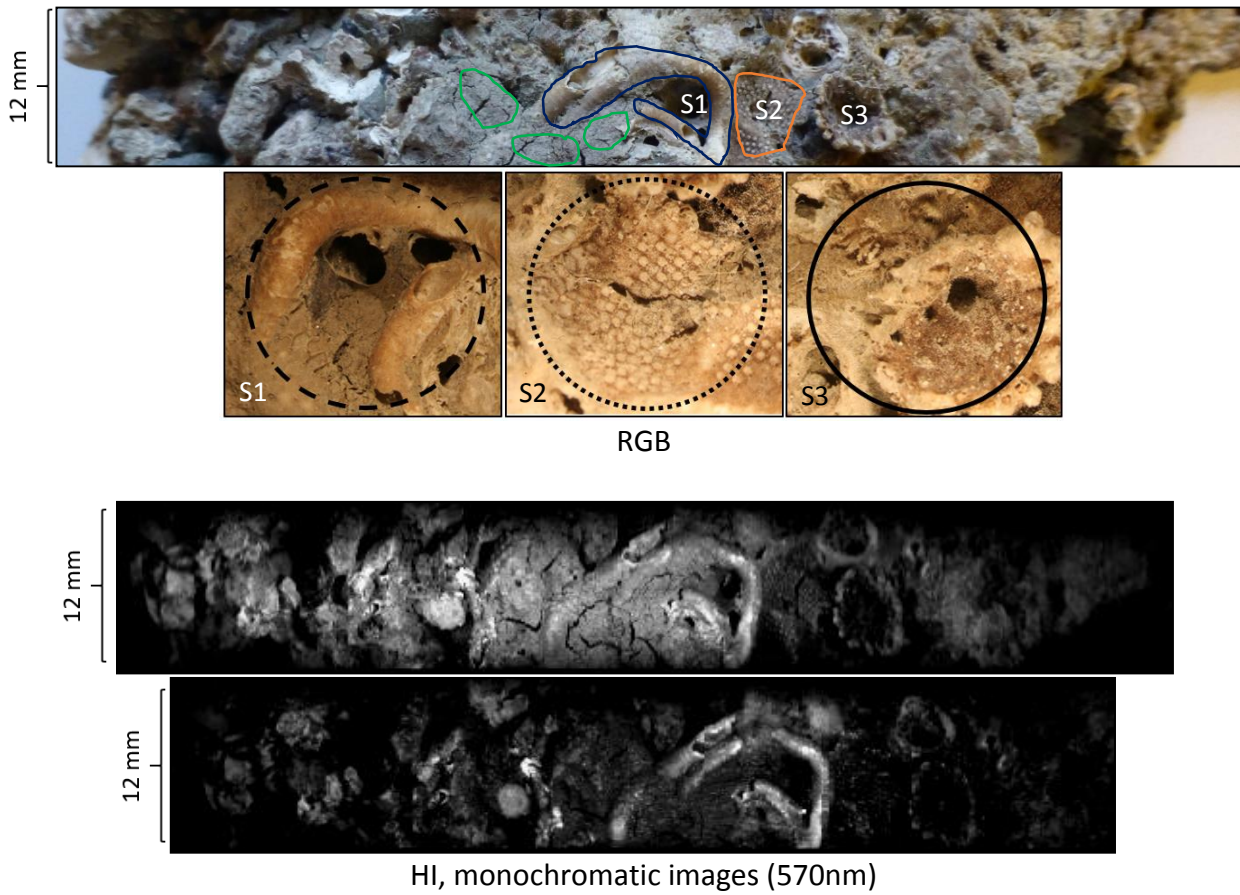
RGB images and monochromatic images of the carbonate crusts are shown in Figure 5.24 (fresh surface) and Figure 5.25 (original surface). Colored markings show the areas where pixels used to make the HI reflectance spectra were chosen.

Yellow circles show the areas limiting the Jaz and HI measurements of cemented grain surface (CG1, CG2 and CG3) of the fresh surface. A closer image of these circles are found within the black circles. Red markings limit the areas of HI reflectance measurements of aragonite. There were not done any Jaz measurements of aragonite areas, because these areas were too small for the circle area measured by Jaz.

The areas measured by the Jaz of the original surface are numbered S1 (surface 1), S2 (surface 2) and S3 (surface 3), and objects measured by HI are named Sa (surface a), Sb (surface b) and Sc (surface c). Sa consists of carbonate shell from bristle worms (*Polychaete*), Sb consists of organic mud and Sc of skeleton of moss animals (*Bryozoa*). Sa covers the same area as S1 in the Jaz measurements. Sb is included in S1 and Sc covers the same area as S2. S3 consists of carbonate skeleton from other organisms.



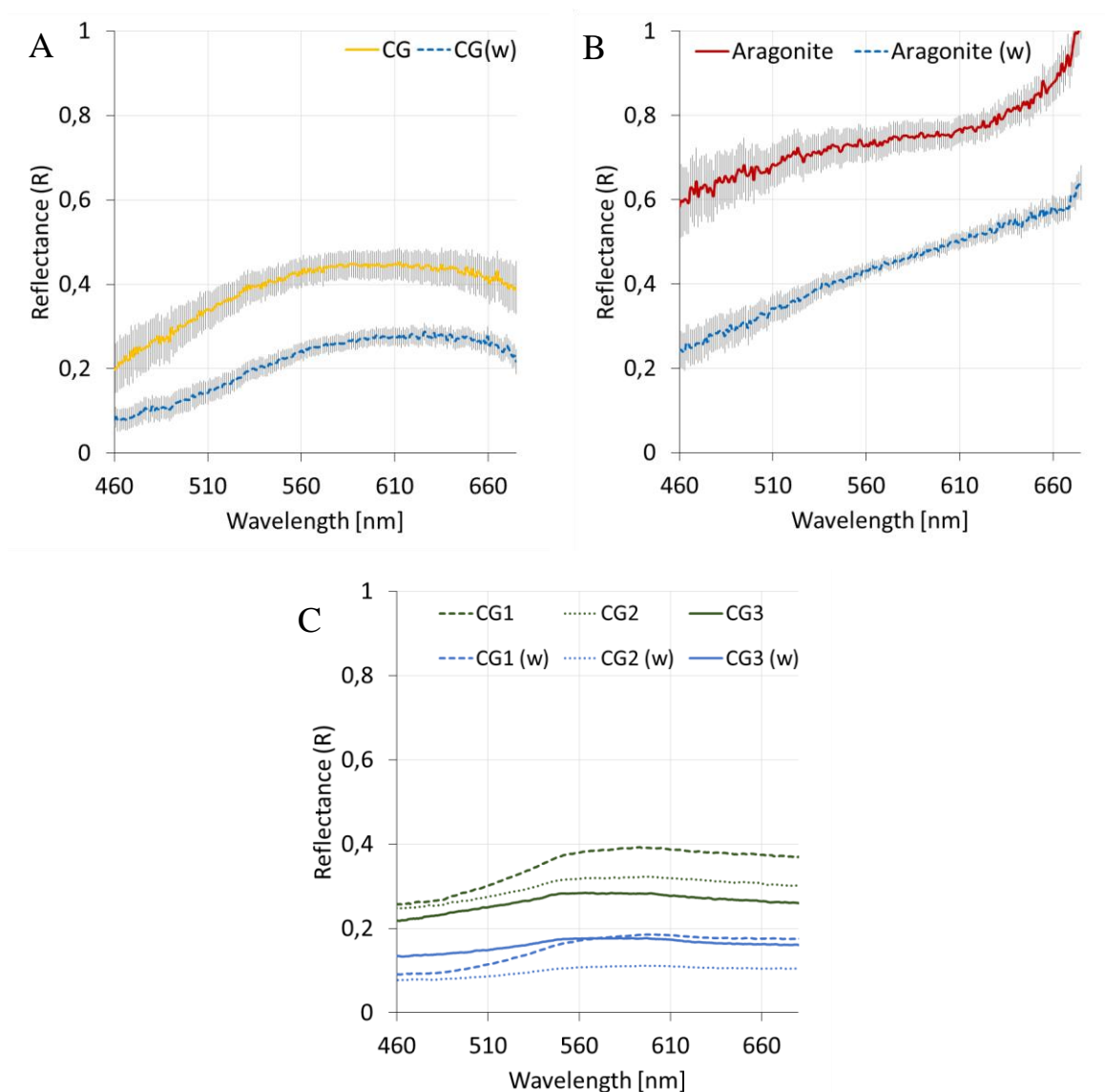
**Figure 5.24** RGB-images and HI monochromatic images (570nm) of the fresh surface of sample P1210006\_4A. CG = cemented grain and explain where the Jaz measurements are captured. Yellow circles limit the areas of HI measurements of CG, while the red lines limit the areas of HI measurements of the aragonite.



**Figure 5.25** RGB-images and HI monochromatic images (570nm) of a original surface of sample P1210035\_1B. S(1,2,3) = surface (1,2,3) and explain where the Jaz measurements are captured. Blue lines limit the areas of HI measurements of surface a (Sa), green lines limit the area of surface b (Sb), while the orange lines limit the areas of surface c (Sc).

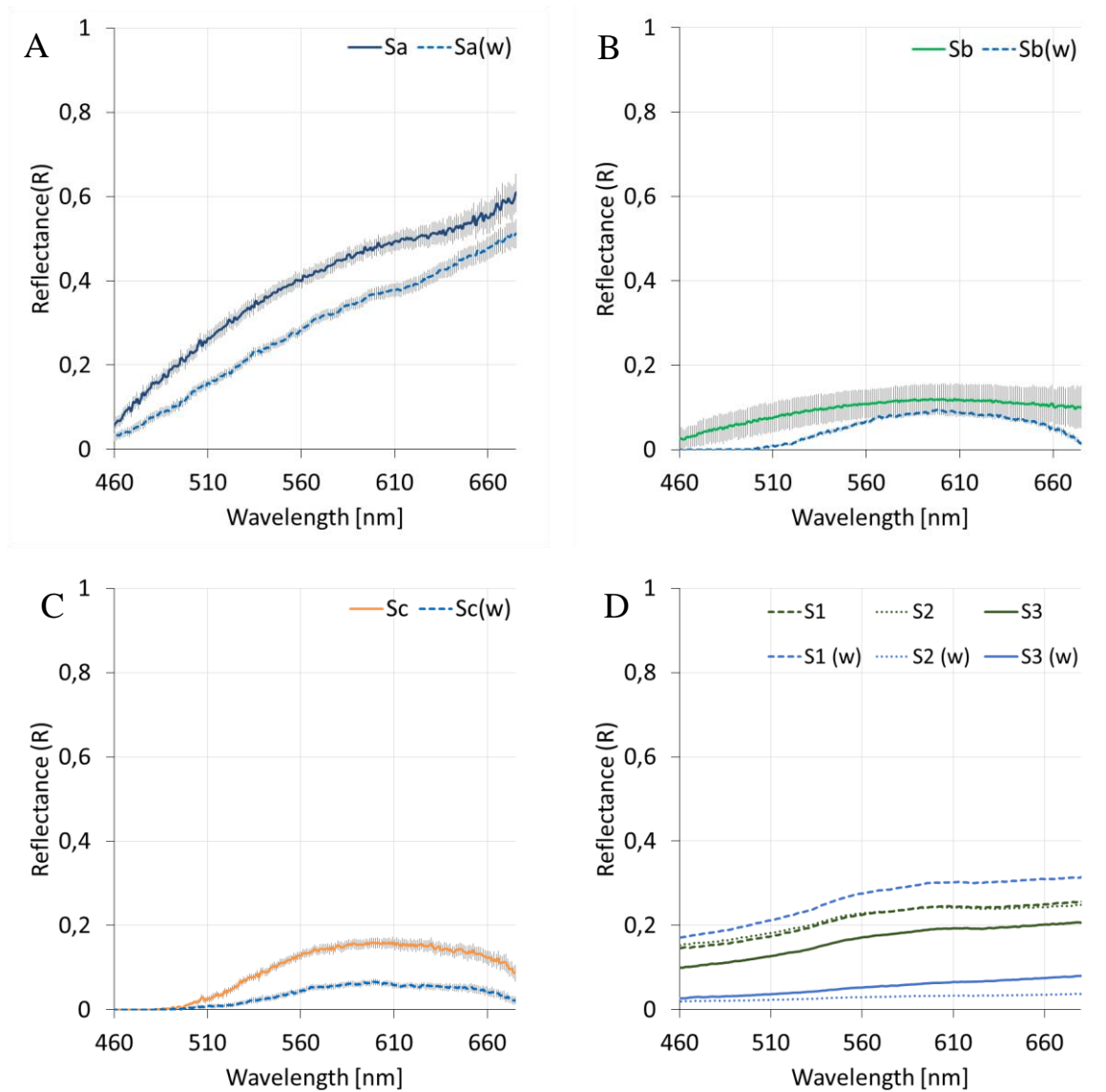
### 5.5.1 Reflectance spectra

Reflectance spectra of the carbonate crust surfaces are presented in Figure 5.26 (fresh surface) and Figure 5.27 (original surface). The HI spectra of the fresh surface include aragonite cemented grains (CG) and pure aragonite. The Jaz spectra include only the cemented grain areas (CG1, CG2 and CG3). The reflectance spectra of the original surface include measurement of three different objects (HI) and three different areas (Jaz).



**Figure 5.26** A) Average reflectance spectra from HI, CG = cemented grains, CG (w) = submerged cemented grains. Error bars show standard error (SE) of the estimated spectra from  $n=9$  reflectance spectra. B) Average aragonite reflectance spectra from HI. Error bars show standard error (SE) of the estimated spectra from  $n=9$  reflectance spectra. C) Reflectance spectra from Jaz spectrometer of cemented grain areas (CG1, CG2, CG3, CG1(w), CG2(w), CG3(w)).



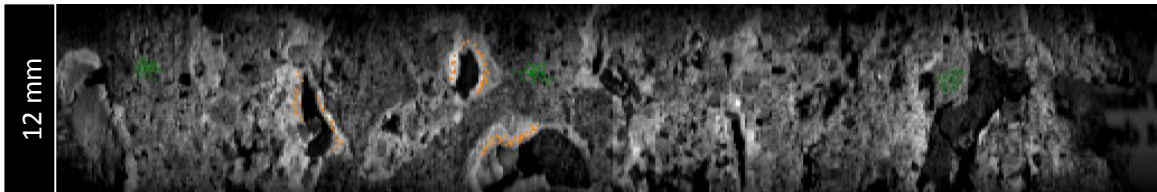


**Figure 5.27** A) Average reflectance spectra from HI for dry and submerged surface a ( $S_a$ ,  $S_a(w)$ ). B) Average reflectance spectra from HI for dry and submerged surface b ( $S_b$ ,  $S_b(w)$ ). C) Average reflectance spectra from HI for dry and submerged surface c ( $S_c$ ,  $S_c(w)$ ). Error bars show standard error (SE) of the estimated spectra from  $n=9$  reflectance spectra. D) Reflectance spectra from Jaz spectrometer of the dry and submerged surface ( $S_1$ ,  $S_2$ ,  $S_3$ ,  $S_1(w)$ ,  $S_2(w)$ ,  $S_3(w)$ ).

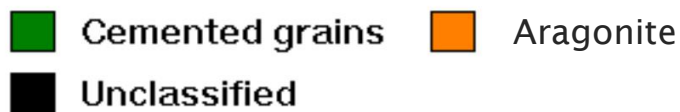
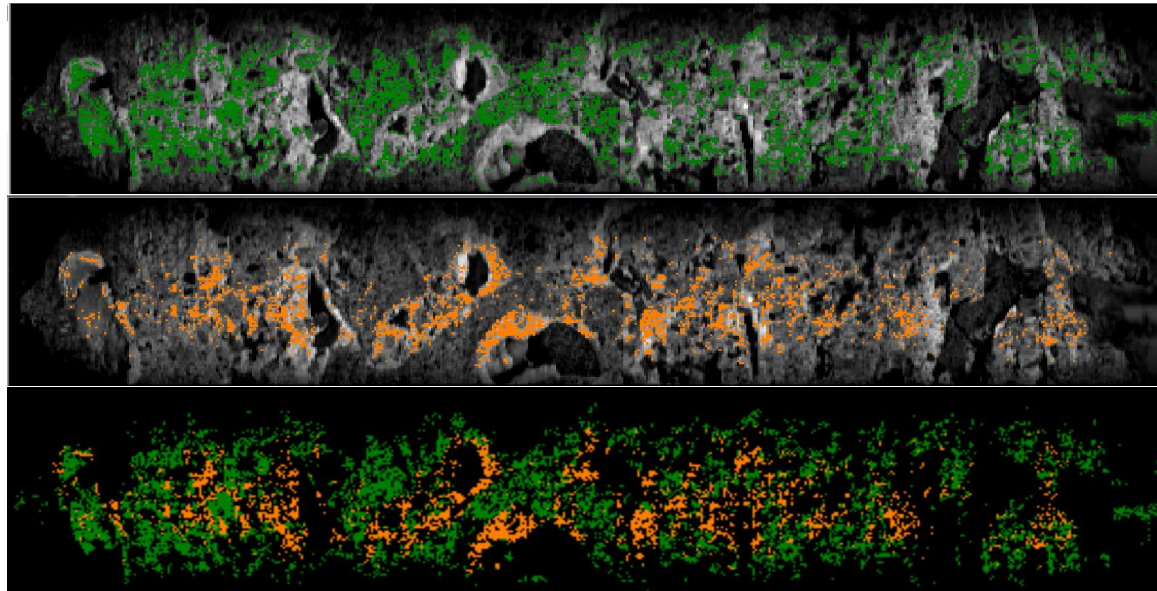
### 5.5.2 Supervised classification

A Bayesian supervised classification was carried out for the dry fresh surface of carbonate crust. The result is shown in Figure 5.28. The two classes, “cemented grains” and “aragonite” were defined by 100 pixels each, and the classification results were overlaid on monochromatic images at 570 nm.

Pixel defined classes:



Classification:



**Figure 5.28** Bayesian supervised classification of the fresh carbonate crust surface of sample P1210006\_4A with pixel defined classes ( $n=100$ ) on top of monochromatic images (570nm).

## Chapter 6 Discussion

### 6.1 Discussion of laboratory results

The hyperspectral images, reflectance spectra and supervised classifications show both advantages and disadvantages of using UHI to map sediment properties on the seabed.

#### 6.1.1 Hyperspectral Images

The main problem regarding capturing of the hyperspectral images was to find the correct light setting to optimize illumination evenness. White and dark samples had to be separated, because there was a need for brighter light to capture the dark samples inducing overexposure of the white samples. There was also a problem with overexposure using the reflectance reference plate. In these cases, only the areas at the edges of the image were used to provide a reference spectrum of the reference plate. A reference plate with lower reflectivity would have been preferable for these samples.

Hematite was the most difficult sample to capture with respect to exposure control. This was due to specular reflection from the surfaces oriented in certain directions, giving overexposure problems (glints). In addition to this, underexposure of mineral surfaces of other orientations resulted in no reflectance data. Submerging in water gave more overexposure problems because the samples became darker and needed brighter light. If the hematite grains were crushed down to clay size, it might have been less problems with overexposure due to smaller mineral surfaces. Other minerals can also provide glints as seen in hyperspectral images of muscovite, k-feldspar, quartz and calcite marble, but glints in these samples are not as dominating as in the hematite sample.

When the grain size of the sample was smaller than 1 mm, it was difficult to distinguish distinct grains in the hyperspectral images, making it difficult to choose pixels with known content. It was possible to detect dark minerals in the calcite marble sample with sand fraction. These dark minerals had low signal-to-noise ratio, and it was not possible to extract spectral information from these. In brighter light conditions, the signal-to-noise ratio of these grains increased, but also resulted in overexposure of the calcite grains.

The entire fresh surface of the carbonate crust is in focus in the hyperspectral image in Figure 5.24. The crust with the original surface was difficult to get in focus due to varying topography of the sample. This resulted in the uppermost parts in focus and blurry edges of the crust. In this case, a smaller aperture could have been used, providing better depth of field that increases the overall focus of samples with varying topography. From the hyperspectral images of the crusts, it is easy to see that dark areas became darker and white became whiter, which gave problems with under- and overexposure.

An improvement of the HI camera to get a better dynamic range would decrease the over- and underexposure problems. Both dark and white minerals can then be mapped in similar light conditions. The radiometric resolution defined as bit per pixel (bit depth) gives the dynamic range of the image. With more bits, better exposure control and color intensity dynamics are obtained. This is important when taking spectral measurements in areas, which include both very dark and bright parts (Johnsen et al., 2013). The prototype HI used in this study has a lower dynamic range than the UHI used by Ecotone AS, which give less under- and overexposed images, and make it possible to get spectral information also in shadow areas. Shadow areas in *in situ* mapping can also be compensated by using sufficient illumination evenness.

### 6.1.2 Reflectance spectra

The main differences between the HI and Jaz measurements are seen in the blue (<500 nm) and the red (>600 nm) part of the spectrum, where the Jaz spectra show a higher reflectance intensity than HI relative to the rest of the spectra. In general, the HI spectra show higher reflectance values than the Jaz spectra.

The Jaz spectra show less variation in the shape, but variations of reflectance intensity often occur. The HI spectra show more variations in shape as well. A reason could be that reflectance intensity was measured in different ways by HI and by Jaz. This affected the measurements and resulted in differences in the spectra. HI measured radiance at a given angular direction and per pixel, while Jaz measured this at a much larger area (circle) making an “average” reflectance spectrum representing a much larger area than HI. Thus, Jaz measurements provided smoother spectra with less variation in reflectance than HI. However, HI can detect small differences in R in a given object, which Jaz cannot detect.

The reflectance spectra measured by HI show large fluctuations in red and blue light. The reason for this can be the HI sensor’s low sensitivity in these parts of the light spectrum caused by low

photon flux from the lamp in blue and red (Figure 5.1A). The optical fiber bundles did not have equal properties for blue light and red light since they attenuate photons of different colors differently. The upwelling radiance of the light source has a spectral range from approx. 440-690 nm, with an intensity peak at ~570 nm decreasing to zero reflection at the ends of the spectral range. The signal-to-noise ratio decreases with lower and higher wavelengths than 570 nm. Another light source and a camera sensor with higher spectral sensitivity in blue and red can decrease the uncertainties in these parts of the spectra. When the reflectance is high, both the HI and the Jaz spectra are in agreement and exhibit a convex shape. This is probably due to intense scattering of light, which is highest for particles at 1.1-1.6  $\mu\text{m}$  (clay fraction) as seen in Figure 3.5.

A systematic trend in the Jaz spectra are two peaks at ~550 nm and ~600 nm. These peaks are not seen in the spectra with low ( $R < 0.1$ ) or high intensity ( $R > 0.9$ ). This is caused by a systematic error in the light source correction in the *SpectraSuite* program. As seen on the light source radiance spectrum in Figure 5.1B, two peaks are present at these wavelengths. These peaks are therefore ignored in further discussions of the shape of these spectra, assuming that they are flat where the peaks are present.

Variations in reflectance intensity of the replicate measurements can be explained by the variations in orientation of the grains or by varying sensitivity across the hyperspectral image. The three replicate samples had different surfaces with respect to orientation and content of impurities. All samples had rough surfaces, which mean that the measured reflectance is diffuse. Specular reflection from smooth surfaces on the mineral grains also occurred. Diffuse and specular reflection varied and affected the reflectance. Another reason for the variation of HI intensity was the varying sensitivity of sensed light across the slit. In the edges of the image, the sensitivity was lower than the middle of the image, which gave a lower reflectance intensity at the edges.

Concerning HI measurements of fine-grained samples (<1 mm), it was not possible to know the mineral composition of selected pixels because the resolution was not high enough. This can be a reason for variations in the measurements due to spectral mixing. *In situ* UHI measurements obtain lower spatial resolution and small differences in any given sediment are therefore averaged, resulting in less variation per image pixel.

### *Mineral samples*

Figure 5.3A shows the HI reflectance spectra of muscovite. Both the dry and the submerged sample spectra show an increase in reflectance intensity from 460 nm to 610 nm, indicating absorption of blue light. Error bars are largest in the red part of the spectrum, and is larger for the dry sample than the submerged sample. Figure 5.3B of the Jaz spectra also show an increase of intensity in the same interval, though with a much gentler slope. In Hunt (1977), a spectral feature in muscovite spectra caused by OH stretches is found at 2.2  $\mu\text{m}$ , which is far beyond the visible light spectrum and do not explain the absorption feature in blue. A possible explanation for the apparent absorption in blue light can be that the HI was not sensitive enough to detect reflectance from grains in different orientation, due to the high spatial resolution.

Figure 5.4A shows large error bars in the reflectance spectrum for dry k-feldspar, especially in blue and red parts. The large variations of the k-feldspar HI spectrum are due to intensity variations. The submerged k-feldspar spectrum has smaller standard errors and does not show the same variations in the measurements. The mineral has an orange color, which is in accordance with the higher reflection of red light compared to blue light. This is seen in both the HI and Jaz spectra (Figure 5.4).

Quartz and calcite reflectance spectra have spectral features in the infrared part of the spectra because of vibrational processes (Hunt, 1977). These features are not seen in the reflectance spectra obtained in this study because infrared reflectance was not detected. These minerals are white in color, which means they reflect all visible light and have flat spectra without distinct absorption features in visible light.

Quartz and all of the carbonate samples show HI spectra with convex shape of the dry samples (Figure 5.5A, Figure 5.6A, Figure 5.7A and Figure 5.8A). The Jaz spectra show flat spectra for all these samples, except for dry pure  $\text{CaCO}_3$  where the convex shape also is present (Figure 5.8B). The reason for getting high values in the red and blue light, is the extreme scattering of light due to the small size of the particles. In addition to the convex shape, all of these minerals show a reflectance higher than  $R = 1$ . The reflectance of a mineral cannot be more than 100%, so this is probably also due to scattering of light. Scattering can be induced by overexposure of the samples, but in this case, the mineral samples were not overexposed.

Based on these results, it is not possible to discriminate between quartz and carbonate minerals on their optical signature in visible light. However, the results of calcite marble in sand fraction compared to clay fraction show a possibility of detecting variations in grain size because the clay samples show a higher reflectance than sand. If the grains are assumed to be non-absorbing

and approximately spherical, these results are in agreement with the scattering theory found in literature (Kirk, 1994). The other minerals contaminating the calcite marble can be the reason for a lower reflectance of the calcite marble clay sample compared to the pure  $\text{CaCO}_3$  sample.

The HI reflectance spectra of hematite show large variations and interesting spectral features not seen in the other mineral samples. Sherman et al. (1982) found reflectance spectra of several iron oxides and showed that they were most diagnostic and highly absorbing in the region 300-1000 nm. They typically show a flat behavior up to 530 nm where a change in the slope occurs and reaches a peak at 800 nm. This is due to crystal field transitions. 13 hematite spectra out of 18 in Figure 5.10 show slope changes between 460 nm and 510 nm. These can be related to the same transitions as in the hematite spectra in Figure 3.4. Only four of these seem to have an increased reflectance towards the infrared region.

The variations in the spectra of hematite can be a result of mixed spectra of hematite and other minerals, or it can be a result of a low signal-to-noise ratio. The Jaz spectra do not show these spectral features. They show a very low reflectance and only a reflectance peak at 550 nm and not at 600 nm like the other mineral spectra (Figure 5.9). The reason is probably due to the difficulties in the reflectance measurements of this mineral.

### *Changes in $\text{CaCO}_3$ content*

The HI spectra of dry samples of the artificial sediments show a change from a concave to a convex curve with increasing  $\text{CaCO}_3$  content (Figure 5.13A). The spectra show a reflectance intensity increase from low to high weight percent, except from the sample with 0.5 wt%  $\text{CaCO}_3$  that has a higher intensity than the sample with 1 wt%  $\text{CaCO}_3$ . In Figure 5.15A it is possible to see an increasing trend of the reflectance intensity from 2 wt%  $\text{CaCO}_3$  to 100 wt%  $\text{CaCO}_3$  for the dry samples. The Jaz measurements are in good agreement with the HI measurements regarding the increase of intensity with  $\text{CaCO}_3$  content. 1 wt%  $\text{CaCO}_3$  and 2 wt%  $\text{CaCO}_3$  show the same reflectance intensity (Figure 5.13B).

For the submerged samples, the HI results show less coherence between the increased intensity and  $\text{CaCO}_3$  content than for the dry samples (Figure 5.14A). Spectra of 0-2 wt%  $\text{CaCO}_3$  do not show an increase in reflectance based on increased  $\text{CaCO}_3$  content. In addition, the spectra of 4 wt% and 10 wt%  $\text{CaCO}_3$  intersect, but 10wt%  $\text{CaCO}_3$  has higher reflectance than 4 wt%  $\text{CaCO}_3$  in most parts of the spectrum. The Jaz spectra show a better discrimination between the samples with more than 4 wt%  $\text{CaCO}_3$  (Figure 5.14B). Figure 5.15B show a total increase in intensity, but not an increase between neighboring points.

As seen in this experiment, samples with varying  $\text{CaCO}_3$  content are possible to discriminate by reflectance intensity. The increase in  $\text{CaCO}_3$  made the sediment whiter and thus reflecting more light. The best results were obtained for large changes in  $\text{CaCO}_3$  content ( $>4$  wt%  $\text{CaCO}_3$ ). For the small changes, it is difficult to see a significant coherence of increasing  $\text{CaCO}_3$  content and an increasing reflectance. There is a larger amount of quartz than  $\text{CaCO}_3$  in these samples. As seen in Figure 5.5, quartz has a high intensity reflectance, and this could be a reason for uncertainties in the intensity variations of these samples.

The calcium carbonate used in this experiment had a small grain size, which reflected more light than grain sizes of sand or gravel. If a larger grain size had been used, the result might have been different. The changes from concave to convex shape of the reflectance spectra can be explained by an increase in scattering because of an increasing amount of clay grain size when  $\text{CaCO}_3$  content increased.

### *Natural sediment samples*

The Jaz measurements show that submerged samples have lower reflectance than dry samples, and that reflectance increases with increasing carbonate content which are in accordance with the artificial sediment experiment. HI measurements show a higher reflectance in blue and red light when the carbonate content increases because of an increase of white minerals.

The organic mud samples absorbed all light up to 500 nm for dry samples and 520 nm for submerged samples according to the HI measurements (Figure 5.18A). The reflectance peak is at 630 nm. The Jaz spectra show a small increase in reflectance between 520 nm and 660 nm, and in contrast to the HI measurements, they show some reflectance in the region lower than 500 nm for the dry sample (Figure 5.18B). The HI measured reflectance from the submerged samples is extremely low, but has the same shape as the dry sample. The small standard errors explain the small variability across the sample surface.

The high absorption in the blue region is probably due to the organic content of the sample, which is in accordance with the article by Bartholomeus et al. (2008) on reflectance of soil organic carbon (SOC). In addition to organic carbon, iron oxides can be present in the organic mud resulting in absorption of blue light. Hunt (1977) explains that weathered material is the reason for the most commonly observed feature in the spectra of terrestrial geological material. Weathered material where both iron and oxygen are present, have spectra with intensity fall-off from the visible into the ultraviolet region. This intensity fall-off due to weathering can also be present in marine sediments. In addition, the fine sand and the medium sand samples show



an increase from the blue to the red part of the spectra (Figure 5.19 and Figure 5.20). Biological film due to growth of bacteria and microalgae may affect absorption properties of natural sediments. Microalgae absorb in the red and blue part of the spectra, while bacteria typically absorb in the blue part (Roy et al., 2011).

The large variation in the red region of the fine sand spectra from the HI measurements can be explained by intensity variations. Jaz spectra of organic mud, fine sand and medium sand show an absorption feature at ~670 nm. This is also shown in the HI spectra. These spectra are in accordance with the in situ spectra of bottom types in the study by Hochberg et al. (2003), which determined the absorption features to be a result of chlorophyll from a benthic microalgae (Figure 3.13). Since possible microalgae in the natural sediment samples are dead, the degradation products, which also absorb blue and red light, can explain the absorption (Roy et al., 2011).

The shell sand and shell gravel spectra are quite similar in shape and intensity (Figure 5.21 and Figure 5.22). These spectra also show an increase in intensity from the blue to the red region, but they are missing the absorption feature at 670 nm. The low reflectance of blue light could be a result of organic content or iron, but it could also be a result of the pink color of the shells due to pigments absorbing blue light. Shell gravel samples show larger fluctuations in reflectance intensity than the shell sand samples, and the reason for this is probably the larger grain size. When the grain size increases, the importance of the grain distribution on the surface becomes larger.

### *Carbonate crusts*

In the HI reflectance spectra of the fresh surface, it is possible to see a difference between the areas of cemented grains (CG) and the areas of pure aragonite (Figure 5.26). The shape of the CG reflectance spectra is similar to the fine and medium sand of the natural sediment samples because these areas have a similar content of mixed carbonate and non-carbonate material. The reflectance intensity increases from blue to red light in both the cemented grains and the aragonite spectra. The aragonite reflectance spectra show a rapid increase of intensity for longer wavelengths than 660 nm, while the CG reflectance spectra show a gentle decrease of intensity. Concerning the Jaz measurements, the spectrum of area CG1 shows a more intense reflectance increase from blue to red light than in the other two spectra. The fresh surface has an orange color indicating weathering of iron and this can be the reason for the intensity fall-off into the blue region.

For the carbonate crust with the original surface, a variation of the spectra of the different surface areas can be seen (Figure 5.27). Absorption of blue light is present in the spectra of all areas - this is probably due to organic material as in the organic mud sample. Surface *a* consists of the carbonate shell from bristle worms and has a characteristic spectrum increasing from low reflectance in blue light to high reflectance in red light. Surface *b* is organic mud and shows a low reflectance. Red and blue light are not reflected from the submerged surfaces of this organic mud. Surface *c*, which consists of carbonate skeleton from other marine organisms, absorb blue light and has similar reflectance spectra as the reflectance spectra of surface *b*.

The Jaz reflectance spectra are similar in shape and have small variations in reflectance intensity, except the S1(w) reflectance spectrum that shows a reflectance intensity higher than all the other samples. This is due to a smaller distance between the light source and objects in the area, increasing the reflectance. Similarities of the shapes of these spectra are due to the averaged pixels of areas with mixed content, in contrast to the variation of the HI spectra extracted from selected pixels/areas.

### ***Changes due to submerging***

A general trend in both HI and Jaz spectra is that submerged samples show lower reflectance intensity than the dry samples. Minerals show a decrease of reflectance intensity with a value (*R*) of approx. 0.2-0.3 when they are submerged in seawater. Submerged natural sediments show a varying decrease of the reflectance intensity. For instance, fine sand only show a decrease in the red region. A smaller variation of the submerged HI spectra compared to the dry sample HI spectra is also observed. This may be due to less scattering of light from submerged samples. This is not seen in the Jaz spectra. However, there are only small differences in shape of the spectra due to the submerging, which indicate that the submerged reference plate was able to correct for the absorption/scattering of light in the seawater. The small differences are seen as higher absorption in blue and red part of the spectra.

### **6.1.3 Supervised classification**

Supervised classifications were carried out to check if it is possible to get successful classifications despite few identifying spectral features in the reflectance spectra. Dark areas and shadows were often misclassified as the darkest class in the classification (e.g. muscovite). Because several pixels in the samples had mixed contents, it was expected that there would be some misinterpretation in the classifications and several pixels were not identified by the

defined classes. Differences in orientation of grains and light conditions also resulted in unclassified pixels.

The classification of the mineral samples was the most successful (Figure 5.11). Hematite was not a part of this classification because the hyperspectral image did not include this mineral. Pixels in the k-feldspar sample were all correct, probably because this mineral has an orange color, while the other minerals are white. No other pixels were classified as k-feldspar. Even though all the other minerals are white, there were many correctly classified pixels of these minerals as well.

The classification of carbonate content in the artificial sediments was not as successful as the mineral classification (Figure 5.16). Calcium carbonate were only classified in the samples with more than 10 wt% calcium carbonate. This can be due to mixed mineral content in the pixels. Despite this, it was possible to classify differences between the basis sediment without calcium carbonate and the sediment with 50-100 wt% calcium carbonate.

Fine sand was the best classified natural sediment sample (Figure 5.23). The samples with medium sand, shell sand and shell gravel all consisted of grain sizes of similar minerals varying from fine to coarse sand. This made the classification of the samples difficult, because all the classes were represented in one sample. However, it is possible to see classifications of the major content in the samples. Pixels were classified as fine sand in all four samples, but mostly in samples FS1 and MS1. Pixels of medium sand were mostly classified in MS1, but a small amount of pixels were classified as medium sand in FS1, SS1 and SG1 as well. Shell sand pixels were mostly classified in the correct sample, but some pixels are classified as shell sand in MS1 and SG1. Shell gravel pixels were mostly found on large grains in the SG1 sample, but some pixels were also classified as shell gravel in SS1 and MS1.

The classification of the fresh surface of a carbonate crust managed to discriminate between the aragonite areas and the cemented grain areas (Figure 5.28). Since aragonite is the mineral cementing the grains there were some aragonite-classified pixels in between the cemented grains classified pixels. The HI images of the original surface were too dark to give a good classification, so a classification of this sample was not included in the results.

The results from the supervised classification show that it is possible to discriminate between different minerals, even though the reflectance spectra were without absorption features. The classification of the three calcium carbonate samples show that *Image Calculator* differentiate samples with different grain size and with different types of carbonate minerals.

A statistical verification of the classification success and errors are not accomplished in this thesis because there is no automated method of statistical analyses in the software making it a time-consuming task. However, Pettersen (2013) gives an example of a statistical verification of classification images of corals, counting the successful and unsuccessful pixels and placing them in classification matrixes. Without this verification, the classification success of the results in this study can only be deemed approximately correct. An aspect, which can cause errors in classifications, is the amount of pixels defining the classes. There were used 100 pixels for defining the samples in these classifications. A large number of class-defining pixels increases the probability of the pixels to be defined in a class. With a smaller number, the classifications get less unsuccessful classified pixels.

#### 6.1.4 Evaluation of the methodology of the laboratory work

The cuvette setup of the samples was an appropriate setup for the reflectance tests of dry samples. Disadvantages of the setup were the shadows from the cuvette walls giving lower reflectance intensity in the edges of the samples. Choosing five pixels in three independent areas of the sample gave good results for making mean spectra, since the surface area of the samples are small. However, this will not work *in situ* at the seabed when the spatial resolution is lower. Several pixels and larger areas have to be used to get a better averaging of the spectra. Because of the diversity of the content of sediments, mixed spectra can be found in the pixels. The spectral unmixing method (Figure 3.8), can be recommended for this purpose. Absorption features can then be separated and it is possible to find the abundance of the endmember classes. Submerging some of the samples gave some problems. Suspended minerals in the water column above the sample surface probably increased the scattering of light. The contraction of wet sediments and sediment floating on the top the water membrane might have been less problematic if the sample holder (cuvette) had a larger area (e.g. Petri dish). However, if Petri dishes had been used, it would not be possible to capture hyperspectral images of several samples simultaneously. In addition, the distribution of the minerals in the sample surfaces changed during submerging. This is seen in the RGB images - for instance, the hematite grains are gathered in upper right corner in several of the artificial sediment samples (Figure 5.12).

## 6.2 Use of UHI in marine geological mapping

The results from the laboratory tests and the literature study show that UHI can be used to detect and identify some properties of marine sediments including geochemical and organic contents and grain size. The data obtained from UHI are in addition of very high resolution.

### 6.2.1 Mapping marine sediments

The major question concerning the UHIs usefulness in marine geological mapping, is how it can contribute to, or complement the traditional mapping methods. These methods were described in chapter 2.2. UHI is a non-destructive and efficient method of mapping the seabed. It has better resolution at large depths than other remote sensing mapping methods, because of the proximity to the target. The automated classification of the sediments reduces the subjective interpretation of the data. The classification is limited and not comparable to qualitative analysis of sampled sediments, but it can be used as an efficient method of measuring the abundance of some sediment properties and sediment contents.

#### *Detecting and identifying properties of marine sediments*

Literature shows that HI can measure mineralogy, soil texture (sand, silt and clay), soil organic carbon, soil moisture, iron content, salinity, carbonates and weathering state of terrestrial soil (Mulder et al., 2011). Not all of these properties are possible to measure in underwater settings, due to the limitations of using light only in the visible spectrum. Studies of airborne HI used to identify and discriminate different marine features on shallow water seabed including sediments show some possibilities that can be applicable underwater (Fearn et al., 2011; Johnsen et al., 2009; Volent et al., 2007).

Both the laboratory results and literature indicate that UHI can detect variations in grain size, iron content, organic content and carbonate content (Johnsen et al., 2013). Grain size variations can be detected by variations in reflectance intensity and not by spectral shape. Variations of carbonate content can be detected by the whiteness of the sediment, shown by the artificial sediment experiment and by the natural sediment samples. Iron content and organic content can potentially be estimated from absorption features in the reflectance spectra.

Orientation of grains, sorting and particle shape affected the laboratory measurements. However, it is not possible to determine these properties based on reflectance results, neither in laboratory nor in the field. UHI map with longer distances from the object during *in situ*

measurements than done in laboratory measurements. This means that small differences in scattering properties not are detected because each image pixel will detect a much larger area of a given sediment site. Numerical and graphical distributions of grain size and sorting are not possible to obtain from UHI.

Topography influences the reflectance intensity measurements. Objects close to the light source show a higher reflectance than objects with a longer distance to the light source. This is shown in the HI monochromatic image of the carbonate crust with the original surface (Figure 5.25). Boulders might be identified from hyperspectral images of the seabed if these show a higher reflectance due to higher altitude than the surrounding sediments, or if they have different optical signatures than the surrounding sediments.

Acoustic backscatter can provide proxy signals indicating variations in grain size of sediments. Backscatter resolution is generally a compromise between coverage (swath width) and resolution (feature detection). Similarly, UHI has to find a compromise survey altitude for light/detection ability. In practice, it is likely that the optimal survey altitude for UHI is lower than for multibeam backscatter by HiSAS mapping. This may result in a better coverage of grain size variations by HiSAS than UHI.

### ***Detecting and identifying mineralogy***

Literature show that the most abundant minerals in marine sediments (quartz, carbonates, feldspar, micas etc.) have most distinctive absorption features in IR and UV light. Since these parts of the electromagnetic spectrum are heavily attenuated in water, UHI cannot be used to make qualitative maps of all minerals compounding a particular sediment. Only some specific minerals can be classified in visible light. None of the traditional remote sensing mapping methods can detect minerals in the sediments. Sampling has to be carried out to find the sediment mineral content. Even though UHI does not give a classification of all minerals, it can be used to find the presence of some minerals.

White minerals will not show absorption features in visible light. Therefore it is not possible to distinguish between minerals like calcite, aragonite and quartz by absorption features. However, the results from supervised classification show that differences in reflectance intensity can be used in discrimination. This will not be as easy in natural conditions, because the whiteness of these minerals vary with location.

The k-feldspar results show classification due to an orange color. No information on reflectance of k-feldspar was found in available literature. A classification based on color of this mineral will not be reliable, because the color of the same kind of mineral can vary.

Literature shows that transition metals are possible to detect in UV-VNIR light. This include metals like iron (Fe), copper (Cu), silver (Ag), gold (Au), cobalt (Co), manganese (Mn), nickel (Ni), zinc (Zn), chromium (Cr), molybdenum (Mo), titanium (Ti) etc. Several of these have absorption features in visible light. Laboratory results in this study show that hematite has spectral features in visible light, but the feature positions vary between the samples. UHI tested by Johnsen et al. (2013) show that manganese nodules,  $\text{Fe}_2\text{O}_3$ ,  $\text{FeSO}_4$ ,  $\text{MnO}_2$  and  $\text{MnSO}_4$  can be classified by an unsupervised classification of the images. (Figure 3.18).

Pelagic red clay is often found in marine sediments (Pinet, et al., 2009). The color comes from iron oxide coating on the minerals, which would be possible to trace with UHI. An example from Svalbard measuring red clay reflectance in a river plume (Figure 3.15) support this theory (Johnsen et al., 2009).

### ***Detecting and identifying carbonate deposits***

Both the natural sediment samples and the artificial sediment samples show an increase of reflectance intensity with increasing carbonate content. The samples of natural sediments demonstrate reality better than the artificial sediments. In addition to the overall increased reflectance, the natural sediments show a difference in shape of the spectra, where the spectra reflect more light in blue and red part for increasing carbonate content, indicating that the sediment is whiter. This is probably due to decreasing organic material in the natural sediments, not present in the artificial sediment mix. This is important to note when transferring these reflectance properties to mapping sediments *in situ*.

Based on these experiments, carbonate deposits can be recognized by their high reflectance for all wavelengths in visible light. For instance, shell sand and shell gravel deposits can be mapped by their high ratio of white material resulting in a high reflectance values. This is a more efficient method to find the spatial distribution of shell sand than the traditional method of shell sand mapping described in chapter 2.2.4. Still, to find the thickness of the deposits seismic data interpretation must be used. In addition, carbonate ooze would be possible to map by UHI. This gives possibilities of mapping the CCD contour line as well, which goes down to 4500 m depth at some locations.

Carbonate crusts, coral reefs, carbonate mounds and the spatial distribution of bioclastic sediment surrounding these can possibly be mapped by their high reflectance values. These deposits will have high reflectance intensity due to topography as well. It is possible to get closer and map smaller reefs by UHI than by the mapping methods described in Somoza et al. (2014) in chapter 2.2.4. The morphological similarity between carbonate mounds and mounds created by sliding described in Bellec et al. (2014), may be distinguished by UHI.

Dierssen et al. (2009) described reflectance mapping of whittings (suspended aragonite needles) in the Bahamas by airborne HI. Their results on optical signatures of whittings and carbonate sand are different from the results in this study. This may be due to the reflectance measurements through 5 m of tropical seawater, while the reflectance in this study was measured through 2 mm of filtered seawater. However, the spectra in the Bahamas study show that carbonate mud have higher reflectance than carbonate sand and that algal biofilm lowers the reflectance, which are in accordance with this study.

### ***Spatial resolution of mapping methods***

Spatial resolution include the proximity to the target and the signal-to-noise ratio of the sensor. The distance to target being ~2 m using UHI gives a resolution of ~2 mm making this method ideal for mapping underwater habitat variations on sub-meter scales (Johnsen et al., 2013).

The spatial resolution of other mapping techniques with equipment used by MAREANO are compared to the UHI in Table 6.1 – this include multibeam echosounder (MBES), TOPAS shallow seismic, video analysis and synthetic aperture sonar (SAS). The maximum mapping depth and range of application is also included in the table. Video and SAS have a very good spatial resolution, but video can only be used for visual interpretations and SAS cannot map geochemistry. To map topography and determining sediment properties such as grain size and geotechnical properties like compaction, porosity and sorting, SAS might be a better choice than UHI.



**Table 6.1** Comparison of marine mapping methods. Numbers are based on subsea systems from Kongsberg Maritime (2014), except UHI numbers that are based on Johnsen et al. (2013).

Method	Range of application	Spatial resolution	Max. depth
<b>UHI</b>	Automated method of mapping metals, grain size, iron content, organic content and carbonate content.	~2 mm	~6000 m with AUV
<b>MBES EM 710 EM 302</b>	Bathymetry and backscatter (topography, grain size, compaction, porosity and sorting).	Depending on depth and sensor (5-50 m grid size on terrain maps)	~2000 m (EM 710) ~7000 m (EM 302)
<b>TOPAS PS 18</b>	Shallow seismic	Depending on depth and sensor (range resolution >15 cm)	~11 000 m
<b>Video</b>	Visual description, mapping marine habitats.	~2 cm	~3000 m
<b>SAS</b>	Bathymetry and backscatter (topography, grain size, compaction, porosity and sorting).	~2 cm	~3000 m with AUV (HiSAS)

### 6.2.2 Application in industry

A field where UHI can be useful, based on the results of the carbonate changes, is in the oil and gas industry. This shows a potential for application in monitoring changes of carbonate content in sediments around gas leakages from carbon capture in reservoirs. The laboratory results show that only large changes in carbonate content can be traced, but this might be different for sensors with better sensitivity. There is also a potential to detect spreading of cutting materials on the seabed if these consist of minerals that can be identified by the hyperspectral imager and distinguished from the rest of the sediments.

The ability to detect and classify amounts of metals on the seabed is a great advantage in the marine mining industry. Enormous resources of different metals eroded from land are found on the seabed. Manganese nodules are formed by terrestrial manganese transferred to the deep by biogeochemical cycling. Metals like Cu, Fe, Zn, Au and Ag are also found around hydrothermal vents (“black smokers”) in plate tectonic areas. These precipitate from the vent fluids as

polymetallic sulfate when they react with seawater sulfate (Rona, 2003). These metals are all transition elements and can potentially be mapped by UHI. Since the mining industry is the main driver in geological hyperspectral imaging, good information on reflectance from different metals may be expected to come from industrial driven research.

Another field of application of UHI is in the land based mining industry. Deposition of mine tailings in fjords is a subject of current interest. This is a potential method of monitoring how the deposits spread on the seabed because grain size, mineralogy and other factors may be different from the natural sediments in the fjord. Another possibility can be to trace acid-generating minerals such as pyrite and the oxidation product as indicator on pollution. Tracing of these minerals in terrestrial mine-tailings by HI have been successful (Riaza & Müller, 2010; Shang et al., 2009).

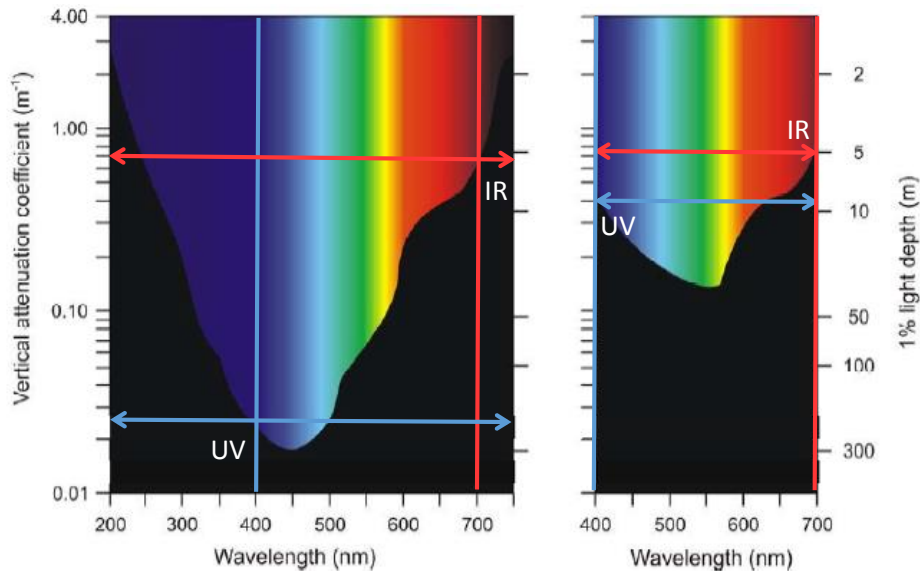
The laboratory results (supervised classification) show that the whiteness of different samples is highly applicable for discrimination analyses. This can be used to find the whiteness of carbonate deposits in the mining industry. There are several other fields where terrestrial HI can be useful, but these will not be discussed here. One example is the detection of expansive clay by HI, which can be used in engineering geology and geotechnical mapping (Chabillant et al., 2002).

### 6.2.3 Challenges and limitation of UHI for geological purposes

The main problem of UHI for geological mapping is that IR and UV light is heavily attenuated in seawater. If a method of using IR and UV light underwater is developed, the UHI will get a larger range of application. Sensing IR and UV reflectance could be possible if the light source and sensor get close enough to the sediments. The attenuation of visible light and the limits of UV and IR light depths are shown in Figure 6.1. For deep ocean water (case 1 water), the distance has to be less than 6 m (1% light depth) to sense light at 700 nm and the distance decreases rapidly to less than 2 m at 750 nm. In fjord water (case 2 water) the 1% light depth is 5 m at 700 nm. This gives an indication of how close the UHI has to be to the seabed, which would be less than 1 m.

The vertical attenuation coefficient of UV light is smaller, which indicates a better potential for reflectance measurements in this part of the spectra. Light at 400 nm can be measured at several 100 meters depth and decreases to 2 m at 200 nm. At 1 m distance from the seabed, UV light

with wavelength down to 200 nm can be measured. In fjord waters, the vertical attenuation coefficient is larger and UV light get a 1% light depth at less than 10 m.



**Figure 6.1** Illustration of the attenuation of light in seawater. Vertical red lines indicate the limit of IR light, and vertical blue lines the UV light limit. The cross of the vertical and horizontal lines show the vertical attenuation coefficient and 1% light depth at these limits. Modification of figure 3.2 (Sakshaug et al., 2009).

The attenuation in water is not the only challenge regarding IR and UV reflectance measurements. The UHI sensor needs to be developed more UV and IR sensitive for this purpose as well. Measuring UV light is difficult because the reflectance instruments attenuate light in the instruments and there is a need for developing other optical fibers and spectrometer instruments. The prototype HI sensor used in this study had low sensitivity at wavelengths below 420 nm and above 680 nm, and would not be sufficient for this purpose. A sensor with better UV and IR sensitivity (350-850 nm) and with higher spatial and radiometric resolution has recently been developed by Ecotone AS and tested on a ROV. The result was successful, covering large areas of seabed and creating geo-localized seabed maps (Johnsen et al., 2013; Ludvigsen et al., 2014).

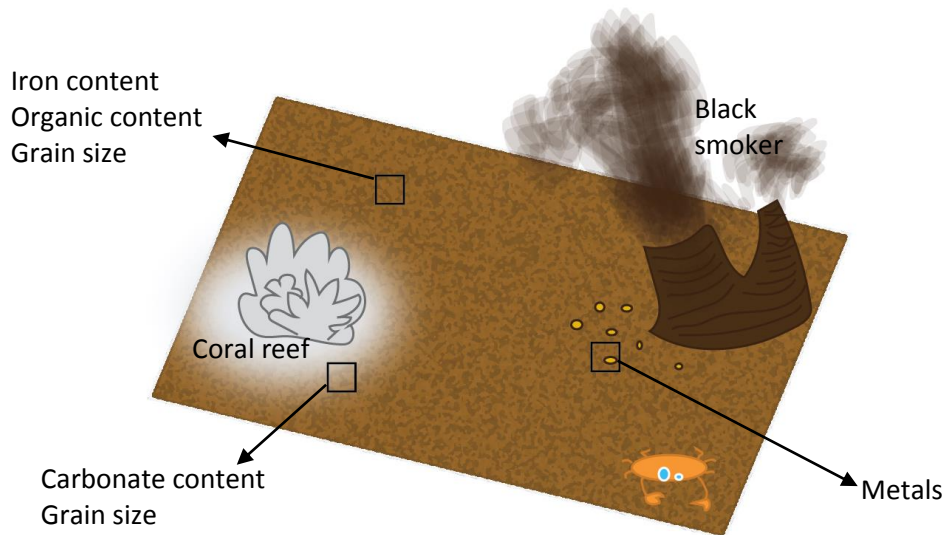
With normal operation of the present AUVs, the distance between the UHI sensor and light source, and the seabed is a challenge. Development of more advanced AUVs, being able to stop and get close to the seabed for close-up imagery, could be a way of overcoming this problem. A similar approach can be envisaged for ROV based UHI imagery acquisition.

Other limitations of optical measurements of the seabed include algal/bacterial biofilm and fauna on the seabed, covering sediments and features like carbonate crust and boulders. Reflectance from these features can be obscured by the biofilm. The crust with the original surface in this study is partly covered by organic mud, so this can also obscure the reflectance results.

Since white minerals are difficult to classify by reflectance spectra shape, it is possible that other minerals with high reflectance like quartz can be misclassified as calcium carbonate. Then the calcium carbonate content will be overestimated. In addition, the absorption features of iron content and organic content can be difficult to distinguish.

The variations in sediment content across different locations give site-specific optical signatures and mixed spectra. This has to be considered in *in situ* UHI measurements of sediments. A possible mapping approach can be - setting the optical signature of different content (iron, metals etc.) as endmembers and identify them within the reflectance spectra of the recorded pixels. A spectral unmixing has to be carried out for the pixels to make abundance maps of the seabed. Fearn et al. (2011) showed HI data from airborne mapping overlaid on bathymetry data. A similar approach probably makes it easier to verify the results from UHI. If bathymetry data from SAS could be used in addition to the optical signatures from UHI, the result would be high resolution 3D maps with great interpretation possibilities.

Because of these limitations, UHI cannot replace the traditional mapping methods to map seabed geology, but it can serve as a valuable contribution that facilitates the acquisition of geochemical remote sensing data with good spatial resolution. Such data can also be used to calibrate other data, such as multibeam backscatter data. Figure 6.2 show an illustration of some of the marine geological applications of UHI, including metals from black smokers, coral reefs and carbonate sediments.



**Figure 6.2** Illustration of the seabed and possible geological application of UHI. Features are not in correct scale.



# Chapter 7    Conclusions and recommendations

## 7.1 Conclusions

Literature studies and laboratory results give a reason to believe that the following properties of marine sediments can be detected and identified by UHI:

- ❖ Iron content and organic content due to absorption features in UV and visible light.
- ❖ Minerals containing transition metals (e.g. hematite) with absorption features in UV and visible light.
- ❖ Grain size changes due to changes in reflectance intensities.
- ❖ Carbonate content variations due to the whiteness of the sediment. This can be used in mapping of bioclastic sediments, carbonate crusts and coral reefs.

Challenges regarding UHI in marine geological mapping include the following points:

- ❖ UHI has limited abilities to detect spectral reflectance of UV and IR light due to attenuation in seawater and limitations in the instruments.
- ❖ The most abundant minerals in marine sediments are “white” minerals (quartz, calcium carbonate, feldspar, muscovite, etc.), which do not show spectral features in visible light and therefore are difficult to distinguish, based on optical signature. In addition, the absorption features from iron content and organic content can be difficult to distinguish.
- ❖ Biofilm on the sediments and seabed features can obscure the reflectance signal from minerals.

Comparing UHI to established mapping methods results in the following conclusions:

- ❖ UHI can detect geochemical properties - no other remote sensing mapping method can do this.
- ❖ UHI give better spatial resolution at large depths than traditional mapping methods.
- ❖ UHI do not give precise qualitative values of sediment content, thus it cannot replace sediment sampling and analysis.
- ❖ Using high-resolution bathymetry data and UHI data together show great potentials of mapping a range of geological properties of the seabed with high spatial resolution.

## 7.2 Further work

UHI is a marine mapping method with great potentials. However, to verify its range of applications, there is a need for further studies and development of the instruments. The newest developed equipment and software, with fewer limitations than the equipment used in this thesis, must be used in further research to obtain more precise data. Here are some recommendations for further work:

- ❖ Develop more UV and IR sensitive instruments and test these underwater.
- ❖ Test UHI on geological material *in situ* (carbonate changes, grain size, organic material, iron content, metals etc.). Combine these measurements with established mapping methods and compare the data gained.
- ❖ Find more information on optical remote sensing of metals and optical signatures of these. This can be relevant for exploration of marine minerals.
- ❖ Develop a methodology of mapping sediments *in situ* with UHI, e.g. using spectral unmixing of the reflectance spectra.



## Chapter 8    References

- Bartholomeus, H. M., Epema, G., & Schaepman, M. E. (2007). Determining iron content in Mediterranean soils in partly vegetated areas, using spectral reflectance and imaging spectroscopy. *International Journal of Applied Earth Observation and Geoinformation*, 9(2), 194-203.
- Bartholomeus, H. M., Schaepman, M. E., Kooistra, L., Stevens, A., Hoogmoed, W. B., & Spaargaren, O. S. P. (2008). Spectral reflectance based indices for soil organic carbon quantification. *Geoderma*, 145(1), 28-36.
- Bekkby, T., Bodvin, T., Bøe, R., Moy, F. E., Olsen, H., & Rinde, E. (2011). Nasjonalt program for kartlegging og overvåking av biologisk mangfold-marint. Sluttrapport for perioden 2007-2010. Norge: Norsk Institutt for Vannforskning. Rapport L.Nr. 6105-2011.
- Bellec, V., Thorsnes, T., & Bøe, R. (2014). Mapping of bioclastic sediments - data, methods and confidence. Trondheim: Geological Survey of Norway. Rapport.nr. 2014.006.
- Boggs, S. J. (2010). *Principles of Sedimentology and Stratigraphy*. (4th international ed.). Upper Saddle River, Pearson Prentice Hall.
- Brown, C. J., Smith, S. J., Lawton, P., & Anderson, J. T. (2011). Benthic habitat mapping: A review of progress towards improved understanding of the spatial ecology of the seafloor using acoustic techniques. *Estuarine, Coastal and Shelf Science*, 92, 502-520.
- Buhl-Mortensen, L., Hodnesdal, H., & Thorsnes, T. (Eds.) (2010). *Til bunns i Barentshavet og havområdene utenfor Lofoten–ny kunnskap fra MAREANO for økosystembasert forvaltning*. Trondheim: Norges geologiske undersøkelse.
- Bøe, R., & Olsen, H. A. (2011). Skjellsandforekomster i Austrheim og Fitjar kommune, Hordaland. Trondheim: Norges Geologiske Undersøkelse. Rapport nr. 2011.027.
- Chabrilant, S., Goetz, A., Krosley, L., & Olsen, H. (2002). Use of hyperspectral images in the identification and mapping of expansive clay soils and the role of spatial resolution. *Remote Sensing of Environment*, 82, 431-445.
- Dierssen, H. M., Zimmerman, R. C., & Burdige, D. J. (2009). Optics and remote sensing of Bahamian carbonate sediment whittings and potential relationship to wind-driven Langmuir circulation. *Biogeosciences*, 6, 487-500.
- Doney, S. C., Fabry, V. J., Feely, R. A., & Kleypas, J. A. (2009). Ocean acidification: the other CO<sub>2</sub> problem. *Marine Science*, 1, 169-192.
- Falkowski, P. G., & Raven, J. A. (2013). *Aquatic photosynthesis*. New Jersey: Princeton University Press.
- Fearn, P. R. C., Klonowski, W., Babcock, R. C., England, P., & Phillips, J. (2011). Shallow water substrate mapping using hyperspectral remote sensing. *Continental Shelf Research*, 31, 1249-1259.
- FME SUCCESS (2014). 08.01.2014, from <http://www.fme-success.no/index.cfm?id=408031>
- Fosså, J. H., Lindberg, B., Christensen, O., Lundälv, T., Svellingen, I., Mortensen, P. B., & Alvsvåg, J. (2005). Mapping of *Lophelia* reefs in Norway: experiences and survey methods. In A. Freiwald & J. M. Roberts (Eds.), *Cold-water Corals and Ecosystems*. (pp. 359-391). Berlin Heidelberg: Springer-Verlag.

- Hall-Spencer, J. M., Rodolfo-Metalpa, R., Martin, S., Ransome, E., Fine, M., Turner, S. M., Rowley, S. J., Tedesco, D., & Buia, M.-C. (2008). Volcanic carbon dioxide vents show ecosystem effects of ocean acidification. *Nature*, 454(7200), 96-99.
- Hochberg, E. J., Atkinson, M. J., & Andréfouët, S. (2003). Spectral reflectance of coral reef bottom-types worldwide and implications for coral reef remote sensing. *Remote Sensing of Environment*, 85, 159-173.
- Hovland, M., & Mortensen, P. B. (1999). *Norske korallrev og prosesser i havbunnen*. Bergen: Grieg.
- Hovland, M., Talbot, M. R., Qvale, H., Olausen, S., & Aasberg, L. (1987). Methane-related carbonate cements in pockmarks of the North Sea. *Journal of Sedimentary Research*, 57(5), 881-892.
- Hunt, G. R. (1977). Spectral signatures of particulate minerals in the visible and near infrared. *Geophysics*, 42(3), 501-513.
- IOCCG (2000). Remote Sensing of Ocean Colour in Coastal and Other Optically-Complex Waters. In S. Sathyendranath (Ed.), *Reports of the International Ocean-Colour Coordinating Group*. Dartmouth, Canada: IOCCG.
- Jerlov, N. G. (1976). *Marine Optics*. Amsterdam: Elsevier Science.
- Johnsen, G., Volent, Z., Dierssen, H., Pettersen, R., Van Ardelan, M., Søreide, F., Fearn, P., Ludvigsen, M., & Moline, M. (2013). Underwater hyperspectral imagery to create biogeochemical maps of seafloor properties. In J. Watson & O. Zielinski (Eds.), *Subsea optics and imaging* (pp. 508-535). Cambridge, UK: Woodhead Publishing.
- Johnsen, G., Volent, Z., Sakshaug, E., Sigernes, F., & Pettersson, L. H. (2009). Remote sensing in the Barents Sea. In E. Sakshaug, G. Johnsen & K. Kovacs (Eds.), *Ecosystem Barents Sea* (pp. 139-166). Trondheim, Norway: Tapir Academic Press.
- Kirk, J. T. O. (1994). *Light and photosynthesis in aquatic ecosystems*. New York: Cambridge university press.
- Kongsberg Maritime (2014). Subsea systems. Retrieved 04.12., 2014, from <http://www.km.kongsberg.com/ks/web/nokbg0240.nsf/AllWeb/246BFAD18090EC5CC12573170024580A?OpenDocument>
- Kruse, F. A. (2010). *Mineral Mapping Using Spectroscopy - From Field Measurements to Airborne Satellite-Based Imaging Spectrometry*. Paper presented at the Art, Science and Applications of Reflectance Spectroscopy Symposium, Boulder, Colorado.
- Kruse, F. A., Boardman, J. W., & Huntington, J. F. (2003). Comparison of Airborne Hyperspectral Data and EO-1 Hyperion for Mineral Mapping. *IEEE Transactions on Geoscience and Remote Sensing*, 41(6), 1388-1400.
- Ludvigsen, M., Johnsen, G., Lågstad, P. A., Sørensen, A. J., & Ødegård, Ø. (2013). *Scientific operations combining ROV and AUV in the Trondheim Fjord*. Paper presented at the OCEANS-Bergen, 2013 MTS/IEEE.
- Ludvigsen, M., Johnsen, G., Sørensen, A. J., Lågstad, P. A., & Ødegård, Ø. (2014). Scientific Operations Combining ROV and AUV in the Trondheim Fjord. *Marine Technology Society Journal*, 48(2), 59-71.
- Malenovský, Z., Bartholomeus, H. M., Acerbi-Junior, F. W., Schopfer, J. T., Painter, T. H., Epema, G. F., & Bregt, A. K. (2007). Scaling dimensions in spectroscopy of soil and vegetation. *International Journal of Applied Earth Observation and Geoinformation*, 9(2), 137-164.

- Mulder, V. L., de Bruin, S., Schaepman, M. E., & Mayr, T. R. (2011). The use of remote sensing in soil and terrain mapping - A review. *Geoderma*, 162, 1-19.
- Ocean Optics (2009). SpectraSuite Spectrometer Operating Software - Installation and Operation Manual. Florida, USA: Ocean Optics Inc.
- Pettersen, R. (2013). *Identification of Marine Organisms using Chemotaxonomy and Hyperspectral Imaging*. (Philosophiae Doctor), Norwegian University of Science and Technology, Trondheim.
- Pettersen, R., Johnsen, G., Bruheim, P., & Andreassen, T. (2013). Development of hyperspectral imaging as a bio-optical taxonomic tool for pigmented marine organisms. *Organisms, Diversity and Evolution*, 14(2). 237-246.
- Pinet, P. R. (2009). *Invitation to Oceanography* (Fifth ed.). Sudbury, Massachusetts: Jones and Bartlett Publishers, LLC.
- Raven, J., Caldeira, K., Elderfield, H., Hoegh-Guldberg, O., Liss, P., Riebesell, U., Shepherd, J., Turley, C., & Watson, A. (2005). *Ocean acidification due to increasing atmospheric carbon dioxide*. Cardiff: The Royal Society.
- Riaza, A., & Müller, A. (2010). Hyperspectral remote sensing monitoring of pyrite mine wastes: a record of climate variability (Pyrite Belt, Spain). *Environmental Earth Sciences*, 61(3), 575-594.
- Richards, J. A. (1999). *Remote sensing digital image analysis* (Vol. 3). Canberra: Springer.
- Roberts, J. M., Wheeler, A. J., & Freiwald, A. (2006). Reefs of the Deep: The Biology and Geology of Cold-Water Coral Ecosystems. *Science*, 312(5773), 543-547.
- Rona, P. A. (2003). Resources of the sea floor. *Science*, 299(5607), 673-674.
- Roy, S., Llewellyn, C. A., Egeland, E. S., & Johnsen, G. (2011). *Phytoplankton pigments: characterization, chemotaxonomy and applications in oceanography*. New York: Cambridge University Press.
- Sabins, F. F. (1999). Remote sensing for mineral exploration. *Ore Geology Reviews*, 14, 157-183.
- Sakshaug, E., Johnsen, G., & Volent, Z. (2009). Light. In E. Sakshaug, G. Johnsen & K. Kovacs (Eds.), *Ecosystem Barents Sea* (pp. 117-138). Trondheim, Norway: Tapir Academic Press.
- Shang, J., Morris, B., Howarth, P., Lévesque, J., Staenz, K., & Neville, B. (2009). Mapping mine tailing surface mineralogy using hyperspectral remote sensing. *Canadian Journal of Remote Sensing*, 35(1), 126-141.
- Sherman, D. M., Burns, R. G., & Burns, V. M. (1982). Spectral characteristics of the iron oxides with application to the Martian bright region mineralogy. *Journal of Geophysical Research: Solid Earth*, 87(B12), 10169-10180.
- Somoza, L., Ercilla, G., Urgorri, V., León, R., Medialdea, T., Paredes, M., Gonzalez, F. J., & Nombela, M. A. (2014). Detection and mapping of cold-water coral mounds and living *Lophelia* reefs in the Galicia Bank, Atlantic NW Iberia margin. *Marine Geology*, 349, 73-90.
- Statens Kartverk (2006). SOSI standard - generell objektkatalog versjon 4.0. Fagområde: Løsmassegeologi. Norge: Statens Kartverk.

- van der Meer, F. D., van der Werff, H. M. A., van Ruitenbeek, F. J. A., Hecker, C. A., Bakker, W. H., Noomen, M. F., van der Meijde, M., Carranza, E. J. M., Boudewijn de Smeth, J., & Woldai, T. (2012). Multi- and hyperspectral geologic remote sensing: A review. *International Journal of Applied Earth Observation and Geoinformation*, *14*, 112-128.
- Van Lancker, V., Van Heteren, S., Leth, J., Kupschus, S., Coggan, R., Mason, C., Monteys, X., Scott, G., & Hardy, D. (2012). Standardisation and harmonisation in seabed habitat mapping: role and added value of geological data and information. Part A: Sediment characterization. British Geological Survey.
- Viscarra Rossel, R. A., McGlynn, R. N., & McBratney, A. B. (2006). Determining the composition of mineral-organic mixes using UV-vis-NIR diffuse reflectance spectroscopy. *Geoderma*, *137*(1-2), 70-82.
- Volent, Z. (2009). *Remote sensing of marine environment: Applied surveillance with focus on optical properties of phytoplankton, coloured organic matter and suspended matter*. (Philosophiae Doctor), Norwegian University of Science and Technology, Trondheim.
- Volent, Z., Johnsen, G., & Sigernes, F. (2007). Kelp forest mapping by use of airborne hyperspectral imager. *Journal of Applied Remote Sensing*, *1*(011503), 1-21.
- Volent, Z., Johnsen, G., & Sigernes, F. (2009). Microscopic hyperspectral imaging used as bio-optical taxonomic tool for micro- and macroalgae. *Applied Optics*, *48*, 4170-4176.
- Wentworth, C. K. (1922). A scale of grade and class terms for clastic sediments. *The Journal of Geology*, *30*(5), 377-392.

# Appendices

A – RGB images of all samples

B – Hyperspectral images



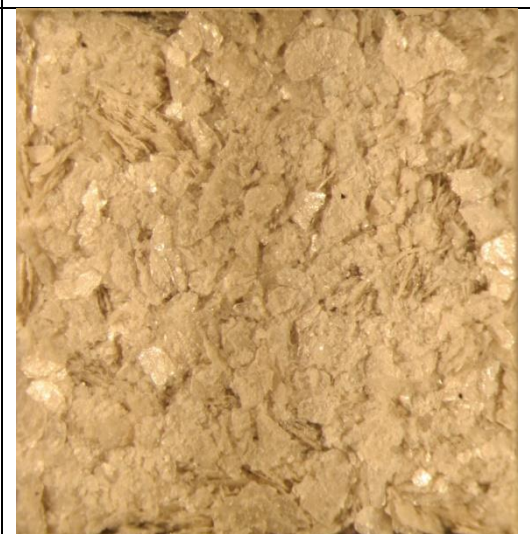
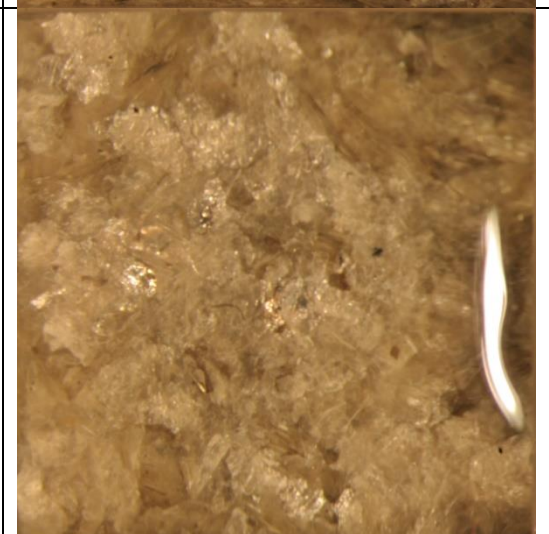

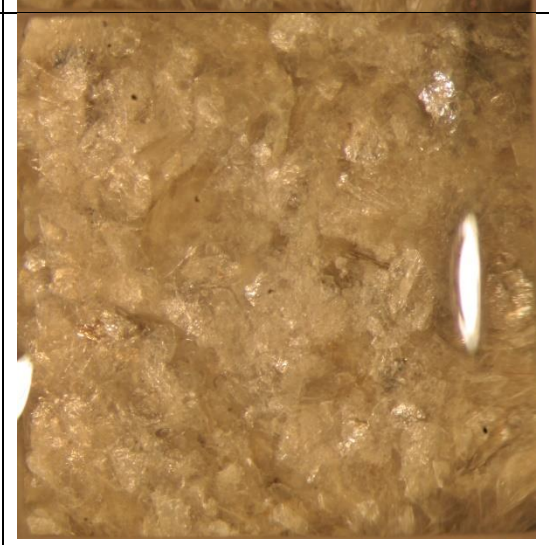
C – HI spectra of each sample


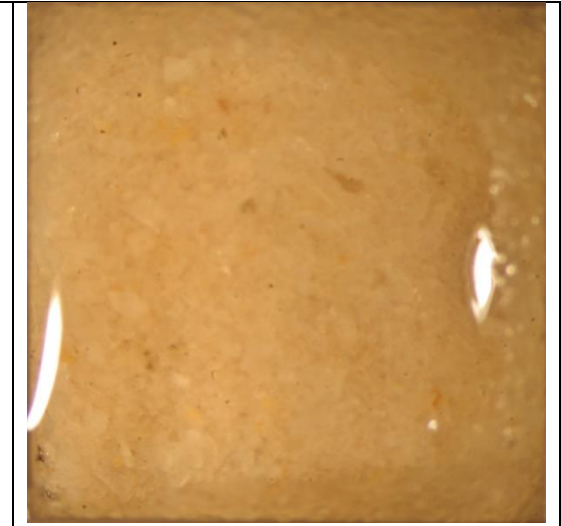

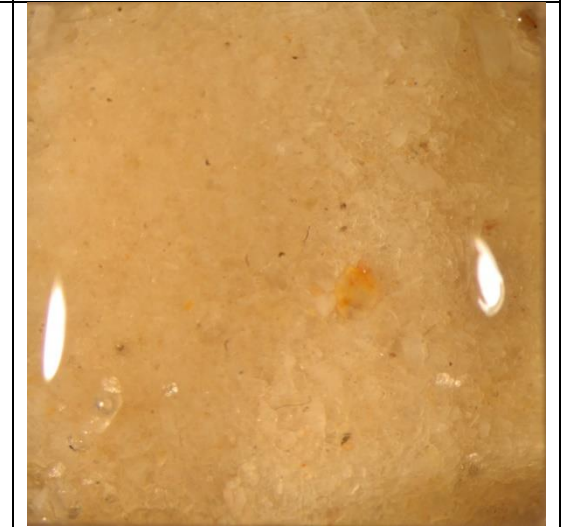


D – Visual description of natural sediment samples provided by NGU





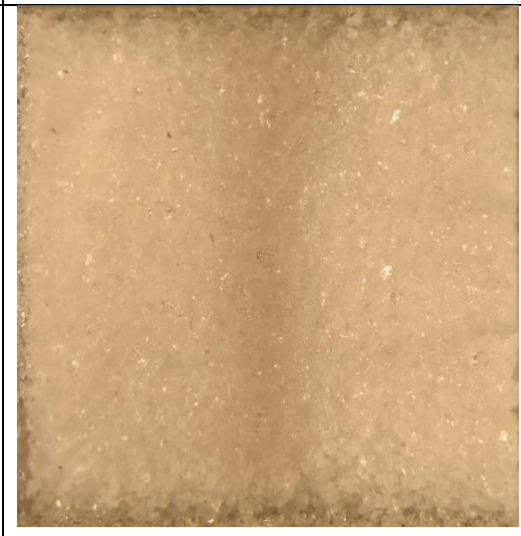
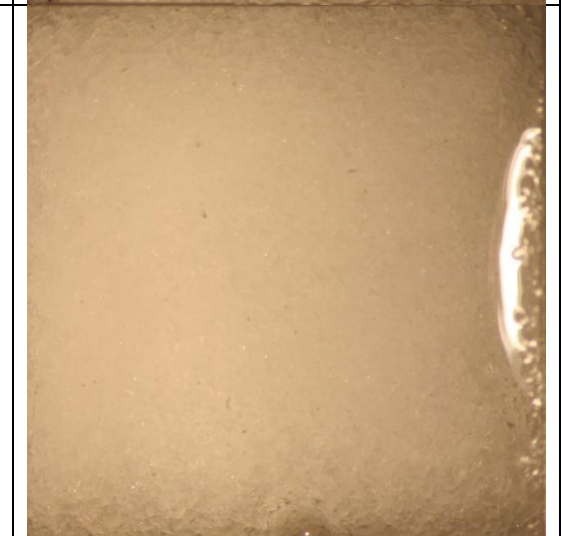
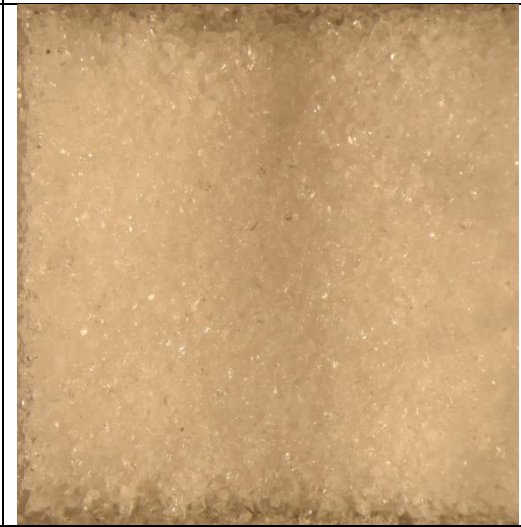
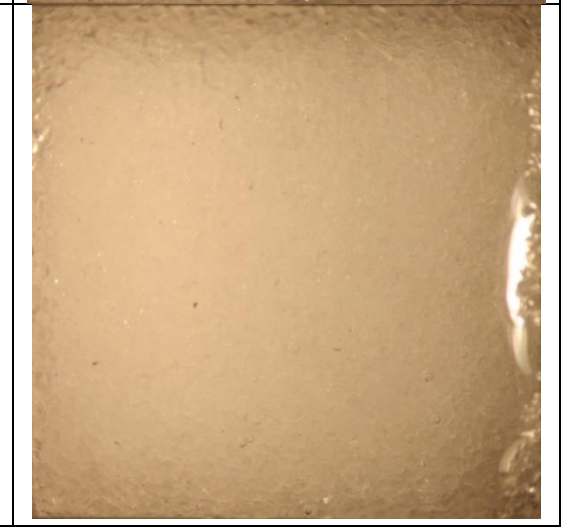
**Appendix A – RGB images of all samples**

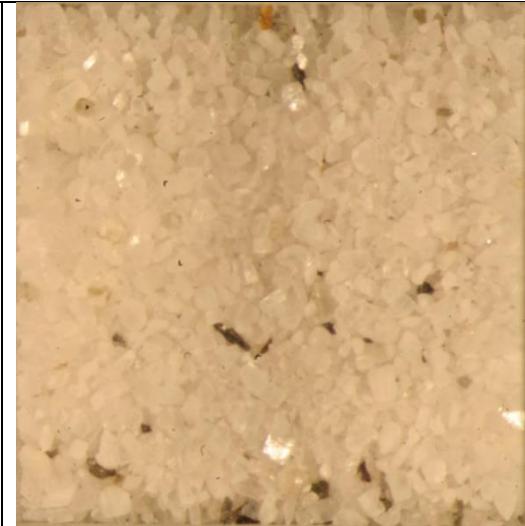


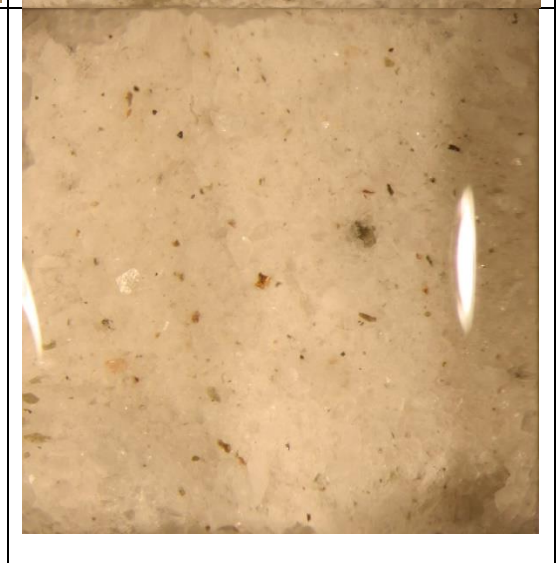


*Table A.1 RGB images off all samples (dry and submerged). Scale of images: 10\*10 mm.*


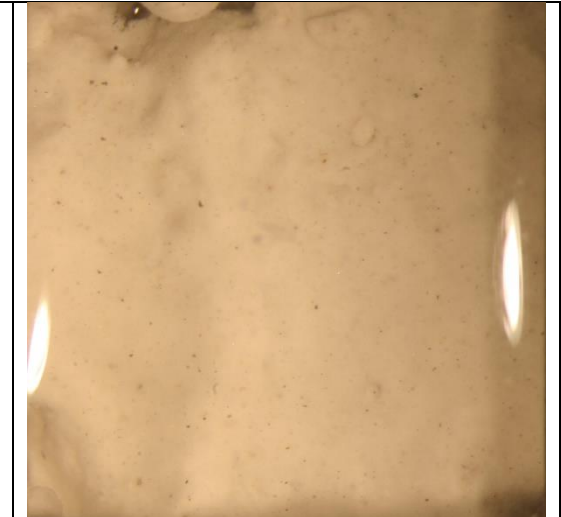
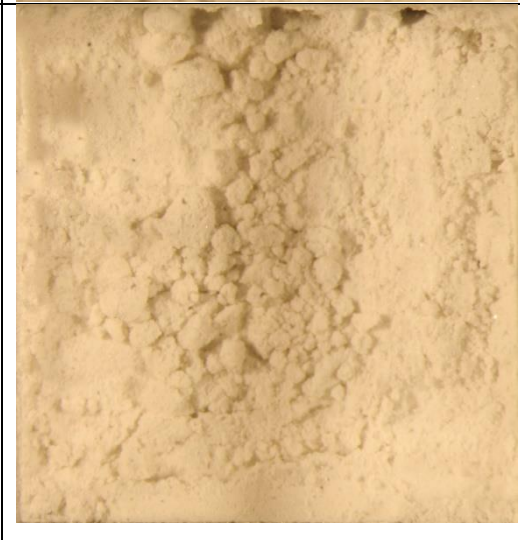

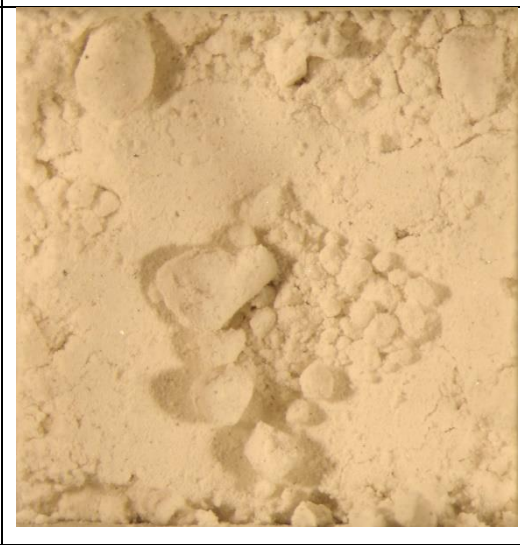
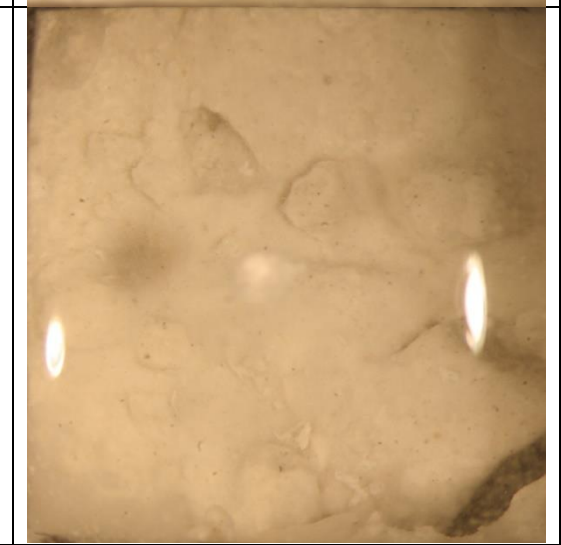
Sample	Dry	Submerged
M1	 A close-up photograph of a dry, brown, fibrous material with a rough, irregular texture. The fibers are densely packed and appear somewhat clumped together.	 A close-up photograph of the same material submerged in water. The material is darker brown and appears more saturated and slightly more cohesive than in the dry state.
M2	 A close-up photograph of a dry, brown, fibrous material with a rough, irregular texture, similar to M1.	 A close-up photograph of the same material submerged in water. The material is darker brown and appears more saturated. A prominent, bright white, curved object is visible on the right side of the frame.
M3	 A close-up photograph of a dry, brown, fibrous material with a rough, irregular texture, similar to M1.	 A close-up photograph of the same material submerged in water. The material is darker brown and appears more saturated. A prominent, bright white, curved object is visible on the right side of the frame, similar to the one in M2.



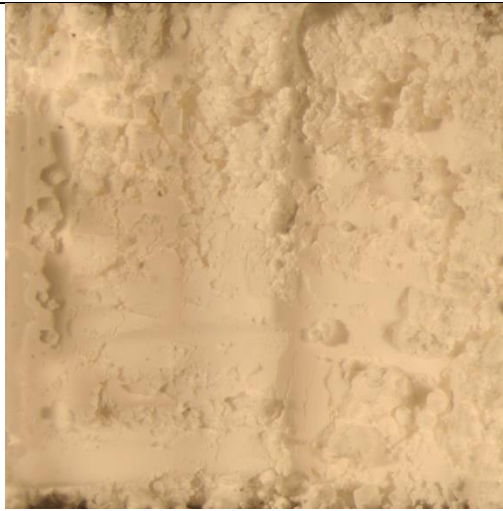


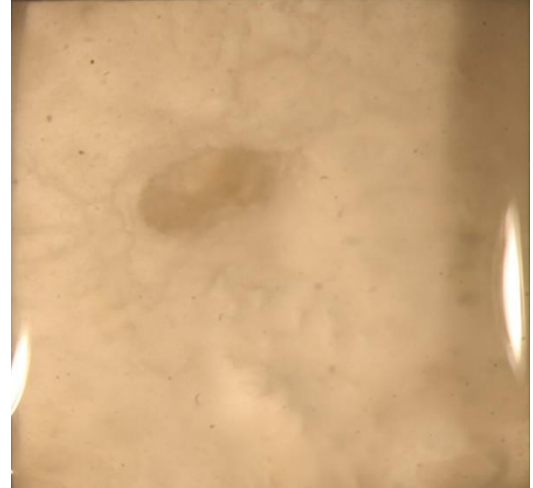
K1	 Micrograph showing a dense, granular, light brown material with small, irregular particles and some bright spots.	 Micrograph showing a smoother, light brown surface with a few bright spots and small dark inclusions.
K2	 Micrograph showing a dense, granular, light brown material with small, irregular particles and some bright spots.	 Micrograph showing a smoother, light brown surface with a few bright spots and small dark inclusions.
K3	 Micrograph showing a dense, granular, light brown material with small, irregular particles and some bright spots.	 Micrograph showing a smoother, light brown surface with a few bright spots and small dark inclusions.

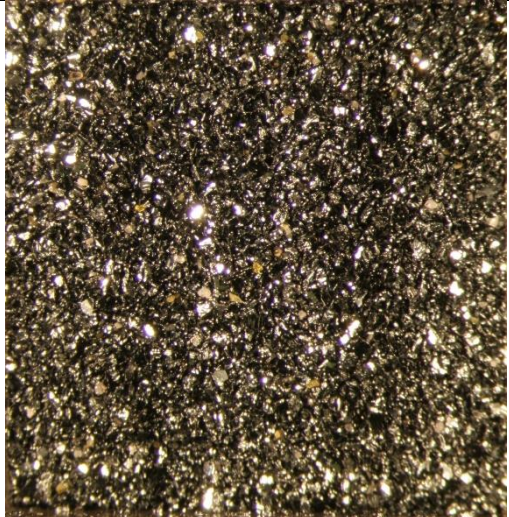
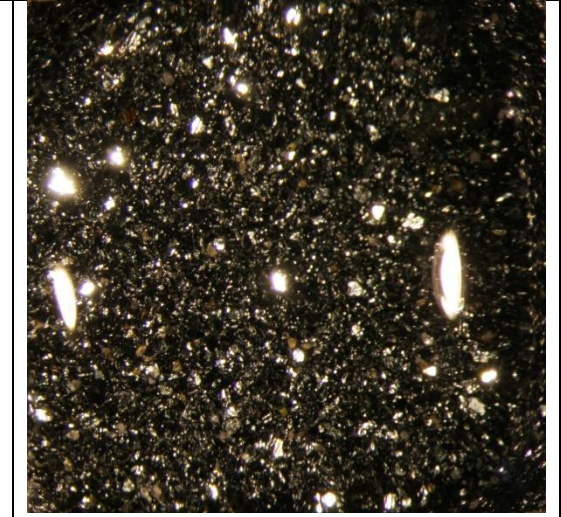
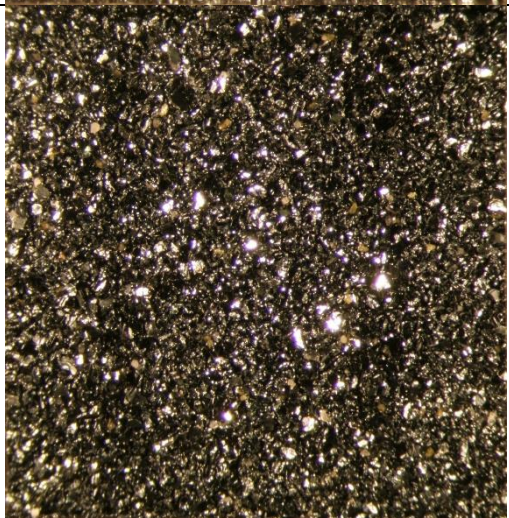
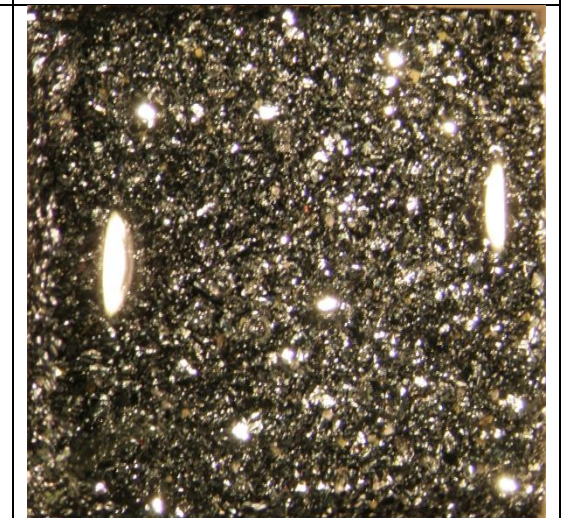
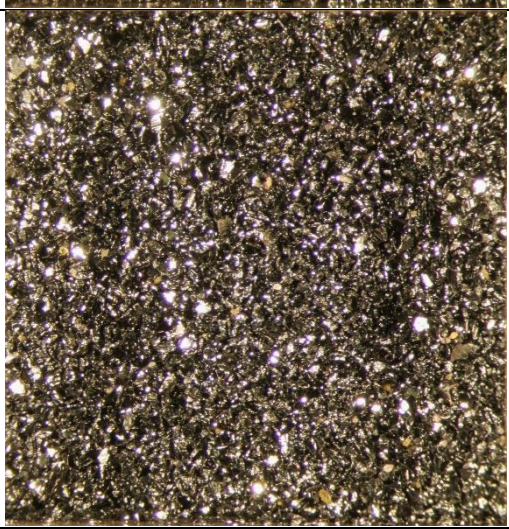
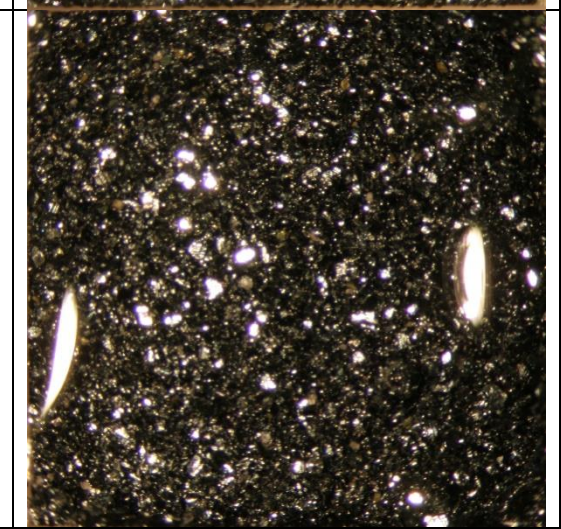





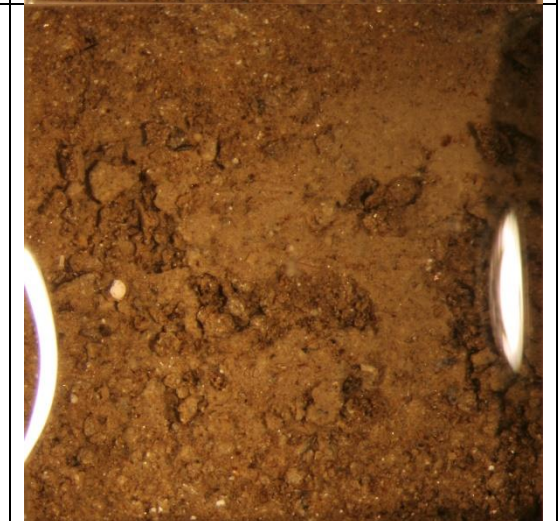


Q1		
Q2		
Q3		


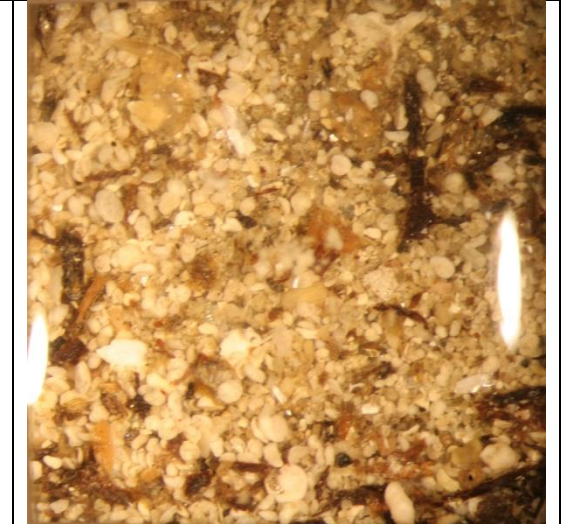




Cs1	 Microscopic view of a light-colored, granular material with small, dark, irregular inclusions. The texture appears somewhat crystalline or fibrous.	 Microscopic view of a light-colored, granular material with small, dark, irregular inclusions. The texture appears somewhat crystalline or fibrous.
Cs2	 Microscopic view of a light-colored, granular material with small, dark, irregular inclusions. The texture appears somewhat crystalline or fibrous.	 Microscopic view of a light-colored, granular material with small, dark, irregular inclusions. The texture appears somewhat crystalline or fibrous.
Cs3	 Microscopic view of a light-colored, granular material with small, dark, irregular inclusions. The texture appears somewhat crystalline or fibrous.	 Microscopic view of a light-colored, granular material with small, dark, irregular inclusions. The texture appears somewhat crystalline or fibrous.



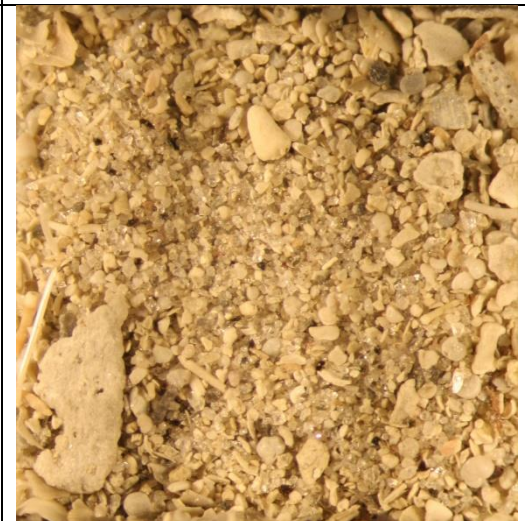
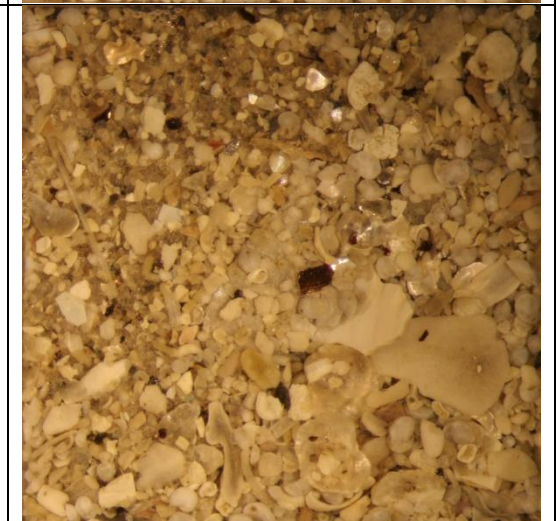

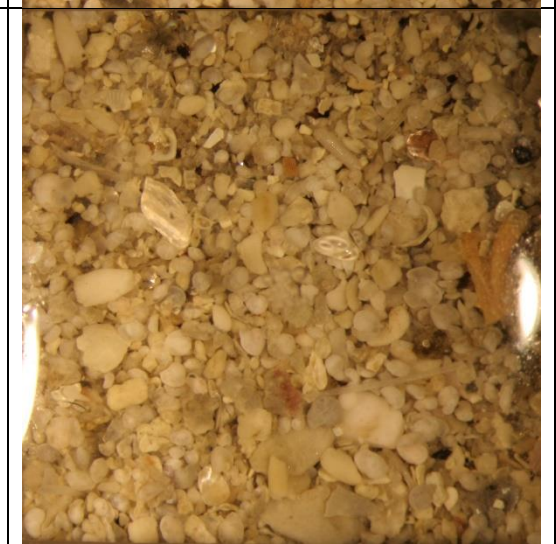
Cc1	 Micrograph showing a dense, granular, light-colored material with irregular, interconnected particles.	 Micrograph showing a smooth, light-colored surface with a vertical light reflection on the right side.
Cc2	 Micrograph showing a dense, granular, light-colored material with irregular, interconnected particles.	 Micrograph showing a smooth, light-colored surface with a vertical light reflection on the right side.
Cc3	 Micrograph showing a dense, granular, light-colored material with irregular, interconnected particles.	 Micrograph showing a smooth, light-colored surface with a vertical light reflection on the right side.

Cp1	 Micrograph showing a highly textured, porous surface with irregular, interconnected features, characteristic of a foamed or granular material.	 Micrograph showing a smoother, more uniform surface texture with subtle variations in tone, possibly representing a different layer or a different view of the same material.
Cp2	 Micrograph showing a textured surface with a distinct vertical channel or groove running through the center, surrounded by porous, irregular features.	 Micrograph showing a smooth surface with a prominent, dark, oval-shaped feature or inclusion, possibly a defect or a specific component.
Cp3	 Micrograph showing a textured surface with a vertical channel or groove, similar to Cp2, but with a slightly different internal structure or depth.	 Micrograph showing a smooth surface with a dark, oval-shaped feature, similar to Cp2, but with a different surrounding texture or color.

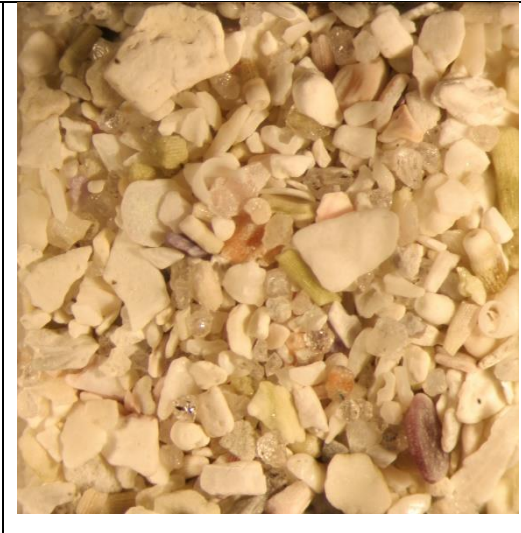





H1		
H2		
H3		





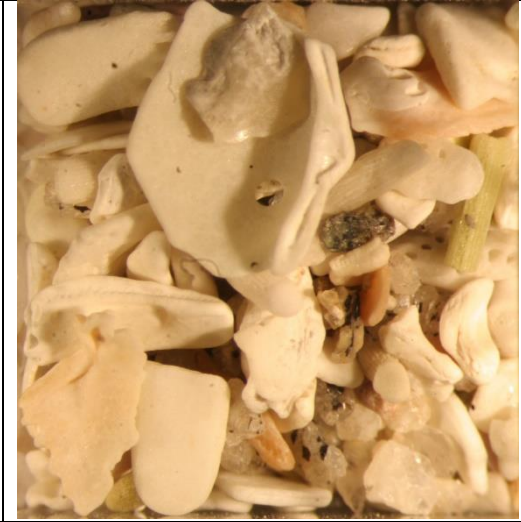

OM1		
OM2		
OM3		


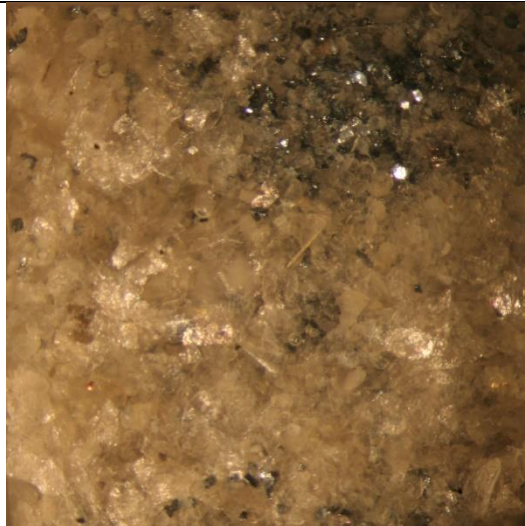
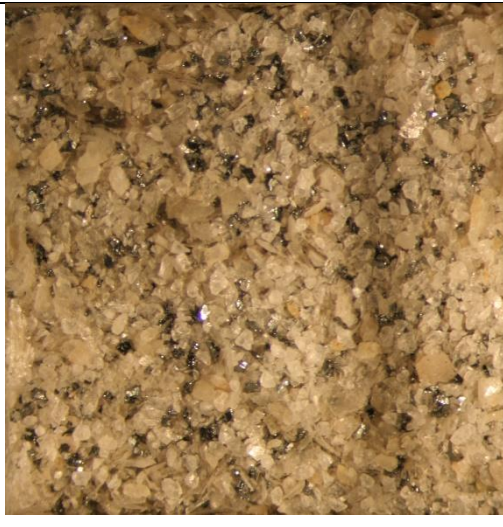
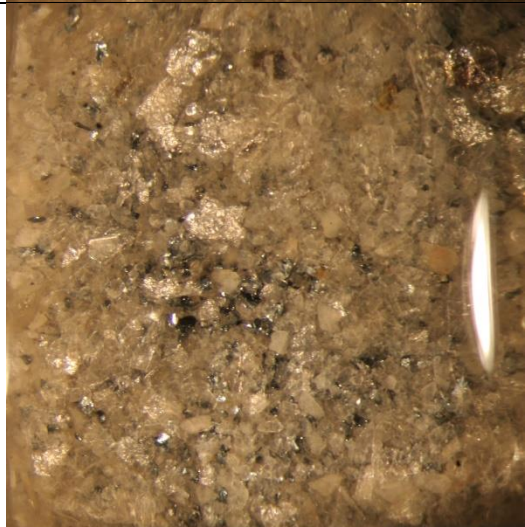

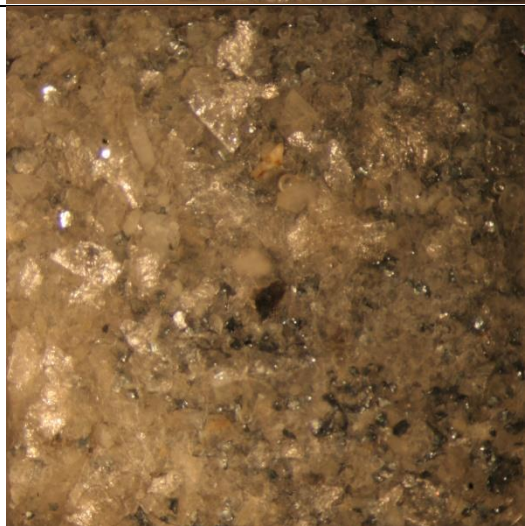
FS1		
FS2		
FS3		


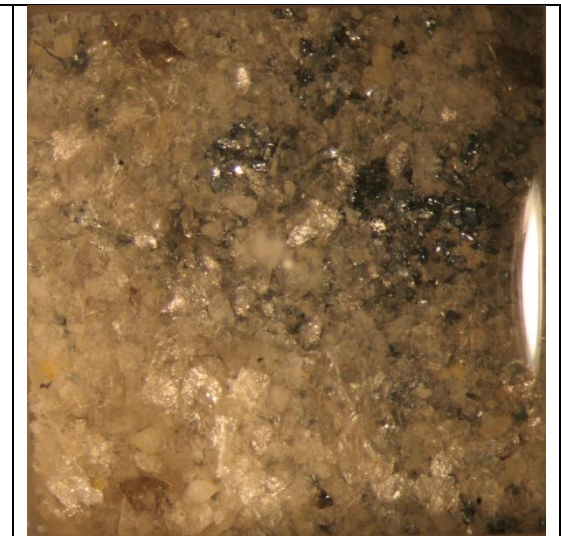
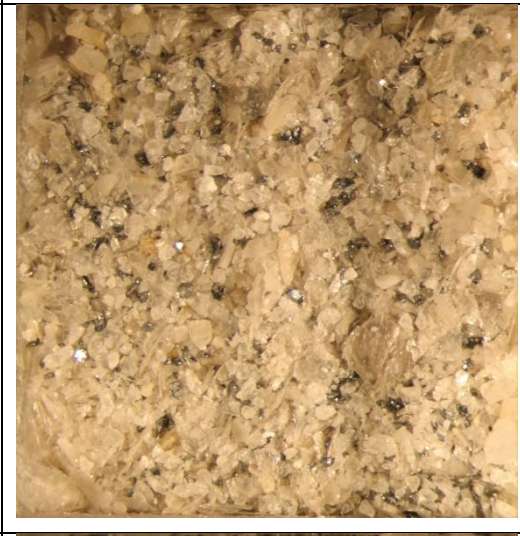
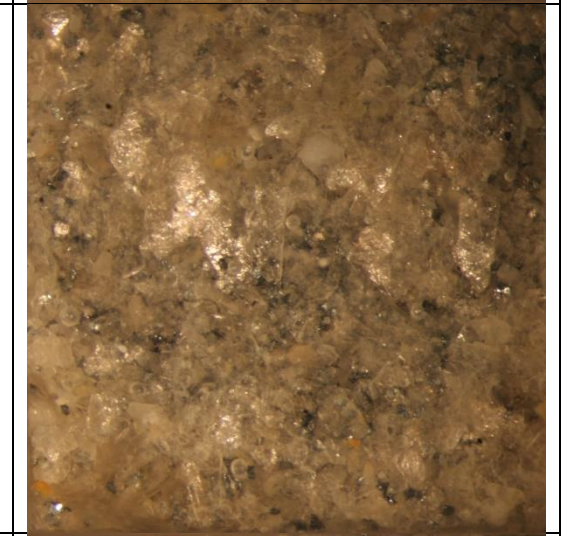

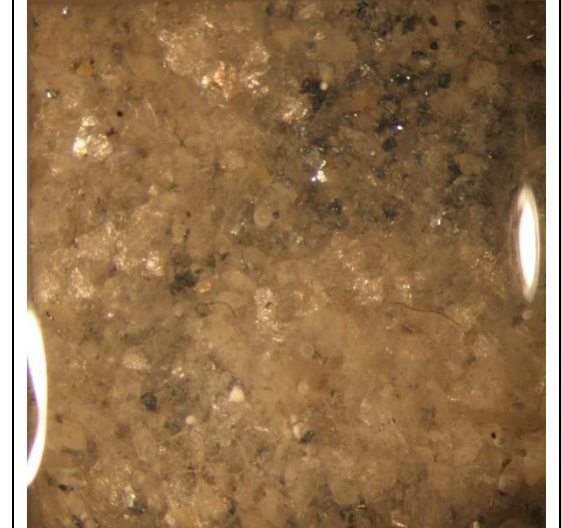
MS1	 Micrograph showing a dense distribution of small, light-colored, angular particles, likely shell fragments, embedded in a darker, finer matrix. The particles vary in size and shape, with some appearing as thin, flat flakes.	 Micrograph showing a dense distribution of small, light-colored, angular particles, likely shell fragments, embedded in a darker, finer matrix. The particles are more uniform in size compared to the left view.
MS2	 Micrograph showing a dense distribution of small, light-colored, angular particles, likely shell fragments, embedded in a darker, finer matrix. A larger, more irregularly shaped fragment is visible on the left side.	 Micrograph showing a dense distribution of small, light-colored, angular particles, likely shell fragments, embedded in a darker, finer matrix. The particles are more uniform in size compared to the left view.
MS3	 Micrograph showing a dense distribution of small, light-colored, angular particles, likely shell fragments, embedded in a darker, finer matrix. A larger, more irregularly shaped fragment is visible in the upper center.	 Micrograph showing a dense distribution of small, light-colored, angular particles, likely shell fragments, embedded in a darker, finer matrix. The particles are more uniform in size compared to the left view.


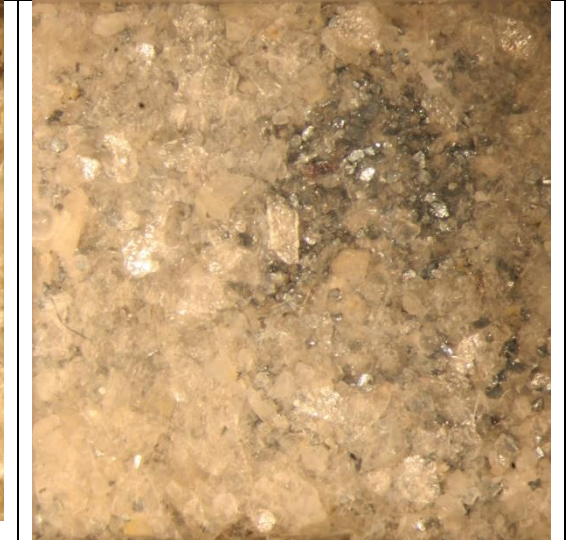
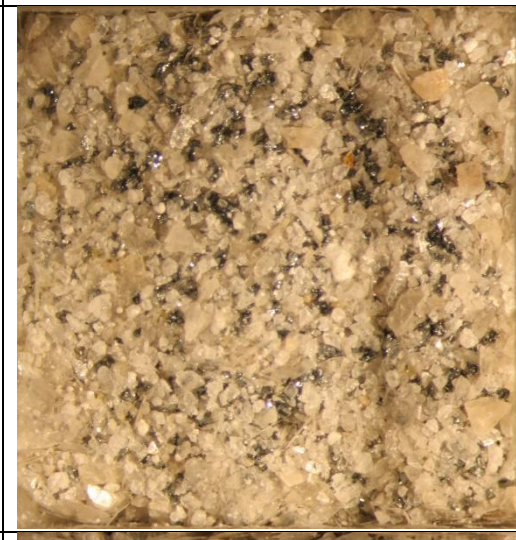
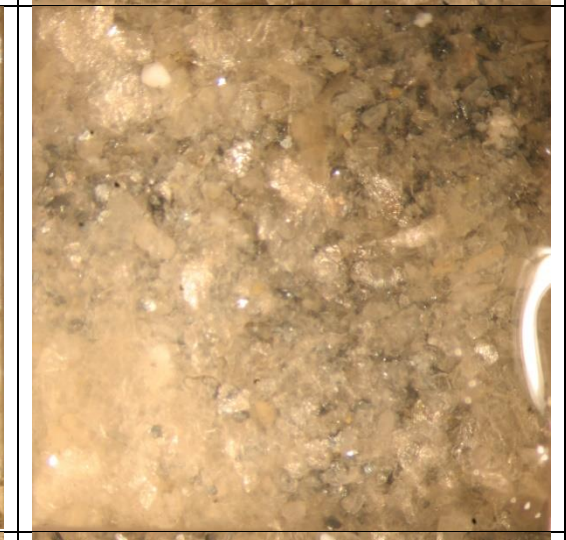
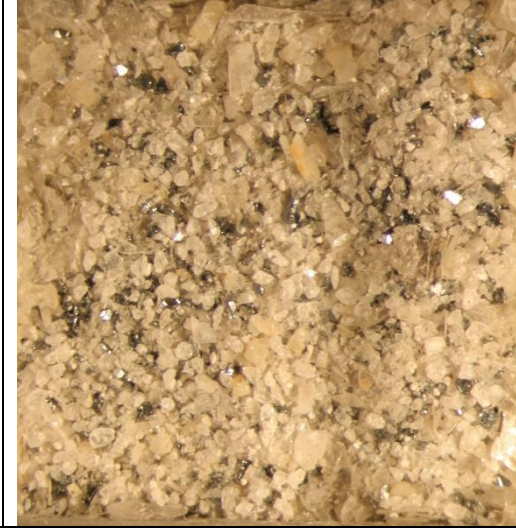



SS1	 Photomicrograph of sediment sample SS1, left view. The image shows a dense collection of small, angular, light-colored grains, likely quartz and feldspar, with some darker, possibly organic or mineral inclusions.
	 Photomicrograph of sediment sample SS1, right view. This view shows a similar composition of light-colored grains, but with a slightly different arrangement and some larger, more irregularly shaped particles.
SS2	 Photomicrograph of sediment sample SS2, left view. The grains are predominantly light-colored and angular, with some reddish-brown and yellowish inclusions scattered throughout.
	 Photomicrograph of sediment sample SS2, right view. This view highlights a prominent reddish-brown elongated grain in the center, surrounded by other light-colored angular grains.
SS3	 Photomicrograph of sediment sample SS3, left view. This sample contains larger, more rounded grains compared to SS1 and SS2, including a prominent reddish-brown grain and a dark, irregularly shaped grain.
	 Photomicrograph of sediment sample SS3, right view. This view shows a dark, elongated grain in the lower-left quadrant, surrounded by other light-colored grains.

SG1		
SG2		
SG3		

0%A	 Micrograph showing a dense, granular material with a light tan to beige color. The surface is highly textured with numerous small, irregular particles and some darker, possibly carbonaceous, inclusions.	 Micrograph showing a similar granular material to the left view, but with a darker, more brownish-tan hue. The texture is less uniform, with some larger, more distinct particles and a higher concentration of dark inclusions.
0%B	 Micrograph showing a granular material with a light tan to beige color, similar to 0%A. The texture is dense and irregular, with many small particles and some dark inclusions.	 Micrograph showing a granular material with a darker, brownish-tan hue, similar to 0%A. The texture is dense and irregular, with many small particles and some dark inclusions. A prominent, bright, vertical streak is visible on the right side of the image.
0%C	 Micrograph showing a granular material with a light tan to beige color, similar to 0%A. The texture is dense and irregular, with many small particles and some dark inclusions.	 Micrograph showing a granular material with a darker, brownish-tan hue, similar to 0%A. The texture is dense and irregular, with many small particles and some dark inclusions.

0.5%A	 Micrograph showing a dense, granular material with a light tan to brown color. The texture is highly irregular and porous, with many small, dark, angular particles dispersed throughout the matrix. A prominent, bright, rectangular feature is visible near the top center.	 Micrograph showing a dense, granular material with a light tan to brown color. The texture is highly irregular and porous, with many small, dark, angular particles dispersed throughout the matrix. A bright, curved feature is visible on the right side.
0.5%B	 Micrograph showing a dense, granular material with a light tan to brown color. The texture is highly irregular and porous, with many small, dark, angular particles dispersed throughout the matrix.	 Micrograph showing a dense, granular material with a light tan to brown color. The texture is highly irregular and porous, with many small, dark, angular particles dispersed throughout the matrix. A bright, curved feature is visible on the right side.
0.5%C	 Micrograph showing a dense, granular material with a light tan to brown color. The texture is highly irregular and porous, with many small, dark, angular particles dispersed throughout the matrix.	 Micrograph showing a dense, granular material with a light tan to brown color. The texture is highly irregular and porous, with many small, dark, angular particles dispersed throughout the matrix. A bright, curved feature is visible on the right side.

1%A	 Micrograph showing soil particles with a light tan matrix and dark, irregular inclusions.	 Micrograph showing soil particles with a light tan matrix and dark, irregular inclusions, similar to the left view.
1%B	 Micrograph showing soil particles with a light tan matrix and dark, irregular inclusions.	 Micrograph showing soil particles with a light tan matrix and dark, irregular inclusions, similar to the left view.
1%C	 Micrograph showing soil particles with a light tan matrix and dark, irregular inclusions.	 Micrograph showing soil particles with a light tan matrix and dark, irregular inclusions, similar to the left view.

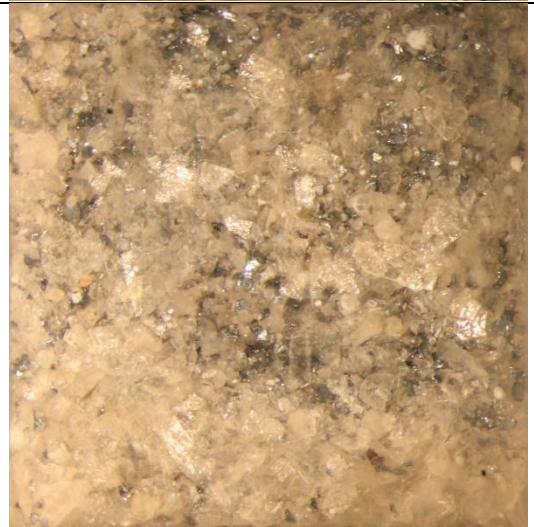
2%A


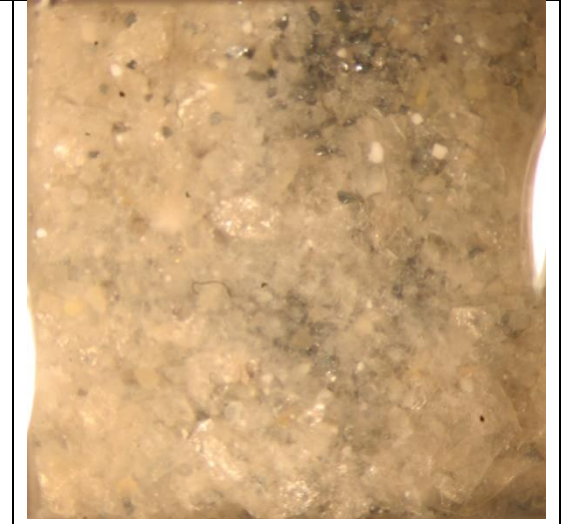
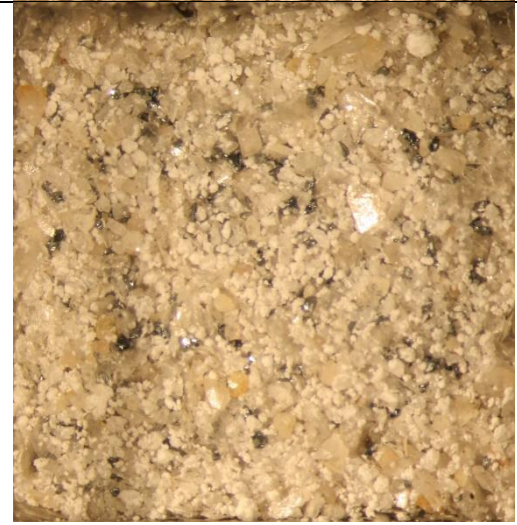


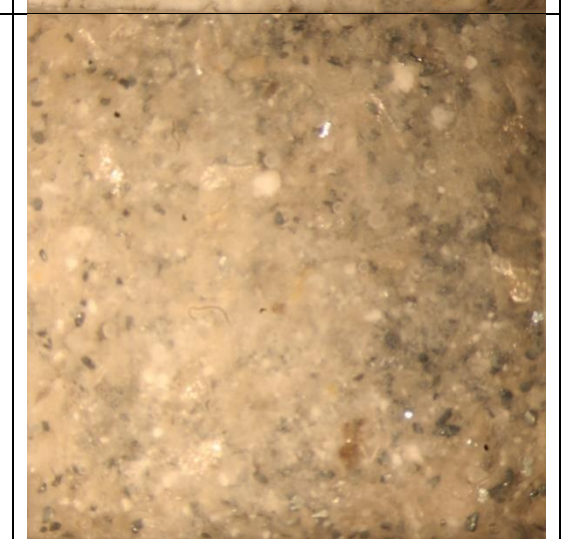


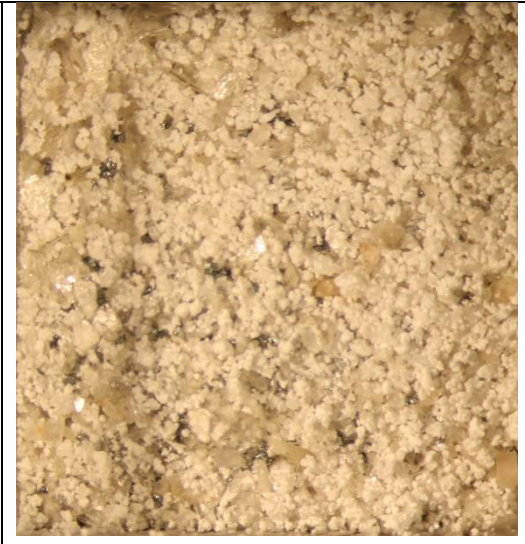
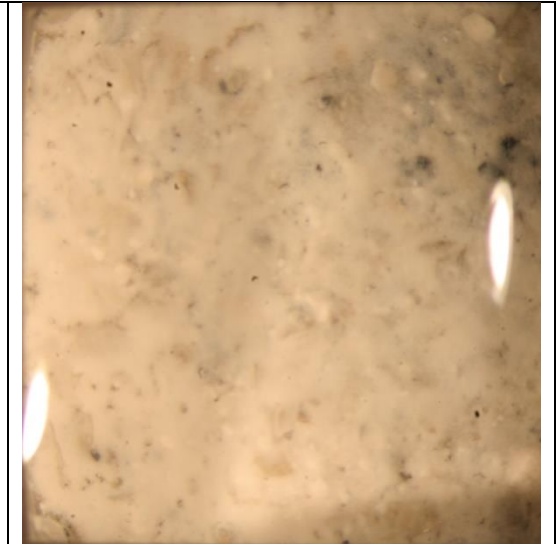

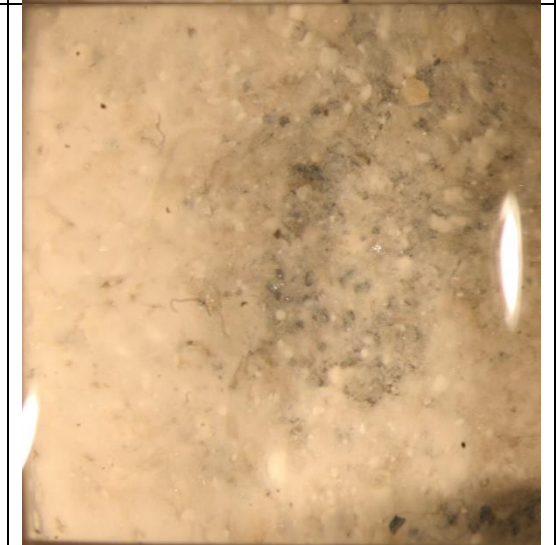

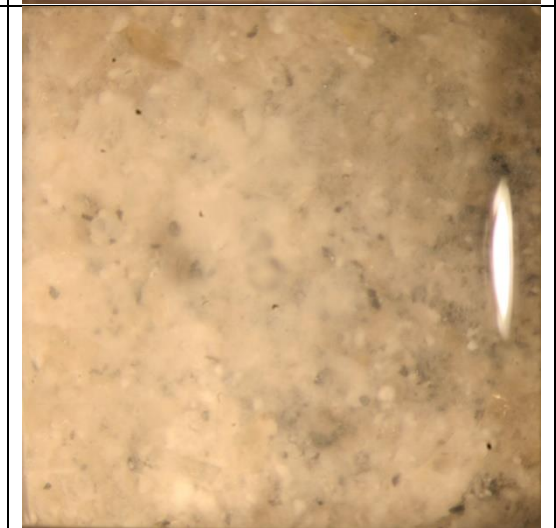
2%B




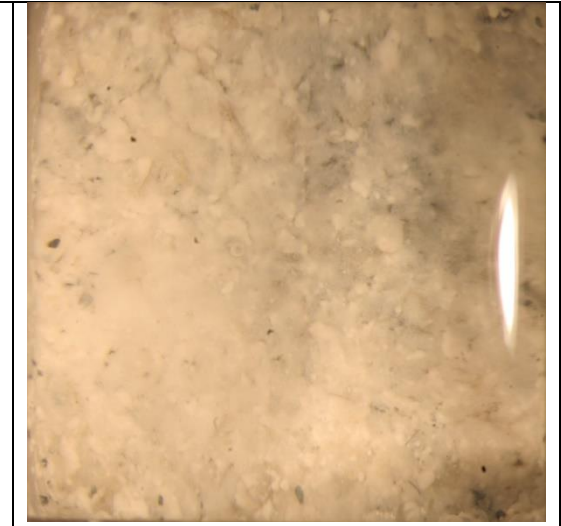


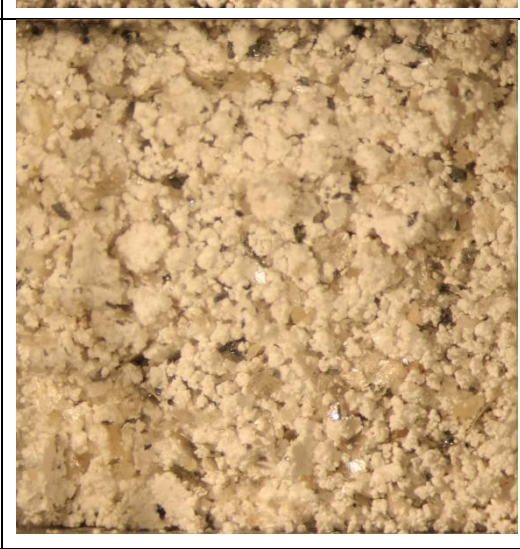
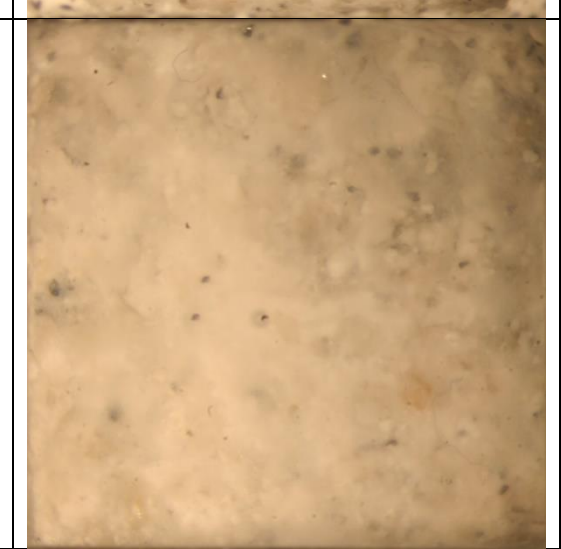
2%C


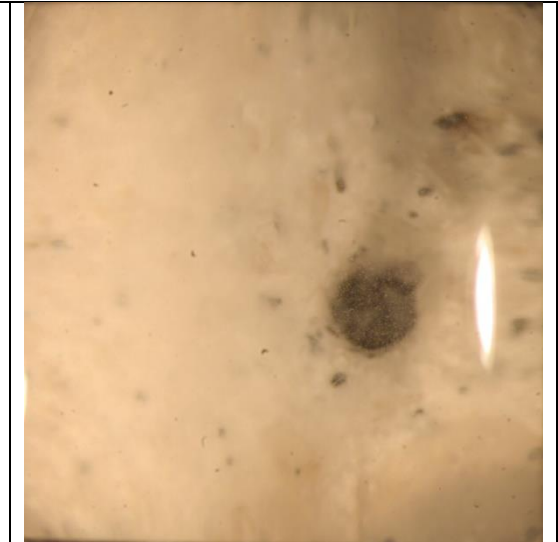

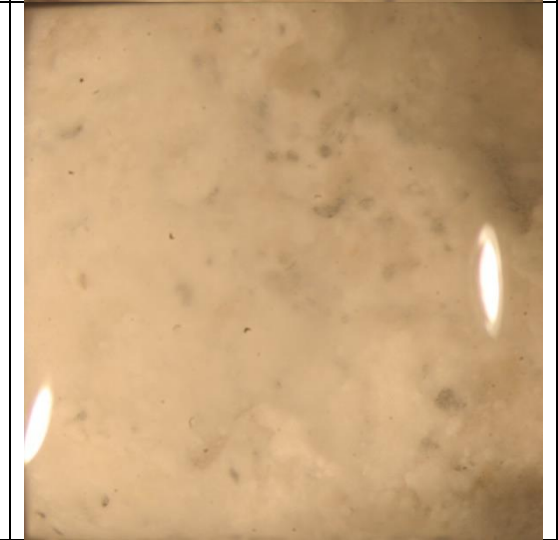

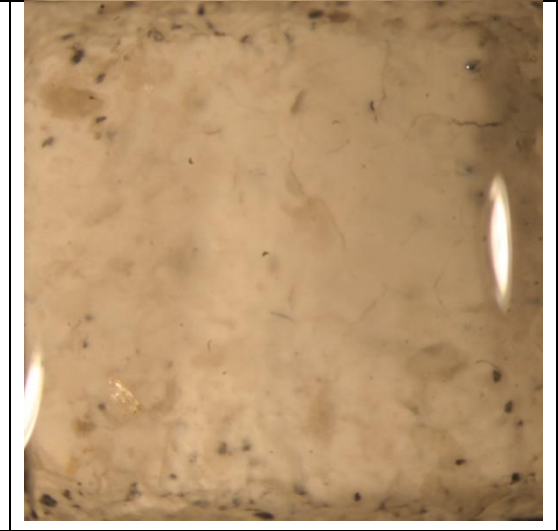


4%A	 Micrograph showing a granular, light brown material with numerous small, dark, irregularly shaped particles dispersed throughout. The texture appears somewhat porous and uneven.	 Micrograph showing a similar granular material to the left view, but with a more uniform, slightly smoother appearance. The dark particles are still present but appear less densely packed.
4%B	 Micrograph showing a granular, light brown material with numerous small, dark, irregularly shaped particles dispersed throughout. The texture appears somewhat porous and uneven.	 Micrograph showing a similar granular material to the left view, but with a more uniform, slightly smoother appearance. The dark particles are still present but appear less densely packed.
4%C	 Micrograph showing a granular, light brown material with numerous small, dark, irregularly shaped particles dispersed throughout. The texture appears somewhat porous and uneven.	 Micrograph showing a similar granular material to the left view, but with a more uniform, slightly smoother appearance. The dark particles are still present but appear less densely packed.

10%A	 Micrograph showing a dense, granular, light brown material with small dark inclusions, likely a composite or mineral aggregate.	 Micrograph showing a smoother, more uniform light brown surface with a vertical light streak on the right side, possibly a different view or a polished surface of the same material.
10%B	 Micrograph showing a dense, granular, light brown material with small dark inclusions, similar to 10%A.	 Micrograph showing a smoother, more uniform light brown surface with a vertical light streak on the right side, similar to 10%A.
10%C	 Micrograph showing a dense, granular, light brown material with small dark inclusions, similar to 10%A.	 Micrograph showing a smoother, more uniform light brown surface with a vertical light streak on the right side, similar to 10%A.

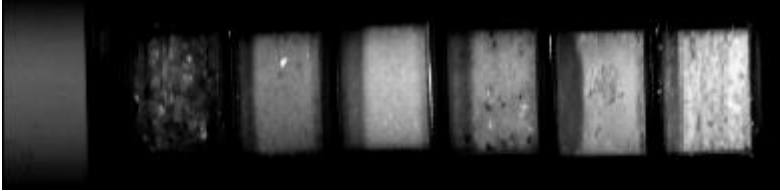

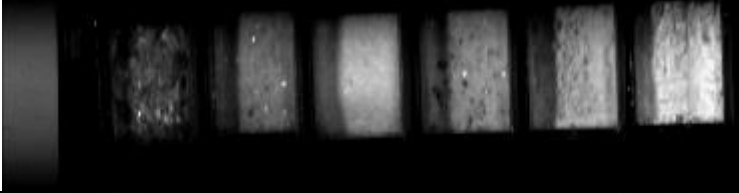



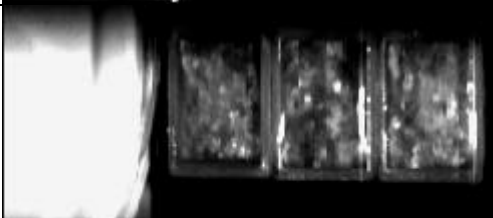


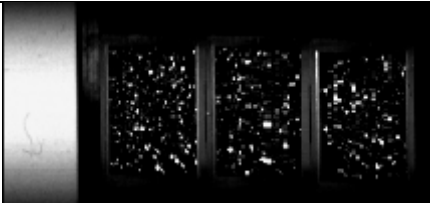

25%A		
25%B		
25%C		

50%A		
50%B		
50%C		

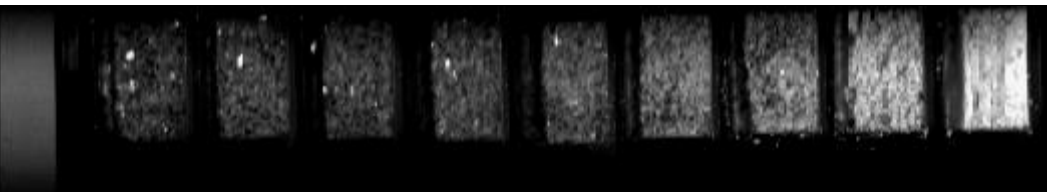
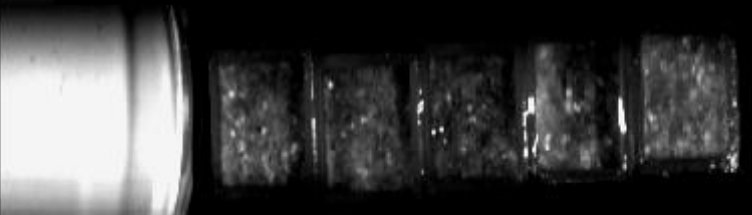

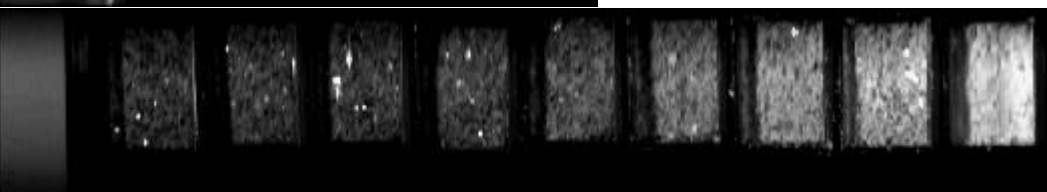
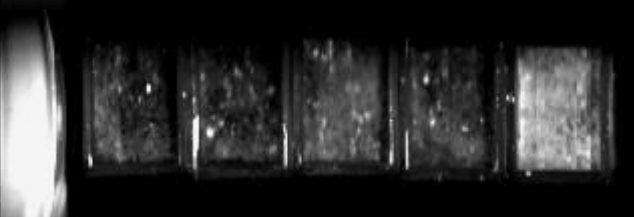
## Appendix B – Hyperspectral images

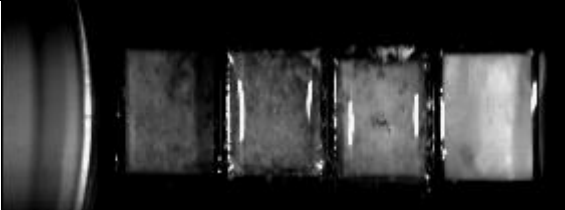
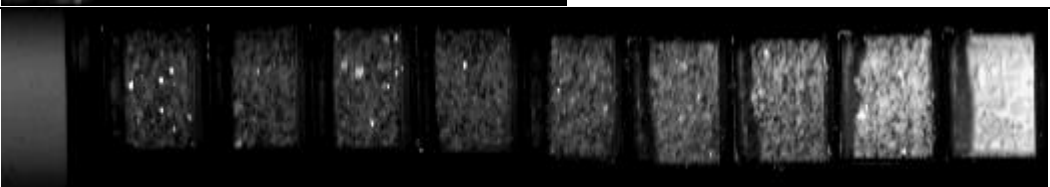
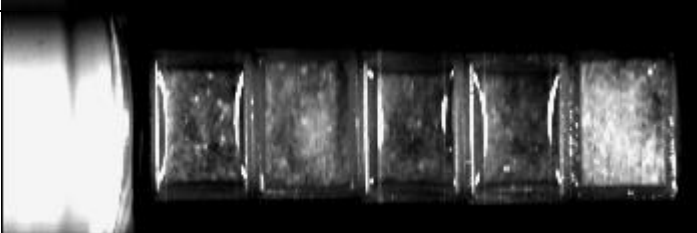

*Table B.1 Monochromatic images of mineral samples. Scale of images: cuvette samples are 10\*10 mm. The reference plate is seen to the left in the images.*

<b>Minerals</b>	
Set 1 (dry) at 590 nm	
Set 1 (w) at 570 nm	
Set 2 (dry) at 590 nm	
Set 2 (w) at 570 nm	
Set 3 (dry) at 590 nm	
Set 3 (w) at 570 nm	
Muscovite (set 1, set 2 and set 3) at 570 nm (w)	

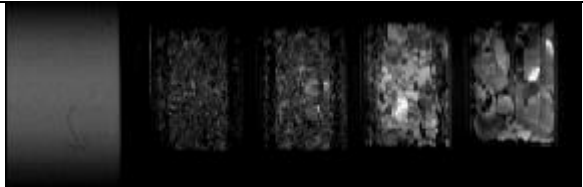
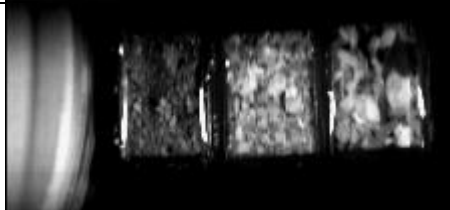
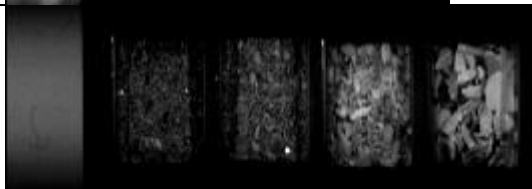
Hematite (set 1, set 2 and set 3) at 640 nm (dry)	
Hematite (set 1, set 2 and set 3) at 570 nm (w)	

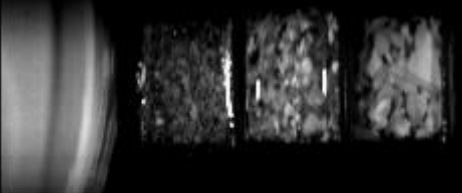

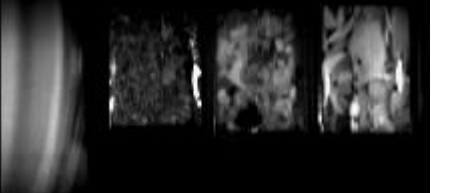


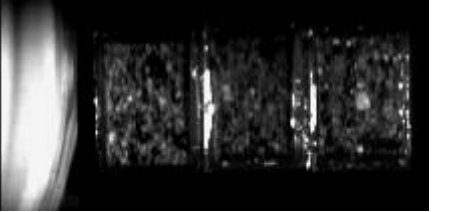
**Table B.2** Monochromatic images of the artificial sediment samples. Scale of images: cuvette samples are 10\*10 mm.

<b>Artificial sediments</b>	
Set A at 570 nm (dry)	
Set A at 570 nm (w)	
Set A at 570 nm (w)	
Set B at 570 nm (dry)	
Set B at 570 nm (w)	




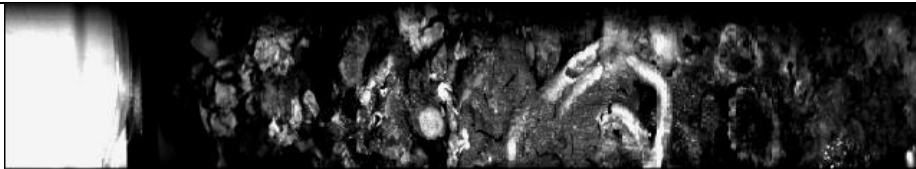
Set B at 570 nm (w)		
Set C at 570 nm (dry)		
Set C at 570 nm (w)		
Set C at 570 nm (w)		

**Table B.3** Monochromatic images of natural sediment samples. Scale of images: cuvette samples are 10\*10 mm.

<b>Natural sediments</b>		
Set 1 at 640 nm (dry)		
Set 1 at 570 nm (w)		
Set 2 at 640 nm (dry)		

Set 2 at 570 nm (w)		
Set 3 at 640 nm (dry)		
Set 3 at 570 nm (w)		
OM (set 1, set 2 and set 3) at 590 nm (dry)		
OM (set 1, set 2 and set 3) at 570 nm (w)		
Fine sand (set 1, set 2 and set 3) at 570 nm (w)		

**Table B.4** Monochromatic images of carbonate crust samples. Scale of images: height of the images are approx. 12 mm.

<b>Carbonate crusts</b>	
Fresh surface at 570 nm (dry)	
Fresh surface at 570 nm (w)	
Original surface at 570 nm (dry)	
Original surface at 570 nm (w)	





## **Appendix C – HI spectra of each sample**

Reflectance spectra from HI measurements used in the estimation of the mean spectra of each sample are presented in:

Table C.1 – Minerals (except hematite, which is shown in the results)

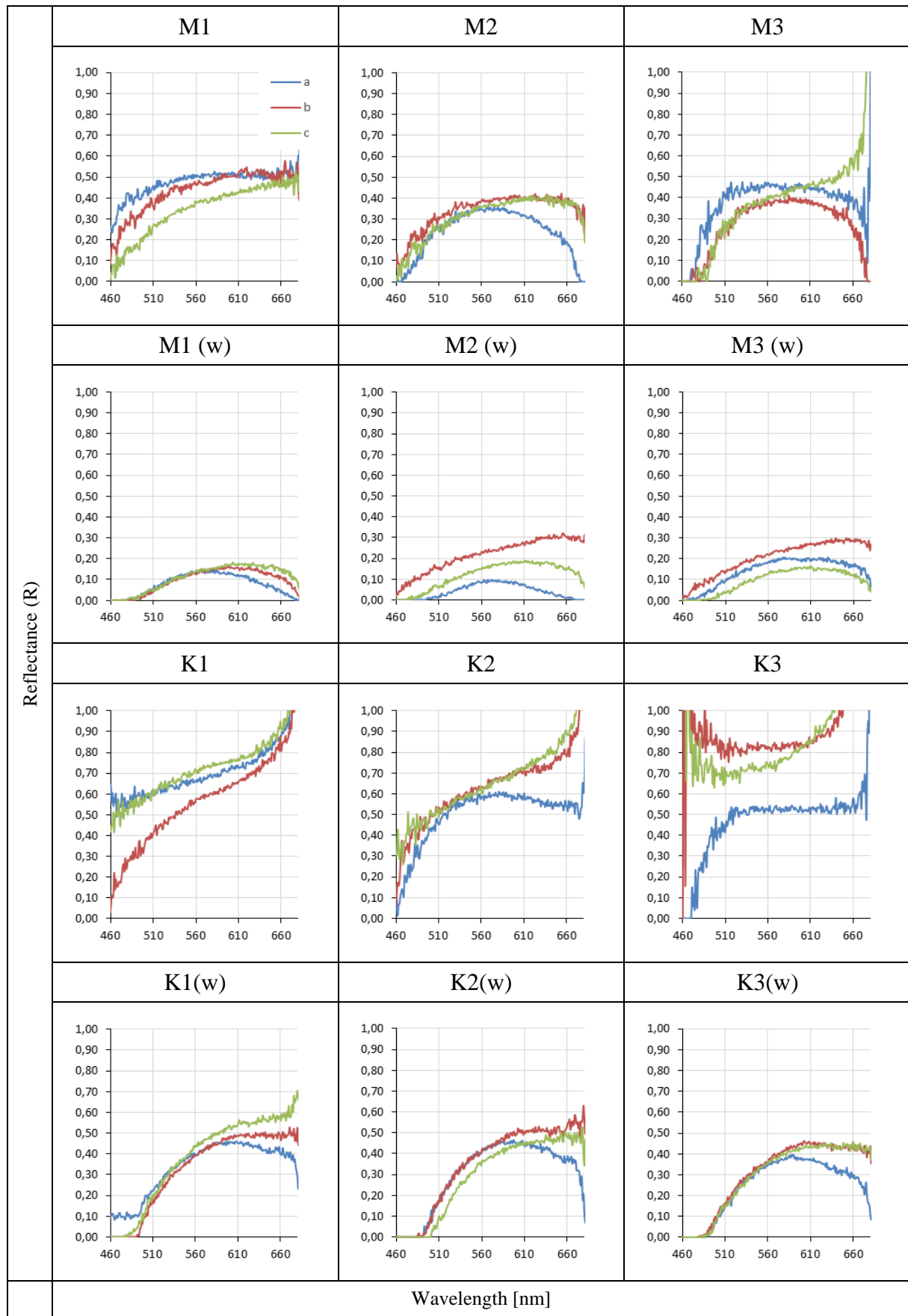
Table C.2 – Artificial sediments

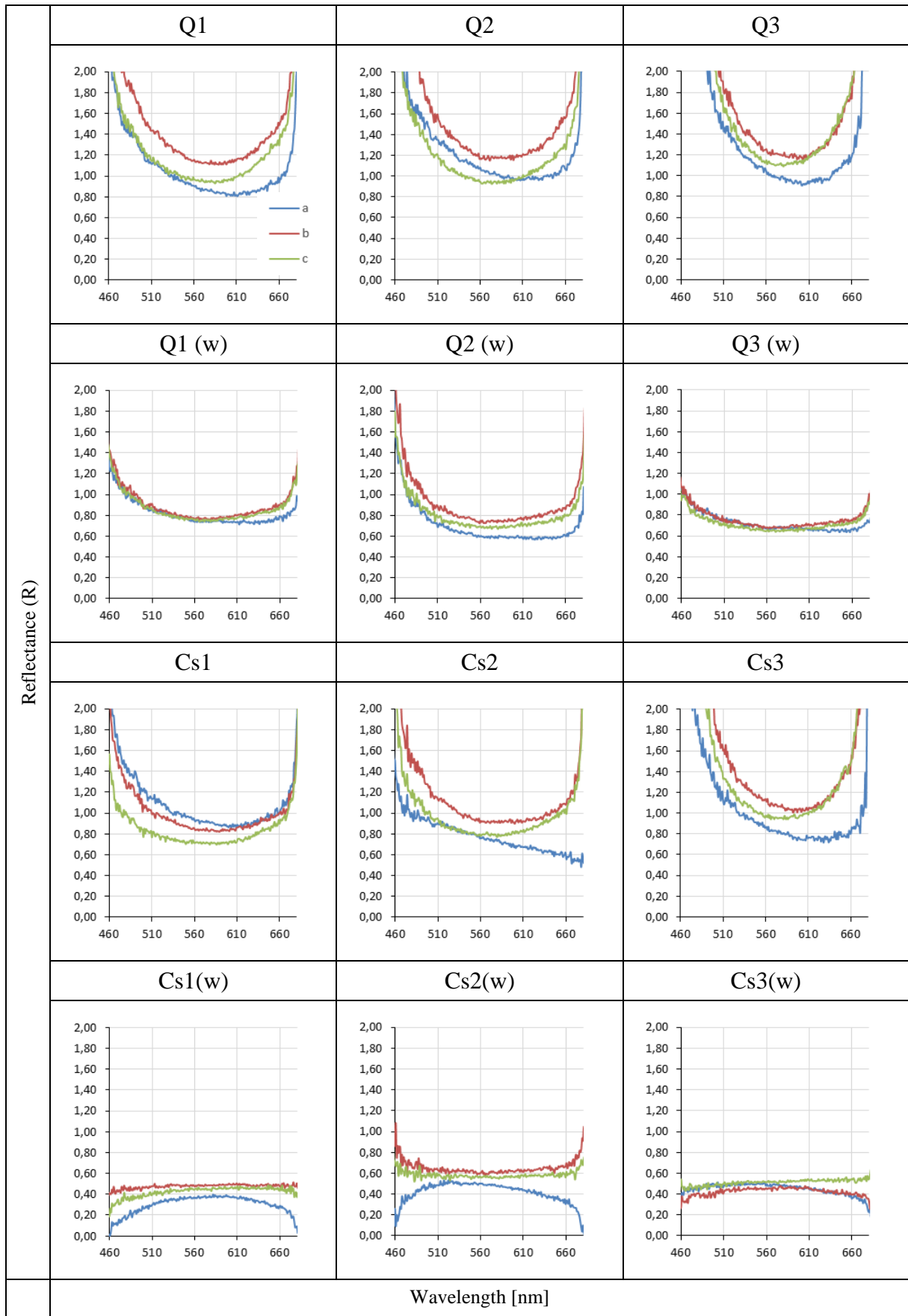
Table C.3 – Natural samples

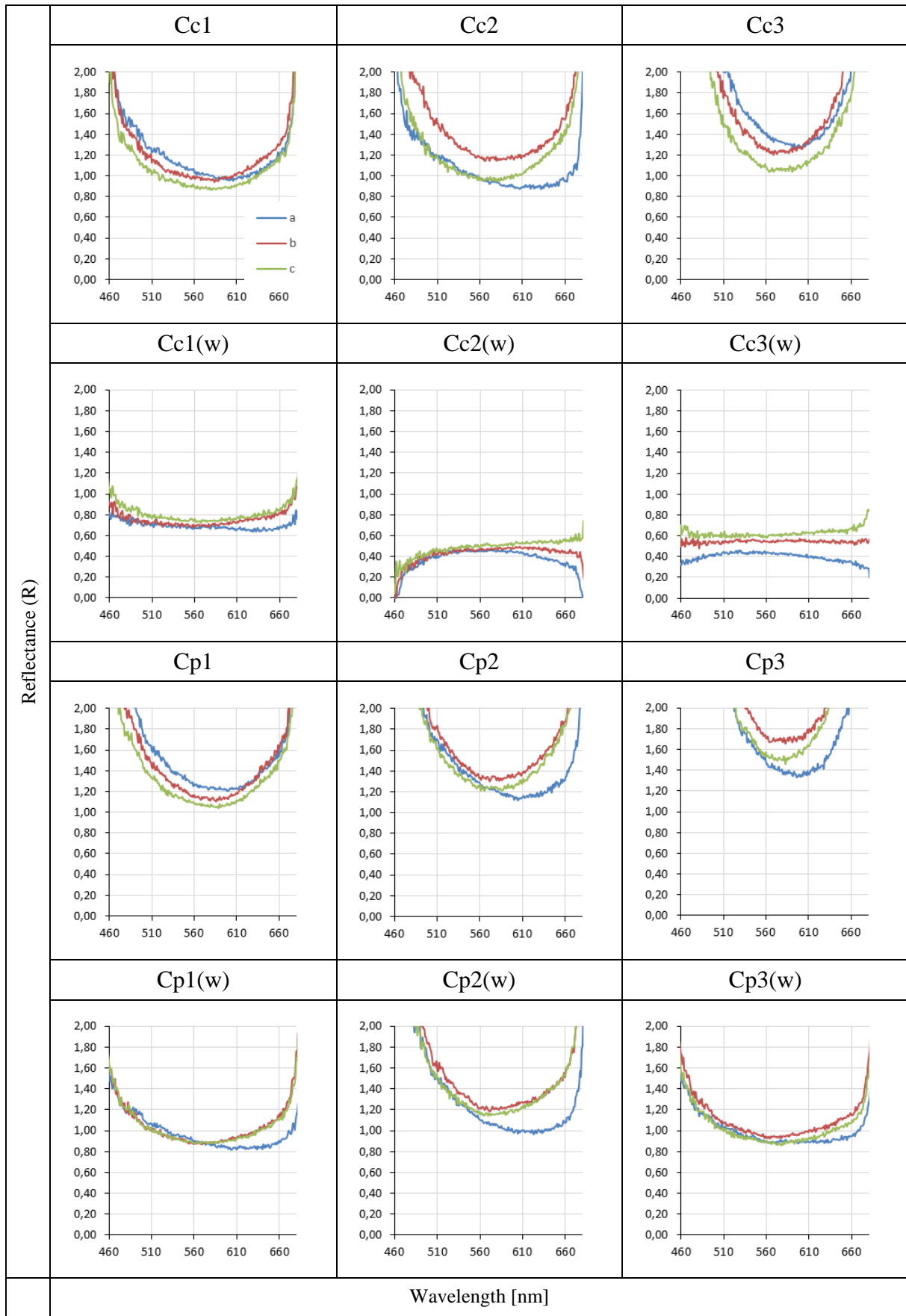
Table C.4 – Carbonate crusts

*a*, *b* and *c* spectra in each sample represent spectra from three different areas of sample surface.

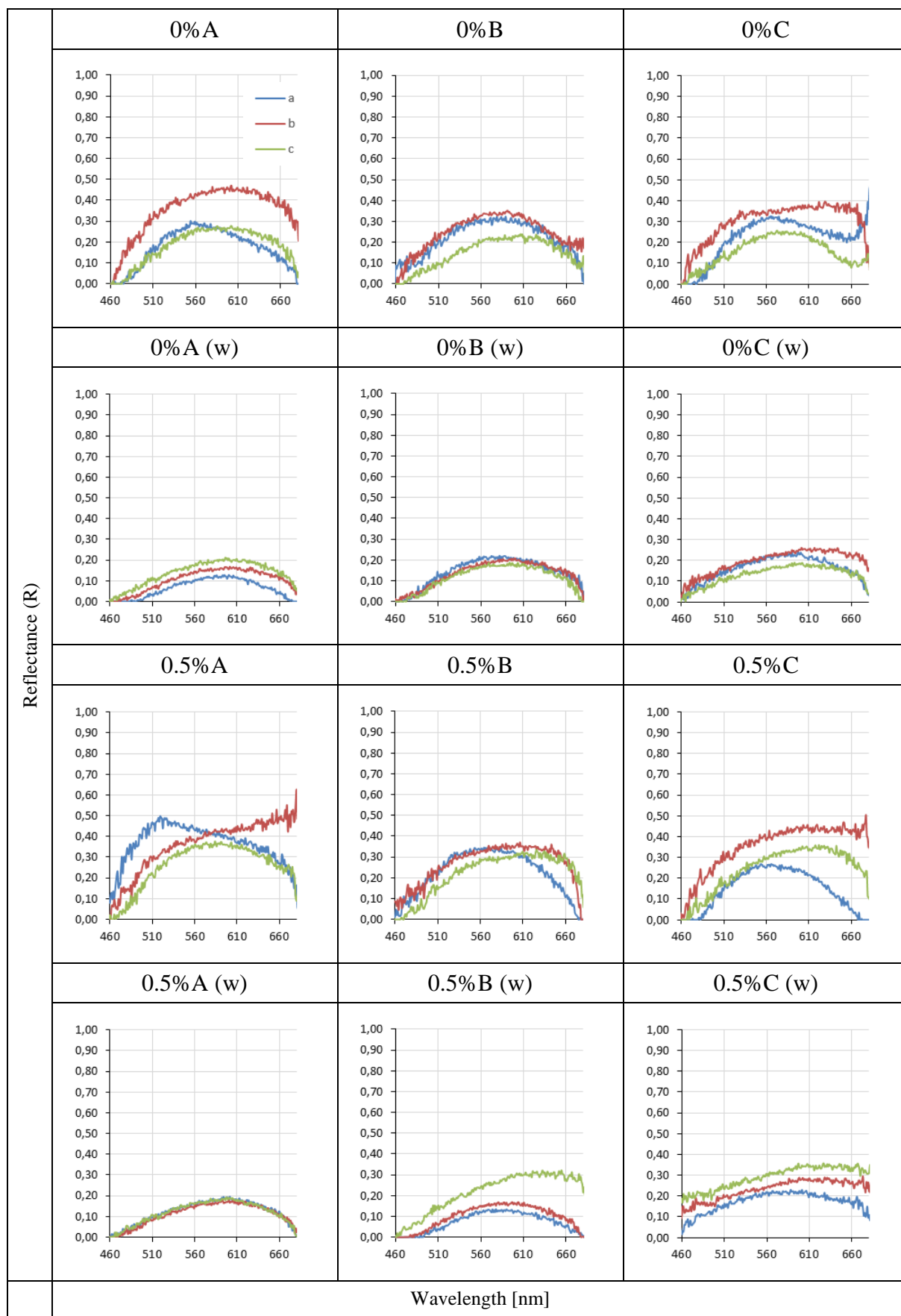
**Table C.1** Mineral samples

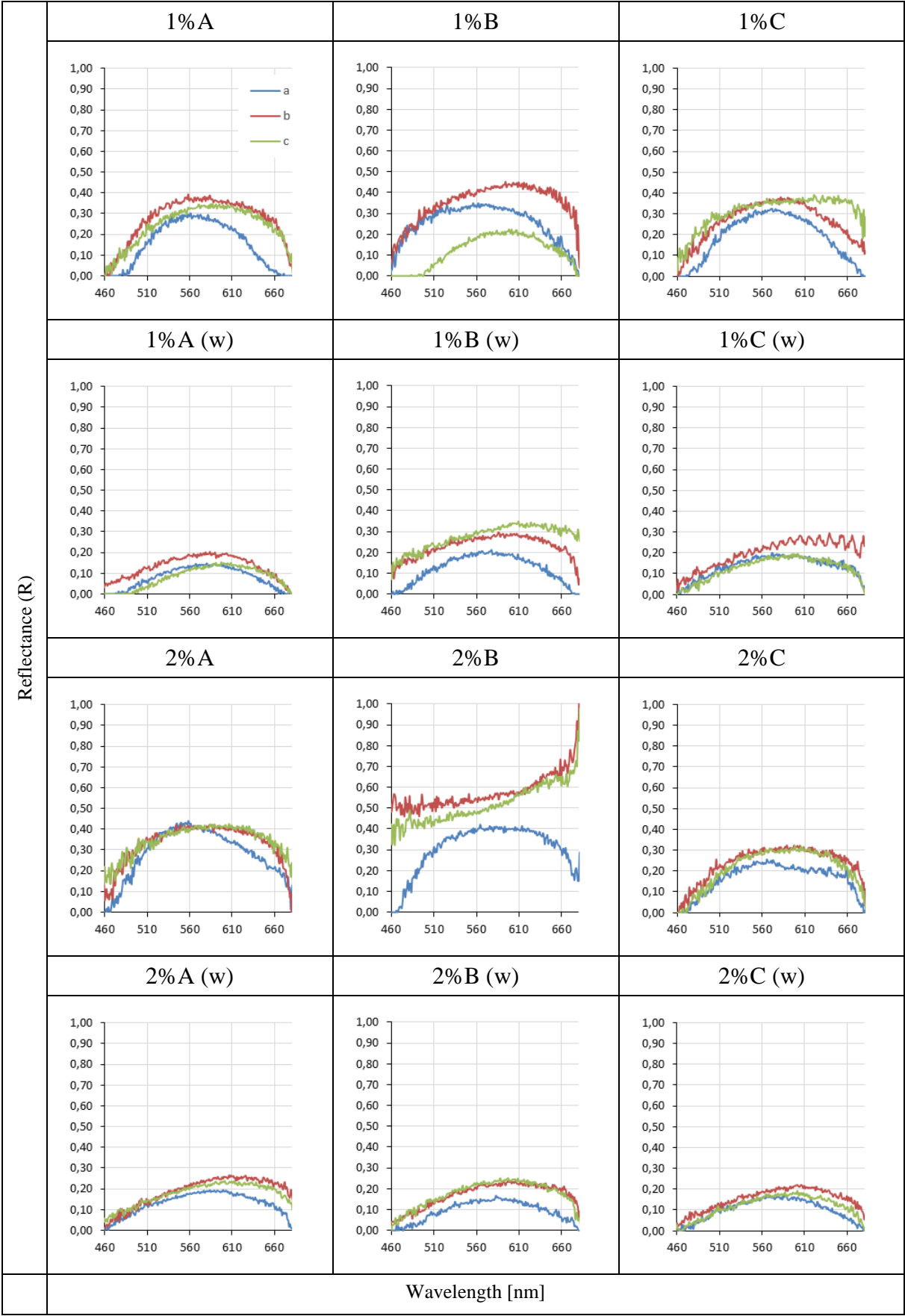


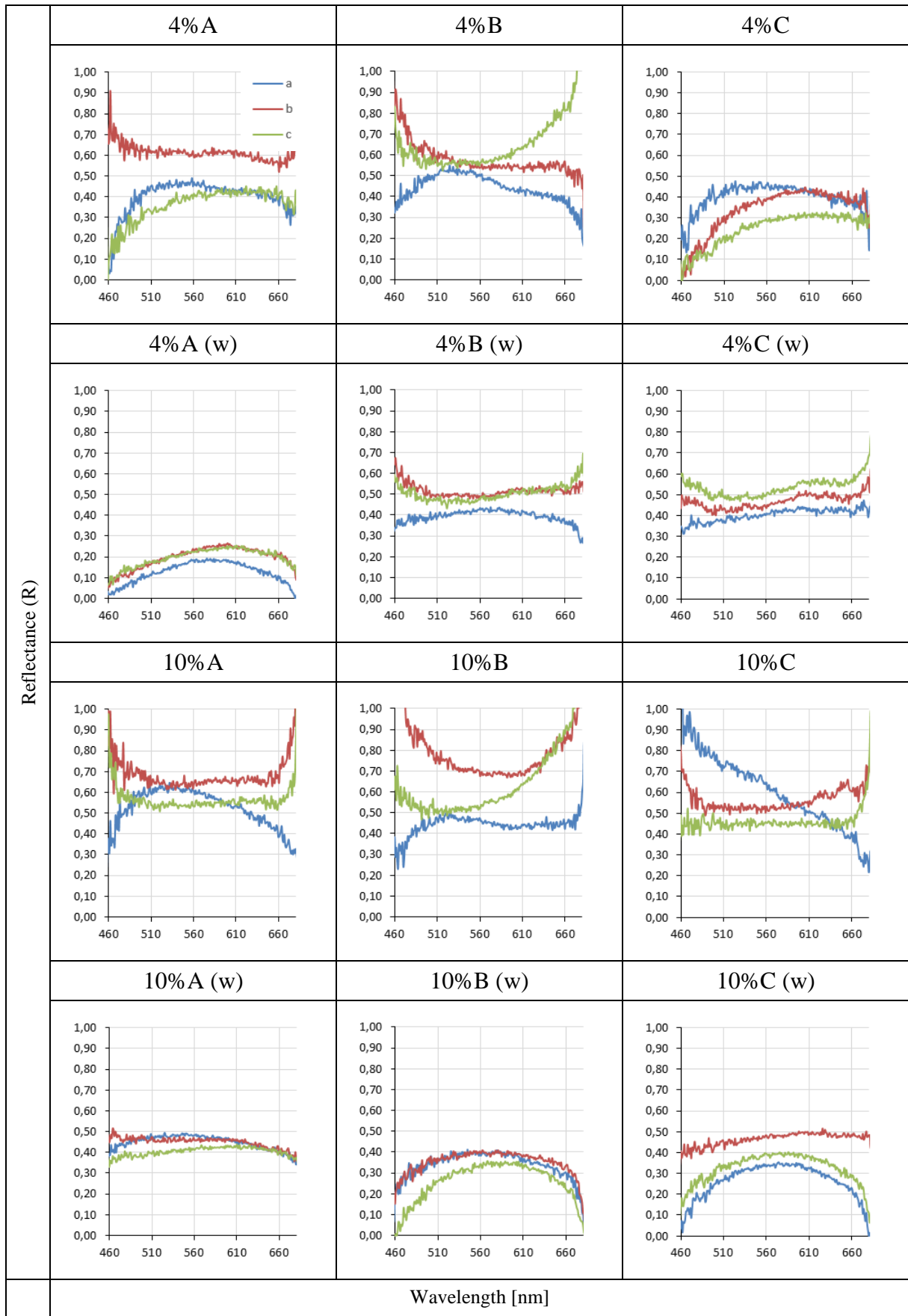


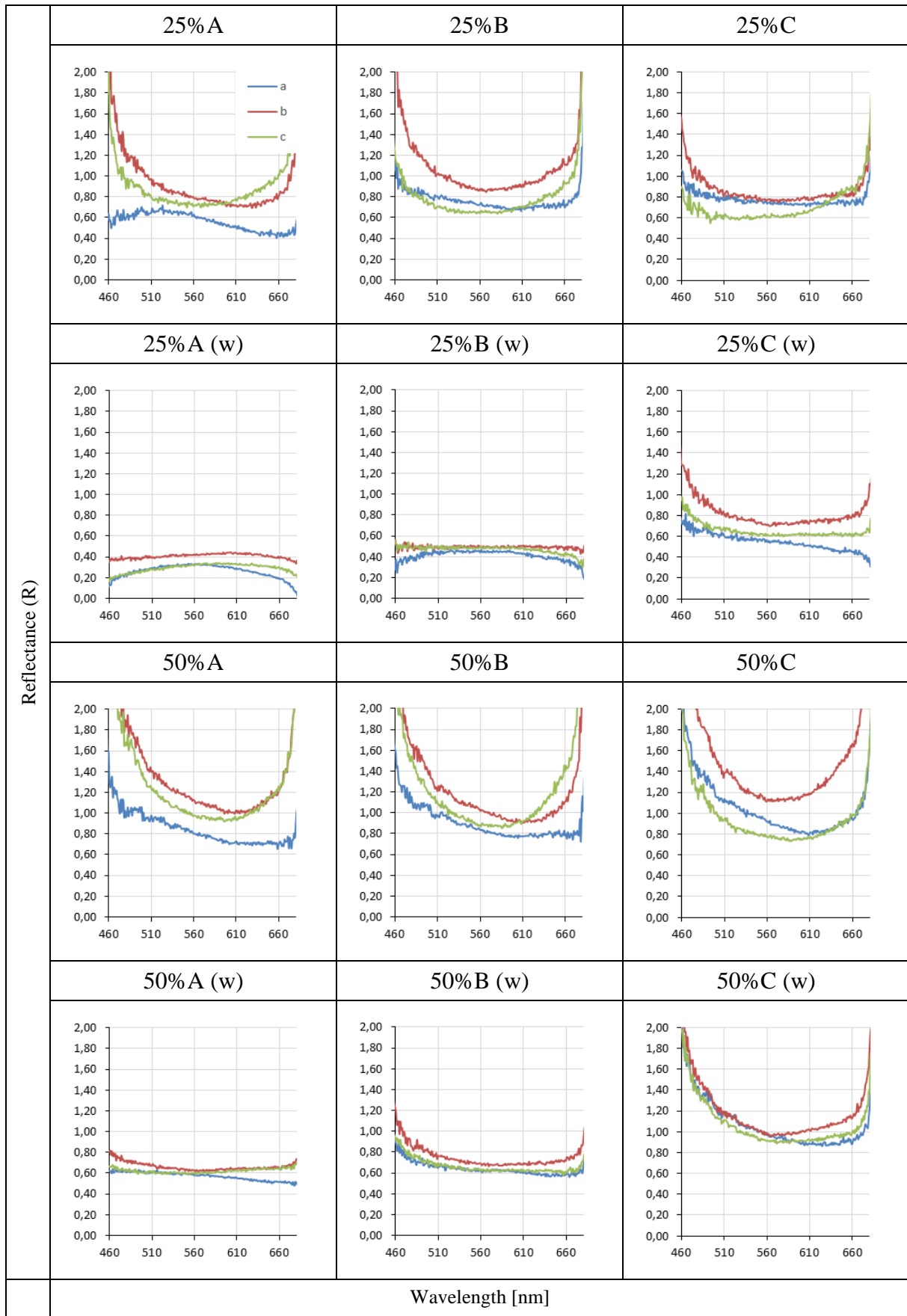


**Table A.2** Artificial sediment samples

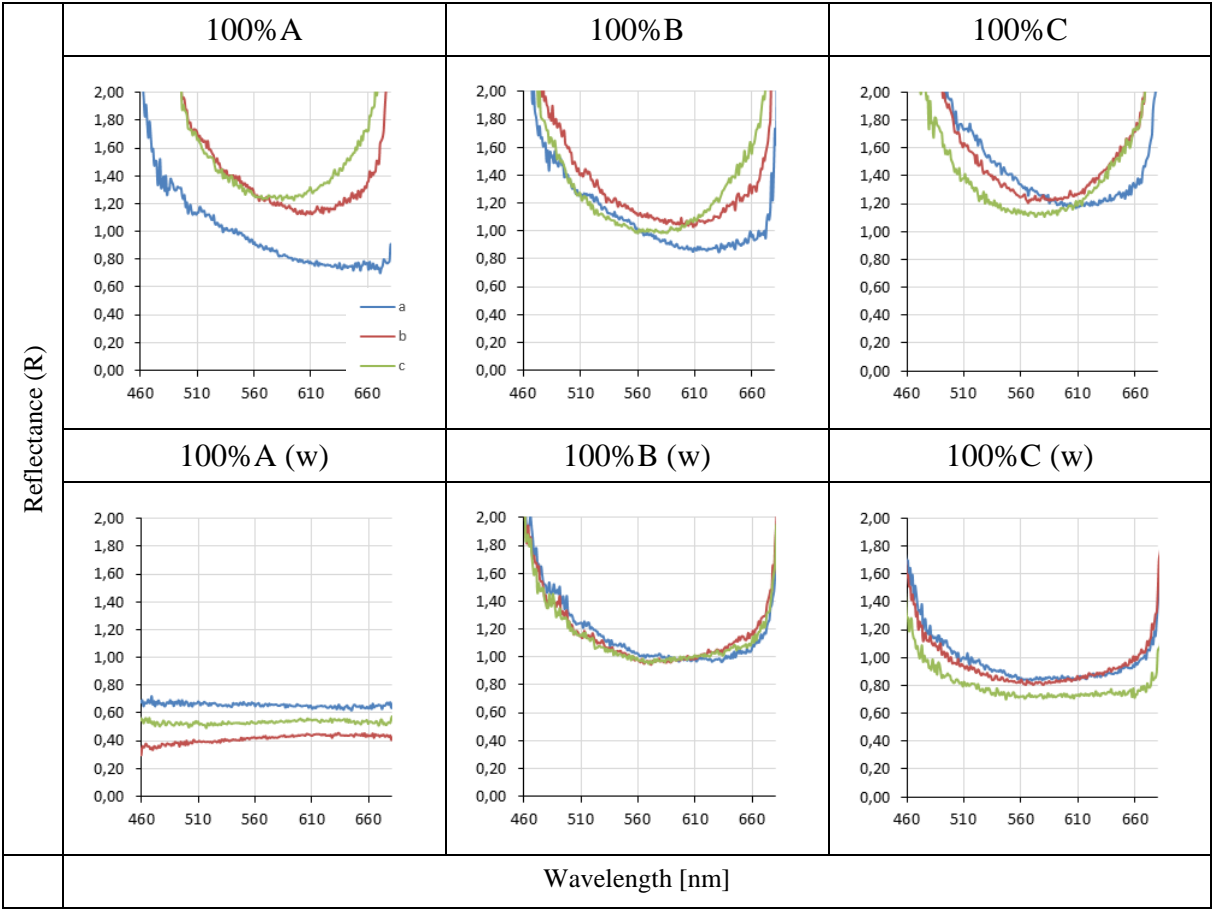




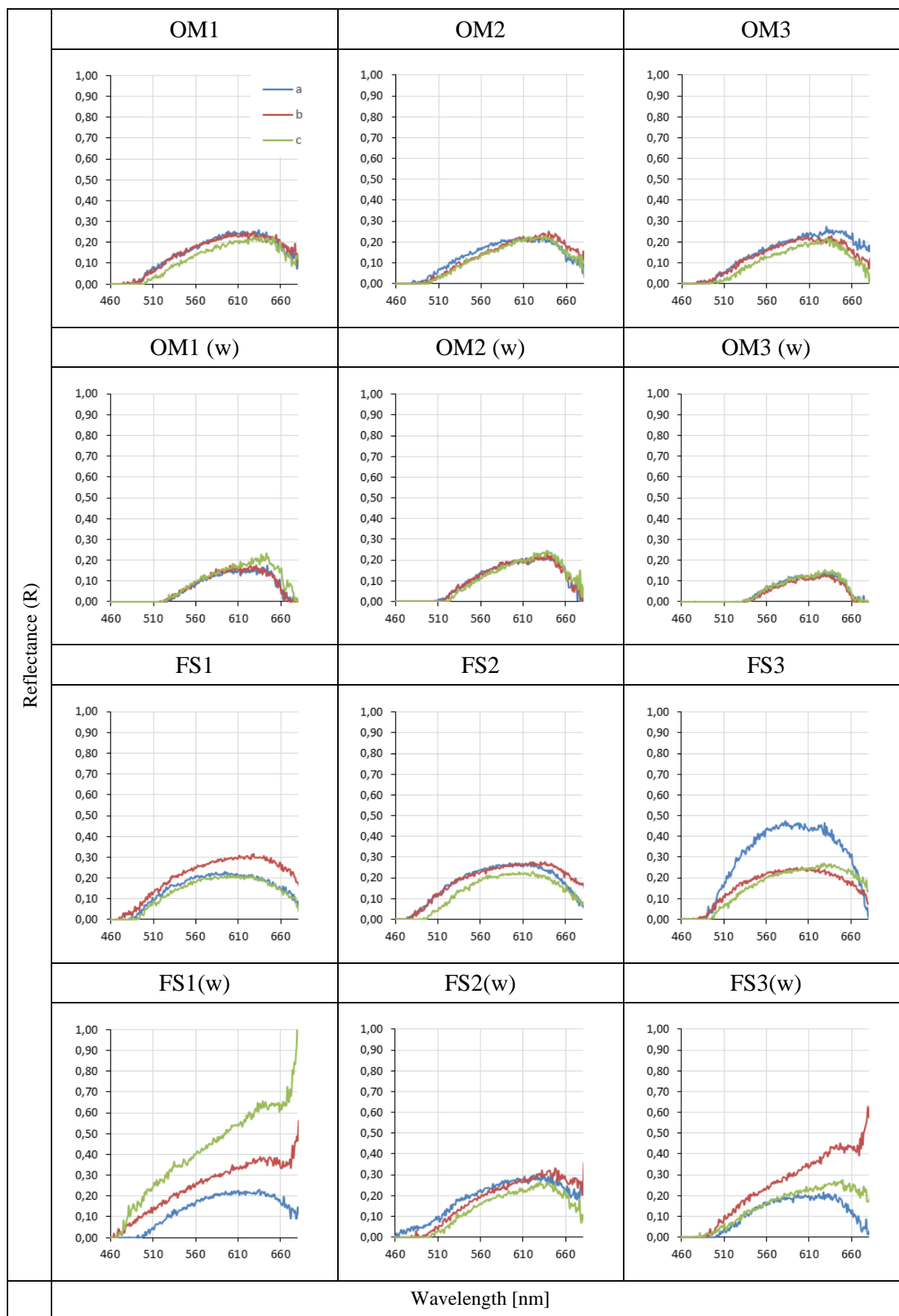


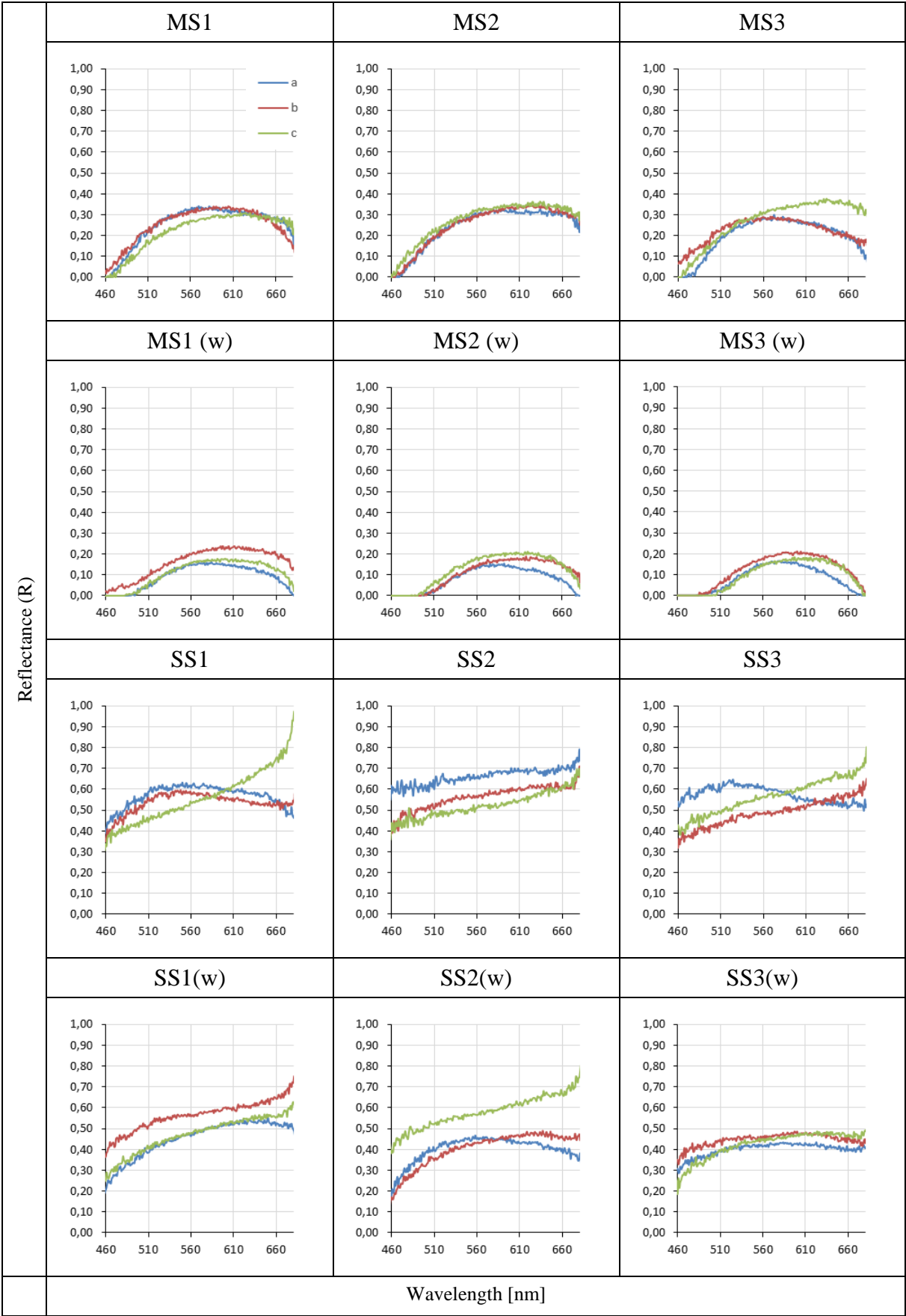


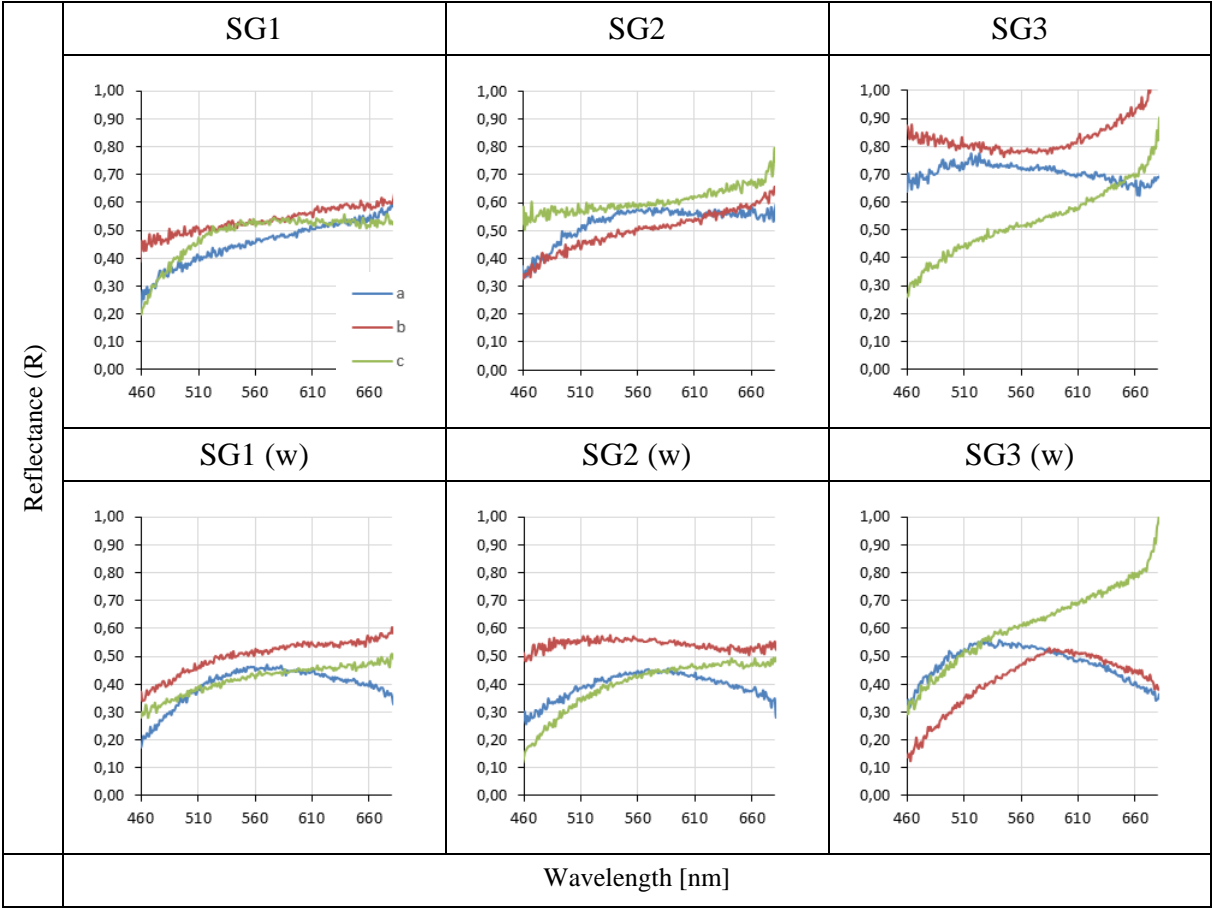




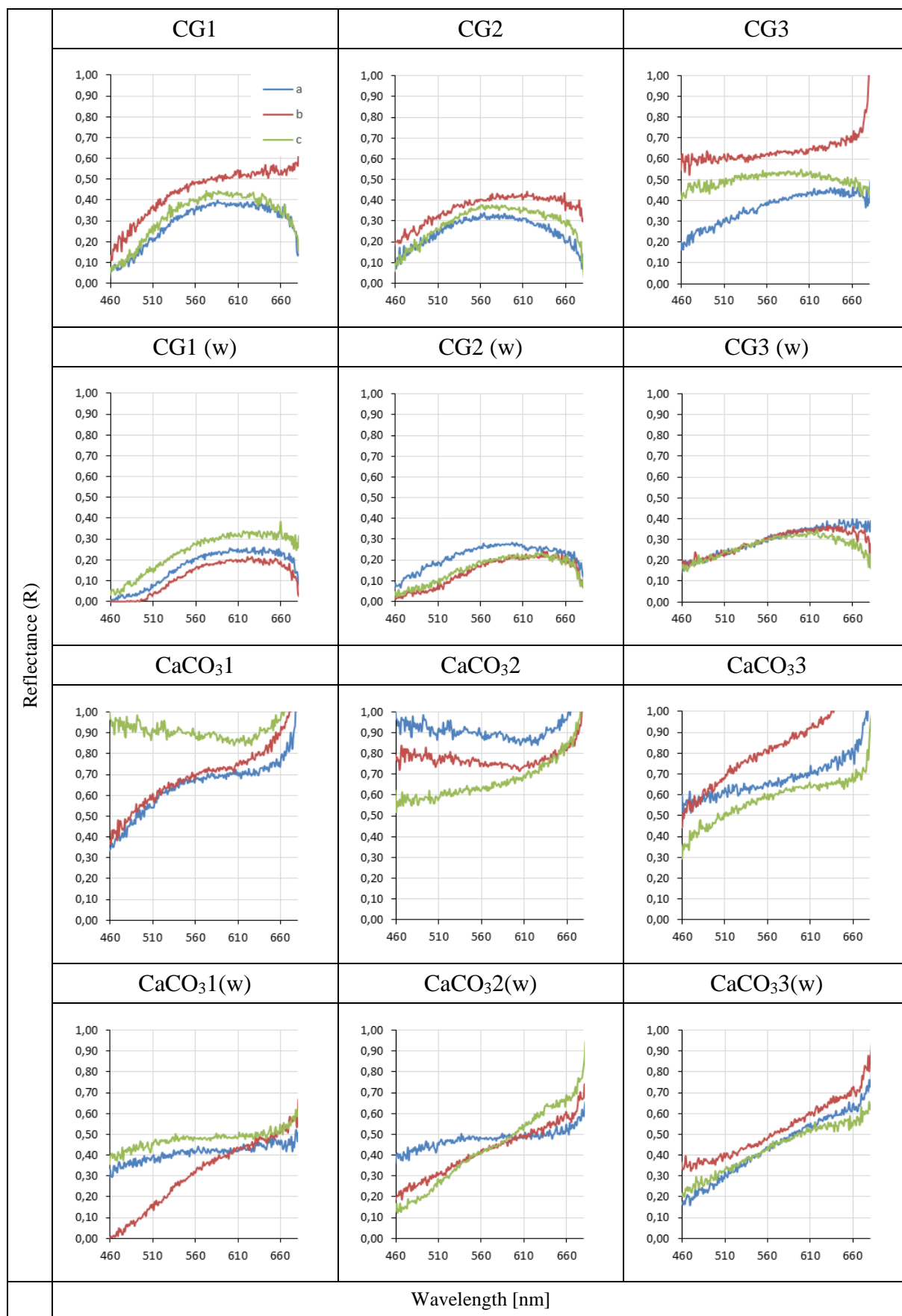
**Table B.3** Natural sediment samples

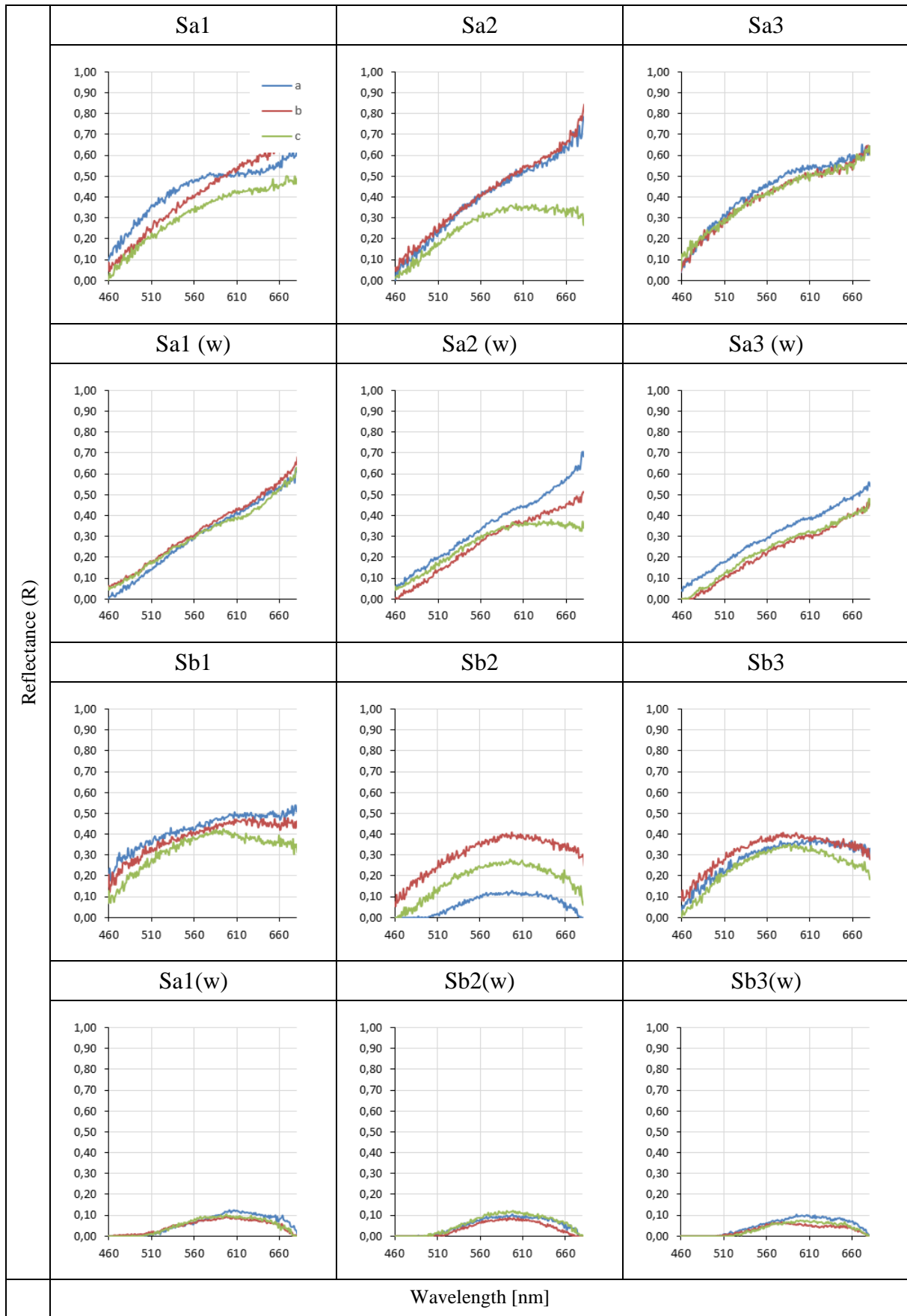


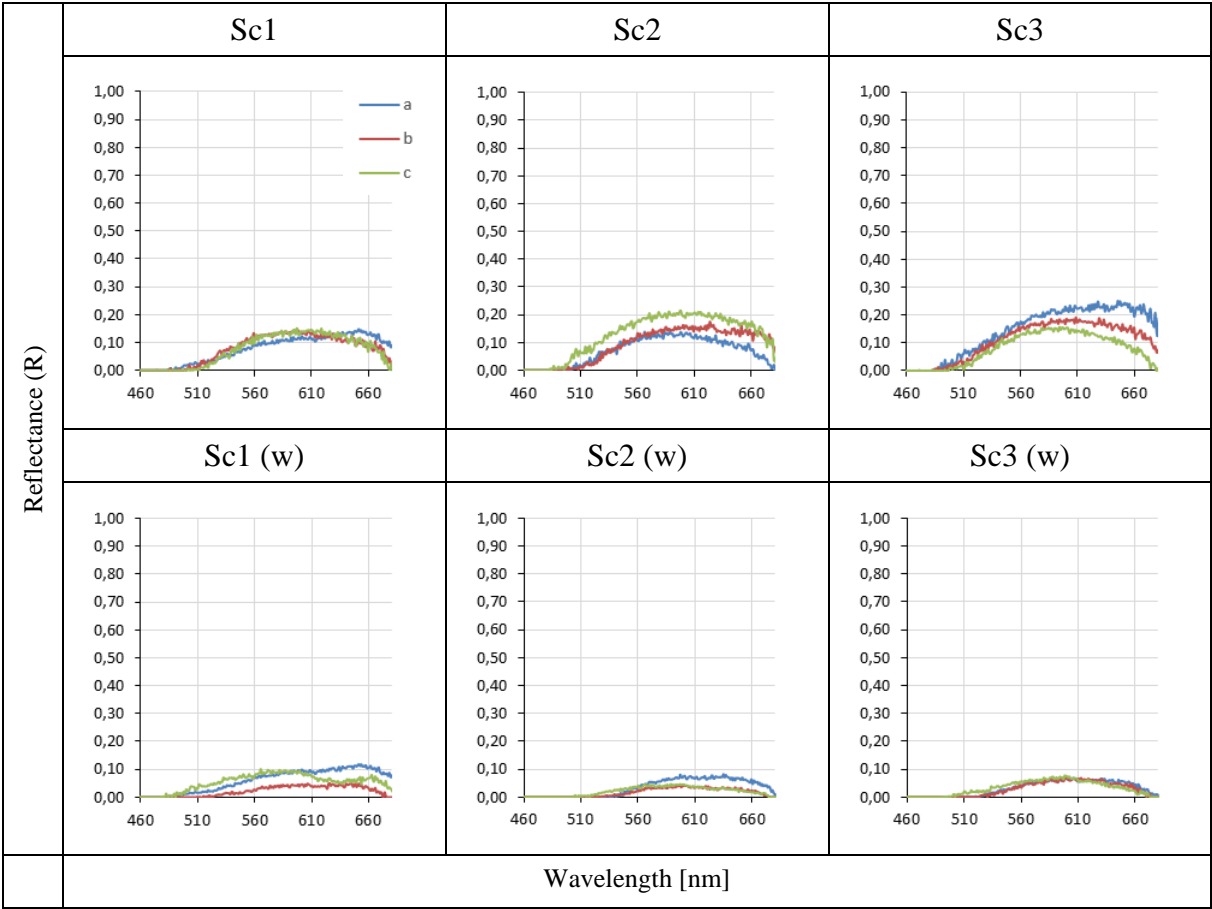




**Table B.4** Carbonate crust samples











## Appendix D – Visual description of natural sediment samples provided by NGU

*Table D.1 A visual description by NGU of the samples provided to the laboratory tests.*

Prøve-nummer	Vanddyb	Skjellsand-kategori	Sedkorn Str_Tekst	Karbonatinnhold-prosent	Sortering Visuelt	Prosentandel Skjellbiter over 1cm	Farge	Kornfraksjoner avtagende	Fauna	Kalk-alger	Kommentar	Bildefil
P1306019	30	Rein skjellsand	Grov sand	90	G	<1	Gråhvit	gs,ms,vgs			Tobis (fisk), Munida (crustacea)	P6172323
P1306020	28	Rein skjellsand	Grov sand	90	G	1	Gråhvit	gs,ms,vgs	A,B	E	4 kuskjell, 1 blåskjell	P6172324
P1306021	18	Rein skjellgrus	Sandholdig grus	90	G	1	Gråhvit	gr,vgs,ms	A			P6172325
P1306025	28	Ikke skjellsand	Organisk slam	0	G	<1	Brun	s,l,vfs	G		brun alge blandet it sedimenter, dårlig lukt	P6182332
P1306026	36	Ikke skjellsand	Organisk slam	0	G	<1	Brun	s,l,vfs			brun alge blandet it sedimenter, dårlig lukt, noen få skjellbiter	P6182333
P1306042	42	Rein skjellgrus	Sandholdig grus	90	M	5	Hvit/grå/rosa	gr,vgs,gs			knust og uknust skjell	P6182354
P1306046	33	Rein skjellgrus	Sandholdig grus	90	M	8	Hvit/lila/grå	gr,vgs			noen små stein	P6182367
P1306054	28	Rein skjellsand	Grov sand	85	G	3	hvit,grå,+div	vgs,gs,gr,ms	D	E	liten E (rugl)	P6182375
P1306079	9	Ikke skjellsand	Sand	20	G	1	mørk brun/grå/svart	ms,fs	A		liten prøve. blandet korn farger	P6202405
P1306108	85	Urein skjellgrus	Sandholdig grus	70	M	1	brun + div	gr,vgs,gs			2 forsøk.grus av små kuskjeller + polychaete rør. Litt sand, noen stein.	P6212448
P1306118	51	Urein skjellgrus	Sand	50	G	<1	lysbrun + div	ms,gs,vgs	A		små levende kuskell.	P6212464
P1306127	66	Ikke skjellsand	Sand	40	G	<1	olivengrå/lysbrun	ms,gs,fs	D		litt knust skjell/polychaete rør	P6212471
P1306131	76	Ikke skjellsand	Sand	30	G	<1	lysbrun + svart	ms,gs,vgs,gr			noen stein 1-7cm (several angular), noen skjellbiter	P6212473
P1306148	58	Ikke skjellsand	Fin sand	10	G	<1	mørk gråbrun	fs,s,gs			dårlig lukt. Litt brun alge.	P6222501